HAL
open science

Surface properties of complex intermetallics at the nanoscale : from fundamentals to applications

Kanika Anand

To cite this version:

Kanika Anand. Surface properties of complex intermetallics at the nanoscale : from fundamentals to applications. Materials Science [cond-mat.mtrl-sci]. Université de Lorraine, 2018. English. NNT : 2018LORR0239 . tel-02103063

HAL Id: tel-02103063

https://hal.univ-lorraine.fr/tel-02103063v1

Submitted on 18 Apr 2019

HAL is a multi-disciplinary open access archive for the deposit and dissemination of scientific research documents, whether they are published or not. The documents may come from teaching and research institutions in France or abroad, or from public or private research centers.

L'archive ouverte pluridisciplinaire **HAL**, est destinée au dépôt et à la diffusion de documents scientifiques de niveau recherche, publiés ou non, émanant des établissements d'enseignement et de recherche français ou étrangers, des laboratoires publics ou privés.

UNIVERSITÉ DE LORRAINE

AVERTISSEMENT

Ce document est le fruit d'un long travail approuvé par le jury de soutenance et mis à disposition de l'ensemble de la communauté universitaire élargie.

Il est soumis à la propriété intellectuelle de l'auteur. Ceci implique une obligation de citation et de référencement lors de l'utilisation de ce document.

D'autre part, toute contrefaçon, plagiat, reproduction illicite encourt une poursuite pénale.

Contact : ddoc-theses-contact@univ-lorraine.fr

LIENS

Code de la Propriété Intellectuelle. articles L 122. 4
Code de la Propriété Intellectuelle. articles L 335.2- L 335.10
http://www.cfcopies.com/V2/leg/leg_droi.php
http://www.culture.gouv.fr/culture/infos-pratiques/droits/protection.htm

THÈSE

pour l'obtention du diplôme de:

Docteur de l'Université de Lorraine

Spécialité: Science des matériaux

Présentée par:

KANIKA ANAND

Surface properties of complex intermetallics at the nanoscale: from fundamentals to applications

Thèse défendue le 13 décembre 2018 à Nancy

Composition du jury:

M. Stéphane Andrieu	Professeur	Examinateur
M. Geoffroy Prévot	Chargé de recherche	Examinateur
Mme. Christine Goyhenex	Chargée de recherche	Rapporteure
Mme. Corinne Lacaze-Dufaure	Professeur	Rapporteure
Mme. Émilie Gaudry	Professeur	Co-directrice
M. Julian Ledieu	Directeur de recherche	Directeur

Equipe 203, métallurgie et surfaces

IJL, UMR CNRS *7198, Université de Lorraine, 54011 Nancy cedex, France*

"Il y avait dans le monde un langage que tous comprenaient. C'était le langage de l'enthousiasme, des choses faites avec amour et envie, à la recherche de quelque chose que l'on désirait ou en quoi l'on croyait. "

L'Alchimiste

"The only way to do great work is to love what you do. If you haven't found it yet, keep looking. Don't settle."

-Steve Jobs

Acknowledgements

I would like to express my sincere gratitude to my two supervisors Prof. Émilie Gaudry and Dr. Julian Ledieu for their unconditional support during my thesis. Their guidance helped me in all respect of research and effective writing of this manuscript. I could not have imagined having better advisors for my Ph.D study. My thesis wouldn't have been complete without the mentor-ship of Dr. Vincent Fournée, who introduced me to the world of complex intermetallic surfaces and gave me the opportunity to work in équipe 203. I feel extremely blessed to have worked with these three researchers who have taught me that nothing is impossible if you have a passion for it.

Besides my advisors, I would like to specially thank Prof. Corinne Lacaze-Dufaure and Dr. Christine Goyhenex for investing their time to review and report on this thesis. My sincere thanks to Dr. Geoffroy Prévot and Prof. Stéphane Andrieu for their insightful comments and encouragement. I thank all my jury members for their thoughtful questions and remarks which inspired me to see my research from various new perspectives.

Thanks to Prof. Yuri Grin for sharing his expertise in understanding the subtleties of clathrate compounds. Thanks as well to Dr. Christophe Candolfi for having a brief discussion on clathrate compounds in order to prepare well for my defense.

I would like to deeply thank Dr. Ajay Shukla and Dr. J.J. Pulikkotil for enlightening my way in research and for their precious support.

A big thank you to rest of my team members and colleagues Marie-Cécile De Weerd, Muriel Sicot, Joris Kadok, Firas Abdel Hamid, Matthias Meier, Philippe Scheid, Yanis Sassi, Valentin Desbuis, Grégoire Caron, Corentin Chatelier, Dominique Dubaux for interesting discussions and conversations. Special thanks to my friends in IJL Jacob Kennedy, Martín Cisternas, Karthik Jeyabalan, Suresh Kumar Pillai, Yuze Li, Jiaqi Luo, Fahad Mohammed F. Alnjiman, Dorra Ibrahim, Selma Sassi, Soufiane EL Oualid, Shantanu Misra and Catalina Ruano-Merchan for fun-filled lunch and coffee breaks making time spent in IJL cheerful and memorable.
Thanks of course to all the administrative staff and IT staff specially Christine Schwartz and Francis Kosior for their assistance in managing the administrative things.

Thank you Saikat da for your friendship, pleasant presence and for all the spiced up food. Thank you Christel and Franck for your kind friendship. Christel, I cannot be more grateful to you for teaching me and being my loving Professor of French. Thanks to all my friends back home.

Last but not the least, I would like to thank and express my sincere regards to all my family members and also members of my new family. Thank you momi and papa for life, your love, support and encouragement to pursue my dreams. I feel proud to be your daughter. Thanks to Yatin (*my bro*) for being my dearest friend and a big support.

Thank you love of my life Akshay *aka* AB. You are first my best buddy and then an extremely warm person. Somewhere someone was very happy with me that I could have a partner like you. I would also like to thank my mother-in-law and father-in-law for bringing AB in this world and for their moral support.

Thank you to all the people (apologies if forgot to mention your names), who I have came across during my life journey and in some way they have affected it positively and have helped me in becoming a better person.

Contents

Acknowledgements v

Table of contents ix

List of Figures xvii

List of Tables xx

List of Abbreviations xxi

1 Introduction 1
- 1.1 Intermetallic clathrate compounds . . . 1
  - 1.1.1 Types of clathrates . . . 2
  - 1.1.2 Zintl-Klemm electron counting rule . . . 2
  - 1.1.3 Structural and electronic properties of Ba-Au-Ge and related type-I clathrates . 4
- 1.2 Wetting properties of Al-based complex intermetallics . . . 6
  - 1.2.1 Definition . . . 6
  - 1.2.2 How to measure the intrinsic wetting properties using a metal as a probe? . . . 7
  - 1.2.3 Wetting of CMA surfaces: previous results . . . 8
- 1.3 Objectives of the thesis . . . 8
- 1.4 Thesis architecture . . . 9

2 Methods 11
- 2.1 Experimental Methods . . . 11
  - 2.1.1 Single Crystal Growth . . . 11
  - 2.1.2 Experiments under UHV . . . 12
  - 2.1.3 Low-Energy Electron Diffraction . . . 13
  - 2.1.4 X-ray Photoelectron Spectroscopy . . . 15
  - 2.1.5 Scanning Tunneling Microscopy . . . 19
  - 2.1.6 Wetting experiments under UHV . . . 21
    - 2.1.6.1 Dosing Pb . . . 21
    - 2.1.6.2 Dewetting . . . 21
    - 2.1.6.3 Scanning Auger Microscopy (SAM) . . . 22
    - 2.1.6.4 Scanning Electron Microscopy (SEM) . . . 23
    - 2.1.6.5 AES . . . 24
    - 2.1.6.6 Instrumentation: Scienta-Omicron Nano-SAM lab . . . 25
- 2.2 Computational Methods . . . 26
  - 2.2.1 Introduction . . . 26
  - 2.2.2 Many-body Schrödinger equation . . . 27
  - 2.2.3 The Density Functional Theory . . . 28
    - 2.2.3.1 The Kohn Sham Method . . . 28
    - 2.2.3.2 Approximate Exchange and Correlation functions . . . 30
    - 2.2.3.3 Self-consistent cycle . . . 31
    - 2.2.3.4 Bloch's theorem and plane-wave basis set . . . 31

2.2.4 Implementation of DFT: VASP code . . . 33
2.2.4.1 Periodic systems: Slabs . . . 33
2.2.4.2 The Pseudopotential Approximation . . . 33
2.2.4.3 Convergence parameters . . . 34
2.2.5 Thermodynamic Calculations . . . 36
2.2.5.1 Cohesive energy and formation enthalpy . . . 36
2.2.5.2 Surface energy . . . 38
2.2.5.3 Adsorption energy . . . 39
2.2.5.4 Adhesion energy . . . 40
2.2.6 Electronic Structure Calculations . . . 40
2.2.6.1 Simulated STM . . . 40
2.2.6.2 Density of States (DOS) . . . 41
2.2.6.3 Electron localization function . . . 41
2.2.6.4 Bader charge analysis . . . 42
2.3 Conclusion . . . 44

3 Structural investigation of BaAuGe(100) surface 45
3.1 Overview . . . 45
3.2 Introduction . . . 45
3.3 Experimental Details . . . 48
3.4 Computational Details . . . 48
3.5 Experimental results . . . 49
3.6 Theoretical results . . . 49
3.7 Discussion . . . 50
3.8 Conclusion . . . 54

4 Structural analysis of the Ba-Au-Ge (110) surface 55
4.1 Introduction . . . 55
4.2 Brief methodology . . . 56
4.3 Experimental Results . . . 57
4.3.1 LEED . . . 57
4.3.2 XPS . . . 58
4.3.3 STM . . . 59
4.4 DFT Results . . . 63
4.4.1 Description of the surface models . . . 63
4.4.2 Energetics . . . 64
4.4.3 Surface relaxations . . . 68
4.4.4 Simulated STM images . . . 69
4.4.5 Comparison of experimental and stimulated STM images . . . 72
4.4.6 Electron localization function . . . 73
4.4.7 Bader charge analysis . . . 74
4.4.8 Density of States . . . 79
4.4.9 Work function . . . 80
4.5 Comparison between the BaAuGe(110) and BaAuGe(100) surfaces . . . 82
4.6 Conclusion . . . 83

5 Wetting properties: from simple metals to Al-based complex intermetallic surfaces 85
5.1 Introduction . . . 85
5.2 Contact angle measurements under UHV . . . 85
5.2.1 Why Pb is used as a metal probe? . . . 85
5.2.2 Sample preparation . . . 86
5.2.3 Measurements of contact angle . . . 86

5.2.4 Determination of contact angles . . . 86
5.2.4.1 Influence of the droplet size . . . 87
5.2.4.2 Influence of tilt . . . 90
5.2.4.3 Summary of contact angle measurements . . . 90
5.2.5 AES on Pb/CMAs . . . 92
5.3 Theoretical Methods . . . 95
5.3.1 Interfacial energy calculations . . . 95
5.3.2 Interfacial energy and contact angle . . . 95
5.3.3 Pb/Al(111) interface . . . 97
5.3.3.1 Structure of the interface . . . 97
5.3.4 Interfacial energy . . . 98
5.3.4.1 Electronic structure of the Pb/Al(111) moiré . . . 100
5.3.5 The Pb/$Al_{13}Co_4$(100) interface . . . 103
5.3.5.1 Interfacial energy calculations . . . 104
5.3.5.2 Electronic structure of Pb/$Al_{13}Co_4$(100) (coverage = 0.084 at./Å^2) . . . 104
5.4 Conclusion . . . 107

6 Conclusions and future outlook **111**
6.1 Conclusions . . . 111
6.1.1 Low index surfaces of the intermetallic clathrate Ba-Au-Ge . . . 111
6.1.2 Wetting properties of Al-based complex intermetallic surfaces . . . 112
6.2 Future outlook . . . 113

7 Résumé en français **115**
7.1 Introduction . . . 115
7.1.1 Les phases intermétalliques complexes et leurs surfaces . . . 115
7.1.2 Objectifs de la thèse . . . 115
7.2 Surfaces de bas indice du composé cage Ba-Au-Ge . . . 116
7.2.1 Le clathrate Ba-Au-Ge . . . 116
7.2.2 Résultats expérimentaux . . . 117
7.2.3 Calcul des énergies de surface et simulation d'images STM . . . 117
7.2.4 Facteurs à l'origine du modèle de surface observé . . . 118
7.3 Propriétés de mouillage d'intermétalliques complexes à base d'aluminium . . . 118
7.3.1 Approche expérimentale . . . 119
7.3.2 Approche théorique . . . 119
7.3.2.1 Pb/Al(111) . . . 119
7.3.2.2 Pb/$Al_{13}Co_4$(100) . . . 119

A Additional information on BaAuGe(100) **121**

B Some additional test calculations using DFT **125**
B.1 Cut-off energy and k-point grid . . . 125
B.2 Smearing methods . . . 125
B.3 DOS of bulk o-$Al_{13}Co_4$ . . . 127

C Supplementary material on wetting properties of metallic surfaces **129**
C.1 Wetting experiments . . . 129
C.2 DFT calculations: electronic structure of Pb/Al(111) moiré . . . 131

Bibliography **133**

List of Figures

1.1 Crystal structures of type-I, type-II, type-III, type-VIII, and type-IX intermetallic clathrates. Different types of cages constituting these structures are also shown [14]. 2
1.2 Classification of intermetallic clathrates based on the charge polarity of the host cages. 3
1.3 (Left) Atomic basins (QTAIM atoms) in the ideal bulk structures of $Ba_8Ge_{40}E_6$ where E is the substitution at $6c$ Wyckoff position. (Right) The effective QTAIM charges depending on relative electronegativity of constituent atoms [17]. 6
1.4 Contact angle and interfacial energies [33]. 7
1.5 Empirical correlation observed between the contact angles of liquid Pb deposited at different substrate surfaces and the melting temperature of substrates (red line is only a guide to the eye). Encircled data point emphasize on the high θ value of Pb deposited on the i-Al-Pd-Mn (QC) single grain [42]. 8

2.1 $Ba_8Au_{5.25}Ge_{40.3}\square_{0.45}$ single crystal showing the faces perpendicular to (a) [100] and (b) [110] directions. 12
2.2 Experimental setup under UHV in the IJL laboratory. 12
2.3 Schematic of LEED apparatus: Electrons of K.E. E_p from electron gun are directed towards the sample and the grids (1-4) ensure only elastically scattered electrons to reach fluorescent screen. (Inspired from [45]) 13
2.4 Schematic of XPS showing the basic principle of the technique. 16
2.5 XPS peak of Ba $3d$ doublet (according to the multiplicity) value on the BE scale. The Shirley background (in blue) has been applied to the peaks and also the fitted components are shown. 19
2.6 Schematic of STM: (a) A simplified model of the STM instrument, where sample and metallic probe (tip) are shown in atomic scale; (b) DOS of the tip and the negatively biased sample (surface) in the vicinity of E_f showing the tunneling of electrons (I_t) from occupied states of the sample to empty states of the tip (adapted from [46]). . . . 20
2.7 Scienta-Omicron Nano-SAM experimental set up in IJL laboratory. 22
2.8 (Left) Dewetting of Pb film on Al_5Co_2(001). (Right) Schematic representation of temperature ramp during dewetting process. 22
2.9 Schematic of SEM [From [64]]. 23
2.10 Schematic showing the three steps involved in the Auger process. The KL_2L_3 Auger transition is illustrated. The open and filled circles represent holes and electrons, respectively. [From [65]]. 25
2.11 A survey scan performed on Pb droplets. Inset: It shows the SEM image imported in Matrix software to define particular area for AES. Top: The N(E) curve showing the AES data for the specific area marked in the inset. Bottom: the Auger spectra in its differential form ($dN(E)/dE$ versus kinetic energy) to highlight the small peaks. The red star marks the main Pb peak in the differentiated Auger spectra. 26
2.12 Flow chart showing the steps executed in a self-consistent cycle [taken from Ref. [86]]. 32
2.13 Illustration of the supercell approach to model surfaces. 33
2.14 Illustration of the pseudopotential concept. 34
2.15 Total energy of bulk $Ba_8Au_6Ge_{40}$ as a function of cut-off energy (ENCUT) for a k-point mesh: $8 \times 8 \times 8$. 35

2.16 Total energy of bulk $Ba_8Au_6Ge_{40}$ as a function of a k-point mesh: $i \times i \times i$ using ENCUT value of 300 eV. 36
2.17 Schematic sketch of the chemical potential ranges of ternary Ba-Au-Ge cage compound (inspired from Ref. [103]). 39
2.18 A free standing slab with two adlayers of Pb. 40
2.19 Bulk density of states. 42
2.20 (Left panel) ELF map at x=0.5 (top) and at x=1.0 showing various localization regions indicating covalent interactions while (Right panel) ELI map taken from Ref.[18] highlight similar features. 43
2.21 Bader atomic regions in $Ba_8Au_6Ge_{40}$ intermetallic clathrate and the effective charge transfer between the atoms. 44

3.1 Top: Structure of the $Ba_8Au_6Ge_{40}$ type-I clathrate, viewed as a stacking of F and P slices along the [100] direction (left) or as a cage compound (right). The tetrakaidecahedra are shown in green while the dodecahedra are represented in blue. Bottom: Surface models (top and side views) considered in the study. Atoms are represented by circles (Ba green, Au yellow, Ge blue). Faded colors indicate atoms lying slightly below the surface. 47
3.2 Distortion index and ECoN of the cages on elongating the bulk in direction perpendicular to its (100) plane. 48
3.3 Elemental near-surface composition measured as a function of the photoelectrons take-off angle for the sample annealed at 833 K. The measurements at 70° are more surface sensitive than those implemented at 20°. The dashed lines correspond to bulk composition, while the solid lines are linear fit to data points and are only a guide for the eyes. 50
3.4 Variation of the near-surface composition as a function of annealing temperature (K) at constant value of take-off angle equal to 45°. 51
3.5 (a) LEED pattern of the $Ba8Au_{5.25}Ge_{40.3}\square_{0.45}$ (100) surface annealed at 785 K and recorded at primary beam energy of 19 eV. (b) 70×70 (nm^2) STM image of the BaAuGe(100) surface prepared at 933 K (V_b = -2 V; I_t = 0.08 nA) with an inset histogram showing the unique step height of this layered material (5.0 ± 0.2 Å). 51
3.6 Top: 4.32 × 4.32 nm^2 STM image obtained at $V_b = \pm$ 0.5 V. The apparent non-periodic pattern may be caused by both the preparation and structural disorder. Bottom: Simulated 4.32 × 4.32 nm^2 STM images using the F^{Ba} model at $V_b = \pm$ 0.5 V. 52
3.7 Surface energies depending on the Ba and Au chemical potentials for the models considered. (a) F^{Ba} (b) P^{Ba} (c) F^{noBa} and (d) P^{noBa}. The white triangle represents the allowed area for chemical potentials. 52
3.8 Electron Localization Function for the F^{Ba} model. Side views plotted along the [010] direction ($\vec{b}$) at $y = 0$ (a) and $y = 0.25$ (b). 53
3.9 Contributions of the surface and subsurface planes (S and S-2, respectively) to the density of states for the F^{Ba} model. The black line is the total DOS of the surface, the dotted blue line is the "bulk-like" contribution. The Au $5d$, Ba $5d$, Ge $4p$ are plotted in cyan, green and magenta, respectively. 53

4.1 (a) Bulk structure of $Ba_8Au_6Ge_{40}$ type-I clathrate ; (b) Bulk tetragonal cell for $Ba_8Au_6Ge_{40}$, viewed as a stacking of planes along the [110] direction or as a cage compound. The atoms are depicted as spheres in cyan (Ba1), green (Ba2), yellow (Au1), magenta (Ge1) and blue (Ge2). The blue cages are dodecahedra while in green tetrakaidecahedra cages are exhibited. 56

4.2 (Left) LEED pattern of the $Ba_8Au_{5.25}Ge_{40.75}$(110) surface annealed at 992 K recorded at primary beam energy of 25 eV. (Right) LEED pattern recorded at 49 eV under almost similar annealing temperature (983 K). Two LEED apparatus have been used here, hence explaining the different sample orientation. 57
4.3 (a) Variation of the near-surface composition as a function of annealing temperature (K) at constant value of take-off angle equal to 45°. (b) Variation of elemental composition of (110) surface of $Ba_{14.9}Au_{9.8}Ge_{75.3}$ clathrate as function of take-off angle at 983 K. The dashed green, orange and blue lines present in both graphs correspond to bulk composition of Ba, Au and Ge, respectively. The solid colored lines in (b) are linear fit to data points for guide to eyes. 58
4.4 (a) A 40×40 nm^2 STM image of the $Ba_8Au_{5.25}Ge_{40.75}$ (110) surface prepared at 1003 K (V_b= -1.4 V ; I_t= 0.09 nA). (b) A histogram showing the unique step height of the (110) surface = 7.60± 0.15 Å∼ $a\sqrt{2}/2$. (c) 40×40 nm^2 STM image showing (110) surface plane obtained at 1003 K (V_b= -1.4 V ; I_t= 0.08 nA) with an inset showing the FFT image of the corresponding STM image. d) A 10×10 nm^2 Fourier filtered image corresponding to Fig. 4.4(c) showing the fine structure on the terrace. The surface unit cell is superimposed on the image. 60
4.5 (a1) A 40×40 nm^2 STM image of the $Ba_8Au_{5.25}Ge_{40.75}$ (110) surface prepared at 886 K (V_b= -0.6 V ; I_t= 0.08 nA) . (a2) FFT image of the surface. (a3) A 10×10 nm^2 Fourier filtered image corresponding to a region of Fig.4.5(a1). (b1) STM image (28.5×28.5 nm^2) of the (110) surface prepared at 926 K (V_b= $+1.4$ V ; I_t= 0.12 nA) (b2) FFT of the surface showing the diffraction pattern. (b3) Fourier filtered zoom (10×10 nm^2) showing an uniform zig-zag pattern for the positive bias. 61
4.6 STM images for the same bias voltage (V_b= -1.0 V) and different annealing temperatures. (Left) (a1) A 20×20 nm^2 STM image (I_t= 0.08 nA) obtained by annealing the surface to 1003 K. (b1) The size of the image is 40×40 nm^2 (I_t= 0.09 nA) and the corresponding annealing temperature is 886 K. (Right) (a2); (b2) Fourier filtered image corresponding to a 10×10 nm^2 region of Fig. 4.6 (a1); (b1), respectively. 62
4.7 STM and LEED images demonstrating the presence of roughening and faceting on the (110) surface prepared at low annealing temperatures or for insufficient annealing time (< 1h). (a1) STM image of size 30×30 nm^2 for V_b= -1.4 V. (a2) Corresponding LEED pattern obtained at 18 eV for the surface prepared at 898 K for 15 min. (a3) Fourier filtered zoom (size: 7.6×5.4 nm^2) of (a1) image. (b1) A 9×12 nm^2 STM image at V_b= $+1.4$ V obtained by annealing the surface first at 540 K for 90 min and then at 797 K for 30 min. (b2) LEED pattern at 18 eV of the surface shown in (b1). (b3) Zoom (size: 7.6×6.2 nm^2) corresponding to (b1). 63
4.8 Schematic demonstrating the link between the cage preserving P- and C-type surface models. The relation of non-cage preserving, p and F models is also shown with C-type models. 64
4.9 Side and top views of P-type surface models, preserving the nanocages at the surface. Atoms are represented by circles (Ba green, Au yellow, Ge blue). Faded colors indicate atoms lying slightly below the surface. 64
4.10 Side and top views of C-type surface models, preserving the nanocages at the surface and of the non-cage preserving models (F;p). Atoms are represented by circles (Ba green, Au yellow, Ge blue). Faded colors indicate atoms lying slightly below the surface. 65
4.11 The three-dimensional (X:$\Delta\mu_{Ba}$,Y: $\Delta\mu_{Au}$ and Z: γ) surface energy diagram for the considered surface models within the potential limits of Ba and Au. 66
4.12 Surface phase diagram for the $Ba_8Au_6Ge_{40}$(110) surface, calculated within DFT-D3. . . 68
4.13 Surface phase diagram for the $Ba_8Au_6Ge_{40}$(110) surface, calculated within PBE. 68

4.14 Distorsion index calculated for the two types of cages [Ge_{20} and $(Ge,Au)_{24}$] of the considered surface models. The ^{P} and ^{B} superscripts stand for Protruding and Buried, respectively. 70
4.15 Simulated STM images of a 3×6 unit cell for the considered models. 71
4.16 (Top) 9.9×4.8 nm^2 STM images obtained at $V_{bias} = \pm 0.6$ V (Top) and $V_{bias} = \pm 1.4$ V (bottom) using P^{Ba}, P^{Ba}_{Au}, C^{Ba} and P models. Experimental STM images (identical bias and image size) are also presented for a comparison with the surface models. 72
4.17 Electron localization function for P-type models is shown, (a) wih 4 surface Ba atoms and (b) with 2 surface Ba atoms. The regions of high charge localization are highlighted in white color. Top view 1 (x=0.61) shows ELF at extreme periphery of the surface while top view 2 (x=0.57) projects ELF at mean height of puckered surface plane. The black lines show the trace of the plane chosen for the side views (along the [1$\bar{1}$0] direction). 74
4.18 Representation of the Electron localization function using (a) C-type models and (b) non-cage preserving models. Top view 1 (x=0.61) shows ELF at extreme periphery of surface while top view 2 (x=0.57) projects ELF at mean height of puckered surface plane. The black lines show the trace of the plane chosen for the side views (along [1$\bar{1}$0] direction). 75
4.19 Average charge gain at each (bulk) Wyckoff site for the considered surface models using Bader charge analysis. The values calculated for the bulk and the one in the Ref. [17] are included. 76
4.20 Top view of surface unit cell of ideal (a) P-type, (b) C-type, (c) p and (d) F models showing the label of surface sites according to the bulk Wyckoff positions as mentioned in Tabs. 4.5 and 4.6. 77
4.21 The projected density of states (PDOS) of series of P^{Ba} models (with a variation in the Au content) showing the surface layer contribution. The Au $5d$, Ba $5d$, Ge $4p$ and Ge $4s$ states depicted cyan, green, magenta and magenta (dotted lines), respectively. . . . 79
4.22 The projected density of states (PDOS) of P-type models (with 2 surface Ba atoms) showing the surface layer contribution. The Au $5d$, Ba $5d$, Ge $4p$ and Ge $4s$ states depicted cyan, green, magenta and magenta (dotted lines), respectively. 80
4.23 Surface contribution of DOS for the C-type models. The Au $5d$, Ba $5d$, Ge $4p$ and Ge $4s$ states depicted cyan, green, magenta and magenta (dotted lines), respectively. 81
4.24 Density of states (PDOS) of non-cage preserving models (a) p and (b) F showing the surface contribution. The Au $5d$, Ba $5d$, Ge $4p$ are plotted in cyan, green and magenta, respectively. 81

5.1 Dewetting scheme used for the quasicrystalline surface. 86
5.2 Schematic for contact angle measurements [33]. 87
5.3 SEM micrographs showing Pb droplets on (a) $Al_{13}Co_4$(010) and (b) Al_5Co_2(001). Some droplets are curve-fitted (black circles) for contact angle measurements. The red labels correspond to the droplet sizes in the respective tables 5.1 and 5.2. 88
5.4 Contact angle, θ_{avg}, of Pb droplets on single crystals: $Al_{13}Co_4$(010) and Al_5Co_2(001) as a function of their droplet size. The red line is a linear fit to the curve. 89
5.5 Contact angle, θ_{avg}, of Pb droplets on single crystal of (a) $Al_{13}Co_4$(010) and (b) Al_5Co_2(001), respectively, for different tilt values. The error bars represent the standard deviation in plotted data. 91
5.6 Contact angle, θ_{avg}, of Pb droplets on i-Al-Pd-Mn as a function of their droplet size. The red line is a linear fit to the curve. 91
5.7 SEM micrographs for different interfaces with Pb as a metal probe. The labels S1,S2 and so on correspond to the distinct interfaces studied in this work and are mentioned in Tab 5.3. 92

5.8 Contact angle, θ as a function of the bulk density of states at the Fermi level for the considered substrate. 93
5.9 Contact angle, θ as a function of melting point (°C) of the considered substrate. The red dotted-line highlights the linear trend for Pb/simple metals. All in-house measurements are shown in the colored labels. The labels in black correspond to the references mentioned in Tab 5.3. 93
5.10 (a) Auger spectra in the derivative mode of the surface $Al_{13}Co_4$(010) in between the Pb droplets obtained after dewetting. (b) The Auger peak of CoLMM on the surface of Al_5Co_2(001) in between the droplets. (c) Auger line scan on the Pb droplet present on the Al_5Co_2(001) surface. 94
5.11 Various interfacial energy contributions present in a slab with vacuum (left) and without vacuum (right). 96
5.12 (a) Schematic diagram of the $\sqrt{31} \times \sqrt{31}\ R8.95°$ higher-order commensurate structure (HOC) with dark circles representing the locations of Al atoms and light circles representing the locations of Pb atoms. The Al substrate, the Pb-layer and the HOC unit cell are shown by the red (2.86 Å), yellow (3.5 Å) and blue rhombi (15.9 Å), respectively [182]. The angle between the Al and Pb primitive unit cells is 19.84°. (b) Top view of theoretical model with 1 ML of Pb built following the experimental model in (a). The shown unit cell has lattice parameter of 15.9 Å. The blue spheres represent Al atoms while gray spheres denote Pb atoms. 98
5.13 (a),(b) Simulated STM images of 6×6 unit cell for bias value of -0.5 V. (c) Fourier filtered STM image obtained at bias voltage of -0.5 V. The size of the STM image is 6×6 nm^2.The green hexagon corresponds to the moiré unit cell in these STM images. . . . 101
5.14 DOS of the bulk (blue) and free standing of Pb (green). The calculation for bulk Pb was performed using ISMEAR = -5 and 45×45×45 k-point grid while for freestanding Pb layer, the latter value is 15×15×1. The lower panel shows DOS of Pb ML adsorbed on the Al(111) surface (using ISMEAR = -5 and 15×15×1 k-point grid). 102
5.15 (Left) DOS at the interface of Pb/Al(111) (moiré slab) with two Pb adlayers. The DOS contribution of Pb atoms at the interface layer is plotted in red and for Al atoms in blue. The DOS contribution from second layer of Pb (*i.e.* Pb_{int+1}) is shown in green. (Right) Zoom of DOS around Fermi level for Pb/Al(111). The calculation was performed using ISMEAR= -5 and 15×15×1 k-point grid. 102
5.16 Pb/$Al_{13}Co_4$(100) interface for the coverage of 0.084 at./$Å^2$. (a) The substrate surface is a puckered plane with 22 Al atoms (S2 model). (b) The substrate surface is represented by a puckered plane with 22 Al atoms and 2 Co atoms (S1 model). The protruding bipentagonal pattern of the topmost substrate layer is shown in pink (black) while the one slightly below the mean position of the topmost substrate layer is shown in grey (blue). The Co atoms are spheres in blue and Pb atoms are represented by large dark-grey spheres. The top view presents a 2×2 surface unit cell while the side view shows a 2×1 surface unit cell in both (a) and (b). 103
5.17 Modified surface energy of Pb/$Al_{13}Co_4$(100) system. 105
5.18 (a) A 18×18 nm^2 STM image showing 1 ML of Pb deposited on $Al_{13}Co_4$(100) at 573 K [191]. Simulated STM images of the Pb/$Al_{13}Co_4$(100) for a coverage of 0.084 at./Å. (b) A constant current and (c) a constant height simulated STM images of Pb on the S2 surface model for V_{bias} = -0.5 V. Similarly (d),(e) are corresponding to constant current and constant height, respectively of a Pb ML on the S1 surface model for the same bias. The size of the simulated STM images is 7.4 ×8.7 nm^2. 106

5.19 DOS at the interface of Pb/$Al_{13}Co_4$(100). Contributions of the interface (blue) and sub-interface (black) planes (*int* and *int-1*, respectively) to the density of states for the (a) S2 model and (b) S1 models representing the substrate. The red line is the total DOS of the adsorbed Pb ML (0.084 at./Å^2. The calculations was performed using ISMEAR =-5 and 1×11×11 k-point grid. 107
5.20 (Top panel) DOS of fcc crystalline Pb (blue) and freestanding layer of Pb (green) for a surface density equal to 0.084 at./Å^2. (Bottom panel) The DOS contribution of the Pb ML supported by S2 (black) and S1 (red) surfaces, respectively. 108

7.1 Structure du massif du composé clathrate $Ba_8Au_{5.25}Ge_{40.75}$. 116
7.2 Cliché de diffraction lents des surfaces $Ba_8Au_{5.25}Ge_{40.75}$(100) et the $Ba_8Au_{5.25}Ge_{40.75}$(110).117
7.3 Modèles de surface stable observée expérimentalent pour les surfaces (gauche) $Ba_8Au_{5.25}Ge_{40.75}$(100) et (droite) $Ba_8Au_{5.25}Ge_{40.75}$(110) 117
7.4 Images STM expérimentales et simulées des surfaces (100) et (110) du composé clathrate de type-I $Ba_8Au_{5.25}Ge_{40.75}$. 118

A.1 (a),(b),(c) Angle-resolved XPS Ba $3d_{5/2}$, Au $4f_{7/2}$ and Ge $2p_{3/2}$ core-level lines (shown by dotted black line), respectively, measured at 45° take-off angle. The red thin lines are XPS fitting curves (deconvoluted spectra) associated to the experimental spectra. The blue thin lines represent the background-type used in XPS fitting. (b) The remaining colored lines are the fit to the peaks appearing with the main Au $4f_{7/2}$ peak. 121
A.2 (a) A 20×20 nm^2 STM image of the $Ba_8Au_{5.25}Ge_{40.3}\square_{0.45}$(100) surface with rotated motifs between adjacent terraces, prepared at 933 K (V_b=-1.4 V ; I_t= 0.08 nA). An inset histogram showing the unique step height of this clathrate compound equal to 5.0±0.2 Å (b) 30×30 nm^2 STM images of the (100) surface plane obtained at 933 K for V_b=+ 0.7 V and V_b= -0.7 V, respectively. (c) 41×41 nm^2 STM image at 933 K for V_b=-1.1 V. (d) A 10×10 nm^2 Fourier filtered image corresponding to Fig. A.2 (c) showing the unit cell of the surface. 122
A.3 Simulated STM images at constant height (2.16 × 2.16 nm^2) obtained at V_b = ± 0.5 V for different models considered. 122
A.4 Electron density (log scale) using the F^{Ba} model. Side views plotted along the [010] direction ($\vec{b}$) at $y = 0$ (a) and $y = 0.25$ (b). The numbers correspond to the charge transfer $\Delta Q_X = Q_X^{iso} - Q_X^{slab}$ where Q_X^{iso} and Q_X^{slab} are the number of electrons of isolated X atoms and of X atoms in the slab, respectively ($X = Ba, Au, Ge$). The number in parenthesis corresponds to Q_{Ge} for surface Ge atoms at $y = 0.75$. The value Q_{Ba1} related to surface Ba1 atoms, located at fractional coordinate, $y = 0$, is +1.30 (not shown). 123

B.1 Total energy of bulk o-$Al_{13}Co_4$ as a function of cut-off energy (ENCUT) for a k-point mesh: $11 \times 7 \times 7$. 125
B.2 Total energy of bulk o-$Al_{13}Co_4$ as a function of a k-point mesh: $(i + 4) \times i \times i$ using ENCUT value of 450 eV. 125
B.3 Total energy of fcc Al as a function of cut-off energy (ENCUT) for a k-point mesh: $21 \times 21 \times 21$. 126
B.4 Total energy of bulk Al as a function of a k-point mesh: $i \times i \times i$ using ENCUT value of 300 eV. 126
B.5 Total energy of bulk $Ba_8Au_6Ge_{40}$ as a function of a smearing parameter (σ) in the range [0.01 - 0.2]. 127
B.6 Density of states of bulk o-$Al_{13}Co_4$. 127

C.1 SEM micrographs showing Pb droplets on (a) $Al_{13}Co_4(010)$ and (b) $Al_5Co_2(001)$ for a tilt value equal to 60°. Some droplets are curve-fitted (black circles) for contact angle measurements. The red labels correspond to the droplet sizes in the respective tables C.1 and C.2. 129
C.2 DOS at the interface of Pb/Al(111) for 3 ML and 4 ML thickness of Pb, respectively. The calculation was performed using ISMEAR= -5 and 5×5×1 k-point grid. 131

List of Tables

1.1 Wyckoff atomic positions in the $Ba_8Au_6Ge_{40}$ bulk model [23, 28]. 4

2.1 Positions and relative intensities of satellite peaks for Al K_α [47]. 17
2.2 Core level photoionization cross section and kinetic energy values corresponding to the constituent elements : Ba, Au and Ge [48]. 18
2.3 Electronic configuration of elements used in this work. ENMAX values from their POTCAR files in VASP are provided. 34
2.4 Cohesive energies (E^{coh}) and lattice constants (a) computed for Ba, Au, Ge, Al, Pb and Co. Here, NL-SOC denote the non-collinear spin orbit coupling calculations. 37
2.5 Cohesive energy and formation enthalpy of the two CMAs studied. 37

4.1 Surface energies (in J/m^2) calculated for the models considered in this study. Values for the stable model of the $Ba_8Au_6Ge_{40}(100)$ surface are given for comparison ($F^{Ba}_{(100)surface}$), [1] with additional surface Ba atoms, [2] with additional surface atoms (2 Au and 2 Ba), [3] with surface Au vacancies, that pulls down a strict definition of the "cage preservation" at the surface. The chemical potentials μ'_{Au} and μ''_{Au} are defined by $\mu'_{Au} = \mu^{bulk}_{Au} + \frac{54}{4\times6}\Delta H_f$ and $\mu''_{Au} = \mu^{bulk}_{Au} + \frac{54}{2\times6}\Delta H_f$ 66
4.2 Adsorption energies for Ba and Au surface atoms at the $Ba_8Au_6Ge_{40}(110)$ surface. . . 67
4.3 Distortion index calculated on relaxed structures for P- and C-type models. These models are characterized by protruding (P) and buried (B) cages at the surface. 69
4.4 Chemical surface composition and number of dangling bonds observed at ELF value equal to 0.9 for all models considered in the study. 73
4.5 Bader charge analysis for surface atoms of the models considered in the study. Atoms are labeled according to Fig. 4.20. The calculations are performed within PBE scheme. 78
4.6 Bader charge analysis for surface atoms of the models (see Fig. 4.20) considered in the study. The calculations are performed using DFT-D3 VDW scheme. 78
4.7 The features of DOS are summarized for the considered models in the study. The values related to bulk and the most stable model of $Ba_8Au_6Ge_{40}(100)$ surface are provided. The d-band center shift (Δd-band) is calculated w.r.t. bulk. 80
4.8 Work function of surface models considered in the study. 82
4.9 Change of the work function induced by the presence of adatoms 82

5.1 Contact angle measurement for interface of $Pb/Al_{13}Co_4(010)$ for a tilt value equal to 70°. 88
5.2 Contact angle measurement for the interface of $Pb/Al_5Co_2(001)$ for a tilt value equal to 70°. 89
5.3 Contact angle values of Pb droplets on different substrates. 92
5.4 Impact of different functionals and dipole correction on the surface energy of Pb and the adsorption energy calculated for Pb/Al(111) system (moiré slab). 97
5.5 Interfacial energies of Pb/Al(111) (a structural model based on the moiré pattern). . . 99
5.6 Interfacial energies of simple (cube-on-cube) Pb/Al(111) interface. 99
5.7 Adhesion energy and adsorption energy measurements for the Pb/Al(111) (moiré slab). 100
5.8 Adsorption energies for non-reconstructed Pb/Al(111)interface. 100
5.9 Average Bader atomic charges computed on layers in the Pb/Al(111) moiré system with 1 ML to 4 MLs of Pb. 103

5.10 Formation of bi-layer of Pb on the $Al_{13}Co_4(100)$ surface after relaxation for certain value of Pb coverage. 104
5.11 Average Bader atomic charges evaluated on layers in the $Pb/Al_{13}Co_4(100)$ system for a coverage of 0.084 at./Å. The charge transfer values $\Delta Q_X = Q_X^{ref} - Q_X^{slab}$ are provided where Q_X^{ref} and Q_X^{slab} are the number of electrons of isolated X atoms and of X atoms in the slab, respectively $(X = Pb, Al, Co)$. The subscript $_{int}$ denotes the atoms present at the interface layer and on moving away from the interface, the atoms in subsequent layers are denoted by subscripts $_{int+1}$ and $_{int+1}$, respectively. 106

C.1 Contact angle measurement for interface of $Pb/Al_{13}Co_4(010)$ for a tilt value equal to 60°.130
C.2 Contact angle measurement for interface of $Pb/Al_5Co_2(001)$ for a tilt value equal to 60°. 130
C.3 Contact angle measurement for interface of Pb/i-Al-Pd-Mn. 130

List of Abbreviations

AES	**A**uger **E**lectron **S**pectroscopy
BCC	**B**ody **C**entered **C**ubic
BSE	**B**ack-**S**cattered **E**lectron
CCD	**C**harge-**C**oupled **D**evice
CHA	**C**oncentric-**H**emispherical **A**nalyzer
CMA	**C**omplex **M**etallic **A**lloy
DFT	**D**ensity **F**unctional **T**heory
DOS	Electronic **D**ensity **O**f **S**tates
EDS	**E**nergy **D**ispersive **S**pectroscopy
ELF	**E**lectron **L**ocalization **F**unction
FCC	**F**ace **C**entered **C**ubic
GGA	**G**eneralized **G**radient **A**pproximation
IMFP	**I**nelastic **M**ean **F**ree **P**ath
LDA	**L**ocal **D**ensity **A**pproximation
LEED	**L**ow **E**nergy **E**lectron **D**iffraction
ML	**M**ono**L**ayer
PBE	**P**erdew **B**urke **E**rnzerhof functional
QC	**Q**uasi**C**rystal
SAM	**S**econdary **A**uger **M**icroscopy
SE	**S**econdary **E**lectron
SED	**S**econdary **E**lectron **D**etector
SEM	**S**canning **E**lectron **M**icroscopy
STM	**S**canning **T**unneling **M**icroscopy
TM	**T**ransition **M**etal
UHV	**U**ltra-**H**igh **V**acuum
VASP	**V**ienna **A**b initio **S**imulation **P**ackage
XPS	**X**-ray **P**hotoelectron **S**pectroscopy
YE	**Y**oung's **E**quation

Chapter 1

Introduction

Intermetallic compounds are formed by the combination of metallic elements, in an ordered crystal structure different from the one of their elemental constituents. They are qualified as complex, when the number of atoms in the periodic cell is large, typically a few tens to several thousand of atoms. The structures of these complex metallic alloys (CMAs) are alternatively described by a stacking of atomic clusters with high symmetries [1]. Quasicrystals are the most complex members of the CMA family as their ordered structure does not present any translational periodicity in a three dimension space. It is why they are often identified as "the limit case" of CMAs. In 2011, the Nobel Prize in Chemistry recognized the discovery of this new type of crystals by Daniel Shechtman [2]. In addition to quasicrystals, the CMA family includes different types of intermetallic compounds like rational approximants to the quasicrystals, Laves phases, clathrates, skutterudites, etc.

The structural complexity may lead to uncommon physical properties. Examples are materials presenting simultaneously a good electrical conductivity with a low thermal one (conforming the phonon-glass/electron-crystal concept or *PGEC* concept) like several clathrates, or a large metallic strength with reduced wetting by liquids [3], as well as metallic materials with a fragile and brittle behavior [4]. CMAs are used in diverse applications. Aluminium-based CMAs find their utility in the aerospace industry due to their high hardness and light weight [5]. The clathrate compounds have been explored as efficient alternative thermoelectric materials. Hydrogen storage in metallic clathrates are predicted to be promising [6]. Besides these bulk properties, Al-based CMAs have interesting surface features such as low adhesion [7] and low coefficient of friction [8]. The formation of a surface passivating layer make Al-based CMA surfaces corrosion resistant [9]. CMAs have been recently considered as potential candidates in the field of heterogeneous catalysis. This is a consequence of their unique structure which is preserved at the topmost surface, fulfilling the site isolation concept proposed by Kovnir *et al.* [10].

During these three years of research work, we have focused on the structure and the wetting properties of several CMAs surfaces. To this end, we started with the investigation of two low-index surfaces of a Ge-based intermetallic clathrate. Such structurally complex surfaces may be used as templates for pattern formations/novel nanoscale architectures. Further in this work, the wetting properties of several Al-based CMAs were investigated. All studies were realized using a combination of experimental techniques (X-ray Photoemission Spectroscopy; Low Energy Electron Diffraction; Scanning Tunneling Microscopy) and computational methods based on the Density Functional Theory (DFT). In the following, we introduce the intermetallic clathrates. We also review the literature on the wetting properties of Al-based CMAs.

1.1 Intermetallic clathrate compounds

Intermetallic clathrate compounds belong to the CMA family. Their structure is a three-dimensional (host) framework featuring large cavities (cages) with 20–28 vertices (see Fig. 1.1). The polyhedral

cages encapsulates guest species. The compounds fulfill the criterion of the *PGEC* concept given by Slack [11] as their lattice thermal conductivity is typically very low (0.9 W/mK), while it is not the case for the electrical conductivity (0.1 $m^{-1}\Omega^{-1}cm{-}1$) [12, 13].

1.1.1 Types of clathrates

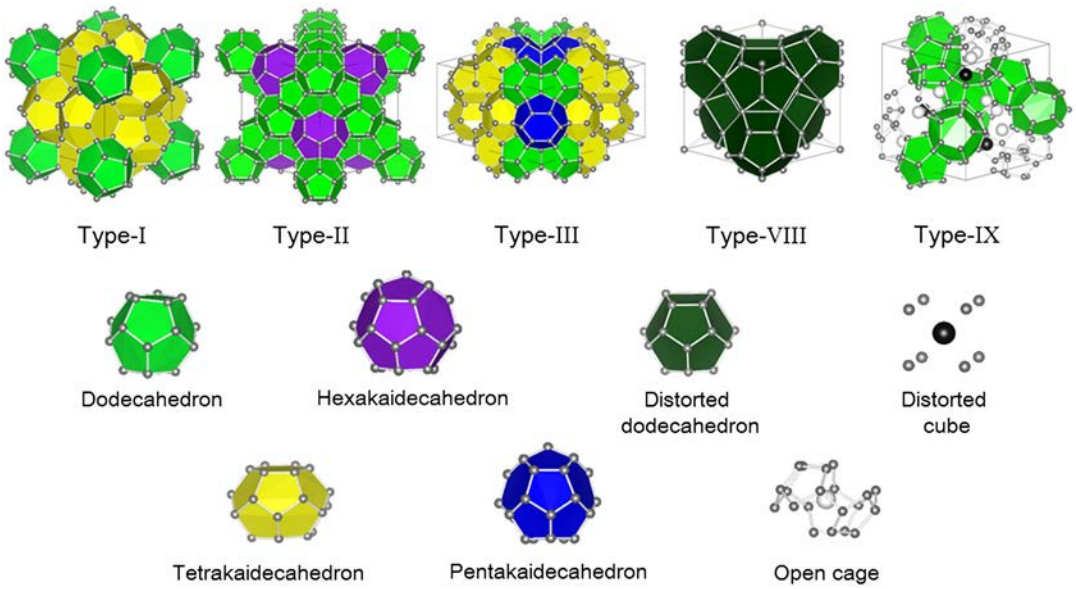

FIGURE 1.1: Crystal structures of type-I, type-II, type-III, type-VIII, and type-IX intermetallic clathrates. Different types of cages constituting these structures are also shown [14].

The clathrates are usually classified into three broad groups: cationic, neutral and anionic clathrates. In cationic clathrates, the host plays the role of an electron donor and the guest is an anion, for example, $Ge_{36}P_8I_8$. Examples of neutral clathrates are molecular ones, with hydrogen-bonded water molecules forming the host cages while the guests atoms are neutral atomic or molecular species (e.g., noble gases, methane). In anionic clathrates the host cages have a negative charge that is compensated by the electropositive guest.

In the present work, we focused on the Ba-Au-Ge type-I clathrate (see Fig. 1.2). It presents a cubic crystal structure defined by the composition A_8E_{46} bearing two types of polyhedral arrangement of atoms: pentagonal dodecahedra (E_{20}) and tetrakaidecahedra (E_{24}) (see Fig. 1.1). Here, A denotes the guest cations which are generally alkali (Na, Rh, Cs), alkaline-earth (Ba, Sr) or rare-earth (Eu) elements and E denotes host anions which are group 14 elements (e.g. Si, Ge, Sn). The presence of the Ba guest cations in the tetrahedrally bonded host cages leads to an excess of electrons and therefore, to a metallic character. The substitution of E by an electron acceptor is required to restore a semiconducting phase. It is then possible to tune the compound electronic structure by a fine control of its bulk composition. Electron counting rules are used to rationalize the electronic structures of intermetallic clathrates. They are presented in the next section.

1.1.2 Zintl-Klemm electron counting rule

The Zintl-Klemm electron counting rule is one of the numerous electron counting rule used to rationalize crystal structures [15, 16]. Originally, this concept was applied to the classical Zintl-phases which are compounds made of electropositive s-block metals and electronegative p-block metals or semimetals. Subsequently, other elements were considered: rare earth elements as electropositive

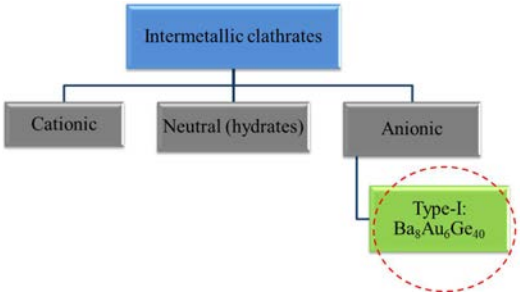

FIGURE 1.2: Classification of intermetallic clathrates based on the charge polarity of the host cages.

bonding partners and heavy transition metal elements as electronegative ones. A complete charge transfer was assumed from the electropositive to the electronegative elements resulting to completely filled valence shells for both of them. The Zintl-Klemm electron counting rule ensures electronically balanced compounds, for example leading to covalently bonded 2 center-2 electron (2c-2e) bonded crystal structures. Depending on the number of electrons donated by the electropositive cation, either isolated anions or polyanions are formed. The atoms in these polyanions are bonded covalently.

In view to apply the Zintl–Klemm concept to clathrates, only the bonds within the covalently bonded host network are considered as 2c-2e bonds [17]. This implies on an average that the number of valence electrons per tetrahedrally bonded framework atom should be four. It is a rather simplistic approach but has been successful to explain the electron balance observed in the cationic (inverse) clathrates. For example, the cationic clathrate $Ge_{36}P_8I_8$ shows the complete charge balance as the electronegative guest anion (I) acts as an electron acceptor:

$$Ge_{36}P_8I_8 = [(4b)Ge^0]_{36}[(4b)P^{1+}]_8[I^{1-}]_8 \times 0e^-,$$

where $4b$ denotes tetrahedrally bonded atom.

In the case of the anionic clathrates, the charge balance is usually not obtained for the ideal composition, *i.e.* for full occupancy of all sites. Semiconducting Zintl-phases often present vacancies, substituted atoms or both. When considering the case of the binary K_8Ge_{46} anionic clathrate, extra electrons are given by the guest cation. They are found to be compensated by defect formation, *i.e.*

$$K_8Ge_{46} = [(4b)Ge^0]_{46}[K^{1+}]_8 \times 8e^-, K_8Ge_{44}\square_2 = [(4b)Ge^0]_{36}[(3b)Ge^{1-}]_8[K^{1+}]_8 \times 0e^-,$$

where $3b$, $4b$ represent 3-bonded and 4-bonded atoms, respectively and $\square$ is a defect or the vacancy formed.

The present work focuses on the ternary Ba-Au-Ge type-I clathrate and hence, we show the application of the Zintl-Klemm charge balance notion in this case. If one considers the full occupancy of Au-substituted $6c$ sites, then the clathrate is p-type with an excess of holes. The equation below shows the unbalanced charge situation for the $Ba_8Au_6Ge_{40}$ ideal composition deviating from the Zintl behavior, *i.e.*

$$Ba_8Au_6Ge_{40} = [(4b)Ge^0]_{40}[(4b)Au^{3-}]_6[Ba^{2+}]_8 \times 2p^+,$$

The charge balance for Ba-Au-Ge type-I clathrate is obtained for a narrow range of composition and is expressed as

$$Ba_8Au_{5.33}Ge_{40.67} = [(4b)Ge^0]_{40.67}[(4b)Au^{3-}]_{5.33}[Ba^{2+}]_8 \times 0e^-.$$

Here, $Ba_8Au_{5.33}Ge_{40.67}$ is expected to be semiconducting. This has been experimentally checked [18, 19].

The Zintl-Klemm concept effectively explains the interactions within the framework of anionic clathrates while more recent quantum chemical tools point towards additional guest-framework interactions [18, 20] which are discussed in next section.

1.1.3 Structural and electronic properties of Ba-Au-Ge and related type-I clathrates

In this section, we present a literature review on the structural and electronic properties of Ba-Au-Ge and related type-I clathrates.

1.1.3.0.1 Structure of the Ba-Au-Ge clathrates

The clathrate studied in this work was primarily defined as a perfectly ordered structure with the $Ba_8Au_6Ge_{40}$ stoichiometry (1991, Cordier *et al.* [21], space group $Pm\bar{3}n$ (no. 223)). The Wyckoff positions of the atoms in this ideal structure are provided in Tab. 1.1.

Clathrates present well defined nano-cages as structural motifs within the covalent bonded framework. But the structure is generally not perfectly ordered. Many experimental and first principles studies were performed on intermetallic clathrates with structural disorders including defects in the framework, mixed occupations, positional disorders of the encapsulated atoms (off-center position of the guest atom in the cages, usually described with the split-site model) etc. [18, 22–26]. A recent investigation of the phonon-based properties of the $Ba_{7.81}Ge_{40.67}Au_{5.33}$ compound underlined the structural complexity and chemical disorder present in this system. However, the ideal ordered bulk model of the $Ba_8Au_6Ge_{40}$ clathrate was demonstrated to reasonably represent the general features of the experimental compound [18, 27].

Atom	Wyckoff site	x	y	z
Ba1	$2a$	0	0	0
Ba2	$6d$	0.25	0.5	0
Au/Ge1	$6c$	0.25	0	0.5
Ge2	$16i$	0.183	x	x
Ge3	$24k$	0	0.308	0.117

TABLE 1.1: Wyckoff atomic positions in the $Ba_8Au_6Ge_{40}$ bulk model [23, 28].

1.1.3.0.2 Electronic properties of Si- and Ge-based clathrates

In 1999, the electronic properties of Ge-clathrates were reported using first principles calculation within the local density approximation [29]. In this study, the differences between the diamond-phase elemental Ge and the Ge_{46} clathrate were pointed out. The clathrate structure was found to be the low-energy phase for Ge. An indirect band gap of 1.46 eV was calculated for Ge_{46} while the value of 0.40 eV was found for Ge in the diamond-phase. The bonding strength in Ge-clathrates was suggested to be weaker as a result of larger atomic volumes compared to the diamond phase.

In the clathrate structure, the filling of the Ge_{20} and Ge_{24} cages with potassium (K), was shown to have an impact on the conduction states, due to the complete charge transfer from the guest atoms (K) to the Ge-framework. This implied a narrowing of the gap and a displacement of the Fermi level towards the conduction band.

The control of the electronic structures by tuning the atomic composition can even lead to superconducting materials. Band structure calculations of the $Na_2Ba_6Si_{46}$ show a strong hybridization of Ba states with Si_{46} states, giving a very high Fermi-level density of states, which should be of essential importance for the superconductivity observed in $Na_xBa_ySi_{46}$ [30, 31].

1.1.3.0.3 Au-doped Si- and Ge-clathrates

In the seminal work of Herrmann *et al.* in 1999 [28], the electronic structures of Au-doped Si- and Ge clathrates were reported using an experimental approach. This work highlighted the defect formation in the perfect cubic structure of the Ba_8Ge_{46} compound, as a non-occupancy of half of the $6c$ sites. This leads to the Ba_8Ge_{43} compound, showing a semiconducting behavior. When the $6c$ sites are occupied by a transition metal like Au, it may stabilize the formation of the type-I clathrates. The $Ba_8Au_6Ge_{40}$ stoichiometry leads to a compounds with a metallic character (N(E_f) = 13 states/eV) according to susceptibility measurements.

In 2011, Zhang *et al.* [18] investigated the influence of chemical bonding on the thermo-electrically relevant properties of the single crystal $Ba_8Au_{5.3}Ge_{40.7}$. A combination of differential scanning calorimetry (DSC) experiments and metallographic analysis shows that the formation of the Ba-Au-Ge ternary phase from the peritectically formed binary phase $Ba_8Ge_{43}\square_3$ is congruent, the phase change occurring by increasing the temperature from 810 to 913°C. More generally, the ternary phase $Ba_8Au_xGe_{46-x}$ ($1 \leq x \leq 6$) was revealed to extend at 800°C from binary $Ba_8Ge_{43}\square_3$ ($\square$ is a vacancy) and the lattice parameters of the solid showed a linear increase with positive variation in Au content [19].

The analysis of the chemical bonding by means of the electron localizability / electron density approach (ELI-D/ED) revealed covalent-like interactions within the rigid framework, as well as between the guest Ba atoms located at the center of the Ge_{24} cages and the Au atoms located at the edges the hexagonal faces of the same cages. The remaining guest-host interactions are identified as ionic interactions.

Further density of states calculations, using the ideal bulk structure $Ba_8Au_6Ge_{40}$, lead to a metallic behavior with N(E_f)=10 states/eV. Based on the rigid band approximation, a hole-type semiconducting behavior is predicted for $Ba_8Au_{5.3}Ge_{40.7}$, and confirmed by experimental measurements.

The magnetic susceptibility measured using the $Ba_8Au_{5.3}Ge_{40.7}$ single crystal revealed a diamagnetic compound. The thermoelectric measurements showed a p-type semiconductor with a low thermal conductivity. The thermoelectric figure of merit (ZT) was measured to be 0.3 using the single crystal (the figure of merit obviously depends on the temperature, it was measured to be $ZT_{max} \sim 0.4$ at 527°C), while a spark plasma sintered-compacted finely ground sample with a very similar composition showed a considerable increase of ZT up to 0.9 at 680 K.

1.1.3.0.4 Chemical bonding picture in Ba-Au-Ge

The chemical bonding picture of intermetallic clathrates is detailed in Ref. [17]. Quantum chemical tools such as the electron-localizability and the 3D representation of atomic basins in real space based on QTAIM (quantum theory of atoms in molecules) adds to the understanding of the atomic interactions and structural features in intermetallic clathrates.

In the case of Ba-Ge clathrates, atomic basins corresponding to Ba atoms exhibited approximately spherical shapes (only inner-shells presenting a spherical electronic distribution is found by QTAIM).

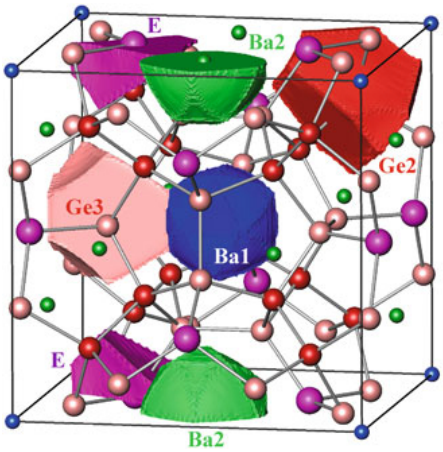

E	Ba1	Ba2	Ge2	Ge3	E
Li	+1.18	+1.32	-0.20	-0.49	+0.78
Mg	+1.15	+1.20	-0.17	-0.61	+1.31
Al	+1.17	+1.17	-0.18	-0.62	+1.40
Ga	+1.15	+1.18	-0.17	-0.32	+0.17
Ge	+1.17	+1.24	-0.15	-0.25	-0.23
Co	+1.20	+1.26	-0.21	-0.17	-0.43
Rh	+1.19	+1.28	-0.17	-0.11	-0.78
Ir	+1.19	+1.27	-0.14	-0.06	-1.05
Ni	+1.20	+1.30	-0.15	-0.21	-0.46
Pd	+1.21	+1.33	-0.11	-0.20	-0.64
Pt	+1.23	+1.29	-0.15	-0.05	-1.10
Cu	+1.19	+1.31	-0.16	-0.25	-0.28
Ag	+1.11	+1.26	-0.18	-0.20	-0.35
Au	+1.21	+1.36	-0.14	-0.10	-0.99
Zn	+1.20	+1.26	-0.27	-0.28	+0.18
Cd	+1.18	+1.26	-0.16	-0.33	+0.09
Hg	+1.18	+1.28	-0.11	-0.22	-0.50

FIGURE 1.3: (Left) Atomic basins (QTAIM atoms) in the ideal bulk structures of $Ba_8Ge_{40}E_6$ where E is the substitution at $6c$ Wyckoff position. (Right) The effective QTAIM charges depending on relative electronegativity of constituent atoms [17].

The effective charges for Ba are calculated to be independent of the substitution element, (E in $Ba_8E_6Ge_{40}$) and much lower than the expected value +2, corresponding to the complete shell configuration.

The shapes of atomic basins for the host-framework positions were found to largely depart from the spherical symmetry. This implicated difference between Ba-(Ge,E) atomic interactions and the ones within the host-framework. The electronegativity difference between element E and Ge at position 3 dictated the effective charge accumulation at the sites E1 and Ge3. While charge at Ge2 site (surrounded only by Ge atoms) is independent of substitution (see Fig. 1.3).
The surfaces of the structurally complex Ba-Au-Ge clathrates may be used as templates for pattern formations/novel nanoscale architectures. In these, the intrinsic wetting properties of several complex intermetallics are investigated by a combination of experimental and theoretical methods. In the following, we focus on the wetting properties of Al-based CMA surfaces.

1.2 Wetting properties of Al-based complex intermetallics

The topic of wetting is of great interest from both fundamental and applied points of view. It plays an important role in many industrial processes, such as lubrication and coating, for example. Low wetting and small coefficients of friction are two essential surface properties for potential technological applications of complex intermetallics and quasicrystals, as reported in Refs. [4, 7].

1.2.1 Definition

Wetting can be defined as the contact between a liquid and a solid surface [32]. It involves interactions among three separated phases (S,L,V) where S, L and V, respectively, denote the solid, liquid and vapor phases [33]. The contact angle (the angle at which the liquid/vapor interface meets the solid/liquid interface) and the interfacial energies are largely used to quantify the wetting. Theoretically, the contact angle is expected to be characteristic for a given solid-liquid system in a specific environment [34].

As first described by Thomas Young [35] in 1805, the contact angle of a liquid drop on an ideal solid surface is defined by the mechanical equilibrium of the drop under the action of three interfacial tensions:

$$\gamma_{\mathrm{SV}} = \gamma_{\mathrm{LV}} cos\theta + \gamma_{\mathrm{SL}}$$

where θ is the equilibrium contact angle. The terms γ_{SL}, γ_{SV}, γ_{SL} are the interfacial tension of the liquid-vapor, the solid-vapor and the solid-liquid, respectively (see Fig. 1.4).

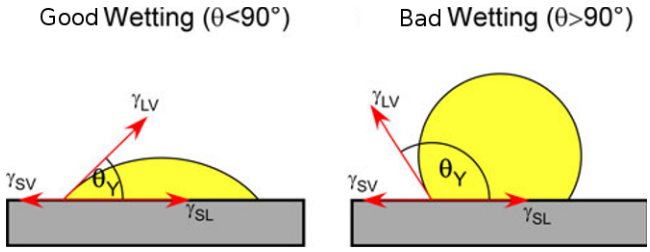

FIGURE 1.4: Contact angle and interfacial energies [33].

Small contact angles (<<90°) correspond to high wettability (the contact area between the solid and the liquid is large), while large contact angles (>>90°) correspond to low wettability.

1.2.2 How to measure the intrinsic wetting properties using a metal as a probe?

Several experimental methods do exist to measure the contact angle. The measurement of wetting of solid surfaces can be split into parts: one related to macroscopic (continuum) and the other to a microscopic (or atomistic) approach. At the macroscopic scale, a liquid on a flat horizontal substrate acquires a shape generally referred to as a sessile drop (see Fig. 1.4). The shape of the drop is influenced by gravity and it changes due to equilibrium between capillary and hydrostatic pressures. Methods used in wetting at the macro-scale are a direct measurement of a sessile drop profile using a telescope-goniometer, or the tilting plate method (for contact angle hysteresis). The liquid surface tension can also be evaluated by the Wilhelmy balance method. Wetting phenomena have been extensively studied at the macro-scale while its studies at micro- and nanoscale are yet to be fully developed [36].
At the micro- or nanoscale, influence of gravity is absent compared to the impact of surface tension. Also, at the microscopic scale it is important to consider the role of the composition as well as the structure of the interfaces/surfaces [33]. The common techniques used to study the ultra-small droplets include atomic force microscopy (AFM), environmental scanning electron microscopy (ESEM), transmission electron microscopy (TEM). Generally, these microscopies are *ex situ* and thus the samples are exposed to atmosphere. However, no air contamination has been reported in certain cases of *ex situ* microscopies when a metal probe is a chemically inert element (such as Pb). In Ref. [37] Pb droplets have been used as a probe to study the wetting properties as well as interfacial energies and contact angles *ex situ* at Cu(111) and Cu(110) surfaces.

Here, we focus on the study of intrinsic properties of Al-based CMA surfaces by performing *in situ* SEM measurements along with Auger spectroscopy. This allows us to see the influence of the surface energies of the pristine surfaces on the wetting phenomena at the nanoscale.

Wettability studies at the micro- and nanoscale have led to the progress of wetting patterns. Now the possibilities such as to deposit droplets onto surfaces with a chemical or topographical imposed micro- or nanoscale pattern are explored [38, 39].

1.2.3 Wetting of CMA surfaces: previous results

The wetting of CMA surfaces has been investigated using several liquids. Experimental investigations of water on various CMA surfaces show that the adhesion energy depends on the thickness of the oxide layer formed at the surface, as well as the density of the states at the Fermi level [7, 40]. When oxidized, it is not possible to really probe the intrinsic wetting properties of CMA surfaces. Avoiding the oxide layer implies to make experiments under controlled conditions, like ultra high vacuum (UHV).

The following experiments have been done using clean surfaces under UHV conditions. Lead has been used as a metal probe to deduce the contact angle on different phases of Al-based intermetallics (of increasing structural complexity, *i.e.* from simple to quasicrystalline structures). In Ref. [41], it has been shown that the contact angle between frozen-in Pb droplets and several Al-Co substrates depends on the sample roughness. The simple AlCo surfaces (CsCl structure) have been found to present similar wetting angles as the quasicrystalline surfaces of d-$Al_{13}Co_4$ films. From these measurements, the wetting behavior was said to be almost not influenced by the crystal structure.

In Ref. [42], several wetting angles (Pb/substrates) are plotted as a function of the substrate melting points (Fig. 1.5). On the 5-fold quasicrystalline i-Al-Pd-Mn surface, the contact angle is measured to be around 70°. It is very different from the value measured for Pb/Al, even if in both cases the surface is made of Al atoms.

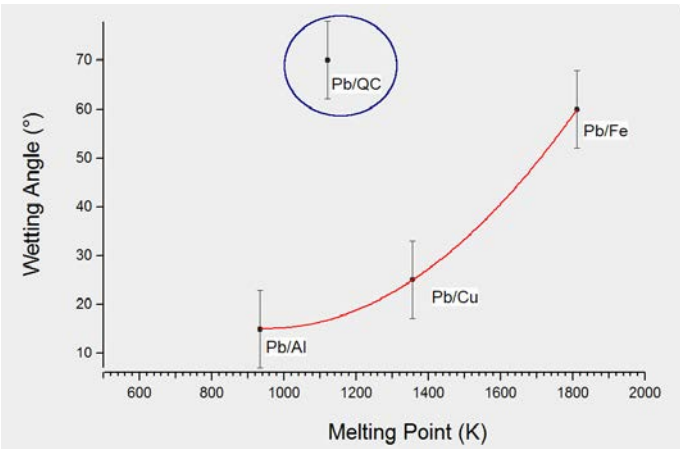

FIGURE 1.5: Empirical correlation observed between the contact angles of liquid Pb deposited at different substrate surfaces and the melting temperature of substrates (red line is only a guide to the eye). Encircled data point emphasize on the high θ value of Pb deposited on the i-Al-Pd-Mn (QC) single grain [42].

1.3 Objectives of the thesis

In the previous sections, we have reviewed the literature on clathrate compounds and wetting properties of CMAs.

We have shown that up to now, the clathrates compounds were largely studied for possible thermoelectric application. However, to-date there is little to no attention provided to their surface structures. It is surprising, since the covalently bonded nano-cages may lead to nanostructured surfaces, with tunable electronic properties.

Our literature review also highlighted a few results on the wetting properties of Al-based CMA surfaces. A limited number of surfaces were investigated, using an experimental approach only.

The main objectives of the thesis are then the following:

1. In a first part, the objective is to determine the structures of two low-index surfaces of the type-I Ba-Au-Ge clathrate single crystal. This structural study would give insights to a few fundamental questions related to the interplay between the 3D cages in bulk and the 2D surface. The absence of surface reconstruction, the possibility to tailor the surface electronic structure, similarly to what is done for the bulk materials, will be investigated. The comparison of the (100) and (110) surface structures will provide insights into the surface anisotropy.

2. In a second part, the aim is to explore the wetting properties of several Al-based complex intermetallic surfaces. Here, the knowledge gained about the intrinsic origin of wetting will help to propose solutions to develop this type of materials as functional coating materials. The theoretical comparison of the Pb(111)/Al(111) and Pb/$Al_{13}Co_4$(100) interfaces will bring insights into the main factors controlling the wetting. Experimentally, the wetting properties of a few other Al-based CMA surfaces (such as Al_5Co_2(001), $Al_{13}Co_4$(010), Al(111), i-Al-Pd-Mn (QC), d-Al-Ni-Co (QC)) will be determined.

1.4 Thesis architecture

After presenting the thesis context and reinforcing the objectives of the thesis, chapter 2 presents the methodology applied in this work. It is divided into two parts. The first part details the experimental methods used in this work, starting from the single crystal growth, followed by surface science experiments under UHV (surface preparation and characterization), as well as the wetting experiments. The second part of this chapter deals with the density functional theory (DFT) formalism followed by its practical implementation using the VASP code. A few examples are provided to illustrate our approach.

Chapters 3-4 focus on the low index surfaces of the Ba-Au-Ge clathrate. In both cases, the surface structures are investigated by a combination of experimental and theoretical methods. The results are discussed and compared to the mechanism occurring at the surfaces of other covalent-bonded solids.

Chapter 5 is dedicated to the wetting properties of Al-based CMAs using Pb as a metal probe. A thermodynamical approach to evaluate the wetting properties is discussed. The interfacial properties calculated for an interface between two simple metals (Pb/Al) is compared to the one involving a complex intermetallic surface (Pb/$Al_{13}Co_4$). The experimental contact angles obtained from *in situ* wetting experiments on different CMA surfaces are reported and discussed.

Chapter 2

Methods

In this thesis, both experimental and computational approaches are used to study the CMA surfaces. The methodology related to each approach is explained briefly in this chapter. The explanation of certain techniques are also accompanied by few examples. In the following, the experimental methods are presented and later computational methods based on *ab initio* calculations are given in section 2.2.

2.1 Experimental Methods

We performed experiments under UHV with single crystal samples of CMAs. The different CMA surfaces investigated in this work were characterized using surface science techniques discussed in the coming sections. We start with methodology related to surface structural analysis and conclude this section with experimental approach for wetting properties of CMAs.

2.1.1 Single Crystal Growth

The Bridgman method was used to grow a single crystal of $Ba_8Au_{5.25}Ge_{40.3}\square_{0.45}$[17, 18] approximately 1 cm thick and 3 cm long. Czochralski technique is not adopted in this work due to its limitation of working well with materials having low vapor pressure [17]. On the other hand, the Bridgman technique has less complexity and can be easily applied to this type-I clathrate system.
In the process of obtaining a single grain, a polycrystalline sample of Ba-Au-Ge with nominal composition was taken in a glassy graphite crucible. The crucible was heated at a rate of 10 K/min to 1398 K under an Ar atmosphere, for 12 h. The bottom of the crucible is brought in contact with a seed (which is a piece of a single crystal) and then translated very slowly from the hot zone to cold zone of furnace. The temperature at the bottom of the glassy carbon crucible falls below the solidification temperature and the crystal growth is initiated at the melt-seed interface. Once the entire melt is translated through the cold part of the furnace, it converts into a solid single-crystalline ingot with undefined orientation. The crystallinity of the obtained ingot was verified by X-ray diffraction. The crystal composition was analyzed using energy-dispersive x-ray spectroscopy (EDX) and $Ba_{14.9} - Au_{9.8} - Ge_{75.3}$ (at.%) was confirmed. The at. % composition was consistent with the established range for $Ba_8Au_{5.25}Ge_{40.3}\square_{0.45}$ compound and in agreement with the works of Zhang *et al.* [18]. To investigate the (100) and (110) surfaces of $Ba_8Au_{5.25}Ge_{40.3}\square_{0.45}$ compound, the single crystal was oriented using back reflection Laue x-ray diffraction. This leads to extraction of two different samples from the single crystal with surfaces perpendicular to [100] and [110] directions, respectively. These samples were provided to us by our collaborators: C. Allio; C. Krellner from Physikalisches Institut, Goethe-Universität, Frankfurt, Frankfurt am Main, Germany and H. D. Nguyen, M. Baitinger, Yu. Grin from Max-Plank Institut für ChemischePhysik fester Stoffe, Dresden, Germany.

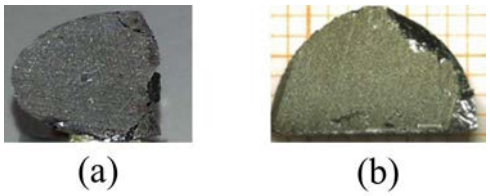

FIGURE 2.1: $Ba_8Au_{5.25}Ge_{40.3}\square_{0.45}$ single crystal showing the faces perpendicular to (a) [100] and (b) [110] directions.

2.1.2 Experiments under UHV

The surface samples under UHV were investigated in three interconnected chambers namely preparation chamber, analysis chamber, and scanning probe microscopy (SPM) chamber. For these *in situ* experiments, transfer arms with magnetic gallons are used to transfer the sample from one chamber to another. Our in-house experimental set-up (Fig. 2.2) provides access to mainly three surface characterization techniques : Low-Energy Electron Diffraction (LEED), X-ray Photoelectron Spectroscopy (XPS) and Scanning Tunneling Microscopy (STM). These three techniques were used to investigate the surface structure of BaAuGe(100) and BaAuGe(110) surfaces. Before surface analysis, the samples are always prepared to ensure atomically clean surfaces.

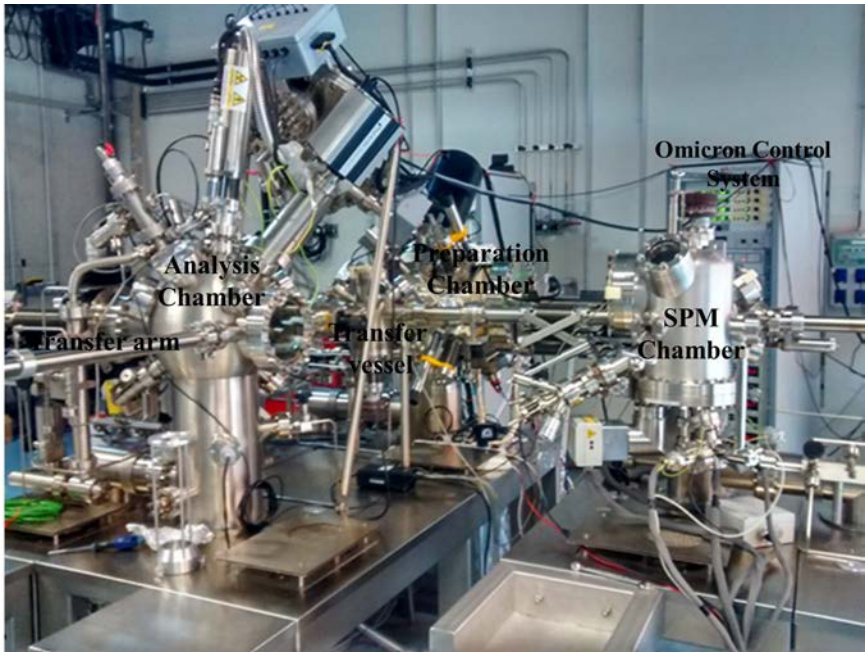

FIGURE 2.2: Experimental setup under UHV in the IJL laboratory.

Clean surface preparation: The two BaAuGe surfaces were polished using a diamond paste down to 0.25 μm. To obtain a clean surface, the experiments were performed under UHV conditions with a base pressure of 2.0×10^{-10} mbar. Clean surfaces for both orientations were prepared by Ar^+ ion sputtering (2 keV for 30 min) and annealing cycles up to 973 K for 1-2 h. The temperature of the samples was checked using an infrared optical pyrometer with the emissivity set to 0.1 coupled with a K-type thermocouple. The process of sputtering removes the few atomic layers of the sample leaving the surface rough. Hence, it is usually followed by annealing the sample to have well ordered flat surface for analysis. The two processes are repeated few times depending on the sample surface to ideally ensure re-ordering without chemical segregation of impurities from the bulk [43].

2.1.3 Low-Energy Electron Diffraction

This technique acquires information about the surface structure from the reciprocal space lattice [44, 45]. To obtain the LEED patterns, the sample surface is exposed to a collimated beam of low-energy electrons (20 – 600 eV). The diffracted electrons (elastically back-scattered) from the surface form spots on a fluorescent screen which constitute the LEED pattern. The sampling area for LEED patterns is proportional to the e-beam diameter ($\sim 1\,\mathrm{mm}^2$).
As shown in schematic of LEED apparatus (Fig. 2.3), its main components are the electron gun, four (or three) metallic grids, LEED control unit, and a luminescent screen. The grid optics and screen have been placed concentrically in the instrument and the sample is mounted at the center. The gun which sends the primary beam of energy in a specified range is directed towards the grounded sample. The (elastically back-scattered) diffracted electrons from the surface travel towards the concentric grids which ensure that electrons travel without distortion towards the screen at voltage ($\sim$ 3-6 keV). The outer grids are grounded so that back-scattered electrons can travel in field-free region while the inner grids are applied with suppressor (retard) voltage that is usually 10-20 % lower than the gun voltage. The inner grids with suppressor voltage eliminate inelastically scattered and secondary electrons which can form a high background making the diffraction beams (or spots) on the screen almost inconspicuous. A high voltage is applied to the luminescent screen (typically 5 keV) in order to accelerate the diffracted electrons transmitted through the high-pass filter grids onto it so that they produce bright diffraction spots. The lens voltage and wehnelt adjustments are also done to obtain optimal sharpness of the diffraction spots [46]. The diffracted electrons give rise to a pattern consisting of bright spots on a dark background, which reflect the symmetry and crystalline order of the surface.

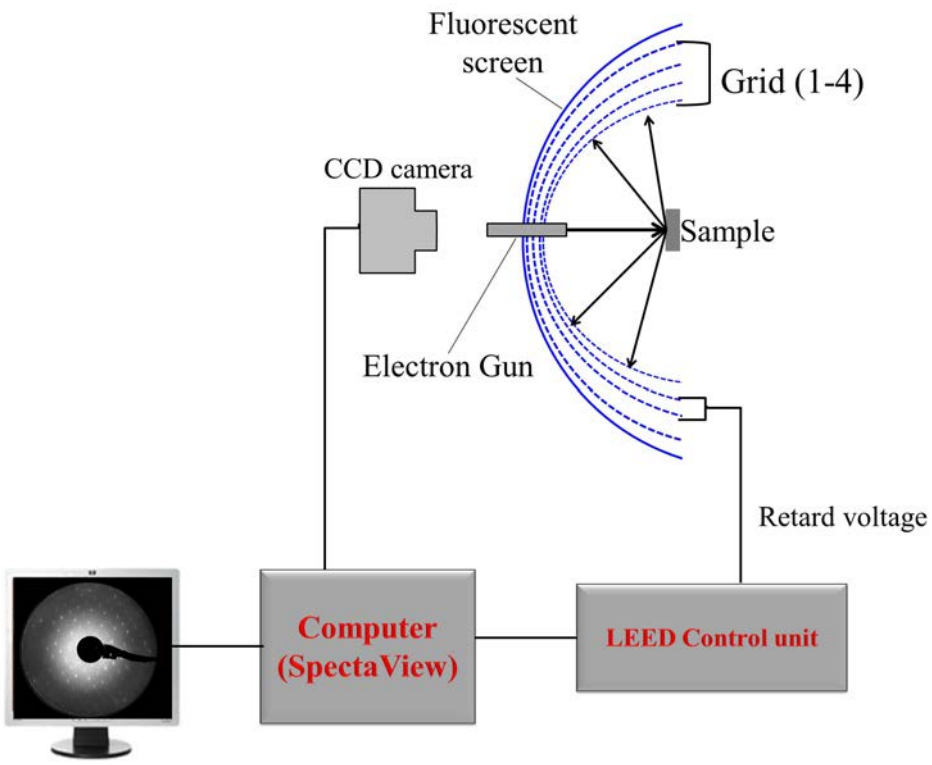

FIGURE 2.3: Schematic of LEED apparatus: Electrons of K.E. E_p from electron gun are directed towards the sample and the grids (1-4) ensure only elastically scattered electrons to reach fluorescent screen. (Inspired from [45])

Conceptually, the working of LEED technique is based on wave-particle duality given by de Broglie's hypothesis and the wavelength of electron (de Broglie's wavelength) is expressed as

$$\lambda_B = h/p \qquad p = (2mE)^{\frac{1}{2}}$$
$$\lambda_B(\text{Å}) = \left(\frac{150.4}{E(eV)}\right)^{\frac{1}{2}} \tag{2.1}$$

where h is Planck's constant, p is the electron momentum, E is the electron energy in eV and m is the electron mass.

By substituting the value of primary beam energy in the range (10-600 eV) in above Equation 2.1, we get the values of λ in the range 3.88-0.5 Å. This implies that the change in wavelength is of the same order as the interatomic spacing or lattice parameter a of unit cell in solids. The technique is very surface sensitive with the probing depth of around 5-10 Å (few atomic layers), it is due to the fact that inelastic mean free path (IMFP) of electrons is short in solids as supported by the "Universal Curve". On application of Bragg's law (Equation 2.2), the angle determined between the incident and diffracted beams (θ_n) are large enough in order to obtain well-resolved diffraction spots [46]:

$$n\lambda = asin\theta_n \tag{2.2}$$

where n is an integer value for defining atomic planes. On rearranging Eqns. 2.2 and 2.1, we obtain the relation between the diffraction angle and the primary beam energy, $sin\theta_n \propto \frac{1}{\sqrt{E}}$. A geometrical method of determining the number of diffracted beams from a surface at a given beam energy is provided by Ewald sphere construction.

Qualitatively, analysis of the spot positions reveals the symmetry of the surface structure. One can know about the surface reconstruction if the surface unit cell parameters do not match those expected from the perfect bulk truncation. In case of adsorption, the size and the rotational alignment of adsorbates w.r.t. the substrate unit cell can be deduced. Quantitatively, the intensities of diffracted beams are recorded as a function of incident electron beam energy to generate I-V curves. The spot intensity analysis, not performed in this work, can lead to accurate atomic positions at the surface.

In case of the BaAuGe(100) square unit cell, we had the surface defined perpendicular to the a-direction and hence the translational vector in 2D-real space case can be written as

$$\overrightarrow{R} = m\overrightarrow{b} + n\overrightarrow{c}, \tag{2.3}$$

where the lattice parameter $b = c$ and the angle between the lattice vectors is 90°. The definition of reciprocal space given by :

$$e^{i\vec{G}\cdot\vec{R}} = 1. \tag{2.4}$$

and the reciprocal lattice vector can be defined as

$$\overrightarrow{G} = m'\overrightarrow{b^*} + n'\overrightarrow{c^*}, \tag{2.5}$$

We can write the reciprocal lattice vectors explicitly as

$$\overrightarrow{b^*} = 2\pi\frac{\overrightarrow{c} \times \hat{n}}{|\overrightarrow{b} \times \overrightarrow{c}|} = \frac{2\pi}{b}\hat{b}; \qquad \overrightarrow{c^*} = 2\pi\frac{\overrightarrow{b} \times \hat{n}}{|\overrightarrow{b} \times \overrightarrow{c}|} = \frac{2\pi}{c}\hat{c} \tag{2.6}$$

where $\hat{n}$ is the surface unit normal, $\hat{b}$ is unit vector along y-direction and $\hat{c}$ is the unit vector along the z-direction. The values of lattice vectors deduced from the above equations (reported in chapters 3 and 4) were calibrated with a reference LEED pattern of $Al_{13}Co_4(100)$ obtained under the same experimental conditions.

It is important to note that vectors in real and reciprocal space obey the condition of orthogonality formulated as

$$\vec{a}_i \cdot \vec{a}_j^* = 2\pi\delta_{ij}, \tag{2.7}$$

where $\vec{a}_i$, i = 1, 2, 3, the vectors defining the unit cell and $\vec{a}_j^*$, j = 1, 2, 3, the vectors defining the unit cell in reciprocal space. δ_{ij} = 1 if $i = j$, = 0 if $i \neq j$.

LEED instrument and the parameters used: These experiments were operated using a 4-Grid LEED and an Omicron SPECTALEED control unit. The measurements were recorded at room temperature (RT) by a CCD camera and SpectaView Pro-Video LEED package. The data for experiments pertaining to Ba-Au-Ge clathrate were recorded for values of E_p mainly in the range [10-200 eV] with an average of 20 frames/image. The post processing of recorded LEED pattern video for the specified range of E_p was performed using 'SpectaView to EASY LEED' *plug-in* in ImageJ software.

2.1.4 X-ray Photoelectron Spectroscopy

XPS is also called Electron Spectroscopy for Chemical Analysis (ESCA). It corresponds to acquiring data on the elemental constituents on the surface. It is a quantitative spectroscopic tool that measures the elemental composition, provides chemical state and electronic state of the elements that exist within a sample. The signal measured by XPS is an exponentially surface-weighted signal and usually the depth probed is 30-100 Å. The technique of x-ray photoelectron spectroscopy relies on the electronic structure as the peaks obtained are corresponding to the binding energies of the core electrons (*i.e.* the electrons in the inner shells which are very characteristic of different elements).

The underlying principle of this technique is the photoelectric effect and the law of energy conservation (see Fig. 2.4). X-rays of particular wavelength (Al K_α or Mg K_α) hit the surface ejecting photoelectrons from the surface with some kinetic energy after overcoming the work function of the sample surface (ϕ_s). The true kinetic energy ($E_K^{'}$) of the photoelectrons leaving the surface depends on the work function of the sample. The emitted electron from the surface with a certain kinetic energy is decelerated at the input of the analyzer (see Fig 2.4 (a)) in order to have the constant pass energy of the electron analyzer, E_{pass}. The delay is obtained by applying retardation voltage at the lens system that can be adjusted according to the initial kinetic energy of the electrons, in this way a complete spectrum of the kinetic energy of the emitted electrons is obtained. This constant analyzer energy (CAE) method allows a good constant resolution to be obtained without loss of sensitivity, *i.e.* without loss of many electrons. The measured kinetic energy (E_K) of photoelectrons finally depends upon the binding energy of elements ($E_B = h\nu - E_K - \phi_{spec}$) present at the surface and potential barrier at the spectrometer/analyzer (ϕ_{spec}) (see Fig 2.4 (b)).
While it is the kinetic energy of the outgoing electrons that is measured, spectra are usually shown on a binding energy scale to facilitate elemental identification. It is interesting to acquire XPS data on different kinetic energy ranges, as the core level peaks have fixed binding energy values (*i.e.* they show a shift on K.E. scale) while the Auger peaks have fixed K.E. values. This peculiarity is used to distinguish between the two kind of peaks and to avoid the overlapping of peaks too in XPS spectra. A typical XPS spectrum is a plot of the count of electrons detected per second (intensity proportional to concentration of the element present) as ordinate value versus the binding energy of the

electrons detected as abscissa. Each element produces a characteristic set of spectral peaks at characteristic binding energy values, correspondingly quantifying the elemental composition of surface of the sample being analyzed. It also suggests the chemical environment of the sample and in this way impurities (if present) are identified.

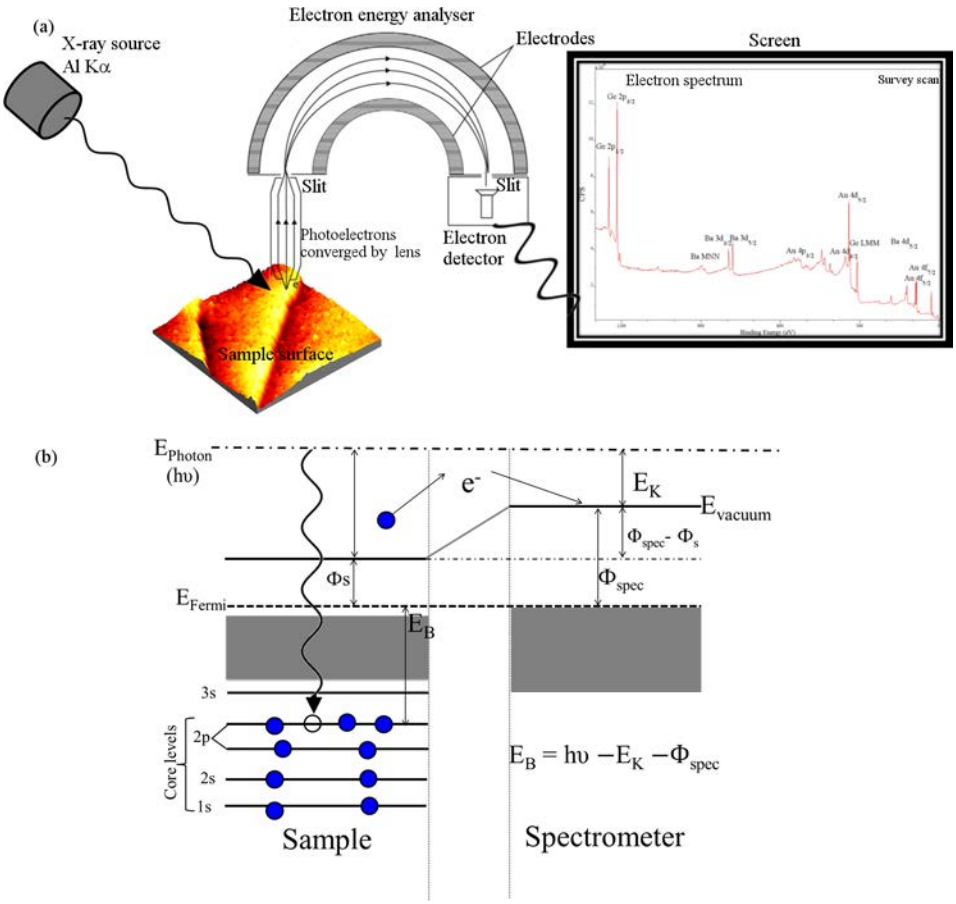

FIGURE 2.4: Schematic of XPS showing the basic principle of the technique.

All core levels with orbital angular momentum quantum number (l) $\geqslant 1$ (p, d, f, ...) are split into doublets by spin-orbit coupling ($l \pm \frac{1}{2}$). The XPS peaks corresponding to chemical states denoted by higher (n, l, j) values appear at lower binding energy. This can be noticed from the spectrum of $Ba_8Au_{5.25}Ge_{40.3}\square_{0.45}$ shown in schematic (Fig 2.4 (a)). Also, typically the background intensity at high binding energies increases owing to inelastically scattered electrons (secondary electrons) arising from the parent XPS peaks.

Features of in-house experimental apparatus and the parameters used to acquire data:

We used Omicron DAR400 (twin-anode high intensity X-ray source) with default anodes of Al K_α and Mg K_α. In particular for our Ba-Au-Ge samples, we utilized Al K_α (1486.6 eV) X-ray source to obtain incident photons and thus emitted photoelectrons were detected by an Omicron sphera hemispherical electron analyzer EA125. The detected signal was amplified using 7-channel (Channeltron) electron multipliers. Determination of the chemical homogeneity of the sample surface for different depths was performed by rotating the sample with respect to the analyzer. The measurements have been performed by varying the take-off angle, θ defined with respect to the surface normal from 0 °to 70 °. The surface sensitivity was increased on going from lower to higher value of θ. We also employed XPS analysis to find the trend of surface composition with annealing temperature for a constant angle of 45 °. All the scans were performed in CAE mode. The survey scans were executed

for an energy range [1000 : -5 eV] and a pass energy of 20 eV. Line scans of the constituent elements were carried out for a dwell time of 0.2 s and E_{pass} equal to 10 eV. The electron analyzer is capable of providing a better resolution $\sim$ 0.02 eV but the resolution of non-monochromatic X-ray source was the restrictive parameter. When X-rays are not filtered (non-monochromatic source), one can observe satellite peaks, *i.e.* photoelectric peaks that can be found at a specific energy from the main XPS peaks. The table 2.1 provides the value of relative positions and intensities of satellite peaks associated with Al K_α, which were deleted upon data analysis.

TABLE 2.1: Positions and relative intensities of satellite peaks for Al K_α [47].

	$\alpha_{1,2}$ (doublet)	α_3	α_4	α_5	α_6	β
Displacement (eV)	0	9.8	11.8	20.1	23.4	69.7
Relative intensities	100	6.4	3.2	0.4	0.3	0.55

Quantification of XPS data with an example:

The quantification of XPS data requires finding the area under the XPS peaks accounting for their intensities and normalization factor for the core level atomic subshells of the constituent elements. The concentration of element i in a compound composed of j elements is given by the following relation:

$$C_i = \frac{\frac{(Area)_i}{N_i}}{\sum_j \frac{(Area)_j}{N_j}} \tag{2.8}$$

The normalization coefficient (N_i), which is the correction factor to have more reliable concentration values, was calculated for each element i corresponding to its core level atomic subshell as described in the equation below:

$$N_i = \lambda_i \times \sigma_i \times ATF_i \tag{2.9}$$

where ATF_i is the analyzer transmission function, σ_i is the photoionization cross section and λ_i is the photoelectron IMFP in nm corresponding to the element i core level atomic subshell. The expression for ATF_i is:

$$ATF_i = \left(\frac{\mathrm{a}^2}{\mathrm{a}^2 + R^2}\right)^{\mathrm{b}} \tag{2.10}$$

where $R = \mathrm{E_K}/\mathrm{E_{pass}}$ (the retard ratio) and (a,b) are parameters related to energy analyzer given by the manufacturer (here, for Sphera analyzer : a $= 21.0025$ and b $= 0.2015$). As mentioned above, the pass energy ($\mathrm{E_{pass}}$) for line scans is fixed at 10 eV while the kinetic energy of photoelectrons depend on the surface elements.

Here, we present the XPS data for the BaAuGe(110) surface as an example. The values of σ_i and $\mathrm{E_K}$ used in the analysis has been tabulated below:

The IMFP is an index of the distance traveled by electron between two inelastic collisions and photoelectrons with small IMFP values escape from near surface region. In practice, the majority of photoelectrons originate from a depth less than IMFP and up to 3λ at most.
The IMPF parameter of photoelectrons is thus a gauge of the surface sensitivity here and it is important to calculate it accurately. The IMPF values were calculated using the empirical relation given

TABLE 2.2: Core level photoionization cross section and kinetic energy values corresponding to the constituent elements : Ba, Au and Ge [48].

	σ_i	E_K (eV)
Ba $3d_{5/2}$	25.84	706
Au $4f_{3/2}$	9.58	1400
Ge $2p_{3/2}$	24.15	270

by Seah and Dench in 1979 [49]. The relation for IMFP (λ_i) in terms of thickness of monolayer of compound, a (nm) and E_K is given by equation 2.11.

$$\lambda_i[nm] = \frac{538a}{{E_K}^2} + 0.41a^{\frac{3}{2}}{E_K}^{\frac{1}{2}} \tag{2.11}$$

where the a is derived as

$$a[nm] = \left(\frac{A * 10^{24}}{\rho * n * N_A}\right)^{\frac{1}{3}} \tag{2.12}$$

In the above equation, A is the molecular weight in g/mol, ρ is the calculated density of the bulk, n is the number of atoms in the bulk, N_A is the Avogadro's number. Here, for the $Ba_8Au_{5.25}Ge_{40.3}\square_{0.45}$ compound we used the values: ρ = 6.84×10^6 g.m^{-3} , N_A = 6.023×10^{23} mol^{-1} and A_{Ba}=137 ; A_{Au}=196 and A_{Ge}=72.6. In order to calculate the concentration values of surface elements, it is required to find the area under the observed XPS peaks.

In this study the fitting of XPS peaks was performed using Casa XPS (version 2.3.16) software. The data obtained by fitting the binding energy curves are then used to plot the concentration of constituent elements as a function of the take-off angle and annealing temperature (using Igor software).

In Fig. 2.5, the peak scan of Ba $3d$ doublet is shown where the area of the two peaks was constrained using ratio of multiplicity of total angular momentum (*i.e.* Area of Ba $3d_{3/2}$ = $\frac{2}{3}$ Area of Ba $3d_{5/2}$). The Shirley background (shown in blue) was applied to Ba $3d$ doublet, in this particular case the end-points were in the range [786.8 : 776.7 eV]. Here, the doublet peaks were fitted using Lorentzian Asymmetric Lineshape (LA (α, β, m)) function which is based on a numerical convolution of a Lorentzian with a Gaussian to produce a lineshape which is a superset of the Voigt (symmetric) functions [50]. The α, β values in this function defines the asymmetric aspect of the line shape as the increase in these values leads to the reduction in tail spread of the Lorentzian shape. The value m in LA function is an integer in the range (0-49) defining the width of the Gaussian. We used the function as LA(2.8,2,2) for the fitting of Ba XPS peaks shown in Fig. 2.5 obtained using the BaAuGe(110) sample.

For the rest of the XPS data pertaining to the Ba-Au-Ge clathrate, we subtracted a Shirley background from the Ba $3d$, Au $4f$ spectrum while a linear background was removed for the peak of the Ge$2p_{3/2}$. We used LA (α, β, m) line shape for these three elements but satisfactory results can also be obtained using Doniach-Sunjic (DS) functions [51].
The core level spectra of the three constituent elements Ba,Au,Ge are also shown in Fig.A.1(a), A.1(b), A.1(c). The binding energies of Ba $3d_{5/2}$, Au $4f_{3/2}$ and Ge $2p_{3/2}$ in $Ba_8Au_{5.25}Ge_{40.3}\square_{0.45}$ single crystal are 780.68 eV, 84.54 eV and 1217.78 eV, respectively. On comparison with binding energy values found in literature [52–55] for the pure constituent elements, the core level peak of Au $4f_{3/2}$ and Ge $2p_{3/2}$ are shifted towards higher binding energy values by 0.65 eV and 0.60 eV, respectively. There is a negligible peak shift for Ba $3d_{5/2}$.

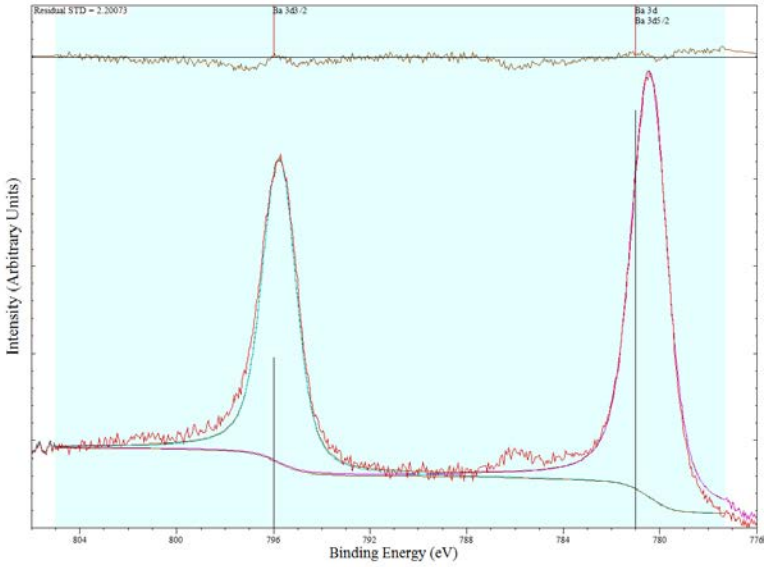

FIGURE 2.5: XPS peak of Ba 3*d* doublet (according to the multiplicity) value on the BE scale. The Shirley background (in blue) has been applied to the peaks and also the fitted components are shown.

2.1.5 Scanning Tunneling Microscopy

Scanning probe methods have developed into essential tools in surface science experiments, and here we discuss one of the most commonly used technique : scanning tunneling microscopy. This technique was the technological breakthrough and enabled the atomic scale view of metal and semiconductor surfaces. It helped in the structure determination of surface reconstructions and revealed that the surface cannot be treated as a static substrate for deposition. Also, it led to the understanding that reactive adsorbates can promote the adsorbate-induced surface reconstructions. Overall, its various applications include surface topography, electronic properties, film growth and molecular manipulation. The singular experimental limitation for STM is a need of conducting surfaces [56].

Scanning Tunneling Microscope was invented in 1981 by Gerd Binnig and Heinrich Rohrer at IBM, Switzerland [57] which led them to the Nobel Prize in 1986. This technique is based on the phenomenon of quantum tunneling. It employs the measurement of tunneling current which occurs because of the quantum probability of penetration of electrons across the potential barrier applied between the sample and the conducting tip. It is only possible quantum mechanically, which considers dual wave-particle nature of matter unlike classical theory [58].

The schematic shown in Fig. 2.6 (a) represents the simplified interpretation of the STM apparatus and illustrates its basic working principle. A sharp electrically conducting metallic probe (tip) is driven into close proximity of a conducting surface (the sample), *i.e.* a distance of a few hundred picometers. The tip-sample distance (z) is small enough for the wave functions of the topmost tip atom(s) and the surface atoms to overlap sufficiently in order to have quantum mechanical tunneling of electrons between the tip and the sample. On applying a bias voltage V_b, current I_t can be measured between the tip and the sample due to the tunneling effect. As the tunneling current is strongly dependent on the tip–sample distance z, it can in turn be used for topographical imaging of the surface. On changing the polarity of V_b, the flow of electrons is affected. In Fig. 2.6 (b) where $V_b < 0$, electrons tunnel from filled states of sample to the empty states of the tip (occupied state imaging of the sample). On reversing the bias voltage ($V_b > 0$) electrons tunnel from filled states of the tip to the empty states of the sample (unoccupied state imaging of the sample).

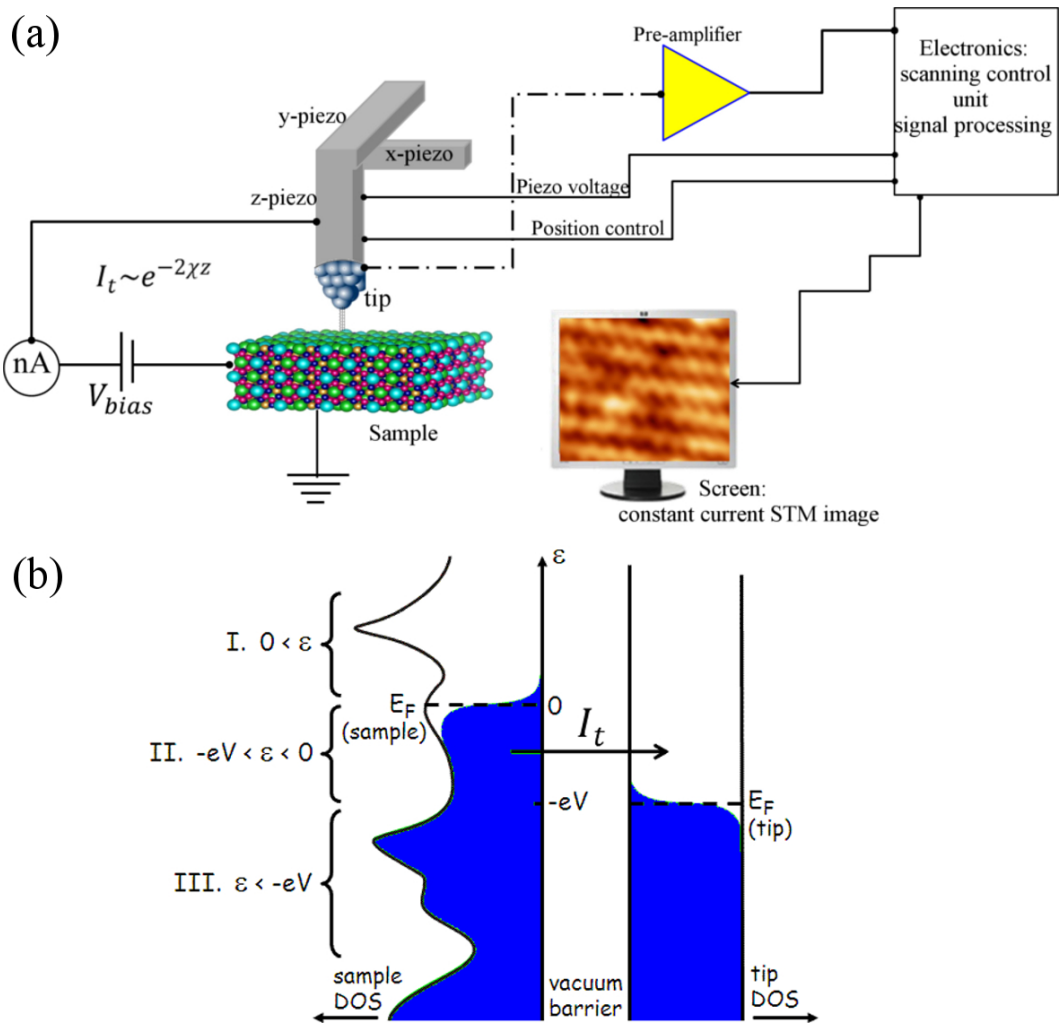

FIGURE 2.6: Schematic of STM: (a) A simplified model of the STM instrument, where sample and metallic probe (tip) are shown in atomic scale; (b) DOS of the tip and the negatively biased sample (surface) in the vicinity of E_f showing the tunneling of electrons (I_t) from occupied states of the sample to empty states of the tip (adapted from [46]).

Within Bardeen's transfer Hamiltonian approach (1961) based on first order time-dependent perturbation theory, the tunneling current (I_t) for a bias voltage $V_b > 0$ can be expressed as follows:

$$I_t = \frac{2\pi e}{\hbar}\sum_{t,S}|M_{tS}|^2\delta(E_S - E_t)\left\{\left[\underbrace{f(E_t+V_b)}_{\substack{\text{filled states}\\\text{of the tip}}}\underbrace{(1-f(E_S))}_{\substack{\text{empty states}\\\text{of the surface}}}\right] - \left[\underbrace{(1-f(E_t+V_b))}_{\substack{\text{empty states}\\\text{of the tip}}}\underbrace{f(E_S)}_{\substack{\text{filled states}\\\text{of the surface}}}\right]\right\} \tag{2.13}$$

where e is the charge of the electron, $\hbar$ the Planck constant, M_{tS} the matrix coupling the unperturbed electronic states of the tip and the surface. The energy conservation is ensured by $\delta(E_S - E_t)$ and $f(E)$ is the Fermi-Dirac distribution function:

$$\frac{1}{1+e^{E/k_BT}} \tag{2.14}$$

where k_B is the Boltzmann constant and T is the temperature.

Although being a very realistic approach the main complication with Bardeen's formalism (Equation 2.13) is the calculation of the wave function for the tip (ψ_t). Since, the atomic structure of tip

is generally unknown. Hence, a model *s-type* tip ψ_t with local spherical symmetry was assumed by Tersoff and Hamman in 1983 [59, 60]. With further approximation of low bias voltage (typically $\pm$ 1 V), the tunneling current is exponentially related to the tip-sample distance z ($I_t \propto V_b e^{-2\chi z}$) where χ depends on the tip-surface potential barrier height ϕ [58]. The Tersoff-Hamman approximation in terms of local density of states (LDOS) of the surface near E_f is discussed in section of simulated STM images using DFT.
An STM image acquisition can be performed generally in two modes : constant-current (CI) mode and constant-height (CH) mode. In the former, the tip is scanned over the surface in x- and y-directions maintaining a constant current defined by set point, I_s while adjusting the tip-sample distance and lateral displacement of the tip using the feedback controlled piezoelectric elements. The constant current STM image reflects as a first approximation the surface topography influenced by the local electronic structure as the tip moves across the surface. In the CH mode, the contrast in the STM image is a direct result of the variation in tunneling current while maintaining a constant z value during the scan.

Instrument and software used: Obtaining meaningful STM data can be challenging, as it requires extremely clean and stable surfaces, sharp tips, excellent vibration insulation and sophisticated electronics. We used an Omicron VT-STM operating at room temperature. The tip used in our case is a tungsten wire with a sharp tip formed by chemical etching. All the STM images were obtained at constant current mode using Omicron Matrix SPM control system [61]. The images obtained were further treated by WxSM solutions (V 5.0) software to acquire information such as step height of different layers or terrace features, profile of surface, atomic inter-planar distances, roughness of surface etc. [62]. An example of STM images after post processing with WxSM software is shown in Fig. A.2 (Appendix A).

2.1.6 Wetting experiments under UHV

Experimentally, we performed the wetting experiments under UHV on Al-based CMA surfaces using Pb as a metal probe. This study was made possible using the in-house state of the art experimental set-up (see Fig. 2.7). This set-up is connected to the ultimate 40 m long transfer tunnel under UHV, "TUBE-DAUM", which facilitates the in-situ synthesis and characterization of novel materials at the nano-scale.

The sample preparation for these wetting experiments is similar to those described in section 2.1.2. Experiments under UHV absolutely require clean sample surfaces obtained using an iterative process of sputtering- annealing the surface.

2.1.6.1 Dosing Pb

The dosing of Pb on the clean Al-based CMA surfaces were carried out using a Knudsen cell (effusion evaporator source). The pressure during depositions was kept in the low 10^{-9} mbar range. The Pb deposition time was 50 minutes for a current value of 3.8 A and a voltage equal to 4.8 V. The temperature of the source during dosing was 420 °C, as recorded by a thermocouple in the source controller.

2.1.6.2 Dewetting

After dosing few layers of Pb on the CMA surface, the sample was heated with a temperature ramp. The temperature variation includes the melting point of Pb (a melting step) to produce liquid Pb

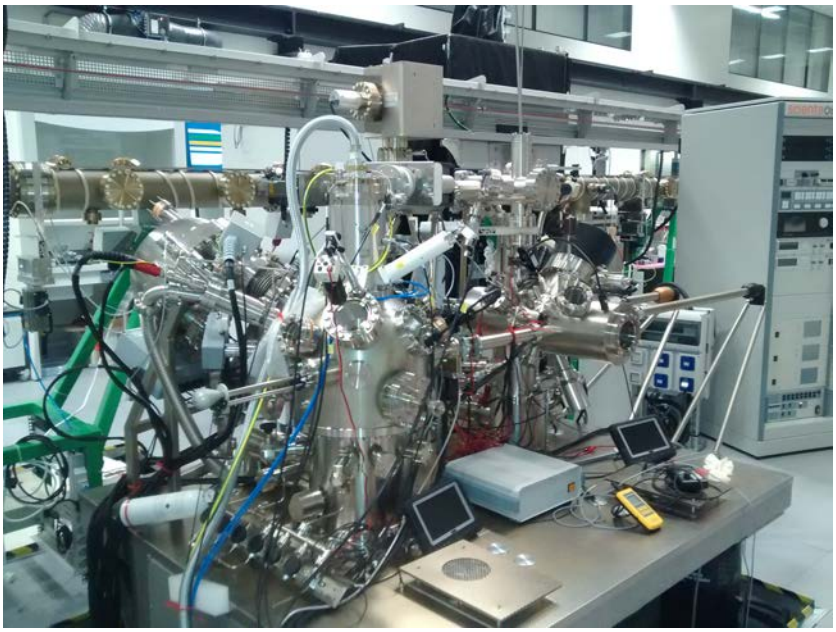

FIGURE 2.7: Scienta-Omicron Nano-SAM experimental set up in IJL laboratory.

droplets. This is followed by subsequent cooling of the surface down to room temperature to get "frozen-in" Pb droplets on the surface. The heating of the Pb film depends on its thickness in turn its dosing time. The Pb film on $Al_5Co_2(001)$ was heated for 42 mins with the temperature slightly above the melting point of Pb (see Fig. 2.8).

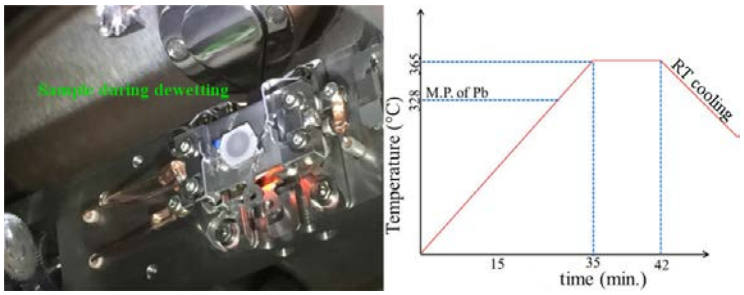

FIGURE 2.8: (Left) Dewetting of Pb film on $Al_5Co_2(001)$. (Right) Schematic representation of temperature ramp during dewetting process.

2.1.6.3 Scanning Auger Microscopy (SAM)

SAM can be considered as the combinational derivative of the Scanning Electron Microscopy (SEM) and the Auger Electron Spectroscopy (AES). The instrumental parts of SAM are enlisted below [63]:

- An electron optical column for generating, focusing and scanning the incident electron beam. Typically, beam energy has a range 0-30 keV, a beam current over 1–100 nA, and beam diameter varying over 10–100 nm.
- A secondary electron detector (SED) for imaging of the sample.
- A concentric hemispherical analyzer (CHA) with multi-channel detection.
- A scanning Ar-ion gun for in situ sample cleaning and sputter depth profiling.

- A UHV preparation chamber (base pressure in 10^{-10} mbar range) with a load lock sample introduction system.
- A motorized sample stage with 4 degree of freedom, *i.e.*, x,y,z,rotation. The stage is mounted on a goniometer for a variable tilt angle. The tilt range depends on system configuration and is typically between $\pm 70°$.
- Necessary electronics for digital control of all functionalities of the system and data acquisition. A computer system with instrument control, sophisticated softwares for data acquisition, data analysis, and data presentation. A display monitor for live and stored images, spectra and profiles.

Here we focus on the imaging and spectroscopic capabilities of the SAM technique. Since, it is based on two intrinsic techniques: SEM and AES, we explain each briefly for understanding their simultaneous usage in SAM. The following section starts with the introduction of the basic principles behind the SEM technique. Also, we discuss the physical aspects of the Auger process. Later, the instrumentation details of Nano-SAM microscope is provided. At last, an example of data acquired using Nano-SAM is shown.

2.1.6.4 Scanning Electron Microscopy (SEM)

Scanning electron microscopy is one of the key techniques for the microstructural analysis and is also considered important for observation of surface topography. The SEM provides information not only related to topographical features but also morphology, phase distribution, compositional differences, crystal structure and orientation. The strength of the SEM lies in its inherent versatility due to the multiple signals generated, simple image formation process, wide magnification range, and excellent depth of field.

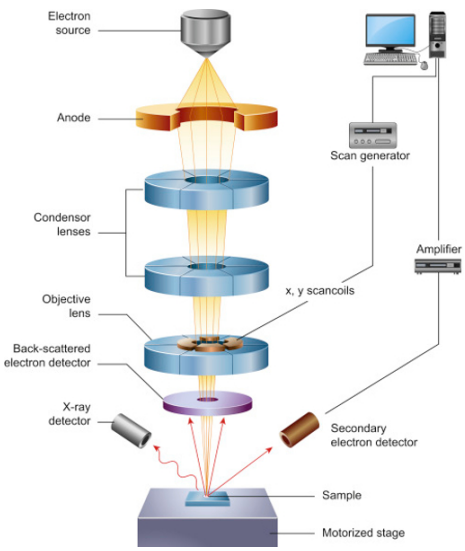

FIGURE 2.9: Schematic of SEM [From [64]].

In Fig. 2.9, we represent a general schematic of SEM explaining its working principle. As shown, an electron beam is generated within the electron source using thermal field emission from tungsten crystal. The beam produced is accelerated by a high voltage and is passed through a combination of condenser and objective lenses. The beam diameter is controlled by these lenses. Increasing the strength of condenser lenses reduces the probe current in turn the probe diameter. The objective lens produces a smaller probe diameter when the working distance is reduced and provide higher resolution. Also, the scanning process of the surface in SEM is steered by the (x,y) deflection coils.

Finally, a focused beam of electrons pass from the aperture and interact with the sample surface. The interaction of electron beam with sample surface leads to production of secondary electrons (SEs), backscattered electrons (BSEs) and characteristic X-rays. These different signals are collected by appropriate detectors to form images on the screen. Each of these three signals correspond to different escaping depths within the sample due to the unique physical properties and energies.

Secondary electrons have low energy (typically 2 to 5 eV) and are generated due to inelastic interactions. They are influenced more by surface properties than by atomic number. The SEs are emitted from an outer shell of a specimen atom upon energy transfer from incident electron. Thus, the term "secondary" points to the fact that this signal is not a scattered portion of the beam. In practice, SEs are sometimes defined as electrons with energy < 50 eV. The depth from which SEs escape the sample is generally 5-50 nm due to their low energy. The SE sampling volume (sample depth) is smaller than the BSE and provides a high-resolution image of the sample surface. Secondary electron intensity depends on the surface orientation with respect to the beam and the SE detector and thus produces a morphological image of the scanned surface.
Backscattered electrons (BSEs) are emitted when the electronic probe interacts elastically with the sample, reverses its direction, and escapes the sample. These are high energy electrons, usually in majority when released from the sample at high beam voltage. The escape depth of BSEs from the sample depends on the incident beam energy and on the sample composition. The intensity of the BSE signal is proportional to the average atomic number (Z) of the sample, with heavier elements (higher Z samples) producing more BSEs. It is thus a useful signal for generating better contrast in phase images, *i.e.* higher Z phases appear brighter than lower Z phases. The BSE intensity and trajectory are also dependent upon the angle of incidence between the beam and the specimen surface. Due to the relatively high energy of the BSE signal, the sampling volume is greater than that of SEs.

Characteristic X-rays and Auger electrons are obtained by inelastic interactions in which an inner shell electron is emitted from an atom of the sample. Following the creation of a hole in an inner shell, the atom relaxes by a transition in which an outer shell electron fills the inner shell. The transition of high energy outer shell electron to the inner level results in a release of energy from the atom. This emission may be radiative in the form of a photon (X-ray) or may lead to the emission of an electron (the Auger electron) from the atom. A single ionization can result in either an X-ray or an Auger electron. The originated X-rays may act as probe and can be used for imaging as well as the identification of elements within the sample volume. This forms the basis of the Energy-Dispersive Spectrometry (EDS). Like-wise, the Auger electrons can be a powerful probe to determine the surface composition of the sample due to their small escape depth. This feature is exploited in AES which is briefly discussed in the next section.

2.1.6.5 AES

As mentioned above, the Auger electrons result from non-radiative relaxation processes of the core hole created during the primary ionization process. In Fig. 2.10, the Auger process in solid is illustrated. This diagram shows the KL_2L_3 transition using a three-fold process. Firstly, the incident beam of electrons remove an inner K shell electron in an atom yielding an electronically excited ion (ionization). Then, a relaxation process occurs in order to fill the vacancy in inner (K) shell by the radiation-less transition of an electron from outer (L_2) level. Finally, the excess energy of the excited state ion is released by the ejection of electron from outer (here, L_3) level. This electron is referred to as "Auger electron" named after its discoverer, the French physicist Pierre Auger.

The Auger transition has a specific three letter nomenclature, which are also used to denote the Auger peaks in the electronic spectrum. It is represented by the X-ray notation of energy levels (from inner

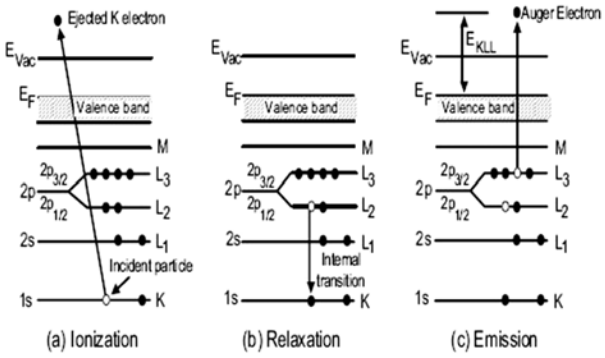

FIGURE 2.10: Schematic showing the three steps involved in the Auger process. The KL_2L_3 Auger transition is illustrated. The open and filled circles represent holes and electrons, respectively. [From [65]].

to outer) involved in 3-step process explained above e.g. KLM,LMM,MNN. The kinetic energy of the Auger electron (E_{kin}) after the KL_2L_3 transition is given by

$$E_{kin} = E_K - E_{L_2} - E_{L_3} - \Phi \tag{2.15}$$

where E_K, E_{L_2}, E_{L_3} are the the binding energies of the K, L_2 and L_3 energy levels, respectively.

The kinetic energy of the Auger electron, in contrast to photoemission is independent of the primary beam energy creating the initial core hole. They are characteristic solely of the binding energies of electrons within the atom. Hence, Auger electrons may be used for elemental identification. Also, Auger processes dominate for elements of low atomic number, Z as found using the relative probabilities of X-ray fluorescence and Auger emission as a function of Z [45].

The Auger spectra is typically shown in their derivative form by plotting $dN(E)/dE$ as a function of the kinetic energy. This is because in the $N(E)$ spectrum, Auger peaks are small and superimposed on a large SE background, making identification difficult. The peak to peak height of the differentiated signal is proportional to the area under $N(E)$ spectrum and, may also be used as a probe of the surface elemental concentration. Also if a Auger peak corresponding to the known surface coverage is available, AES may predict coverage values for monolayer or submonolayer regime of adsorbate deposition [45]. The surface sensitivity of AES in reference to the "Universal curve" arises from the relatively small IMFP values for Auger electrons (5 nm or less), with typical kinetic energy range of [10-2000] eV.

2.1.6.6 Instrumentation: Scienta-Omicron Nano-SAM lab

The NanoSAM Lab is the ultimate tool for the analysis of nano-structures. Driven by the unique performance of the UHV Gemini electron column, it guarantees unrivaled resolution below 5 nm in SAM and better than 3 nm in SEM. In contrast to other Auger tools, the extremely good resolution is not only available at standard 20 keV beam energy, but even at 5 keV the SAM resolution remains below 10 nm. This allows operation in a parameter range where the Auger cross sections are high, and well documented for quantitative analysis. It has 4-axis sample stage with temperature range up to >500 K and lock screw. Motorized, precise sample movement (X/Y= $\pm$ 5 mm, Z = $\pm$ 3 mm) with optional position read-out, tilt range of $\pm$ 70°. Sample dimensions are typically $10\times10\times5$ mm^3. It also has a wobblestick (with rotational movement) to ensure mechanical clamping of the sample plate. Heating is done by a PBN-heater element integrated in the clamping device of the sample holder.

The UHV Gemini is an electron source for scanning electron microscopy with ultra-high resolution, even in the low voltage range. The electron column comprises a thermal field emitter (TFE), an electromagnetic condenser and a combined electromagnetic/electrostatic objective lens. Changing the apertures is achieved fully electromagnetically. Integrated into the column is an in-lens secondary electron detector with an optical light guide to a photomultiplier. The TFE-source chamber is individually pumped by an ion getter pump and can be separated by a gate valve. The beam energy range is 100 eV to 30 keV.

Example of SAM measurement
The NanoSAM lab enables the direct acquisition of the live SEM image into the Matrix Nano-SAM software for performing AES experiments. In this work, we mainly used reduced raster scan spectroscopy. It should be made sure that cycle time in SmartSEM software is shorter than the dwell time per energy step in Matrix for reduced raster survey scan. Also, in order to perform Auger measurements high beam currents (at least 1 nA) and beam energy in range 3-10 keV are required. These requirements are in contrast with High-resolution SEM measurements executed solely. A survey scan carried out on a Pb droplet dewetted on a $Al_{13}Co_4$(010) surface is shown in Fig. 2.11. The survey scan was done in 30-1000 eV energy range with 1 eV energy step and dwell time of 0.5 s. The most intense Pb peak in the Auger spectra (Fig. 2.11) corresponds to the $N_7O_{4,5}O_{4,5}$ transition.

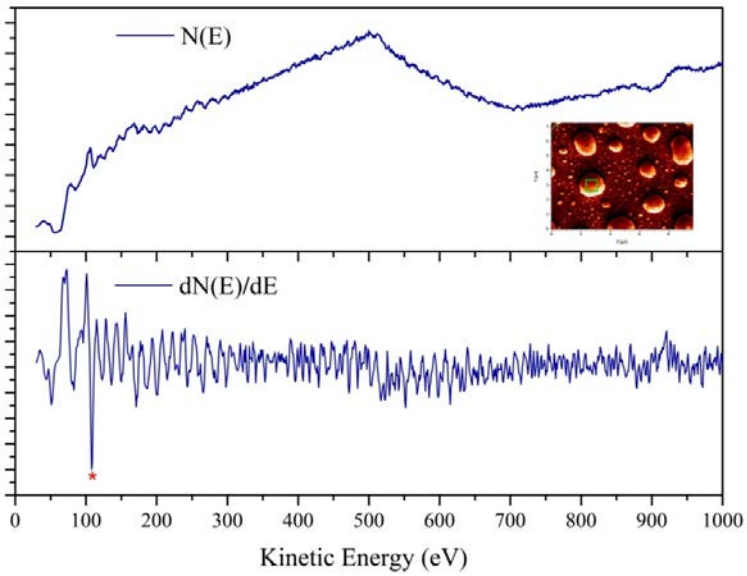

FIGURE 2.11: A survey scan performed on Pb droplets. Inset: It shows the SEM image imported in Matrix software to define particular area for AES. Top: The N(E) curve showing the AES data for the specific area marked in the inset. Bottom: the Auger spectra in its differential form ($dN(E)/dE$ versus kinetic energy) to highlight the small peaks. The red star marks the main Pb peak in the differentiated Auger spectra.

2.2 Computational Methods

2.2.1 Introduction

Simulations based on first principles methods are largely used to determine, explain and predict the materials structures and properties. In this work, it has been applied to unveil the BaAuGe surface structures (chapters 3 and 4) and to investigate the wetting properties of complex surfaces (chapter 5).

DFT is a complementary approach to experiments. It can also be predictive to build a first base for new experiments. There is a variety of *ab initio* methods based on wave functions and electronic density which propose solutions to the time independent non-relativistic Schrödinger equation written as:

$$\hat{H}\Psi = E\Psi \tag{2.16}$$

Here, $\hat{H}$ is the Hamiltonian operator related to the system while Ψ and E are the one eigenstate and its energy (eigenvalue), respectively. This elegant mathematical equation when solved for a material provides insights on its physico-chemical structures and properties at the atomic scale. However, any realistic system contains a large number of electrons, which induces a numerical complexity, preventing any exact solution to Equation 2.16.

Initially many *ab initio* methods were wave function based electronic structure methods of many-body systems such as Hartree-Fock (HF) and Post Hartree-Fock. They were very time consuming. The Density Functional Theory based on electronic density leads to much faster calculations with also a good accuracy. The DFT approach is implemented in many codes. In this work, we used the Vienna ab initio Simulation Package (VASP) [66–69].

In the following, we shortly present the fundamentals of the DFT method (section 2.2.3), along with the practical implementation in the VASP code (section 2.2.4). A few examples of DFT calculations are also given (section 2.2.6).

2.2.2 Many-body Schrödinger equation

The structural and electronic properties of a system with N atoms and n electrons (for simplicity, a non-polarized spin system) result from the following equation:

$$\hat{H} = \underbrace{-\frac{\hbar^2}{2}\sum_{\alpha}^{N}\frac{\nabla_\alpha^2}{M_\alpha}}_{\hat{T}_N} \underbrace{-\frac{\hbar^2}{2m_e}\sum_{i}^{n}\nabla_i^2}_{\hat{T}_e} + \underbrace{\underbrace{\sum_{\alpha}^{N}\sum_{\alpha>\beta}^{N}\frac{e^2 Z_\alpha Z_\beta}{4\pi\epsilon_0 R_{\alpha\beta}}}_{\hat{V}_{NN}} \underbrace{-\sum_{\alpha}^{N}\sum_{i}^{n}\frac{e^2 Z_\alpha}{4\pi\epsilon_0 R_{\alpha i}}}_{\hat{V}_{eN}} + \underbrace{\sum_{i}^{n}\sum_{i>j}^{n}\frac{e^2}{4\pi\epsilon_0 r_{ij}}}_{\hat{V}_{ee}}}_{\hat{V}} \tag{2.17}$$

In this equation, the first term corresponds to the kinetic energy operator ($\hat{T}_N$) of the nuclei, the second to the kinetic energy operator of the electrons ($\hat{T}_e$), the third, fourth, fifth terms correspond to the nuclei- nuclei, electron-nuclei, electron-electron Coulomb interactions, respectively.

∇_α^2 is the Laplace operator, M_α is the mass of the nucleus α, Z_α and Z_β are the atomic numbers of the nuclei and , $R_{\alpha\beta}$, $R_{\alpha i}$ and r_{ij} are the distances between two nuclei α and β, the electron i and the nucleus α, and two electrons i and j.

The Born-Oppenheimer approximation (or "clamped nuclei" approximation) uncouples the nuclear and electronic kinetic terms. It is based on the fact that nuclei are much heavier than electrons. The kinetic energy of the nuclei is then much lower than the kinetic energy of the electrons.

We thus focus on the electronic part of the Schrödinger equation:

$$\left[-\frac{\hbar^2}{2m_e}\sum_{i}^{n}\nabla_i^2 - \sum_{\alpha}^{N}\sum_{i}^{n}\frac{e^2 Z_\alpha}{4\pi\epsilon_0 R_{\alpha i}} + \sum_{i}^{n}\sum_{i>j}^{n}\frac{e^2}{4\pi\epsilon_0 r_{ij}}\right]\Psi_e = E_e\Psi_e \tag{2.18}$$

$$\hat{H}_e = \hat{T}_e + \hat{V}_{eN} + \hat{V}_{ee} \tag{2.19}$$

In the following, we detail the determination of the wave function $\Psi_e(\vec{r}_1, \vec{r}_2, ...\vec{r}_n)$ (where $\vec{r}_i$ represents the position of each electron i), based on the DFT formalism.

2.2.3 The Density Functional Theory

DFT is a quantum mechanical method which has become a standard tool for electronic structure calculations. In 1964, Pierre Hohenberg and Walter Kohn gave two theorems [70] which founded the basis of modern DFT calculations relying on the electronic density to determine the ground state energy of a given n electron system. In this section we use atomic units, *i.e.* $\hbar = m_e = \frac{e^2}{4\pi\epsilon_0} = 1$. The first theorem states that the external potential (V_{Ne}), and hence the total energy, is a unique functional of the electronic density.

From this theorem, it follows that the ground state electronic energy is a functional of $\rho_0(\vec{r})$. Thus, the electronic energy of the n electron system can be defined as

$$E_e[\rho(\vec{r})] = \underbrace{T_e[\rho(\vec{r})] + V_{ee}[\rho(\vec{r}]}_{F_{HK}[\rho(\vec{r})]} + V_{Ne}[\rho(\vec{r}] \tag{2.20}$$

where $F_{HK}[\rho(\vec{r})]$ is the contribution of the kinetic energy of electrons and the inter-electronic interactions.

The electron–nuclei interaction ("external potential") is expressed in terms of the electronic density:

$$V_{Ne}[\rho(\vec{r})] = \int \rho(\vec{r}) V_{ext}(\vec{r}) \mathrm{d}\vec{r}. \tag{2.21}$$

The second theorem states that the ground state energy can be obtained from variational methods, *i.e.*

$$E_e^0[\rho(\vec{r_0})] \leqslant \min_{\rho(\vec{r})} \frac{\langle \Psi_e[\rho(\vec{r})] \mid \hat{H}_e \mid \Psi_e[\rho(\vec{r})] \rangle}{\langle \Psi_e[\rho(\vec{r})] \mid \Psi_e[\rho(\vec{r})] \rangle} = E[\rho(\vec{r})], \text{if} \rho \neq \rho_0 \tag{2.22}$$

where the density ($\rho(\vec{r})$) that minimizes the total energy is the exact ground state density ($\rho(\vec{r_0})$). The two HK theorems established that the electronic density of a system can define the ground state of the system. However, the inter-electronic interaction term, V_{ee}, is not known exactly. Hence, mean field approximation is considered which describes the electronic contribution of the system as:

$$F_{HK}[\rho(\vec{r})] = T_e[\rho(\vec{r})] + V_{ee}[\rho(\vec{r}] = T_e[\rho(\vec{r})] + V_H[\rho(\vec{r})] + V_{unknown}[\rho(\vec{r})]. \tag{2.23}$$

Here, the term $V_H[\rho(\vec{r})] = \frac{1}{2} \int \frac{\rho(r_1)\rho(r_2)}{r_{12}} dr_1 dr_2$ is the Hartree energy which accounts for the classical Coulomb e-e interaction. $V_{unknown}$ is the non-classical potential energy term into which all the complex quantum-mechanical many-body effects are gathered.

2.2.3.1 The Kohn Sham Method

The evaluation of the kinetic energy functional (T_e) and the non-classical functional ($V_{unknown}$) is not straightforward.

A practical method for obtaining $E_e[\rho(\vec{r})]$ and thus minimizing the functional came from Kohn and Sham in 1965 [71]. They proposed that the HK functional in Equation 2.23 can be expressed explicitly by considering the density of a noninteracting reference system having the same electronic density as the real system, *i.e.* $\rho_{ref}(\vec{r}) = \rho(\vec{r})$ and $T_{ref}[\rho(\vec{r})] \neq T[\rho(\vec{r})]$. Then, the electronic contribution from Equation 2.23 becomes

$$F_{HK}[\rho(\vec{r})] = V_H[\rho(\vec{r})] + E_{xc}[\rho(\vec{r})] + T_{ref}[\rho(\vec{r})] \tag{2.24}$$

where $E_{xc}[\rho(\vec{r})]$ is the exchange and correlation energy which accounts for the implicit quantum-mechanical many-body effects. It can be expressed with the exchange energy ($E_c[\rho(\vec{r})]$) and correlation energy terms:

$$E_{xc}[\rho(\vec{r})] = (T[\rho(\vec{r})] - T_{ref}[\rho(\vec{r})]) + (V_{ee}[\rho(\vec{r})] - V_H[\rho(\vec{r})]) \tag{2.25}$$

The Kohn-Sham method defines the electronic energy of the n electron system as

$$E_e[\rho(\vec{r})] = T_{ref}[\rho(\vec{r})] + V_H[\rho(\vec{r})] + E_{xc}[\rho(\vec{r})] + V_{Ne}[\rho(\vec{r})] \tag{2.26}$$

where $T_{ref}[\rho(\vec{r})]$ is the kinetic energy of a noninteracting electron gas and the other terms are the Hartree energy, the exchange and correlation energy and the external nuclei-electron interaction, respectively. The multi-electronic wave function is further expressed as a Slater determinant of the one electron functions using the orthonormal ϕ_i set:

$$\Psi_e(\vec{r}_1, \vec{r}_2 .... \vec{r}_n) = \frac{1}{\sqrt{n!}} \begin{vmatrix} \phi_1(\vec{r}_1) & \phi_2(\vec{r}_1) & \cdots & \phi_n(\vec{r}_1) \\ \phi_1(\vec{r}_2) & \phi_2(\vec{r}_2) & \cdots & \phi_n(\vec{r}_2) \\ \cdots & \cdots & \cdots & \cdots \\ \phi_1(\vec{r}_n) & \phi_2(\vec{r}_n) & \cdots & \phi_n(\vec{r}_n) \end{vmatrix}$$

In Kohn and Sham equation, the concept of orthonormal orbitals is used, *i.e.* $\int \phi_i(\vec{r})\phi_j(\vec{r})\mathrm{d}\vec{r} = \delta_{ij}$. These orbitals are eigenvectors of the Kohn-Sham equation and satisfy $\rho(\vec{r}) = \sum_i^n |\phi_i(\vec{r})|^2$ for the "n" particle system. This equation is usually expressed as:

$$\begin{aligned} &\left(-\frac{1}{2}\nabla^2 + \hat{V}_{eff}(\vec{r_i})\right)\phi_i(\vec{r}) = \varepsilon_i \phi_i(\vec{r}) \\ &(-\frac{1}{2}\nabla^2 + \underbrace{\hat{V}_{Ne}(\vec{r_i}) + \hat{V}_H[\rho(\vec{r_i})] + \hat{V}_{xc}[\rho(\vec{r_i})]}_{\hat{V}_{eff}(\vec{r_i})})\phi_i = \varepsilon_i \phi_i \end{aligned} \tag{2.27}$$

where,

$$\begin{aligned} \hat{V}_{Ne}(\vec{r_i}) &= -\sum_{\alpha}^{N} \frac{Z_\alpha}{R_{i\alpha}} \\ \hat{V}_H[\rho(\vec{r_i})] &= \int \frac{\rho(\vec{r_j})}{r_{ij}} \mathrm{d}\vec{r_j} \\ \hat{V}_{xc}[\rho(\vec{r_i})] &= \frac{\delta E_{xc}[\rho(\vec{r_i})]}{\delta \rho(\vec{r_i})}. \end{aligned}$$

In the above equations, the Hartree and exchange-correlation potentials depend on $\rho(\vec{r_i})$, which depends on the orbitals ϕ, which in turn depends on $\hat{V}_{eff}(\vec{r_i})$. Thus solving the Kohn–Sham (KS) equations has to be performed in a self-consistent (iterative) manner [46].

If the exact form of E_{xc} was known, the Kohn-Sham approach would lead to the exact energy of the system. However, it is not the case. In the next section we discussed exchange and correlation functionals.

2.2.3.2 Approximate Exchange and Correlation functions

Three of the most popular types of exchange-correlation functionals are briefly described below:

- *The local-density approximation (LDA)*: It is a simple approximation which is valid for slowly varying densities [46]. It can be expressed as:

$$E_{xc-LDA}[\rho] = \int \rho(r)\varepsilon_{ex-LDA}(\vec{r})\mathrm{d}^3\vec{r} \tag{2.28}$$

  where ε_{ex-LDA} is the exchange-correlation energy per particle of the homogeneous electron gas of density ρ, *i.e.* the exchange-correlation energy density is taken to be that of a uniform electron gas of the same density. The exchange energy term is known (given by Dirac) [72] and the correlation energy is estimated by quantum mechanical Monte-Carlo simulations [73, 74].

  Modern LDA functionals usually differ in how their correlation contributions have been fitted to the many-body free electron gas data [46].

- *The generalized gradient approximation (GGA)*: In this approximation, the gradient of the density, $\nabla\rho(r)$, at each coordinate along with the density itself are used to define the exchange-correlation energy .

$$E_{xc-GGA}[\rho] = \int \rho(r)\varepsilon_{ex-LDA}(\vec{r})\nabla\rho(\vec{r})\mathrm{d}^3\vec{r} \tag{2.29}$$

  Therefore, GGAs are "semi-local" functionals which are a step forward from LDA but not necessarily superior. Commonly used GGA functionals in surface physics are PW91 [75] and PBE [76]. PBE functional has several derivatives, RPBE [77], RPBEsol [78], optPBE [79] etc.

- Other next-generation functionals include the *meta-GGAs* which use the second derivative of the density. The *hybrid functionals* add an exact exchange term calculated from the Hartree Fock theory to the conventional approach of the DFT exchange correlation. Another functional that explicitly accounts for correlation is the random phase approximation (RPA) within the adiabatic-connection-fluctuation-dissipation theorem.

Consideration of van der Waals interactions:
Popular local and semilocal density functionals are unable to describe correctly the van der Waals interactions resulting from dynamical correlations between fluctuating charge distributions [80]. A pragmatic approach to work around this problem is to add a correction to the conventional Kohn-Sham DFT energy E_{KS-DFT}:

$$E_{DFT-disp} = E_{KS-DFT} + E_{\text{disp}}. \tag{2.30}$$

The term E_{disp} is an empirical atomic-pairwise dispersion correction. In the D3 correction method of Grimme *et al.* [81], the following vdW-energy expression is used:

$$E_{\text{disp}} = -\frac{1}{2}\sum_{i=1}^{N_{at}}\sum_{j=1}^{N_{at}}\sum_{\mathbf{L}}{}' \left(f_{d,6}(R_{ij,L})\,\frac{C_{6ij}}{R_{ij,L}^{6}} + f_{d,8}(R_{ij,L})\,\frac{C_{8ij}}{R_{ij,L}^{8}} \right), \tag{2.31}$$

where the summations are over all atoms N_{at} and all translations of the unit cell $L = (l_1, l_2, l_3)$, the prime indicates that $i \neq j$ for $L = 0$ (reference cell). The 6th and 8th order dispersion coefficients are denoted by C_{6ij} and C_{8ij}, respectively for atom pair ij. The internuclear distance between atom pair ij is represented as R_{ij}. The term $f(R_{ij})$ is a damping function which role is to scale the force field.

In the zero damping D3 method (D3(zero)), damping of the following form is used:

$$f_{d,n}(R_{ij}) = \frac{s_n}{1 + 6(R_{ij}/(s_{Y,n}Y_{0ij}))^{-\alpha_n}}, \tag{2.32}$$

where $Y_{0ij} = \sqrt{\frac{C_{8ij}}{C_{6ij}}}$, the parameters α_6, α_8, $s_{Y,8}$ are fixed at values of 14, 16, and 1, respectively, and s_6, s_8, and $s_{Y,6}$ are adjustable parameters whose values depend on the choice of exchange-correlation functional [80].

The choice of the functional remains always related to the type of material to study (conductor, semiconductor, etc ...) as well as the type of study: surface, solid, molecule, etc. We have used the PBE-GGA [76] exchange-correlation functional in our calculations for complex intermetallic surfaces. Our choice of this functional in this work is governed by the fact that we investigate the surface structures of extended CMA systems like clathrate compounds. These compounds have a large number of atoms in their unit cell and the relaxation of their surfaces with hybrid functionals would have required a significant amount of computational time, while not necessarily improving our results. This assertion is based on a recent paper, comparing the calculated atomic distances, cohesive energies and bulk moduli of 27 metals using hybrid and GGA functionals [82]. Our choice is also backed up by the previous calculations performed on other CMAs surfaces using PBE-GGA functionals leading to reliable results [83–85]. We have also used the DFT-D3 scheme in this work which tends to improve cohesive energy values for Au and Ge (see Tab. 2.4). This scheme has been used in complete surface analysis of BaAuGe(110) (see chapter 4).

2.2.3.3 Self-consistent cycle

The DFT calculations are carried out in a self-consistent, *i.e.* iterative manner (see Fig. 2.12). The calculation starts with an initial guess for $\rho_{in}(\vec{r})$ and then calculates the corresponding $\hat{V}_{eff}$, and solves the Kohn–Sham equations for the refined Ψ_n and $\rho_{out}(\vec{r})$. From these, a new density ($\rho_{new}(\vec{r}) = \mathrm{x}\rho_{in}(\vec{r}) + (\mathrm{x}-1)\rho_{out}(\vec{r})$) is calculated and the loop starts again. Basically, two loops are operated during this cycle : inner electronic loop for optimization of Ψ_n and outer ionic loop for refinement of atomic positions by minimizing forces. This procedure is then repeated until required convergence (satisfying the criteria of minimization of forces) is reached and that what refers to as "well-converged" calculations.

2.2.3.4 Bloch's theorem and plane-wave basis set

The traditional crystalline solids are periodic which introduces elements of simplicity for tackling their electronic structure problem. The Bloch's theorem based on the translational symmetry of periodic systems can be applied for infinite solids to be treated in periodic three-dimensional simulation

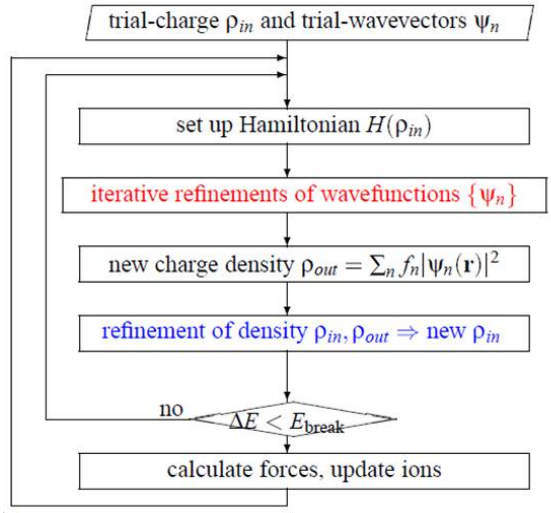

FIGURE 2.12: Flow chart showing the steps executed in a self-consistent cycle [taken from Ref. [86]].

cells, primitive or non-primitive. Thus, the one-electron wave function in a periodic potential can be written as

$$\Psi_{nk}(\vec{r}) = u_{nk}(\vec{r})e^{i\vec{k}\vec{r}} \tag{2.33}$$

where Ψ_{nk} are the Bloch wave functions associated with the band index n, $\vec{k}$ is the Bloch wave vector and $u_{nk}(\vec{r})$ is a periodic function presenting the periodicity of the lattice. This periodic function can be expanded using Fourier transformation in terms of discrete plane-waves basis set in a space defined by the reciprocal vectors ($\vec{G}$) as

$$u_{nk}(\vec{r}) = \sum_G \nu_{nk}(\vec{G})e^{i\vec{G}\vec{r}} \tag{2.34}$$

where $\vec{G} \cdot \vec{R} = 2\pi l$, where l is an integer, **R** are the crystal lattice vectors and $\nu_{nk}(\vec{G})$ are the plane-wave (PW) expansion coefficients. Hence, the electron wave function $\Psi_{nk}(\vec{r})$ can be expressed as a linear combination of plane waves (PWs),

$$\Psi_{nk}(\vec{r}) = \sum_G C_{nk+G}e^{i(\vec{k}+\vec{G})\cdot\vec{r}} \tag{2.35}$$

These PW coefficients $C_{nk+G}e^{i(k+\vec{G})}$ can be varied to determine the lowest energy solution by solving a set of equations using the matrix algebra. As $\Psi_{nk}(\vec{r}) = \Psi_{nk+G}(\vec{r})$, the $\vec{k}$ vectors corresponding to all the $\Psi_{nk}(\vec{r})$ wave functions can be restricted to the first Brillouin zone (BZ). For exact calculations, the dimension of the plane-wave basis set should be infinite. However, the plane-waves at the lower end of the kinetic energy range are the most imperative. So in practice, for a sufficiently large set of well converged $\Psi_{nk}(\vec{r})$ wave functions, the $\vec{G}$ is restricted is such that for a given $\vec{k}$:

$$\frac{1}{2}|\vec{G} + \vec{k}|^2 \leq \mathrm{E}_{cut-off} \tag{2.36}$$

where $\mathrm{E}_{cut-off}$ is the cutoff kinetic energy.

The value of $E_{cut-off}$ determines the size of the plane wave basis set used to solve the KS equations.

2.2.4 Implementation of DFT: VASP code

In a DFT calculation using VASP, the solution of the Kohn–Sham equations for a given atomic structure and chemical composition of the system is calculated. The main quantities, like the one-electron orbitals, the electronic charge density, and the local potential are expressed using plane wave basis sets in VASP code. The interactions between the electrons and ions are described using norm-conserving or ultrasoft pseudopotentials, or the projector-augmented-wave method.

2.2.4.1 Periodic systems: Slabs

The implementation of DFT within the VASP code is done with periodic boundary conditions. Modeling 2D surfaces then requires the use of "slabs", *i.e.* a simulation cell made from a stack of atomic planes separated by a void thickness.

In Fig. 2.13, a vacuum region is added along the a-direction perpendicular to surface, dividing the slab into regions of solid (condensed phase) and vacuum.

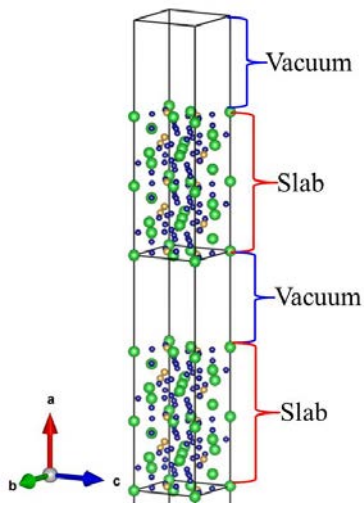

FIGURE 2.13: Illustration of the supercell approach to model surfaces.

On the one hand, the void thickness should be large enough to prevent the interaction between the surface and its periodic images (prevent the interaction of two surfaces located in two neighboring cells). On the second hand, the slab should be sufficiently thick to reproduce the properties of the condensed phase in the middle. In our calculations, the thickness of vacuum $\geqslant 15$ Å and that of slab $\geqslant 14$ Å is considered.

2.2.4.2 The Pseudopotential Approximation

The use of a Plane-Wave basis set also presents certain drawbacks. The core wave functions are sharply peaked near the nucleus, and the valence wave functions present a lot of wiggles near the nucleus. High Fourier components are then present, requiring the consideration of a large number of plane waves.
The pseudopotential approximation replaces the strong ionic potential V in the core region, by a pseudopotential V_{pseudo}. The corresponding set of pseudo-wave functions Ψ_{pseudo} and the all-electron

wave functions Ψ are alike outside a chosen cutoff radius r_c and so display the same dispersion character. However, Ψ_{pseudo} does not possess the nodal structure which cause oscillations inside r_c, implying they can now be described with a feasible number of plane-waves. A schematic illustration of the pseudopotential concept is shown in Fig. 2.14.

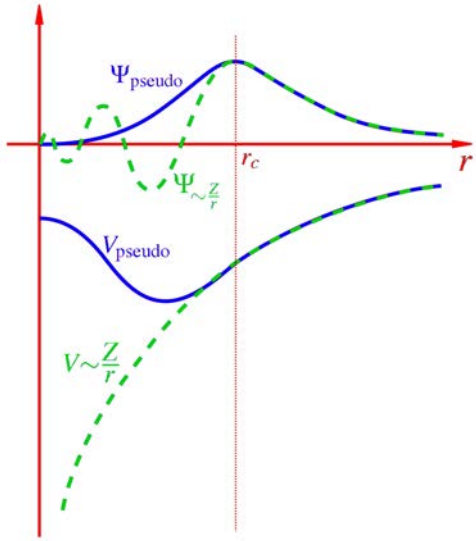

FIGURE 2.14: Illustration of the pseudopotential concept.

In the present work, the core electrons are not considered ("frozen core" approximation) and we used the projector-augmented-wave (PAW) method. This method is a generalization of the ultra-soft pseudo-potentials and the linear augmented plane wave (LPAW) methods [87, 88]. Application of PAW method leads to smooth variation of wave function in augmentation region defined by PAW sphere of radius, r_c. While, in the interstitial region outside r_c pseudo-wavefunctions are well-described. The pseudo-wavefunctions do not have the same variations as the "all-electron" wave-functions inside the spheres (reconstruction) [89].

In VASP, it is the POTCAR files that include all this information. Tab. 2.3 lists the elements studied in this work.

TABLE 2.3: Electronic configuration of elements used in this work. ENMAX values from their POTCAR files in VASP are provided.

Element	Electronic configuration	No. of valence electrons considered	ENMAX (eV)
Ba	[Kr] $4d^{10}$ $5s^2$ $5p^6$ $6s^2$	10	187.81
Au	[Xe] $4f^{14}$ $5d^{10}$ $6s^1$	11	229.94
Ge	[Ar] $3d^{10}$ $4s^2$ $4p^2$	4	173.81
Al	[Ne] $3s^2$ $3p^1$	3	240.30
Co	[Ar] $3d^7$ $4s^2$	9	270.00
Pb	[Xe] $4f^{14}$ $5d^{10}$ $6s^2$ $6p^2$	4	97.97

2.2.4.3 Convergence parameters

For an accurate result, it is necessary that the intrinsic property such as the total energy E_{tot} of a given system is independent of the value of the calculation parameters. Two main parameters that govern the resolution of KS equations, hence the convergence of computation, are:

- the energy of cutoff ($E_{cut-off}$), which determines the size of the plane wave basis set
- the k-point mesh, which corresponds to the number of points k describing the reciprocal space.

On the bulk studied, we performed convergence tests for the total energy E_{tot} of a given system and are presented in the following . **ENCUT parameter**

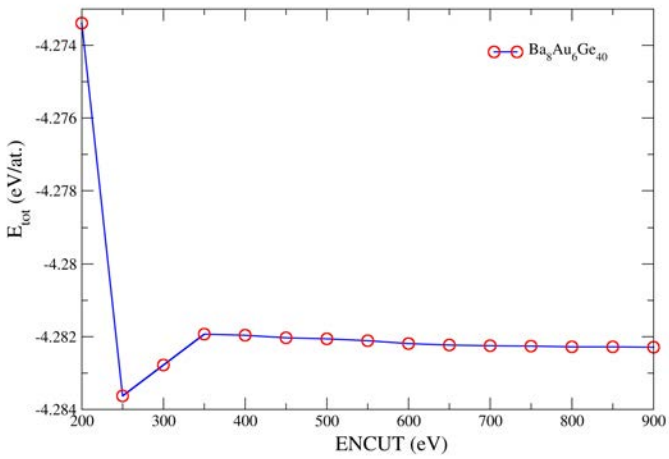

FIGURE 2.15: Total energy of bulk $Ba_8Au_6Ge_{40}$ as a function of cut-off energy (ENCUT) for a k-point mesh: $8 \times 8 \times 8$.

It plays a critical role in the accuracy and duration of the calculation, *i.e.* the larger the size of plane wave basis set, the longer is the calculation time. The cutoff energy ($E_{cut-off}$) depends substantially on the type of chemical element of the system considered, the corresponding pseudo-potentials, as well as the size and shape of the elementary cell.

It is recommended in VASP lectures [90] to choose ENCUT value equal to $\max(\text{ENCUT}) + 0.30 \times \max(\text{ENCUT})$ for a system, to perform good precision calculations. The value of ENCUT equal to 450 eV is chosen for the Ba-Au-Ge compound as well as for the other systems used in interfacial energy calculations. The choice for the ENCUT value was made on the basis of a well-balanced approach considering the convergence tests (see Fig. B.3) for the accuracy of the calculations as well as the computational resources. Also, this value is larger than the recommended criteria to choose the ENCUT value.

K-point sampling

The net effect of the Bloch's theorem has been to change the problem of an infinite number of electrons to the one by considering only the number of electrons in the unit cell (or half that number, depending on whether the states are spin-degenerate or not). It requires to choose a finite number of k-points so as to appropriately sample the Brillouin Zone. The electronic density is then defined as a discrete sum over first Brillouin zone using the weighted k points :

$$\rho(\vec{r}) = \frac{1}{\Omega_{BZ}} \sum_n \sum_k w_{nk} f_{nk} |\Psi_{nk}(\vec{r})|^2 \mathrm{d}\vec{k} \tag{2.37}$$

where Ω_{BZ} is the volume of the first Brillouin zone, f_{nk} are the partial occupancies corresponding to the nk state and w_{nk} are weight factors assigned to the state, *i.e.* $\sum_k w_k = 1$.

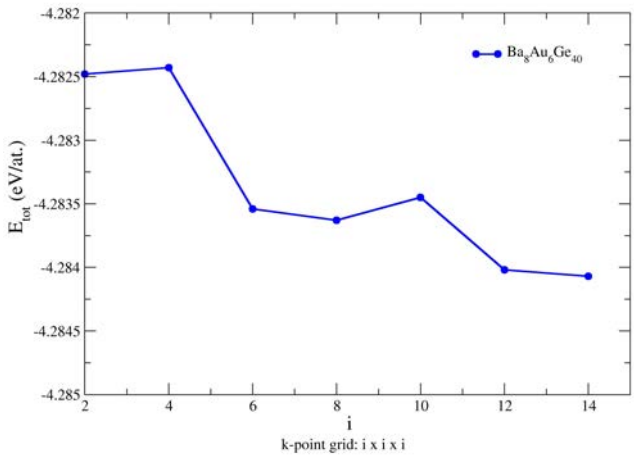

FIGURE 2.16: Total energy of bulk $Ba_8Au_6Ge_{40}$ as a function of a k-point mesh: $i \times i \times i$ using ENCUT value of 300 eV.

The density of k points in the reciprocal space is inversely proportional to the volume of the studied crystal system. Up to a certain extent, the accuracy of the calculation can then be controlled and increased by increasing the mesh size. However, this increase in precision goes hand in hand with the calculation time. The k-points density should ideally be homogeneous. Then, the anisotropy of the system should be mirrored in the k-points grid. By using the symmetry of the crystal, we can reduce the size of the grid without changing the result of the integration and thus facilitating the calculations. In our calculations, we used the automatically generated Monkhorst-Pack type k-point grid [91] implemented in the VASP code. Our test calculation to find the appropriate k-mesh for bulk $Ba_8Au_6Ge_{40}$ is shown in Fig. B.4, this calculation was performed for a ENCUT value equal to 300 eV ($\sim 1.3 \times \max(\mathrm{ENCUT}_{\mathrm{Ba_8Au_6Ge_{40}}})$).

In the next section, examples of DFT calculations are given: cohesive energy, formation enthalpy, surface energy, density of states.

2.2.5 Thermodynamic Calculations

2.2.5.1 Cohesive energy and formation enthalpy

The cohesive energy is one of the basic property of a bulk system. For elemental bulk systems, the corresponding cohesive energy (in eV/at.) is also the chemical potential. This quantity is very useful for surface energy calculations. Here, the cohesive energy (E_i^{coh} or μ_i^{bulk}) is derived from the total energy of the bulk system (E_i^{bulknc}) of the element i and corrected by the energy of an isolated atom in its electronic ground state (E_i^{iso}) as:

$$E_i^{coh} = \frac{E_i^{bulknc} - N_i^{bulk} E_i^{iso}}{N_i^{bulk}} \tag{2.38}$$

where N_i^{bulk} is the number of i atoms in the bulk system. Due to periodic boundary conditions, the isolated atom needs to be calculated in a periodic unit cell as well. We chose an orthorhombic unit

cell, with cell parameters larger than 10 Å. Then, any interaction between periodic images and physically incorrect spherical states are avoided [92]. Tab. 2.4 presents the values of cohesive energies calculated for all the metals studied in this work, along with their crystal structure (Pearson notation). It also includes references from literature for both computed and experimental values.

	a (Å)	E^{coh} (eV/at.)			a (Å)	E^{coh} (eV/at.)	
Ba	5.03	-1.84	PBE	**Al**	4.038	-3.50	PBE
(bcc)	5.03	-1.88	PBE [92]	(fcc)	4.04	-3.43	PBE [92]
$cI2$	4.98	-1.96	DFT-D3	$cF4$	4.008	-3.67	DFT-D3
	5.01	-1.90	exp. [93, 94]		4.04	-3.39	exp [93, 95]
					4.038	-3.43	NL-SOC
Au	4.16	-3.03	PBE	**Pb**	5.03	-2.94	PBE
(fcc)	4.16	-3.11	PBE [92]	(fcc)	5.05	-2.92	PBE [92]
$cF4$	4.17	-3.04	PBE [96]	$cF4$	5.04	-1.98	NL-SOC
	4.10	-3.68	PBEsol [96]		5.05	-1.96	NL-SOC [92]
	4.10	-3.68	DFT-D3		4.97	-3.17	DFT-D3
	4.08	-3.81	exp. [93, 97]		4.95	-2.03	exp. [93, 98]
Ge	5.78	-3.72	PBE	**Co**	2.49	-5.15	PBE
(fcc diamond)	5.76	-3.74	PBE [92]	(hcp)	2.79	-5.14	PBE [92]
$cF8$	5.76	-3.88	DFT-D3	$hp2$	2.46	-5.50	DFT-D3
	5.66	-3.85	exp. [93, 95]		2.50	-4.39	exp. [93, 99]

TABLE 2.4: Cohesive energies (E^{coh}) and lattice constants (a) computed for Ba, Au, Ge, Al, Pb and Co. Here, NL-SOC denote the non-collinear spin orbit coupling calculations.

The cohesive and formation energies of complex compounds were evaluated as well. As an example, the cohesive energy of ternary $Ba_8Au_6Ge_{40}$ compound is calculated as

$$\mu^{bulk}_{\mathrm{Ba_8Au_6Ge_{40}}} = \frac{E^{bulk}_{\mathrm{Ba_8Au_6Ge_{40}}}}{N^{bulk}_{total}} \tag{2.39}$$

where $E^{bulk}_{\mathrm{Ba_8Au_6Ge_{40}}}$ is the corrected energy of the bulk of this compound and N^{bulk}_{total} is the total number of atoms in the bulk (here, 54). The stability of the compound is related to its formation enthalpy, ΔH_f [100]. Here, it is explicitly described for $Ba_8Au_6Ge_{40}$ compound in eV/at. as

$$\Delta H_f = \frac{\mu^{bulk}_{\mathrm{Ba_8Au_6Ge_{40}}} - 8\mu^{bulk}_{\mathrm{Ba}} - 6\mu^{bulk}_{\mathrm{Au}} - 40\mu^{bulk}_{\mathrm{Ge}}}{54} \tag{2.40}$$

The cohesive energy and formation enthalpy of the two CMAs studied in this work: ternary $Ba_8Au_6Ge_{40}$ and binary o-$Al_{13}Co_4$ compounds are tabulated in Tab. 2.5.

Alloy	μ^{bulk}_{Alloy} (eV/at.)	ΔH_f (eV/at.)	
$Ba_8Au_6Ge_{40}$	-3.68	-0.31	PBE
	-3.92	-0.34	DFT-D3
o-$Al_{13}Co_4$	-4.28	-0.39	PBE
	-	-0.39	PBE [101]
	-	-0.41	PW91 [102]

TABLE 2.5: Cohesive energy and formation enthalpy of the two CMAs studied.

2.2.5.2 Surface energy

The surface free energy ($\gamma_s(hkl)$) quantifies the breaking of bonds that occurs when a surface is created. In the DFT, an expression of the surface energy $\gamma_s(hkl)$ for a symmetric slab of a simple metal having total energy E_{slab} can be written as:

$$\gamma_s(hkl) = \frac{E_{slab} - NE^{coh}}{2A} \tag{2.41}$$

where A is the surface area of slab, N is the number of atoms in the slab and E^{coh} is the cohesive energy of the metal. The factor of 2 accounts for the formation of two equivalent surfaces.
The surface stability is influenced by the surface orientation, the interlayer relaxation and possible surface reconstructions even for simple metals. For alloys, the presence of different chemical species offers additional mechanisms to minimize $\gamma_s(hkl)$, through chemical segregation or selection of planes with specific chemical composition [32].

In this thesis, we performed the surface structural analysis for the low-index surfaces of the Ba-Au-Ge intermetallic clathrate. In this section, the calculations of the surface energy are illustrated with the example of the BaAuGe(100) surface.
The computation was carried out with symmetric slabs using a methodology described in references [103–105]. According to the thermodynamic approach, the surface energy of this ternary clathrate is expressed as a function of the Ba, Au and Ge chemical potentials. We can modify equation (2.41) using the definition of the cohesive energy of the compound, i.e $\mu^{bulk}_{\mathrm{Ba_8Au_6Ge_{40}}} = 8\mu_{\mathrm{Ba}} + 6\mu_{\mathrm{Au}} + 40\mu_{\mathrm{Ge}}$. There are three possible ways in which equation (2.41) can be rewritten, one of the possibilities is:

$$\begin{aligned}\gamma_s(hkl) = \frac{1}{2A}\Bigg[E_{slab} - \frac{N^{slab}_{\mathrm{Ge}}}{40}\mu^{bulk}_{\mathrm{Ba_8Au_6Ge_{40}}} - N^{slab}_{\mathrm{Ba}}\mu^{bulk}_{\mathrm{Ba}} - N^{slab}_{\mathrm{Au}}\mu^{bulk}_{\mathrm{Au}} + \\ \frac{8N^{slab}_{\mathrm{Ge}}}{40}\mu^{bulk}_{\mathrm{Ba}} + \frac{6N^{slab}_{\mathrm{Ge}}}{40}\mu^{bulk}_{\mathrm{Au}} + \left(\frac{6N^{slab}_{\mathrm{Ge}}}{40} - N^{slab}_{\mathrm{Au}}\right)\left(\mu_{\mathrm{Au}} - \mu^{bulk}_{\mathrm{Au}}\right) + \\ \left(\frac{8N^{slab}_{\mathrm{Ge}}}{40} - N^{slab}_{\mathrm{Ba}}\right)\left(\mu_{\mathrm{Ba}} - \mu^{bulk}_{\mathrm{Ba}}\right)\Bigg]\end{aligned} \tag{2.42}$$

Considering $\left(\mu_{\mathrm{Au}} - \mu^{bulk}_{\mathrm{Au}}\right)$ as X and $\left(\mu_{\mathrm{Ba}} - \mu^{bulk}_{\mathrm{Ba}}\right)$ as Y, we can rewrite (2.42) in a simplified form as $\gamma_s(hkl) = c + aX + bY$, where a, b, and c are constants. This can be represented by a contour map expressing directly the surface energy of models as a function of chemical potentials of Ba and Au while indirectly with respect to the chemical potential of Ge (constrained by the cohesive energy of the bulk). The bulk energy of the $Ba_8Au_6Ge_{40}$ alloy can also be described in terms of its formation energy (ΔH_f in eV/at.).

The value of the chemical potentials depends on the surface preparation conditions and the precise or exact chemical composition of the bulk system. The range of variation for the chemical potentials is set by the equilibrium condition between the bulk and the surface (no segregation):

$$\Delta H_f \times \frac{N^{total}_{bulk}}{N^{bulk}_i} < \left(\mu_i - \mu^{bulk}_i\right) \leqslant 0 \tag{2.43}$$

where N_{bulk}^{total} is the total number of atoms in bulk, N_i^{bulk} is the number of i atoms in bulk. In our case, the individual limits of chosen pair of elements (Ba and Au) are quantitatively found as $\left(\mu_{\mathrm{Au}} - \mu_{\mathrm{Au}}^{bulk}\right)$ in [-2.83:0] eV and $\left(\mu_{\mathrm{Ba}} - \mu_{\mathrm{Ba}}^{bulk}\right)$ in [-2.12:0] eV .

In the case of the $Ba_8Au_6Ge_{40}$ ternary compound, the variation in $\Delta\mu_{\mathrm{Ba}}$ and $\Delta\mu_{\mathrm{Ba}}$ is given by:

$$\Delta H_f \times \frac{N_{bulk}^{total}}{N_{\mathrm{Ba}}^{bulk}} + \frac{N_{\mathrm{Au}}^{Bulk}}{N_{\mathrm{Ba}}^{bulk}} \times \left(\mu_{\mathrm{Au}}^{bulk} - \mu_{\mathrm{Au}}\right) < \left(\mu_{\mathrm{Ba}} - \mu_{\mathrm{Ba}}^{bulk}\right) \leqslant 0 \tag{2.44}$$

An illustration exhibiting the zone of interest for the ternary Ba-Au-Ge system for comparing the stability of different surface models is shown in Fig. 2.17.

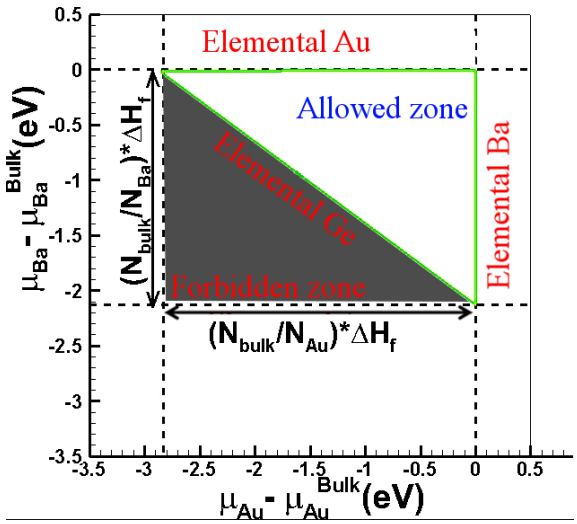

FIGURE 2.17: Schematic sketch of the chemical potential ranges of ternary Ba-Au-Ge cage compound (inspired from Ref. [103]).

Finally, the surface phase diagram is constructed by considering all the surface models and selecting the ones with the minimum surface energy in the allowed region described above (see Figs. 4.12 and 4.13). The uncertainty value of surface energy calculations for Ba-Au-Ge clathrate was calculated to be 15 mJ/m^2.

2.2.5.3 Adsorption energy

In chapter 5, we study the adsorption of Pb on Al(111) and $Al_{13}Co_4$(100) to understand the adhesion properties of the substrate or the interface. The adsorption energy (E_x^{ads}) of N_x atoms of x on the substrate s is given by the equation below:

$$E_x^{ads} = E_{s+x}^{total} - E_s^{total} - N_x E_x^{coh} \tag{2.45}$$

where E_{s+x}^{total} is the total energy of the substrate plus the adsorbate, E_s^{total} is the total energy of the substrate, and E_x^{coh} is the cohesive energy of the adsorbate.

2.2.5.4 Adhesion energy

The energy cost for separating the film from the substrate accounts for its adhesion energy. In order to calculate it, the total energy of the adlayer (or a freestanding slab), $E_x^{free-standing}$ is considered. The adhesion energy ($E_x^{adhesion}$) of x on the substrate s is defined as:

$$E_x^{adhesion} = E_{s+x}^{total} - E_s^{total} - E_x^{free-standing} \tag{2.46}$$

A schematic illustration of a free standing slab of Pb is shown in Fig. 2.18.

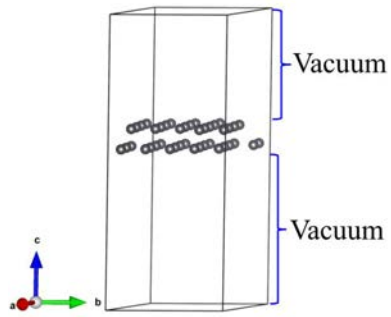

FIGURE 2.18: A free standing slab with two adlayers of Pb.

2.2.6 Electronic Structure Calculations

2.2.6.1 Simulated STM

Theoretical modeling of STM images helps to extract more information from the experimental data as it acts a complementary approach to understand the electronic effects behind the contrast observed. We used the Tersoff-Hamann model [60]. Basically, the Tersoff-Hamann model is based on the surface electronic structure. It provides reliable results by applying suitable approximations to the Bardeen approach (see section 2.1.5). In this work, the STM images for all surface models were calculated within the Tersoff-Hamann approximation [60, 106]. In this algorithm, the tunneling current I_t is proportional to the local density of states at the tip position and is described as:

$$I_t(\mathbf{R}) \propto \sum_{E_n > E_F - eV_{bias}}^{E_n < E_F} \mid \Psi(\mathbf{R}, E_n) \mid^2 =: \rho_s(\mathbf{R}, V_{bias}). \tag{2.47}$$

In the above equation, R is the position of the center of curvature of the tip, E_F is the Fermi level, E_n the eigenstates of the system, V_{bias} the bias voltage and, $\rho_S(\mathbf{R}, V_{bias})$ is the local density of the sample at the position (R) of the tip. The previous works confirm that mostly the Tersoff-Hamann approximation provides sufficiently detailed STM simulations to account qualitatively for the experimental observations [83, 101, 107, 108].

For our experiments we used the constant current mode to obtain STM images. Hence, it makes it interesting to compare it with the STM images simulated using the constant current approach. The

appropriate charge density contour for a given I_t can be estimated [56] by the following:

$$n(I_t)[\text{Å}^{-3}] = 2 \times 10^{-4}\sqrt{I_t}[nA] \tag{2.48}$$

which implies for a current value of 1 nA, the appropriate charge-density contour will thus be at $2 \times 10^{-4}\text{Å}^{-3}$. We used a python-based program p4vasp [109] which plots the isodensity contour which roughly corresponds to I_t. Our STM results were found to be in good agreement with Equation 2.48.

2.2.6.2 Density of States (DOS)

The density of states is mathematically described as

$$N(\varepsilon) = \int \rho(\vec{r}, \varepsilon)\mathrm{d}\vec{r} = \sum_{i=1}^{\infty} \delta(\varepsilon - \varepsilon_i) \tag{2.49}$$

where the sum goes over all eigenstates (orbitals) with eigenvalues, ε_i, of the Kohn–Sham Hamiltonian.
An example of a DOS calculation is given in the case of the Ba-Au-Ge clathrate compound. All the DOS calculations (bulk or surface) were performed using a finer k-point grid than the one used for atomic relaxations. In addition, we used the "tetrahedron method" with Blöch corrections [87]. The state-resolved DOS, also called the projected DOS (PDOS) of bulk-$Ba_8Au_6Ge_{40}$ is shown in Fig. 2.19. This calculation was executed for a $(11 \times 11 \times 11)$ k-point grid and the following surface calculations were adapted to this k-point sampling to have comparison between the bulk and surface DOS. Here, the Ba s states contribute with a small intensity to a wide range of energies below the Fermi level. Also, Ba-states overlap with the Ge-sp and Au-sd states, in agreement with previous calculations [18]. The main contribution of Ba-states is however above the Fermi energy, in agreement with a charge transfer from Ba atoms. A gap is found to be located at 0.27 eV. The presence of Ba atoms induces the filling of the conduction band in this Ge-clathrate while Au doping shift the gap above Fermi energy. The surface calculations for this clathrate compound can be found in sections 3.7 and 4.4.8. The contribution to the DOS of atoms belonging to the surface (S) or subsurface (S-1) planes, allows to understand the extent of the surface. The comparison between the surface and bulk DOS, gives insights on the electronic properties affected by the coordination number of the surface atoms.

2.2.6.3 Electron localization function

The electron localization function (ELF) was formulated by Becke and Edgecombe in 1990 [110]. It has its origins in the Hartree-Fock parallel spin pair probability. This function discerns the correlation of movements between electrons of the same spin and over the years has proved to be a reasonable visual tool for the chemical bond analysis [111, 112].

By definition, ELF is a measure of the probability density of finding a pair of electrons with the same spin value (σ) and mathematically, it is defined using a Lorentzian distribution as:

$$\text{ELF} = \frac{1}{1 + (\frac{D_\sigma}{D_\sigma^h})^2}. \tag{2.50}$$

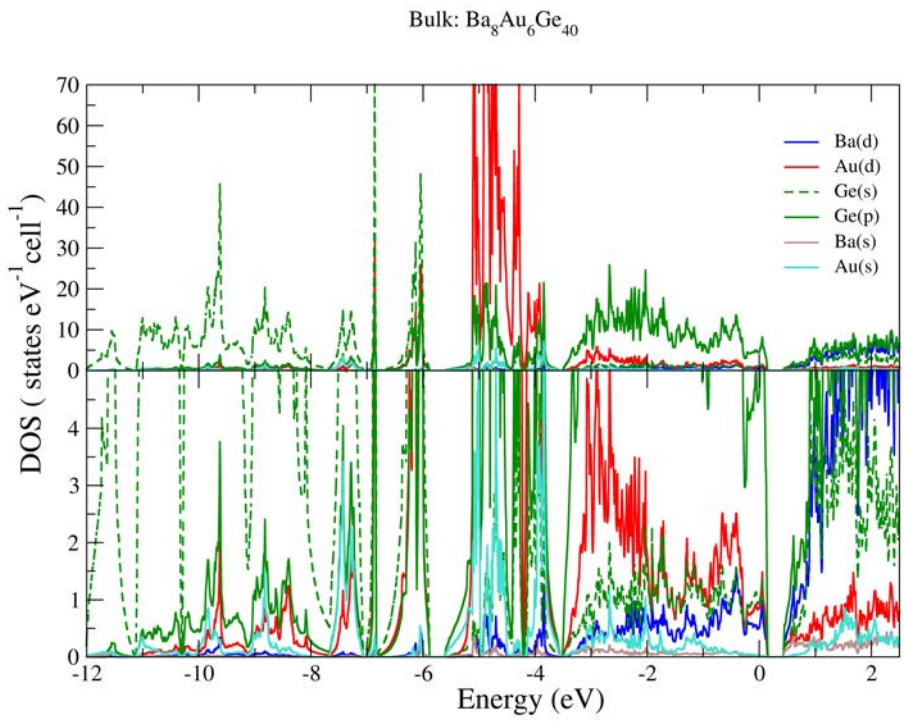

FIGURE 2.19: Bulk density of states.

Here, D_σ is the kinetic energy of the actual system and is defined as:

$$D_\sigma = \frac{1}{2}\sum_i \mid \nabla\Phi_i \mid^2 - \frac{1}{8}\frac{\mid \nabla\rho \mid^2}{\rho} \tag{2.51}$$

The other term in equation 2.50 is $D_\sigma^h = \frac{3}{5}(3\pi^2)^{5/3}\rho^{5/3}$, which is the kinetic energy of a homogeneous electron gas. ELF value ranges from 0 to 1 and it equals to 0.5 when the delocalization is perfect (case of a homogeneous electron gas). The ELF value of 1.0 corresponds to perfect localization.

ELF is a good indicator to identify regions of electron localization, such as bonding and lone-pair regions in solid and molecular systems [110, 112–115]. In our work, we performed calculations using the PAW potentials (core electrons are neglected). As an example in Fig. 2.20 we plotted the ELF map for the bulk Ba-Au-Ge clathrate along with a image taken from Ref. [18] showing the ELI calculations using FPLO ("full-potential local orbital") for the same bulk. This figure seems to present a reasonable agreement between our results and the all-electron calculations ensuring a good accuracy of the qualitative topological analysis done on BaAuGe(100) and BaAuGe(110) surfaces (see sections 3.7 and 4.4.6).

2.2.6.4 Bader charge analysis

The Bader charges identify the electronic transfers in a material. The method is based on the electron density $\rho(\vec{r})$. It divides the 3D space into subsystems, each usually containing one nucleus (but sometimes none). The subsystems are separated by "zero-flux" surfaces. The zero-flux property can

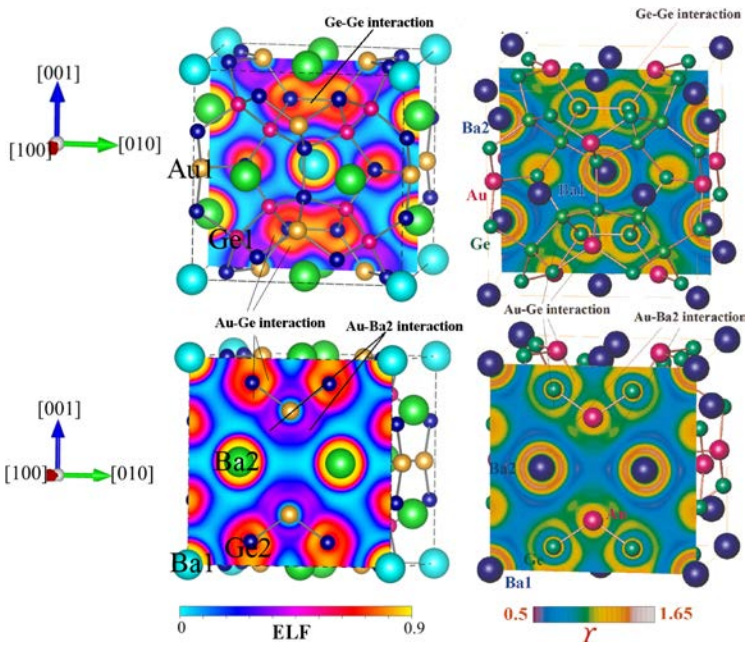

FIGURE 2.20: (Left panel) ELF map at x=0.5 (top) and at x=1.0 showing various localization regions indicating covalent interactions while (Right panel) ELI map taken from Ref.[18] highlight similar features.

be expressed as :

$$\nabla\rho(\vec{r}) \cdot n(\vec{r}) = 0 \tag{2.52}$$

where $n(\vec{r})$ is the normal to the interatomic surface ($\mathbf{S}(\vec{r})$), $\nabla\rho(\vec{r})$ is the gradient of the charge density $\rho(\vec{r})$. The charge enclosed within the Bader volume is a good approximation to the total electronic charge of an atom, making this theory a tool for charge transfer analysis.
One major challenge for the application of the Bader theory was to find a way to computationally partition the space efficiently and many efforts have been put to make the corresponding algorithm more robust and less complex [116, 117]. In 2006, a new fast (computationally less demanding) grid-based algorithm was developed by Henkelman *et al.*, Ref. [118]. It is based on a charge density FFT grid where Bader regions are defined by following a steepest ascent path on the grid. Many further improvements have also been done in this grid-based algorithm and for details the reader is referred to these Refs. [119–121]. We have adopted this method using the open source Bader [122]. Our choice is also driven by the fact that this method is suitable to systems with complicated bonding topologies [118].

The 3D representation of Bader atoms in real space is shown in Fig. 2.21 for the bulk $Ba_8Au_6Ge_{40}$ intermetallic compound. The Bader atomic regions corresponding to Ba atoms display approximately spherical shapes, indicating the cationic character of Ba atoms [17]. The effective charges for both Ba1 and Ba2 are calculated (+1.3 e) to be much lower than the typical +2.0 e (the complete shell configuration). The shapes of Bader atoms for the host-framework positions are found to be deviated from spherical symmetry. It shows a contrast between host-guest (Ba-(Ge,Au)) interactions and the one within the host-framework.

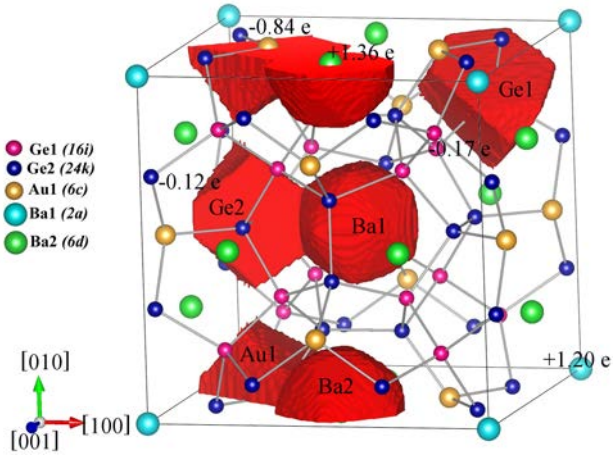

FIGURE 2.21: Bader atomic regions in $Ba_8Au_6Ge_{40}$ intermetallic clathrate and the effective charge transfer between the atoms.

2.3 Conclusion

In this chapter both experimental and DFT computational methods were described. In the experimental method section, we described the preparation and analysis of the clean surface under UHV along with the surface science techniques: LEED, XPS and STM. A separate set-up for *in situ* wetting experiments was reported. The second major part of the chapter was dedicated to the DFT calculations. We first introduced the DFT formalism and its implementation using VASP code. In this chapter a few examples of the results were shown to explain how we applied the methodology and what type of information we get.

Chapter 3

Structural investigation of BaAuGe(100) surface

3.1 Overview

The present chapter focuses on the (100) surface structure of the $Ba_8Au_{5.25}Ge_{40.3}\square_{0.45}$ ($\square$ is a vacancy) type-I clathrate. Basically, here our recent publication [123] is presented in the form of a chapter with some pointers to annex containing supplementary information. We provide a detailed study of the (100) surface structure of a BaAuGe intermetallic clathrate, a class of covalently bonded cage compounds with tunable electronic properties. Using a combination of experimental and computational methods, we demonstrate that the surface structure preserves the cages of the bulk structure up to the surface and contains an ordered arrangement of Ba surface atoms. *Ab initio* calculations show that the surface structure is stabilized through electron charge transfer from protruding Ba to surface Ge and Au atoms, saturating the dangling bonds. As a consequence, surface atoms recover an electronic environment similar to that of the bulk phase. Such charge balanced stabilization mechanism may be general at the surface of intermetallic clathrates.

3.2 Introduction

The performances of molecular-scale components in devices for electronics, sensing, energy conversion or optronics are often defined by the properties of their surfaces. During the last years, a wide range of reliable surface passivation and functionnalization methods have been developed, with the objective to tailor the surface character for optimizing and broadening their applications [124–129]. These methods are based on the interplay among adsorbate/surface interaction, electronic structure, and molecular orientation where applicable. On semiconductor surfaces, they often take advantage of the localized and covalent nature of the bonding network to passivate the surface, assemble nanopatterns, influence subsequent deposition or change the nature of the interfacial electron transfer [130–132].

Another route to control the surface charge and topography relies on the design of new materials surfaces. In the last few years, complex intermetallic compound surfaces have attracted much attention for their specific atomic and electronic structures [108, 133]. Within this family, intermetallic clathrates - a class of cage compounds in which electropositive metal atoms are encapsulated in covalent frameworks of mainly Group 14 elements (Si, Ge, Sn) - are exciting materials since they present both a covalent-like bonding network which can be used for surface functionnalization and tunable electronic properties, by altering the type of guest and host atoms as well as their content [20, 134]. While the empty Ge_{46} clathrate is a semiconductor with a calculated band gap much larger than the one of Ge with the diamond structure, the addition of guest atoms in the cage, and the substitution of Ge atoms in the rigid network can shift the Fermi energy above or below the gap, yielding a metallic

compound [135]. However, surface engineering based on such complex compounds first requires the basic knowledge of their surface structure.

Surfaces of covalent materials generally exhibit a large variety of reconstructions, often depending on preparation conditions [136, 137]. Famous examples are the (111) surfaces of Si and Ge. Room- or low-temperature cleavage produces a (2×1) structure, whereas annealing at high temperature leads to the well-known Si(111)-(7×7) and Ge(111)-c(2×8) surface reconstructions [104]. The driving force behind such reconstructions is the minimization of the number of surface dangling bonds, created by the surface truncation through the formation of new bonds [138]. In this scheme, the previous (2×1) reconstruction is due to a specific rearrangement of the bonding pattern between the surface bilayers and the subsurface atoms, in agreement with the "π-bonded chain model". In Si- and Ge-based clathrates, all atoms of the network are in the same sp^3 environment as in the diamond structure. Although the bonding strength is weaker in clathrates, in relation to their larger atomic volume [29], here we show that the network of such covalent bonds can also dictate their surface structure. We demonstrate this through a complete study of the (100) surface of a $Ba_8Au_xGe_{46-x}$ single crystal.

The Ba-Au-Ge clathrate was first described with the composition $Ba_8Au_6Ge_{40}$ [21]. Later, it was shown that the phase has a homogeneity range which extends at 800^0C from binary $Ba_8Ge_{43}\square_3$ up to ternary $Ba_8Au_6Ge_{40}$ [19]. It includes the composition $Ba_8Au_xGe_{46-x}$ with x=5.33 which is a semiconducting compound following the Zintl electron counting rule [18, 139]. It crystallizes in the space group $Pm\bar{3}n$ with a cubic unit cell of 54 atoms and a lattice parameter equal to 10.7987 Å [18]. As shown in Fig.3.1, the structural model for the composition $x = 6$ consists of two pentagonal dodecahedra (12 pentagonal faces) and six tetrakaidecahedra (12 pentagonal faces and two hexagonal faces). The rigid framework is built with Au1, Ge1 and Ge2 atoms located at the Wyckoff position $6c$, $16i$ and $24k$, respectively. The guest atoms lie at the center of the cages, *i.e.* in the dodecahedra and tetrakaidecahedra for Ba1 ($2a$) and Ba2 ($6d$) atoms, respectively. The analysis of the chemical bonding at $x = 5.33$ identified a covalent character for the Ge-Ge and Ge-Au bonding within the rigid framework. It also highlights a covalent-like (dative) interaction between the guest atom and the cage, more precisely between Ba2 and Au1 [18].

An attempt was made to derive the (100) surface structure of this clathrate through a simulated numerical cleavage process by increasing the tensile deformation of the unit cell along the [100] direction [140]. This process does not lead to any clean cleavage of the bulk system. However, it provides information about the deformation strength of the two (tetrakaidecahedra and pentagonal dodecahedra) types of cages (see Fig. 3.2).

This calculation shows that the tetrakaidecahedra cages $(Ge,Au)_{24}$ are much easily distorted in comparison to the pentagonal dodecahedra cages (Ge_{20}). We used the distortion index (D) [141] and the effective coordination number (ECoN) to quantify the deformation. The D value measures the deformation of the polyhedron, through the evaluation of the averaged deviation of the bond lengths between the central atoms and its nearest neighbors.[1] Alternatively, the ECoN value provides the weighted sum of the number of atoms coordinated to a central atom in a distorted polyhedron.[2] Fig. 3.2 highlights a heavy increase in the D value and an exponential decrease in the ECoN value for the $(Ge,Au)_{24}$ cages. While, the $(Ge)_{20}$ cages are only slightly affected by the deformation (increase of the lattice parameter along the [100] direction).

[1] $D = \frac{1}{n_b}\sum_{i=1}^{n}\frac{|\ell_i-\ell_{avg}|}{\ell_{avg}}$ where n_b is the number of bonds to the central atom, ℓ_i is the distance from the central atom to the ith coordinating atom, and ℓ_{avg} is the average polyhedral bond length.

[2] $\mathrm{ECoN} = \sum_i w_i$ where $w_i = exp[1-(\frac{\ell_i}{\ell_{avg}})^6]$. The quantity w_i is the bond weight of the ith bond and here ℓ_{avg} represents a weighted average bond length.

Focusing on the surface structure, a fundamental question relates to the interplay between the three-dimensional bulk structure described previously and the two-dimensional surface. While this question has been investigated for other types of complex intermetallic compounds like quasicrystals and their approximants [133, 142–147], surface studies of metal-based clathrate compounds have remained untouched. Several scenarios may occur, ranging from the preservation of the cluster substructure at the surface, to surface reconstruction for covalently bonded materials [148]. The present work demonstrates that the prospective surface reconstruction envisaged on the (100) surface of the $Ba_8Au_xGe_{46-x}$ cage compound, is actually lifted by the presence of a well-organized layer of Ba atoms at the surface. The Ba guest atoms in the clathrate can be viewed as intrinsic analogs to extrinsic adsorbates lifting the reconstruction in simple semiconductor systems like the Ge(100) surface [149–152].

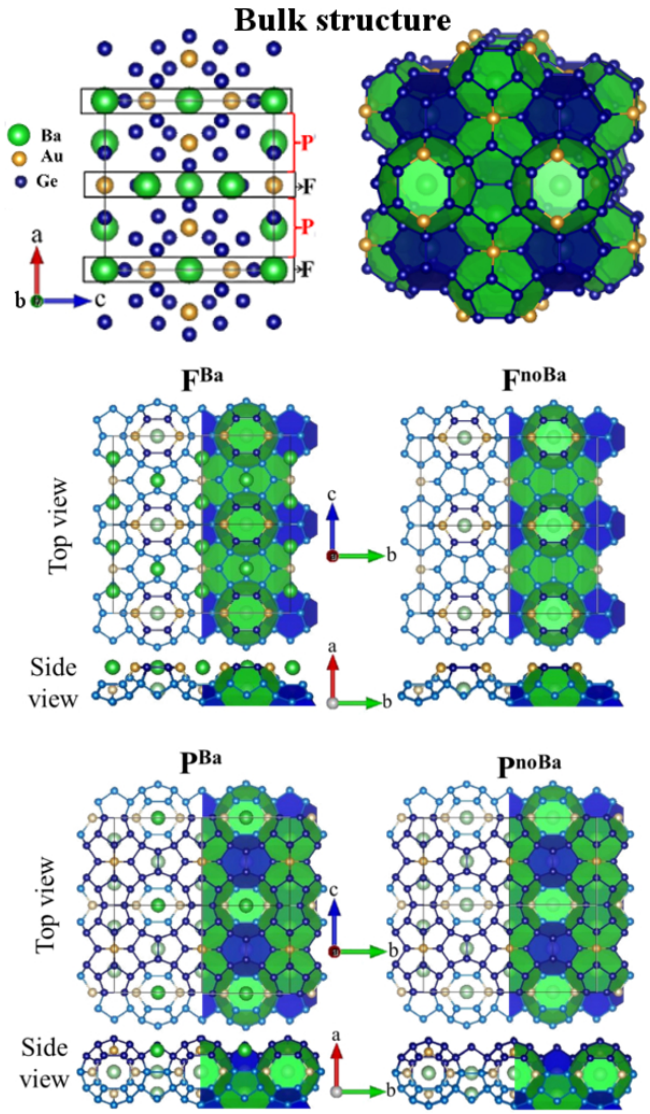

FIGURE 3.1: Top: Structure of the $Ba_8Au_6Ge_{40}$ type-I clathrate, viewed as a stacking of F and P slices along the [100] direction (left) or as a cage compound (right). The tetrakaidecahedra are shown in green while the dodecahedra are represented in blue. Bottom: Surface models (top and side views) considered in the study. Atoms are represented by circles (Ba green, Au yellow, Ge blue). Faded colors indicate atoms lying slightly below the surface.

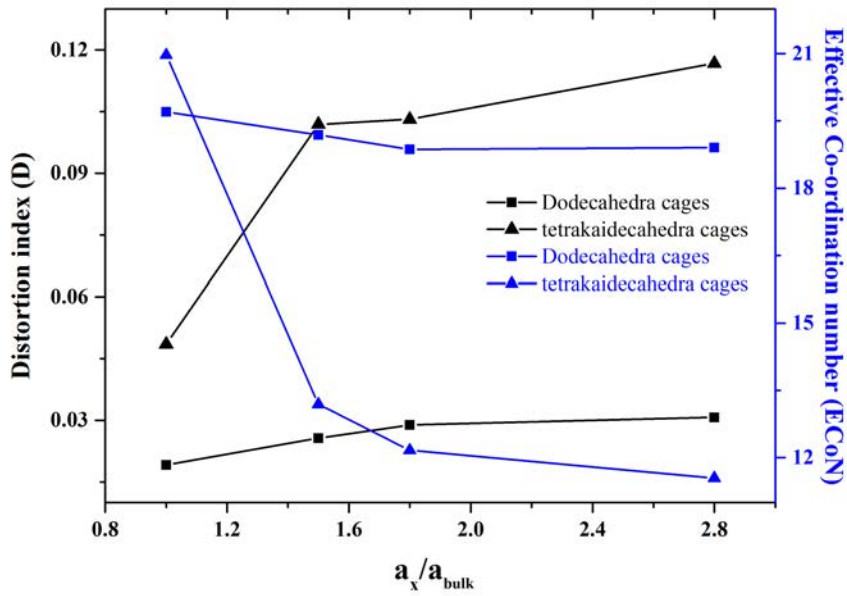

FIGURE 3.2: Distortion index and ECoN of the cages on elongating the bulk in direction perpendicular to its (100) plane.

3.3 Experimental Details

The $Ba_8Au_xGe_{46-x}$ crystal used in the present study was grown by the Bridgman method. Its composition is $Ba_8Au_{5.25}Ge_{40.3}\square_{0.45}$, *i.e.* similar to the one used in Ref. [18] ($Ba_8Au_{5.3}Ge_{40.4}$). The crystal was then oriented using back-reflection Laue X-ray diffraction and cut perpendicular to the [100] direction.

Surface science experiments were performed under ultrahigh vacuum conditions with a base pressure of 2×10^{-10} mbar. The surface was prepared by repeated cycles of Ar^+ sputtering (2 keV for 30 min) and annealing (up to 973 K for 1-2h). The temperature of the samples was checked using an infrared optical pyrometer with the emissivity set to 0.1 coupled with a K-type thermocouple.

The chemical composition of the near surface region has been measured by X-ray photoelectron spectroscopy (XPS) as a function of the photoelectron take-off angle (from 20° to 70° with respect to the surface normal) to vary the probing depth of the measurements as well as a function of the annealing temperature. This ensures a variation of surface sensitivity of the measurements. The surface composition is derived from the area of the Ba $3d_{5/2}$, Au $4f_{7/2}$ and Ge $2p_{3/2}$ core levels after removing the Al Kα satellites. A Shirley background has been subtracted from the Ba 3d, Au 4f spectrum while a linear background has been used for the Ge $2p_{3/2}$ peak (see Appendix A).

3.4 Computational Details

Experimental results are complemented by calculations performed within the DFT framework [66–69], using the PAW method [87, 88] and the generalized gradient approximation (PBE) [76, 153]. The experimental value of the cell parameter (10.80 Å) was used to build the four surface models described in the paper. Plane-wave basis sets for electron wave functions with cutoff energy of 450 eV were used. Integrations in the Brillouin zone were performed using special k-points generated with grids set to 8×8×8 (bulk relaxations) or 11×11×11 (DOS calculations) [91]. The formation energy of

$Ba_8Au_6Ge_{40}$ is calculated to be -0.314 eV/atom. The flat and puckered models are built as symmetric slabs of 9 and 7 layer thickness, respectively ($\simeq$ 22.5 Å and $\simeq$ 19.5 Å thickness, respectively), separated by a void thickness equal to 15 Å. During the structural optimization, all atoms are allowed to relax, except the ones located within the flat layer located in the middle of the slab.

Surface energy calculations were computed within the method described in Ref. [103], as a function of the chemical potentials of the constituting elements Ba and Au. These can vary within the range $\mu_i - \mu_i^{bulk} \in [\Delta H_f \times \frac{54}{N_i} : 0]$, where μ_i and μ_i^{bulk} are the chemical potentials of the element i (i=Ba, Au) in the slab or in the bulk (N_{Ba}=8 and N_{Au}=6) and ΔH_f is the formation energy of the compound. Here, the Ge chemical potential is constrained by the cohesive energy of the compound.

Scanning Tunneling Microscopy images for all surface models have been calculated within the Tersoff-Hamann approximation [60, 154].

Bader charges analysis has been performed on a charge density grid [118–121]. Electron localizability calculations [112] are based on valence densities to qualitatively highlight electronic effects implied by the presence of surface Ba atoms [115, 155, 156]. Such representation yields results in qualitative agreement with those obtained from all-electron calculations of the bulk calculations on $Ba_8Au_6Ge_{40}$ clathrate [18].

3.5 Experimental results

The (100) surface prepared under ultra-high vacuum has a composition as measured by XPS that is consistent with that of the bulk. Angle-resolved measurements (Fig. 3.3) show a slight decrease of the Ge content and a small increase of the Au content at the surface. There is also a small shift in the composition after sputtering but a near-surface composition close to that of the bulk is restored and remains almost constant for annealing temperatures comprised between 750 and 973 K (Fig. 3.4). The LEED exhibits a (1×1) pattern with a square unit mesh of 10.9 ± 0.2 Å, after annealing between 650 and 973 K, in agreement with the bulk parameter (Fig. 3.5a).

The STM images show that the surface has a step-terrace morphology with a single step height of 5.0 ± 0.2 Å (Fig. 3.5b). This distance corresponds approximately to half of the unit cell parameter. Two consecutive terraces show bright elongated motifs rotated by 90°, in agreement with the 4_2 symmetry of the bulk. High-resolution images show an arrangement of oblong-shaped features for negative bias, while a square lattice of bright spots are visible for positive bias (Fig. 3.6). In all cases, the parameter of the square surface unit cell deduced from STM is 10.80 Å ± 0.40 Å, in agreement with the parameter deduced from the LEED analysis.

3.6 Theoretical results

To determine the surface structure, two types of surface terminations, called F and P, are considered. They are obtained by cleaving the ideal $Ba_8Au_6Ge_{40}$ bulk structure, either at a flat (x = 0) or at a puckered (x $\simeq$ 0.25) plane respectively (see Fig. 3.1). In both cases, the cage structure is preserved up to the surface. The corresponding models contain hexagonal atomic arrangements at the surface made of Ge and Au atoms in 2:1 ratio. These motifs are buried in-between dodecahedral Ge units of the P-type models, while they are protruding in the F-type model. For each termination, two models are considered. In the first series, surface Ba atoms are absent (F^{noBa} and P^{noBa}). In the second series, they protrude at the surface and are located in the center of the cage which were dissected following the bulk truncation process (F^{Ba} and P^{Ba}). Two different types of surface Ba atoms are present on

F^{Ba}: one (per surface unit cell) surrounded only by surface Ge atoms, and two (per surface unit cell) having surface Au atoms in their vicinity.

Surface energy calculations lead to the conclusion that X^{noBa} models (X = P, F) present higher surface energies than X^{Ba} models (Fig. 3.7), within the allowed range of chemical potentials (triangular shaped area in the chemical potential diagram). There is a balance between the surface composition and the atomic density for the surface stabilization, a high surface density and the presence of surface Ba atoms both tending to lower the surface energy - Ba being the element with the lowest surface energy ($\gamma_{Ba(100)}$= 0.35 J/m^2, $\gamma_{Au(100)}$ = 1.62 J/m^2, $\gamma_{Ge(110)}$= 1.51 J/m^2) [157, 158]. Here, the surface model with the highest surface Ba content (F^{Ba}) is energetically favored for Ba- and Au-rich limits of the chemical potentials.

Looking at the corresponding STM simulations (Fig. 3.6 and Fig. A.3 in appendix A), it appears that bright stick-shaped features for negative bias are only visible for F-type models. For positive bias, a square lattice of bright spots appears only for F^{Ba}.

Combining the latter observations with the previous surface energy calculations, the best agreement between the calculated and experimental results is obtained for the surface model F^{Ba}, which presents the highest surface Ba atoms content (Fig. 3.6). In the next section, we discuss the role played by these alkaline earth metals on the surface stability.

3.7 Discussion

Dangling bonds, related to the low coordination of surface Ge atoms (Fig. 3.8), are revealed by the Electron Localization Function.

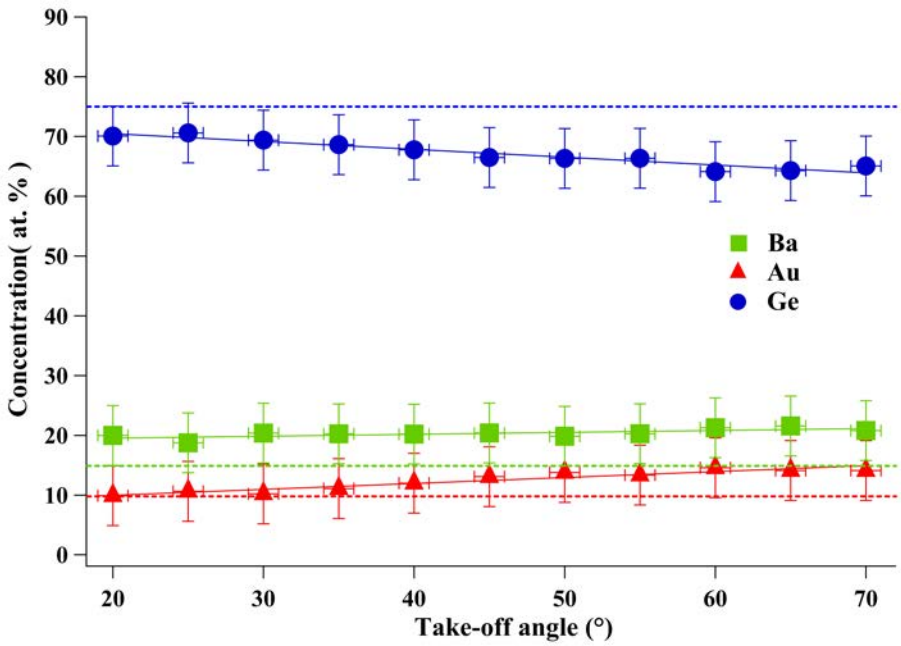

FIGURE 3.3: Elemental near-surface composition measured as a function of the photoelectrons take-off angle for the sample annealed at 833 K. The measurements at 70° are more surface sensitive than those implemented at 20°. The dashed lines correspond to bulk composition, while the solid lines are linear fit to data points and are only a guide for the eyes.

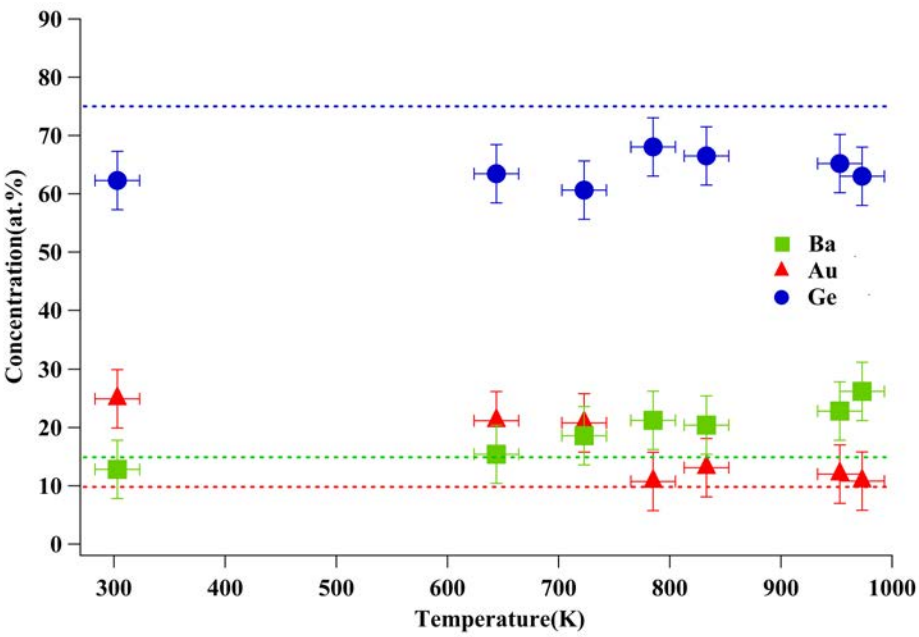

FIGURE 3.4: Variation of the near-surface composition as a function of annealing temperature (K) at constant value of take-off angle equal to 45°.

For F^{Ba}, the destabilizing contribution from dangling bonds is balanced by the charge transfer from the electropositive surface Ba atoms to the neighboring electronegative Ge and Au atoms. This is highlighted by the Bader charge analysis (Fig. A.4 in appendix A), showing a charge transfer from Ba to Au and Ge which is very similar at the surface and in the bulk. Indeed, each of the three surface Ba atoms releases 1.30-1.35 e/at. on average at the surface (1.21 e/at. for Ba1 and 1.37 e/at for Ba2 in the bulk) while the electronic gain is calculated to be 0.67 e for the four closest surface Ge atoms (0.54 e for the corresponding four Ge atoms in the bulk) and 1.34 e for the two closest surface Au atoms (1.61 e for the corresponding two Au atoms in the bulk). As a consequence, the dangling bonds of surface Ge atoms are almost fully saturated, like in the bulk, resulting in an improved stability of the surface model presenting protruding surface Ba atoms. In contrast, in the case of F^{noBa}, a charge depletion is calculated for the same surface Ge atoms (around 0.1-0.2 e/at.), while a charge gain is found for the corresponding Au atoms (around 0.5 e/at.), in agreement with the respective electronegativities

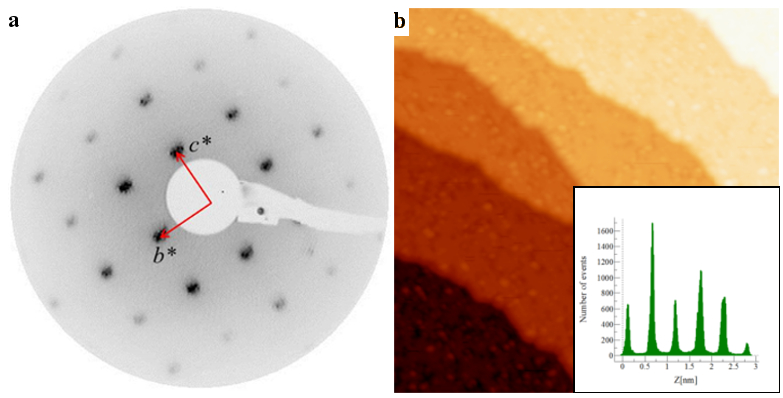

FIGURE 3.5: (a) LEED pattern of the Ba8$Au_{5.25}$$Ge_{40.3}$$\square_{0.45}$ (100) surface annealed at 785 K and recorded at primary beam energy of 19 eV. (b) 70×70 (nm^2) STM image of the BaAuGe(100) surface prepared at 933 K (V_b = -2 V; I_t = 0.08 nA) with an inset histogram showing the unique step height of this layered material (5.0 ± 0.2 Å).

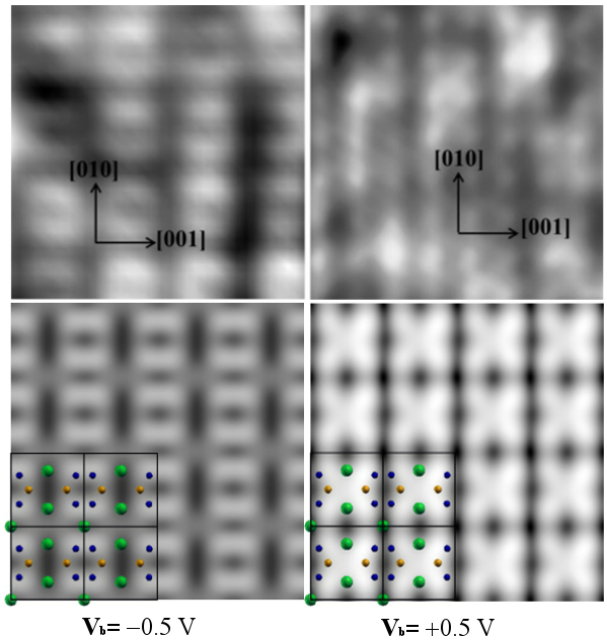

FIGURE 3.6: Top: 4.32 × 4.32 nm^2 STM image obtained at V_b = ± 0.5 V. The apparent non-periodic pattern may be caused by both the preparation and structural disorder. Bottom: Simulated 4.32 × 4.32 nm^2 STM images using the F^{Ba} model at V_b = ± 0.5 V.

of Ge and Au. The order of magnitude of the stabilization resulting from the presence of surface Ba atoms is calculated to be 1.05 J/m^2 (value calculated with μ_{Ba}^{bulk}=-1.88 eV).

The surface electronic structure of the F^{Ba} model shows a metallic character, with an electronic density of states at the Fermi energy (E_F) equals to $n(E_F) = 4.59$ states/eV (Fig. 3.9), larger than the one calculated for the F^{noBa} model (2.83 states/eV). The effect of the surface is mainly confined to the two topmost surface layers (Fig. 3.9), where we can notice a shift of the surface d-band center towards higher energies (0.48 eV for the F^{Ba} model, 0.70 eV for the F^{noBa} model). In addition, the presence of

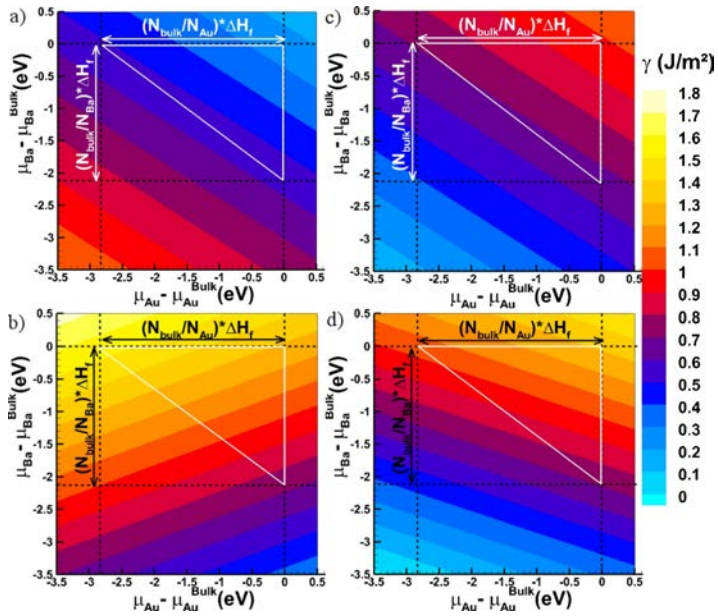

FIGURE 3.7: Surface energies depending on the Ba and Au chemical potentials for the models considered. (a) F^{Ba} (b) P^{Ba} (c) F^{noBa} and (d) P^{noBa}. The white triangle represents the allowed area for chemical potentials.

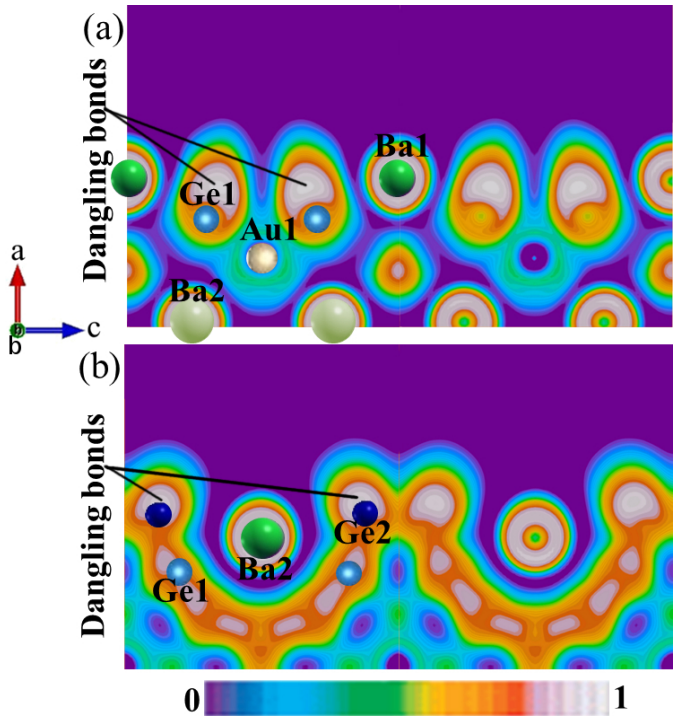

FIGURE 3.8: Electron Localization Function for the F^{Ba} model. Side views plotted along the [010] direction ($\vec{b}$) at $y = 0$ (a) and $y = 0.25$ (b).

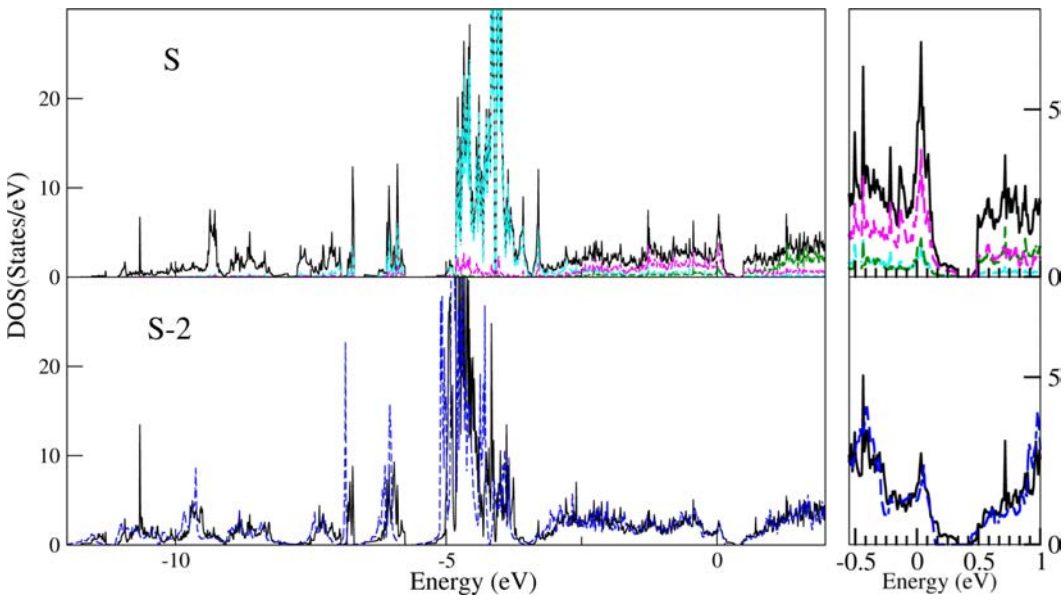

FIGURE 3.9: Contributions of the surface and subsurface planes (S and S-2, respectively) to the density of states for the F^{Ba} model. The black line is the total DOS of the surface, the dotted blue line is the "bulk-like" contribution. The Au $5d$, Ba $5d$, Ge $4p$ are plotted in cyan, green and magenta, respectively.

electropositive Ba at the surface leads to a decrease of the surface work-function ($\Delta\Phi$ = -1.24 eV), in agreement with the charge transfer from Ba adsorbates to the surface.

3.8 Conclusion

In conclusion, we reported here a combination of surface science experiments and *ab initio* calculations showing that the structure of the type-I clathrate $Ba_8Au_xGe_{46-x}$(100) surface results from electronic effects. The dangling bonds created by the bulk truncation process are compensated by electrons from surface Ba atoms, thus stabilizing the surface structure. The cage substructure of the bulk is preserved up to the surface, with an ordered arrangement of intrinsic Ba atoms at the surface, contributing to the surface passivation and stabilization. A similar surface stabilization mechanism may occur among the intermetallic clathrates and cage compounds, with the possibility to tune the surface topology and the surface electronic structure, by controlling the atomic structure (cage sizes) and the chemical composition of the considered compounds.

Chapter 4

Structural analysis of the Ba-Au-Ge (110) surface

4.1 Introduction

This chapter deals with another low-index surface of the cubic Ba-Au-Ge type-I clathrate compound. Over many years, the sequence of low-index surfaces of cubic systems have been studied to understand surface phenomenon depending on their orientation. To decrease the energy required to create a surface, atomic relaxations and reconstructions are likely to occur at the surface. In both cases, the atomic surface positions differ from their initial bulk-truncated positions. Due to the complexity inherent to the Ba-Au-Ge type-I clathrate structure, the determination of the surface structure remains a challenge regardless of the orientation or low index surface selected. Here, in this study we attempt to move a step forward from our knowledge of the (100) surface [123] of $Ba_8Au_{5.25}Ge_{40.75}$ clathrate to explore its (110) surface. The cluster substructure is truncated differently by (110) oriented type of surfaces, which could lead to a different interplay scenario between the 2-dimensional surface and the 3-dimensional cage network. For the purpose of DFT calculations, it is convenient to define a bulk tetragonal unit cell having one of its face oriented perpendicular to the [110] axis. This unit cell has lattice parameter $a = b = a_{[110]} = a_{[100]}\sqrt{2}$=15.28 Å and $c = c_{[100]}$ =10.80 Å, the (b, c) plane being perpendicular to the [110] direction. This surface-oriented bulk unit cell contains 108 atoms as shown in Fig. 4.1. There are 12 tetrakaidecahedra and 4 pentagonal dodecahedra cages in this unit cell. All these cages (4 Ge_{20} and 12 $(Ge,Au)_{24}$) are rotated by 45° with respect to the surface normal, where 4 $(Ge,Au)_{24}$ cages occupy the diagonal of the cell with appearance of Ge_{20} at the corner and in the center of each face of the cell through periodicity.
The [110] oriented bulk structure can be viewed as a stacking of different types of planes depending on whether they are flat (F); puckered (P,p) or a combination of the former two types (C). The planar symmetry of the considered bulk-terminated planes is different and the creation of the surface at each of these planes (by breaking of bonds) occurs in dissimilar fashion. The cage compound $Ba_8Au_{5.25}Ge_{40.75}$ as mentioned in the previous chapters is mainly composed of covalently bonded network of host (Ge,Au) atoms containing guest Ba atoms in their large cages. Since covalently bonded crystal surfaces are formed by breaking of highly directional bonds, there is a higher probability for the presence of reconstruction elements in their formation process. In the previous chapter and Ref. [123], we reported that the (100) surface structure shows similarities with the semiconductor Ge surfaces. In both cases, the surface is built by breaking covalent-like bonds, thus leading to dangling bonds. To saturate the dangling bonds, reconstructions occur for pure Ge surfaces. The mechanism is different in the case of the BaAuGe(100) surface. The surface, which preserves the cluster substructure, is stabilized by charge transfer between the protruding Ba atoms and the surface Ge atoms. The corresponding surface model, which is observed experimentally, presents the highest surface Ba content (F^{Ba}) and a rather low surface atomic density, when compared to other considered surface models. Our study of the (110) surface aims to show that the previous mechanism is of general character for Ge-based intermetallic clathrates.

In this chapter we report the experimental analysis of the (110) surface of $Ba_8Au_{5.25}Ge_{40.3}\square_{0.45}$ type-I clathrate single crystal under UHV conditions. This analysis is combined with extensive numerical simulations for which we consider a bulk model of composition $Ba_8Au_6Ge_{40}$ [18, 21, 23, 28] without vacancies to build the (110) surface models.

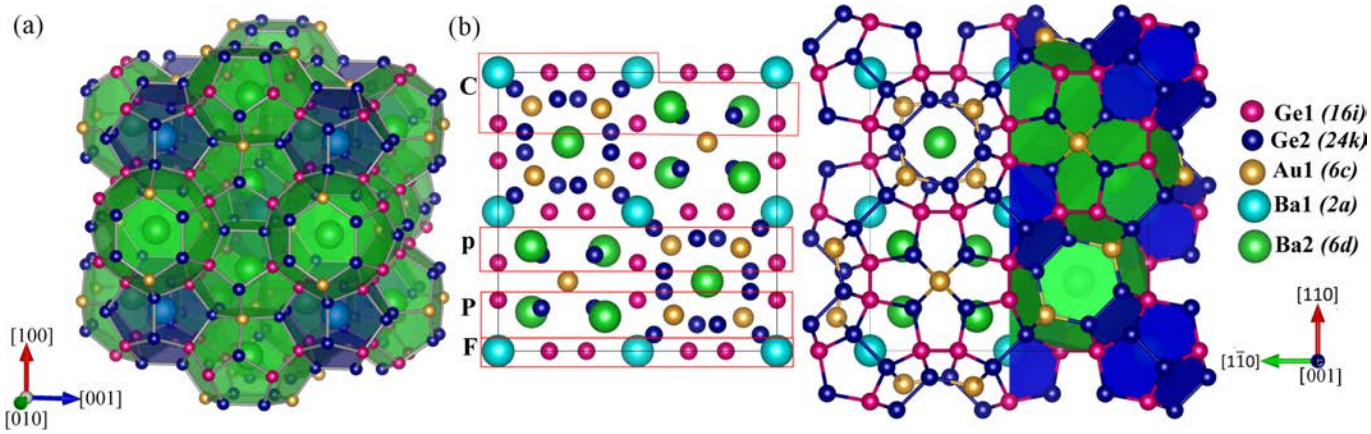

FIGURE 4.1: (a) Bulk structure of $Ba_8Au_6Ge_{40}$ type-I clathrate ; (b) Bulk tetragonal cell for $Ba_8Au_6Ge_{40}$, viewed as a stacking of planes along the [110] direction or as a cage compound. The atoms are depicted as spheres in cyan (Ba1), green (Ba2), yellow (Au1), magenta (Ge1) and blue (Ge2). The blue cages are dodecahedra while in green tetrakaidecahedra cages are exhibited.

This chapter is organized as follows: Section 4.2 gives details of the experimental and computational methodologies used. Section 4.3 describes the experimental results for the (110) surface obtained from three main surface characterization techniques: LEED, XPS and STM techniques. The theoretical results from DFT calculations are presented in section 4.4. The subsection 4.4.5 compares experimentally and computationally obtained STM results to conclude our structural investigation. The subsections 4.4.6 and 4.4.7 describe the electronic structure of the (110) surface while subsection 4.4.8 presents its electronic properties. We also look at the work function of the surface and its changes due to the adsorption of surface adatoms (4.4.9). Section 4.5 presents a synthesis of the *ab initio* results obtained for the (110) and (100) surface structures of the $Ba_8Au_{5.25}Ge_{40.75}$ type-I clathrate. The section 4.6 summarizes the major outcomes drawn from the present study.

4.2 Brief methodology

Most of the methodological details in this chapter are similar to the previous chapter, hence very specific details pertaining to the analysis of the (110) surface are provided in this section. The single crystal of $Ba_8Au_xGe_{46-x}$ oriented in the [110] direction was used in the study. A clean surface was prepared by repeated cycles of Ar^+ sputtering (2-5 keV for 30 min) and annealing (up to 1141 K for 1-2h). In the DFT calculations using VASP, [66–69] a cutoff energy (E_{NCUT}) of 450 eV was used. Calculations for the bulk oriented along the [110] direction (Fig. 4.1) are performed with 6×6×8 k-points grid. In addition, since Van der Waals interactions can be of importance even in densely packed systems, characterized by strong ionic, covalent, or metallic bonds, where these types of interactions are commonly assumed to be negligible [96], we also considered the revised DFT-D method (DFT-D3 [81]) which includes the dispersion energy. The total energy calculations give a formation energy (ΔH_f) of the $Ba_8Au_6Ge_{40}$ compound equal to -0.314 eV/at. within PBE and -0.341 eV/at. within DFT-D3 .

Bulk-terminated symmetric slabs were built using relaxed bulk positions. The slab thickness was set to 22.2-23.5 Å ($\sim$ 11-13 layers) and a void thickness of 15 Å was implemented. In atomic relaxation of these symmetric slabs, all atoms were allowed to relax except those located in the central atomic layer of the slab. A k-point mesh of $(1 \times 6 \times 8)$ was adapted for structural optimization of (110) surface models while calculations of the density of states were performed with a finer k-point grid and using the tetrahedron method. Surface energy calculations were computed within the method described in Ref. [103], as a function of the chemical potentials of the constituting elements Ba and Au. They are allowed to vary within the range $\mu_i - \mu_i^{bulk} \in [\Delta H_f \times \frac{54}{N_i} : 0]$, where μ_i and μ_i^{bulk} are the chemical potentials of the element i (i=Ba, Au) in the slab or in the bulk (N_{Ba}=8 and N_{Au}=6). The Ge chemical potential does not appear explicitly, since it is constrained by the cohesive energy of the compound.

4.3 Experimental Results

The (110) surface structure of the $Ba_8Au_{5.25}Ge_{40.75}$ cage compound has been investigated under UHV conditions using a multi-technique approach. The aim is to explore potential similarities with the prior works on the complex (100) surface of Ba-Au-Ge and (110) Ge surface. It could lead to a better understanding of surface phenomena observed for the complex (110) surface structure of $Ba_8Au_{5.25}Ge_{40.75}$. The experimental results obtained on this surface address the preliminary questions about its atomic and electronic structure.

4.3.1 LEED

Diffraction patterns for the (110) surface have been recorded at room temperature after annealing the sample in the temperature range of $568\,K < T < 1141\,K$. The annealing conditions have almost no effect on the spot distribution and their intensities. A typical (1×1) LEED pattern is observed from 10 eV to 250 eV. Examples of LEED patterns at two different primary beam energies are shown in Fig. 4.2. Some faint and diffused lines can also be seen along $\vec{b^*}$ at low beam energies. The lattice parameters of rectangular unit surface cell derived from LEED measurements are $b = 15.58 \pm 0.40$ Å and $c = 10.45 \pm 0.30$ Å. To calibrate the distances in reciprocal space, diffraction patterns of clean reference surfaces recorded under the same conditions were used. Occasionally additional faint diffuse lines as shown in Fig. 4.7 could be observed. Their appearance may be due to the presence of facets.

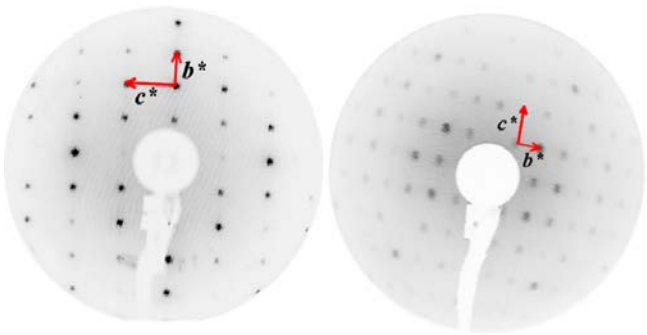

FIGURE 4.2: (Left) LEED pattern of the $Ba_8Au_{5.25}Ge_{40.75}$(110) surface annealed at 992 K recorded at primary beam energy of 25 eV. (Right) LEED pattern recorded at 49 eV under almost similar annealing temperature (983 K). Two LEED apparatus have been used here, hence explaining the different sample orientation.

4.3.2 XPS

The near-surface chemical composition is monitored for a range of annealing temperature varying from 750 K to 1123 K (including the modification after sputtering) at a constant value of take-off angle equal to 45° (Fig. 4.3(a)). A clear deviation from bulk composition of $Ba_{14.9}Au_{9.8}Ge_{75.3}$ (in at.%) is observed after sputtering indicating a preferential sputtering of Ge atoms. The bulk composition is recovered after annealing the surface to 750 K. No significant change occurs up to the highest annealing temperatures used here.

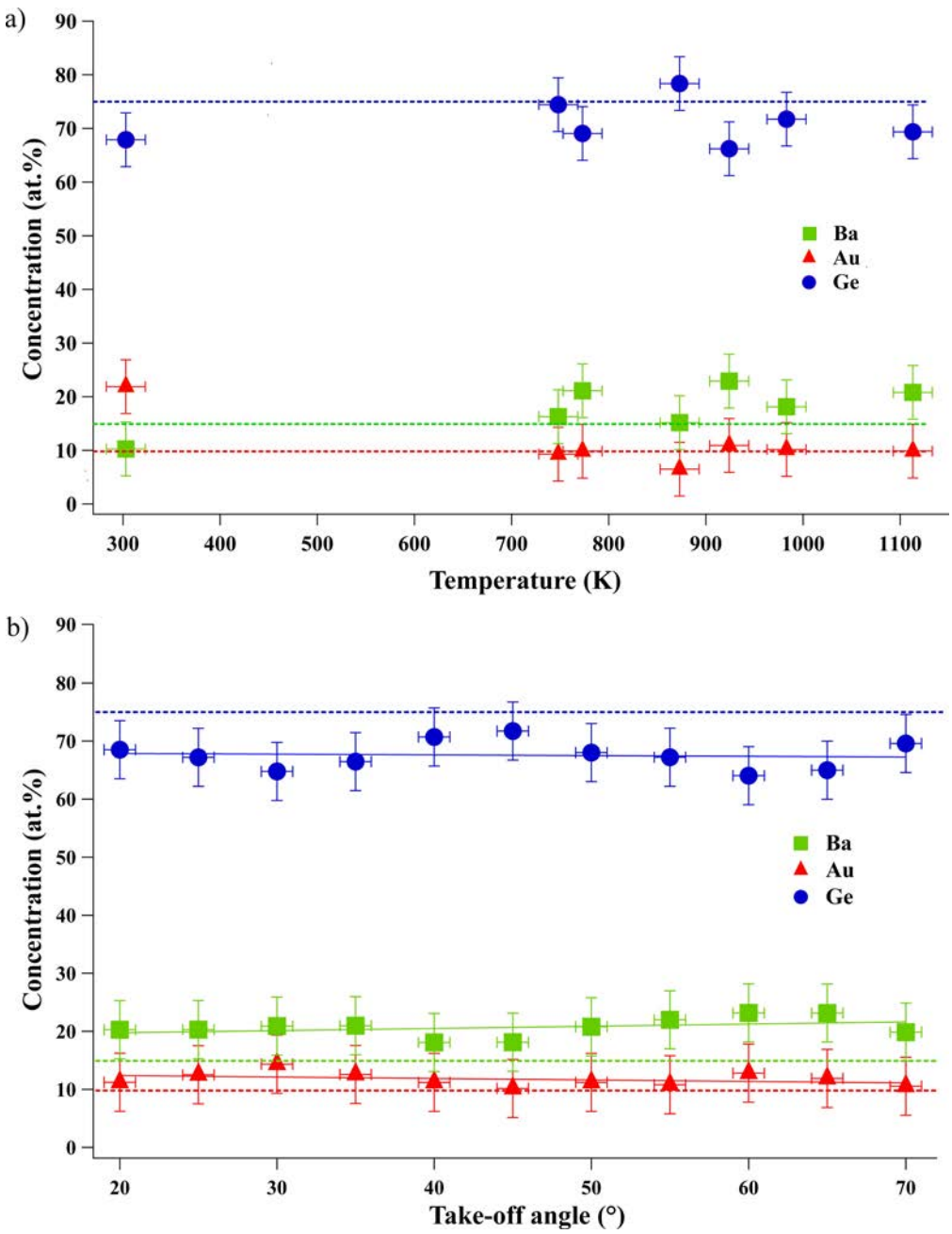

FIGURE 4.3: (a) Variation of the near-surface composition as a function of annealing temperature (K) at constant value of take-off angle equal to 45°. (b) Variation of elemental composition of (110) surface of $Ba_{14.9}Au_{9.8}Ge_{75.3}$ clathrate as function of take-off angle at 983 K. The dashed green, orange and blue lines present in both graphs correspond to bulk composition of Ba, Au and Ge, respectively. The solid colored lines in (b) are linear fit to data points for guide to eyes.

The chemical composition of the near surface region of (110) surface prepared at 983 K has been measured by XPS core level analysis as a function of the photoelectron take-off angle (from 20° to 70°) with respect to the surface normal (see Fig. 4.3(b)). This ensures a variation of the measurements with surface sensitivity. One only observes some slight modulations of the elemental concentrations around the bulk value which could be due to photoelectron diffraction effects in the single crystal. Thus, we conclude that no major surface segregation occurs and surface composition is comparable to bulk composition within error bars associated to the measurement.

4.3.3 STM

The STM images of $Ba_8Au_{5.25}Ge_{40.75}$ (110) surface show a step and terrace morphology with a step height equal to 7.60±0.15 Å (Fig.4.4(a)). The measured step height deduced from the height histogram is equal to $\frac{a\sqrt{2}}{2}$ which corresponds to half the unit cell in the [110] direction for a cubic crystal system (Fig.4.4(b)). This is also indicative of bulk-truncated surface terminations at specific planes for (110) surface. The inset in Fig. 4.4(c) showing Fast Fourier Transform (FFT) of the surface gives the same value of lattice parameters as obtained from the LEED pattern. Figure 4.4(d) shows a 10×10 nm^2 STM image obtained after Fourier filtering. It clearly demonstrates that the surface unit mesh is rectangular. In this case, the structure of the surface seems to be slightly disordered consisting of isolated bright spots forming a zig-zag line pattern with appearance of vacancies in between the lines. In agreement with the LEED pattern, there is no sign of a surface reconstruction. Bright protrusions as seen in Fig. 4.4(c) could be due to adatoms belonging to the next plane, above the mean plane position. The average height difference between the surface and these bright protrusions is equal to 3.1±0.1 Å.

It can be observed from the following STM images that the topography of this (110) surface highly depends on the annealing conditions, the applied bias for imaging the surface and the tip condition. This surface is not trivial to prepare and requires further fine tuning of its surface preparation parameters.
In Fig. 4.5(a1), negative bias (V_b= -0.6 V) STM image shows irregular zig-zag lines very closely located (with almost no space between the consecutive lines). The positive biased STM image (Fig. 4.5(b1)) has zig-zag horizontal lines with a small spacing between them. The zig-zag pattern observed for positive bias is more uniform as compared to the one observed for negative bias (Fig. 4.5(a2)). The bias effect can be observed in Fig. 4.4 as similar preparation conditions were used to acquire these oppositely biased images. The images under consideration (Fig. 4.5) show similar contrast where dark regions are the vacancies present at the surface and bright protrusions are adatoms.

Bright protrusions have been appearing in almost all the STM images irrelevant of the surface preparations. These features over the clean surface are not impurities but most likely belong to an incomplete atomic plane. In order to understand their appearance (random or ordered) we thresholded a STM image keeping only the adlayer. This adlayer produces a faint FFT compatible with the substrate unit cell, suggesting some ordering in their distribution.

The STM images obtained for the same bias voltage (V_b= -1.0 V) at different annealing temperatures ($\Delta T = 117\,K$) are illustrated in Fig. 4.6. Changes in surface features could be seen due to the difference in annealing conditions. In Fig. 4.6(a1), a 20×20 nm^2 STM image (along with a Fourier filtered image) obtained at 1003 K shows lines of isolated bright spots having a zig-zag arrangement. It can be seen from the image that in between the rows of bright spots there exist some contrast variations (originating from atoms located in the subsurface plane) and vacancies. The pattern observed by imaging of the occupied states on (110) surface at 886 K is zig-zag lines with very little spacing between consecutive lines. Also, the surface pattern shown in Fig. 4.6(b1) is seen more frequently and

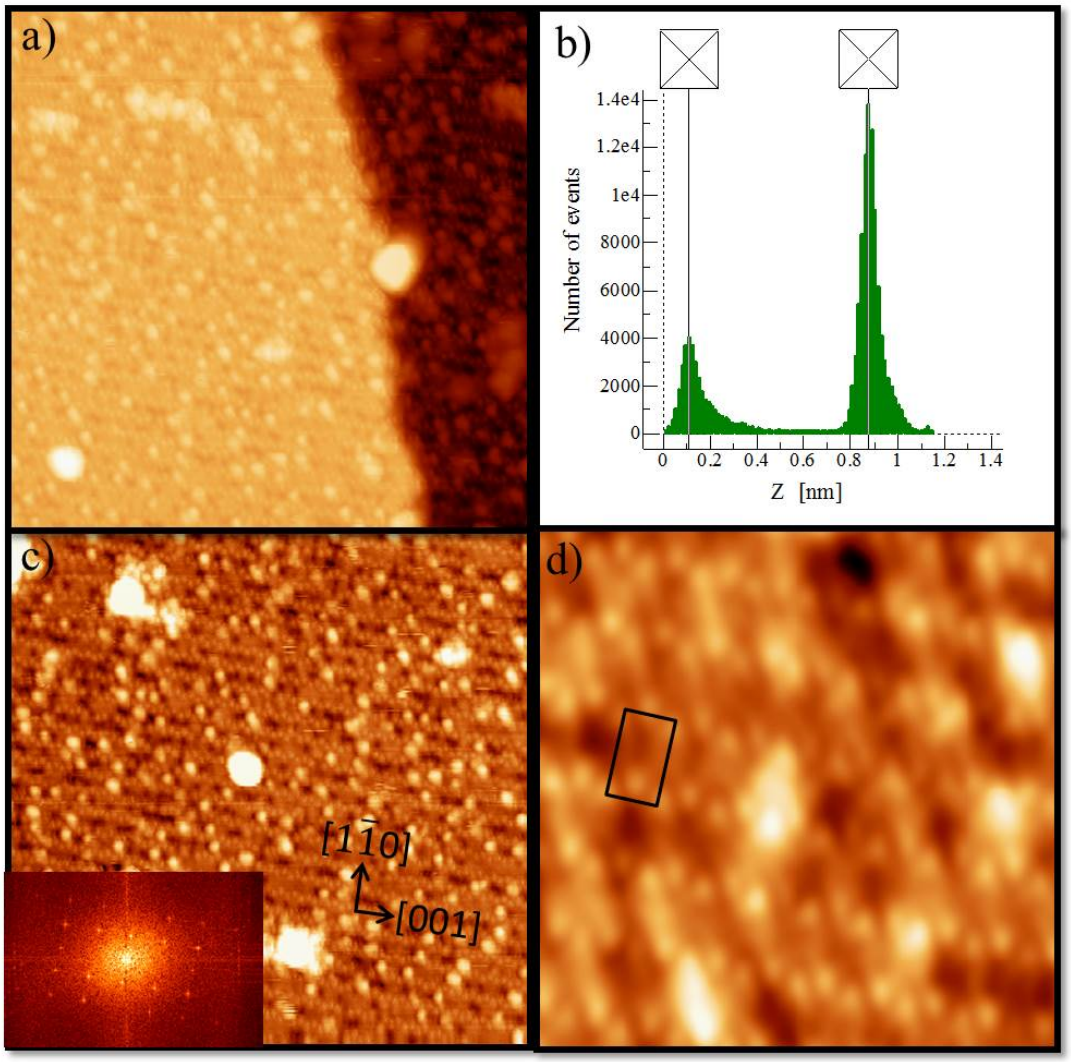

FIGURE 4.4: (a) A 40×40 nm^2 STM image of the $Ba_8Au_{5.25}Ge_{40.75}$ (110) surface prepared at 1003 K (V_b= −1.4 V ; I_t= 0.09 nA). (b) A histogram showing the unique step height of the (110) surface = 7.60± 0.15 Å∼ $a\sqrt{2}/2$. (c) 40×40 nm^2 STM image showing (110) surface plane obtained at 1003 K (V_b= −1.4 V ; I_t= 0.08 nA) with an inset showing the FFT image of the corresponding STM image. d) A 10×10 nm^2 Fourier filtered image corresponding to Fig. 4.4(c) showing the fine structure on the terrace. The surface unit cell is superimposed on the image.

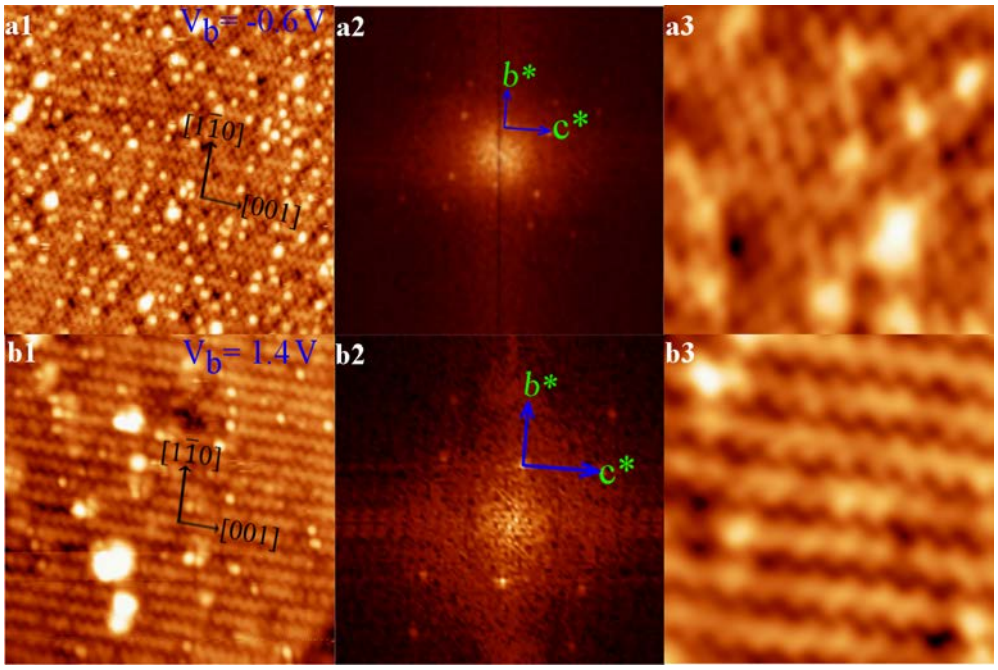

FIGURE 4.5: (a1) A 40×40 nm^2 STM image of the $Ba_8Au_{5.25}Ge_{40.75}$ (110) surface prepared at 886 K (V_b= −0.6 V ; I_t= 0.08 nA) . (a2) FFT image of the surface. (a3) A 10×10 nm^2 Fourier filtered image corresponding to a region of Fig.4.5(a1). (b1) STM image (28.5×28.5 nm^2) of the (110) surface prepared at 926 K (V_b= +1.4 V ; I_t= 0.12 nA) (b2) FFT of the surface showing the diffraction pattern. (b3) Fourier filtered zoom (10×10 nm^2) showing an uniform zig-zag pattern for the positive bias.

has been obtained at annealing temperatures lower than 940 K.

The surfaces of complex metallic alloys are difficult to prepare and require optimized surface preparations to acquire high-resolution STM images. The (110) surface of Ba-Au-Ge is one of this kind. Various recipes have been tested to improve the surface quality in terms of terrace width and reduced surface roughness. As highlighted in Fig. 4.7(a2), annealing at 898 K for short time (15 min) leads to additional diffuse intensity lines in the LEED pattern at low primary beam energies as well as to a significant broadening of the primary spots. It is associated with a rougher surface as observed by STM and smaller terraces as shown in Fig. 4.7(a1) and (a3). Similarly, annealing at temperature below 750 K for 90 minutes followed by another annealing cycle at 797 K for 30 minutes will end up in metastable rough structures (see Fig. 4.7b1)). The LEED pattern shown in Fig. 4.7(b2) corresponding to the latter preparation conditions also exhibits faint lines crossing the diffraction spots. For this particular preparation, faceting of the surface into a small (001) plane of size 15×15 nm^2 (not shown here) is also observed. Annealing the (110) surface higher than 1005 K leads to step bunching, surface diffusion and finally the surface undergoes a roughening transition. In conclusion, we could not find a surface preparation method that leads to a better surface state than the one achieved in Fig. 4.5. It corresponds to an unreconstructed surface termination at specific planes of the bulk separated by a step height of $\frac{a\sqrt{2}}{2}$. The near surface composition is stoichiometric, i.e. there is no surface segregation. The fine structure is observed by STM.

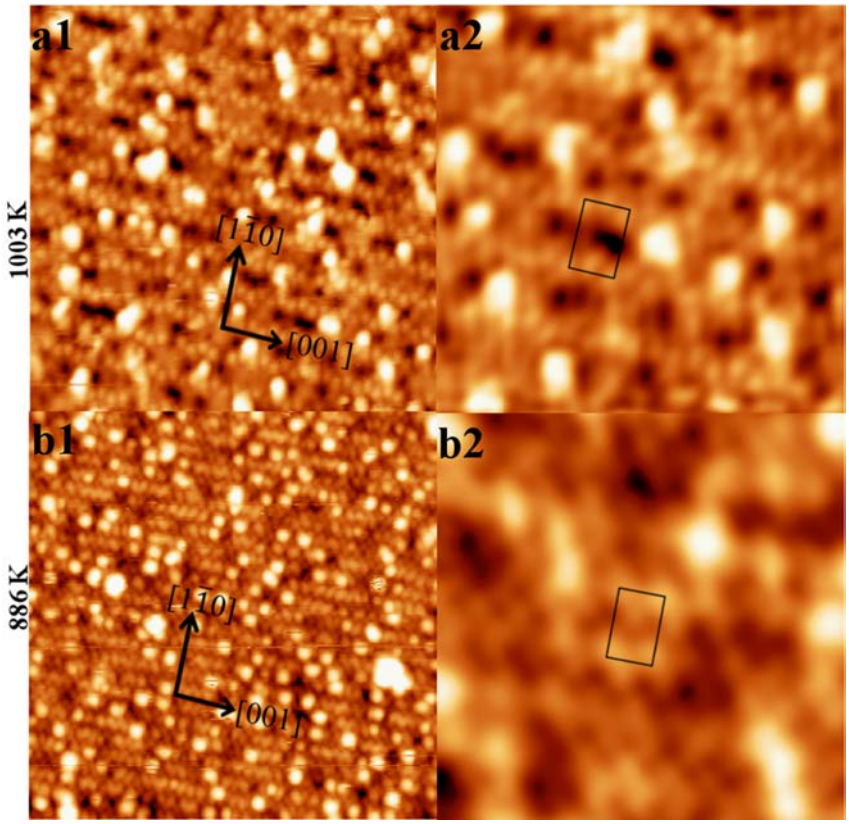

FIGURE 4.6: STM images for the same bias voltage ($V_b = -1.0$ V) and different annealing temperatures. (Left) (a1) A $20\times20\,\mathrm{nm}^2$ STM image ($I_t = 0.08$ nA) obtained by annealing the surface to 1003 K. (b1) The size of the image is $40\times40\,\mathrm{nm}^2$ ($I_t = 0.09$ nA) and the corresponding annealing temperature is 886 K. (Right) (a2); (b2) Fourier filtered image corresponding to a $10\times10\,\mathrm{nm}^2$ region of Fig. 4.6 (a1); (b1), respectively.

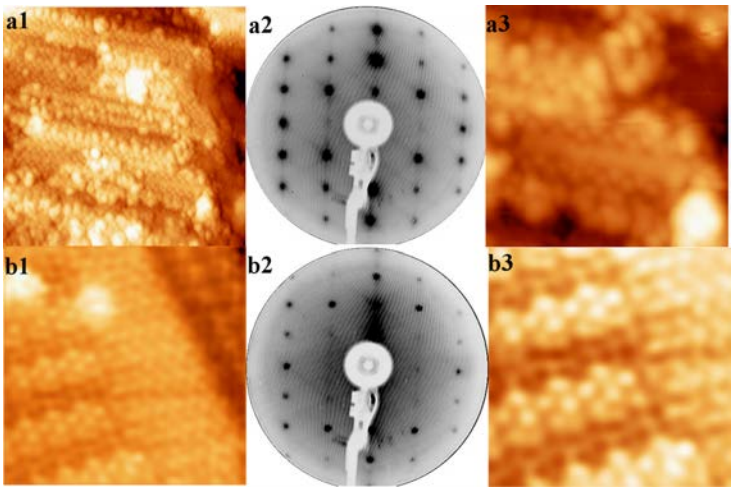

FIGURE 4.7: STM and LEED images demonstrating the presence of roughening and faceting on the (110) surface prepared at low annealing temperatures or for insufficient annealing time (< 1h). (a1) STM image of size 30×30 nm^2 for $V_b = -1.4$ V. (a2) Corresponding LEED pattern obtained at 18 eV for the surface prepared at 898 K for 15 min. (a3) Fourier filtered zoom (size: 7.6×5.4 nm^2) of (a1) image. (b1) A 9×12 nm^2 STM image at $V_b = +1.4$ V obtained by annealing the surface first at 540 K for 90 min and then at 797 K for 30 min. (b2) LEED pattern at 18 eV of the surface shown in (b1). (b3) Zoom (size: 7.6×6.2 nm^2) corresponding to (b1).

4.4 DFT Results

4.4.1 Description of the surface models

The surface-oriented bulk model (Fig. 4.1(b)) was used to construct the different models for the (110) surface. Each of the considered surface models necessarily intersects some of the clusters of the bulk structure. The different surface models are based on either bulk truncation or preservation of the cluster substructure at the surface. They differ by the surface corrugation and the chemical composition (presence of surface Au vacancies, of protruding Ba atoms, etc).

To determine the surface structure, in total eleven surface terminations are considered. Two of them are obtained by cleaving the ideal $Ba_8Au_6Ge_{40}$ bulk structure at a given x abscissa (x=0$^+$ and x=0.5$^-$ for the F and p models, respectively, see Fig. 4.10 bottom). The other models are built by preserving the cluster substructure at the surface. They are divided in two subgroups: P- and C-type models (Figs. 4.9-4.10), which differ by the type of polyhedra emerging at the surface (dodecahedra and tetrakaidecahedra for P- and C-type models, respectively). The P-type models are obtained by cleaving the $Ba_8Au_6Ge_{40}$ crystal at x=0.25$^-$, and slightly differ by the number of topmost Ba and Au atoms (see Fig. 4.8(a)).

A progressive removal of the topmost Ba atoms leads to the following sequence of models: $\mathrm{P}^{\mathrm{Ba}} \xrightarrow{\text{-2 Ba}^{\mathrm{P}}} \mathrm{P} \xrightarrow{\text{-2 Ba}} \mathrm{P}^{\mathrm{noBa}}$ and $\mathrm{P}^{\mathrm{Ba}}_{\mathrm{noAu}} \xrightarrow{\text{-2 Ba}^{\mathrm{P}}} \mathrm{P}_{\mathrm{noAu}}$. The sequence is $\mathrm{P}^{\mathrm{Ba}}_{\mathrm{Au}} \xrightarrow{\text{-2 Au}^{\mathrm{P}}} \mathrm{P}^{\mathrm{Ba}} \xrightarrow{\text{-2 Au}} \mathrm{P}^{\mathrm{Ba}}_{\mathrm{noAu}}$ when progressively removing topmost gold atoms, the $\mathrm{P}_{\mathrm{noAu}}$ and $\mathrm{P}^{\mathrm{Ba}}_{\mathrm{Au}}$ containing surface Au vacancies and additional surface atoms, respectively, that pulls down a strict definition of "cage preservation" at the surface. The C-type models present the highest concentration of surface Ge atoms. Again, relationship between C-type models can be represented as : $\mathrm{C}^{\mathrm{noBa}} \xrightarrow{\text{+4 Ba}} \mathrm{C}^{\mathrm{Ba}} \xrightarrow{\text{-2 Au}} \mathrm{C}^{\mathrm{Ba}}_{\mathrm{noAu}}$, the cages being only roughly preserved at the surface for the $\mathrm{C}^{\mathrm{Ba}}_{\mathrm{noAu}}$ model, since it contains surface Au vacancies. Other links between surface models that can be drawn relate to the two cage non preserving models: p $\xrightarrow{\text{+4 Ge}^{\mathrm{P}} + \text{2 Ba}^{\mathrm{P}}} \mathrm{C}^{\mathrm{Ba}} \xrightarrow{\text{+4 Ge}^{\mathrm{P}}}$ F. The relationships between the surface models are also represented in form of a schematic diagram in Fig. 4.8.

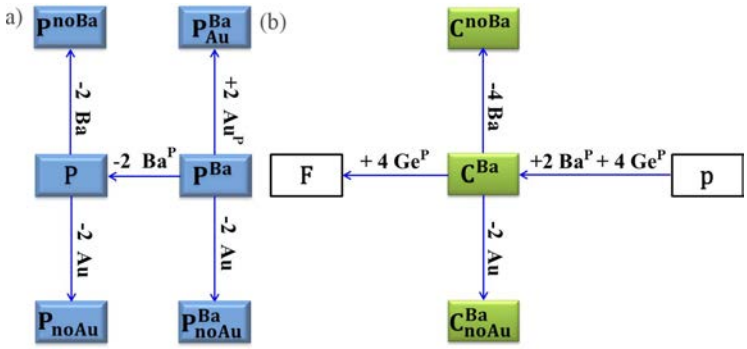

FIGURE 4.8: Schematic demonstrating the link between the cage preserving P- and C-type surface models. The relation of non-cage preserving, p and F models is also shown with C-type models.

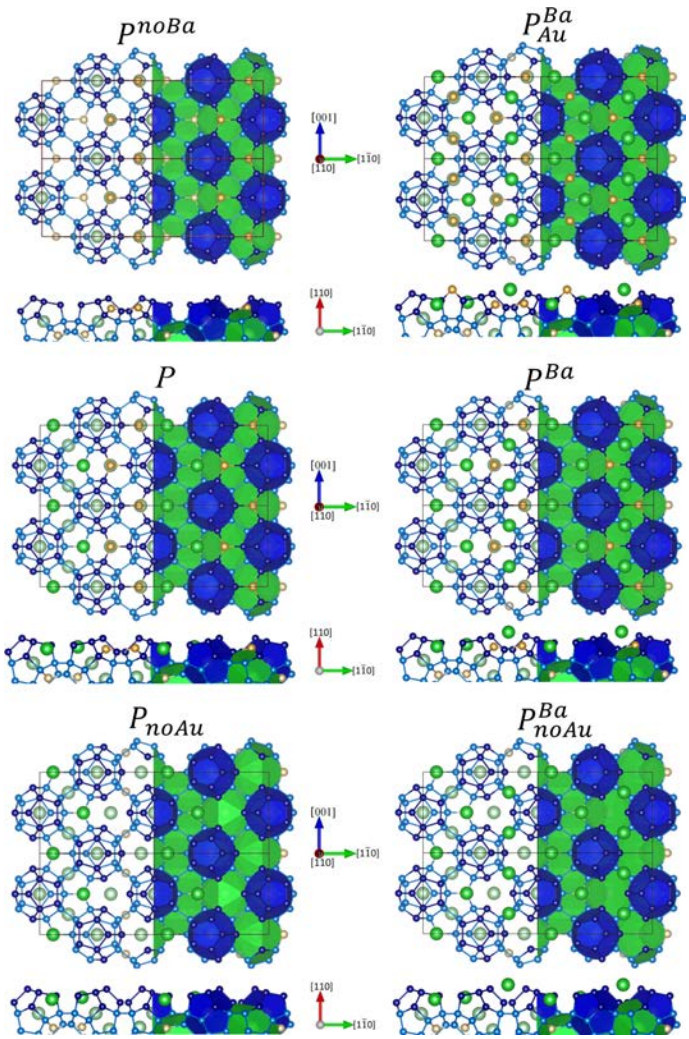

FIGURE 4.9: Side and top views of P-type surface models, preserving the nanocages at the surface. Atoms are represented by circles (Ba green, Au yellow, Ge blue). Faded colors indicate atoms lying slightly below the surface.

4.4.2 Energetics

The surface energy calculations are presented using both PBE and DFT-D3 approaches. The surface energies of the models are computed as a function of the Au and Ba relative chemical potentials and

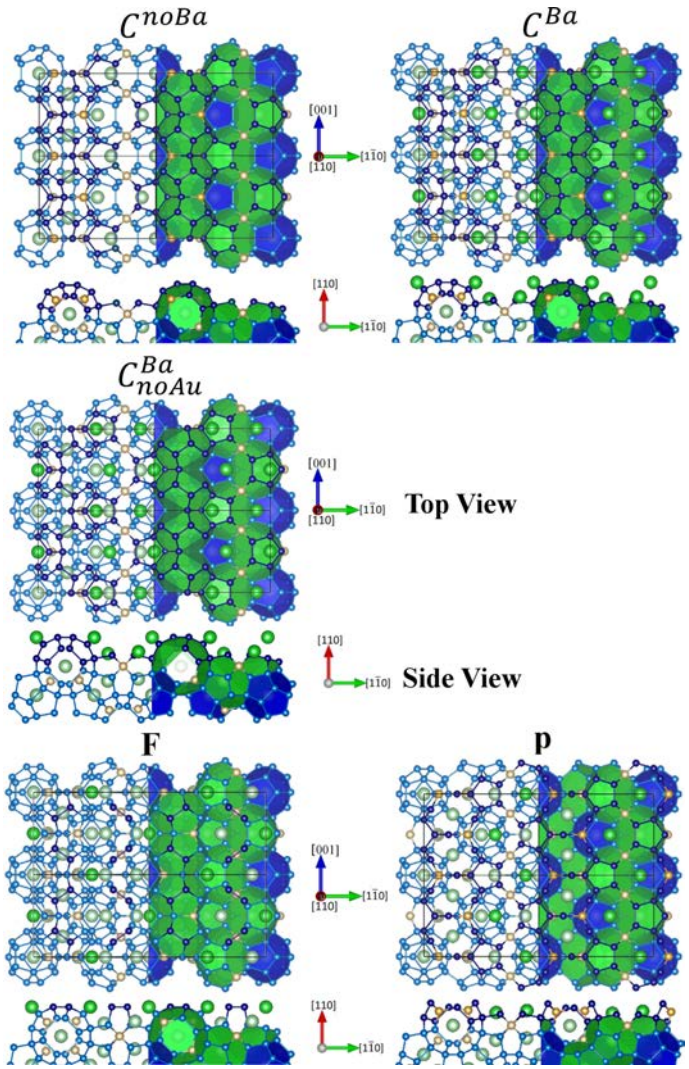

FIGURE 4.10: Side and top views of C-type surface models, preserving the nanocages at the surface and of the non-cage preserving models (F;p). Atoms are represented by circles (Ba green, Au yellow, Ge blue). Faded colors indicate atoms lying slightly below the surface.

plotted in Fig. 4.11 using the DFT-D3 approach. The colors in this graph are used to distinguish between the models presented.

The surface energies (in J/m^2) of the considered models are also gathered in Tab. 4.1. This table presents the surface energy calculations using both approaches. The DFT-D3 approach leads to higher values compared to the PBE calculations (increase roughly equals to 0.3 J/m^2). This behavior is well-known, that the more realistic Perdew-Burke-Ernzerhof functional underestimates surface energies [159]. The choice of the functional slightly modifies the stability domains, but does not question the relative surface energies, which are approximatively the same within both approaches.
The F and p models, which do not preserve the cage substructure up to the surface, present rather high surface energies. Surface energies are even higher for the models that strictly preserve the cage substructure up to the surface (X^{noBa} models with X = P, C), the P^{noBa} being more stable than the C^{noBa} model in the allowed range of chemical potentials. The surface energy depends on the surface atomic density and stoichiometry which is evident from Fig. 4.11. Since elemental surface energy of Ba is much lower than those of Au and Ge ($\gamma_{Ba(110)} = 0.31\,J/m^2$, $\gamma_{Au(110)} = 0.90\,J/m^2$ and $\gamma_{Ge(110)} = 0.97\,J/m^2$ [160, 161]), the non-cage preserving model F is more stable compared to the P (cage preserving model with moderately lower surface Ba density). The BaAuGe(110) surface is a

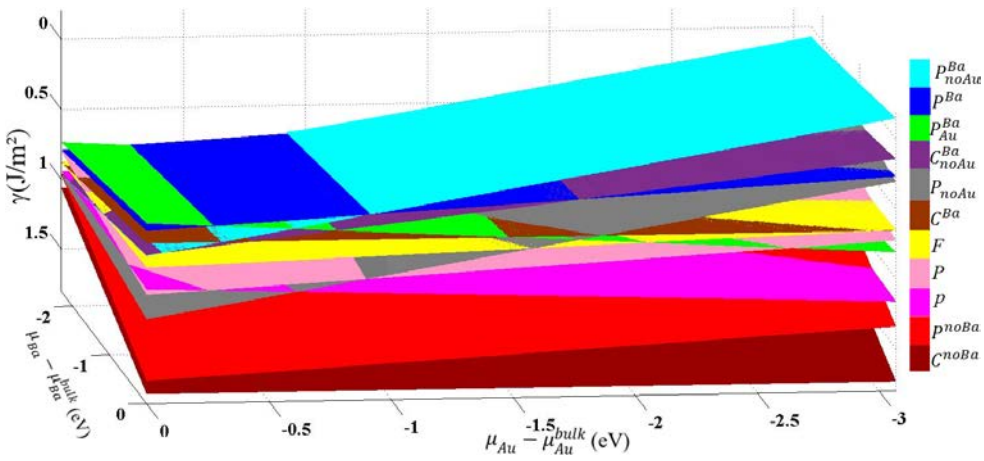

FIGURE 4.11: The three-dimensional (X:$\Delta\mu_{Ba}$,Y: $\Delta\mu_{Au}$ and Z: γ) surface energy diagram for the considered surface models within the potential limits of Ba and Au.

fair balance between the two aspects mentioned before.

Model	Cage Preserv.	PBE			DFT-D3		
	μ_{Au}	μ_{Au}^{bulk}	μ'_{Au}	μ''_{Au}	μ_{Au}^{bulk}	μ'_{Au}	μ''_{Au}
	μ_{Ba}	μ_{Ba}^{bulk}	μ_{Ba}^{bulk}	μ_{Ba}^{bulk}	μ_{Ba}^{bulk}	μ_{Ba}^{bulk}	μ_{Ba}^{bulk}
$\mathrm{P}^{\mathrm{noBa}}$	Yes	1.32	1.25	1.18	1.64	1.57	1.49
P	Yes[1]	0.75	0.68	0.61	1.03	0.95	0.88
$\mathrm{P}_{\mathrm{noAu}}$	Yes[3]	0.95	0.76	0.54	1.20	0.98	0.75
$\mathrm{P}^{\mathrm{Ba}}_{\mathrm{Au}}$	Yes[2]	0.24	0.31	0.37	0.52	0.59	0.66
P^{Ba}	Yes[1]	0.34	0.27	0.20	0.57	0.49	0.42
$\mathrm{P}^{\mathrm{Ba}}_{\mathrm{noAu}}$	Yes[3]	0.53	0.32	0.12	1.75	0.52	0.30
$\mathrm{C}^{\mathrm{noBa}}$	Yes	1.43	1.43	1.43	1.74	1.74	1.74
C^{Ba}	Yes[1]	0.40	0.40	0.40	0.66	0.66	0.66
$\mathrm{C}^{\mathrm{Ba}}_{\mathrm{noAu}}$	Yes[3]	0.51	0.37	0.23	0.74	0.59	0.44
F	No	0.57	0.53	0.49	0.83	0.79	0.75
p	No	0.71	0.75	0.79	0.99	1.03	1.08
$\mathrm{F}^{\mathrm{Ba}}_{(100)\mathrm{surface}}$	Yes[1]	0.24	0.31	0.38	0.49	0.61	0.73

TABLE 4.1: Surface energies (in J/m^2) calculated for the models considered in this study. Values for the stable model of the $Ba_8Au_6Ge_{40}$(100) surface are given for comparison ($\mathrm{F}^{\mathrm{Ba}}_{(100)\mathrm{surface}}$), [1] with additional surface Ba atoms, [2] with additional surface atoms (2 Au and 2 Ba), [3] with surface Au vacancies, that pulls down a strict definition of the "cage preservation" at the surface. The chemical potentials μ'_{Au} and μ''_{Au} are defined by $\mu'_{\mathrm{Au}} = \mu_{\mathrm{Au}}^{bulk} + \frac{54}{4\times6}\Delta H_f$ and $\mu''_{\mathrm{Au}} = \mu_{\mathrm{Au}}^{bulk} + \frac{54}{2\times6}\Delta H_f$

The decrease of the surface energies when the number of surface Ba atoms increases, in the series $\mathrm{P}^{\mathrm{Ba}} \xrightarrow{\text{-2 Ba}} \mathrm{P} \xrightarrow{\text{-2 Ba}} \mathrm{P}^{\mathrm{noBa}}$ and $\mathrm{C}^{\mathrm{Ba}} \xrightarrow{\text{-4 Ba}} \mathrm{C}^{\mathrm{noBa}}$, highlights the key role played by topmost Ba atoms for surface stabilization. This is related to an unbalanced charge distribution at the surface when Ba

atoms are missing or too few, the presence of surface Ba atoms ensuring a charge transfer saturating the dangling bonds at the surface (see section 4.4.7). The decrease of the surface energy with the increase of surface Ba atoms can even lead to negative surface energies. Although the limitations of the exchange-correlation functional used can contribute to such result, as already observed by Refs. [160, 162] for two graphite polymorph surfaces, the exothermic adsorption of Ba on $Ba_8Au_6Ge_{40}(110)$ reduces the solid's surface energy, up to negative surface energies [163]. Indeed, the adsorption energies for Ba in the considered models, calculated with the following equation are rather high (Tab. 4.2):

$$E^{\mathrm{i}}_{ads} = -\frac{1}{n_i}[E^P - E^R + n_i\mu^{bulk}_{\mathrm{i}}] \tag{4.1}$$

In this equation, n_i is the number of i adatoms and E^P and E^R are the energies of the corresponding slabs without and with additional surface adatoms, respectively. The calculated adsorption energies for $Ba/Ba_8Au_6Ge_{40}(110)$ are of the same order of magnitude as the one for Ba/Ge(001) [164], ranging from 2.79 to 4.15 eV/at.

Gold surface atoms also contribute to the surface stability. At the Au-rich limit, their presence increases the surface density, thus stabilizing the $\mathrm{P}^{\mathrm{Ba}}_{\mathrm{Au}}$ surface model. Indeed, the energy required to remove an Au adatom is 0.50 eV/at. at the Au-rich limit (Tab. 4.2), i.e. of the same order of magnitude as the one for a gold monovacancy on a reconstructed Au(100) surface ($\simeq$ 0.4 eV/at.) [165]. When moving to the Au poor limit, the formation of gold surface vacancies becomes endothermic, for the P- and C-type models.

	E^{Ba}_{ads} (eV/at.)			E^{Au}_{ads} (Au-rich limit)	
	PBE	DFT-D3		PBE	DFT-D3
$\mathrm{P}^{\mathrm{Ba}} \xrightarrow{\text{-4 Ba}} \mathrm{P}^{\mathrm{noBa}}$	-2.53	-2.77	$\mathrm{P} \xrightarrow{\text{-2 Au}} \mathrm{P}_{\mathrm{noAu}}$	-1.03	-0.90
$\mathrm{P}^{\mathrm{Ba}} \xrightarrow{\text{-2 Ba}} \mathrm{P}$	-2.92	-3.17	$\mathrm{C}^{\mathrm{Ba}} \xrightarrow{\text{-2 Au}} \mathrm{C}_{\mathrm{noAu}}$	-0.54	-0.43
$\mathrm{C}^{\mathrm{Ba}} \xrightarrow{\text{-4 Ba}} \mathrm{C}^{\mathrm{noBa}}$	-2.64	-2.78	$\mathrm{P}^{\mathrm{Ba}} \xrightarrow{\text{-2 Au}} \mathrm{P}^{\mathrm{Ba}}_{\mathrm{noAu}}$	-0.98	-0.92
			$\mathrm{P}^{\mathrm{Ba}}_{\mathrm{Au}} \xrightarrow{\text{-4 Au}} \mathrm{P}^{\mathrm{Ba}}_{\mathrm{noAu}}$	-0.74	-0.60

TABLE 4.2: Adsorption energies for Ba and Au surface atoms at the $Ba_8Au_6Ge_{40}(110)$ surface.

The allowed region on the 2D chemical potential landscape is formed by the triangle including the Ge poor-limit point. Conclusions of surface energies calculations are summarized in Figs. 4.12 (DFT-D3) and 4.13 (PBE). The surface phase diagrams have been plotted by considering a criterion of the minimum surface energy in the allowed region of the chemical potential. Within the allowed range for chemical potentials, the P-type models with protruding Ba atoms present the lowest surface energies. In the Au-rich limit, the $\mathrm{P}^{\mathrm{Ba}}_{\mathrm{Au}}$ is the most stable one, additional surface Ba and Au atoms contributing to the surface stability. When moving away from the Au-rich limit, the most stable surface model becomes the P^{Ba} model, without additional surface Au atoms. When moving to the Au-poor domain, the most stable model changes to the $\mathrm{P}^{\mathrm{Ba}}_{\mathrm{noAu}}$ model, with surface Au vacancies. The partition between the stability domains in these phase diagrams seems independent of the relative chemical potential of Ba and depends solely on that of Au. We know that Ba plays a key role in the stability of this surface but the concentration of Au at surface can be considered as a secondary factor influencing its stability.

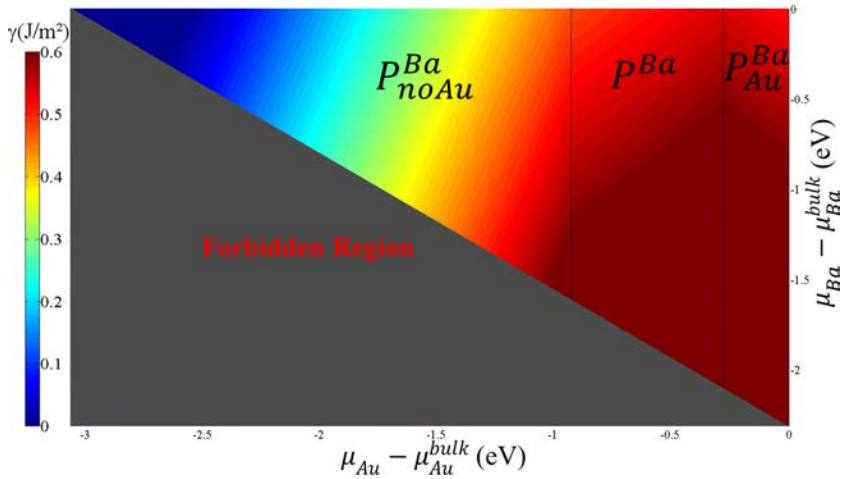

FIGURE 4.12: Surface phase diagram for the $Ba_8Au_6Ge_{40}(110)$ surface, calculated within DFT-D3.

4.4.3 Surface relaxations

The stabilization of the different surface models is achieved by several factors, one of them is surface relaxation. It induces a decrease of the surface corrugation and a deformation of the cages protruding at the surface. The energy gain due to distortion is in the order of 0.4-0.6 J/m^2. It is higher for the most stable models with additional surface atoms and not strictly preserving the cage substructure up to the surface (0.61 J/m^2, 0.48 J/m^2 and 0.51 J/m^2 for the P^{Ba}_{Au}, P^{Ba} and P^{Ba}_{noAu} models, respectively). The stabilization energy gain due to relaxation for C^{Ba} model is 0.43 J/m^2 and for P is 0.46 J/m^2, which is rather low.

For the stable P^{Ba}_{Au}, P^{Ba} and P^{Ba}_{noAu} models, and after relaxation, the surface buckling (Δ^r_x) decreases to 3.16 Å, 2.58 Å and 3.46 Å, respectively (the change of the corrugation is equal to 0.54 Å, 0.45 Å and 0.23 Å, respectively). While this scheme is quite general among the considered models, a few of them presents an increase of the surface corrugation (P, P_{noAu}, C^{Ba}, C^{Ba}_{noAu}, F) and the surface layer relaxes outward (see Tab. 4.3). The general trend in the $Ba_8Au_6Ge_{40}(110)$ relaxations is that Ge atoms relax outward, while Ba atoms relax inward. This quite general behavior can be mirrored against the relaxation of the partially ionic GaAs semiconductors, where anions and cations move in opposite

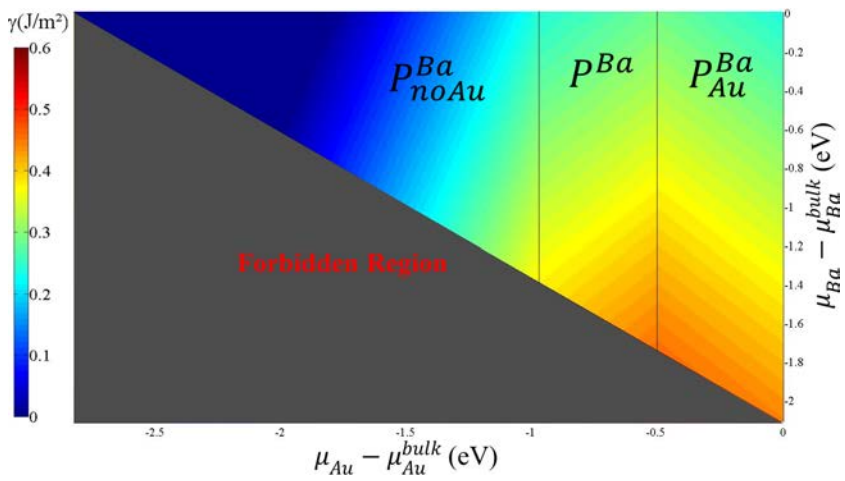

FIGURE 4.13: Surface phase diagram for the $Ba_8Au_6Ge_{40}(110)$ surface, calculated within PBE.

directions (inwards for cations and outwards for anions for GaAs(110), for example [166]) to optimize hybridization and reduce the destabilization due to dangling bonds at the surface.

Model	Distortion index D			Surface Corrugation Å	
P-type	Ge^{P}_{20}		$(Ge,Au)^{B}_{24}$	Δ^{r}_{x}	$\lvert \delta\Delta_x = \Delta^{r}_{x} - \Delta^{nr}_{x} \rvert$
P^{noBa}	0.047		0.057	2.39	0
P	0.049		0.058	2.76	0.37
P_{noAu}	0.051		0.056	2.84	0.45
P^{Ba}_{Au}	0.040		0.044	3.16	0.54
P^{Ba}	0.032		0.046	2.58	1.12
P^{Ba}_{noAu}	0.047		0.052	3.47	0.23
C-type	$(Ge,Au)^{P}_{24}$	$(Ge,Au)_{24}$	Ge^{B}_{20}	Δ^{r}_{x}	$\lvert \delta\Delta_x = \Delta^{r}_{x} - \Delta^{nr}_{x} \rvert$
C^{noBa}	0.059	0.056	0.020	2.91	-0.39
C^{Ba}	0.069	0.067	0.022	3.73	0.43
C^{Ba}_{noAu}	0.054	0.051	0.021	3.50	0.20
p				2.32	0.08
F				1.01	0.59
$F^{Ba}_{(100)surface}$	0.044		0.021	0.03	0.02

TABLE 4.3: Distortion index calculated on relaxed structures for P- and C-type models. These models are characterized by protruding (P) and buried (B) cages at the surface.

Surface relaxations also deform the cages located at the surface. To evaluate such distortions, we calculated the Baur's distortion index (D) [141], defined as $D = \frac{1}{n_b}\sum_{i=1}^{n}\frac{|\ell_i - \ell_{avg}|}{\ell_{avg}}$ where n_b is the number of bonds to the central atom, ℓ_i is the distance from the central atom to the ith coordinating atom, and ℓ_{avg} is the average polyhedral bond length. In the bulk, the dodecahedra and tetrakaidecahedra present distortion index equal to 0.019 and 0.048, respectively. At the surface, they mostly distort, leading to an increase of the D index. From Tab. 4.3, it appears that protruding cages present higher distortions than more buried ones. Among protruding cages, the dodecahedron Ge_{20} shows higher distortions. There are few exceptions to the general tendency, like for P^{Ba}_{Au} and P^{Ba} models where the $(Ge,Au)^{B}_{24}$ shows a decrease in D index compared to bulk. Also in the case of the most stable model for BaAuGe(100) ($F^{Ba}_{(100)surface}$), the $(Ge,Au)^{P}_{24}$ cages show contraction in bond lengths and hence D index lower than the bulk value. Although, at the (100) surface the tetrakaidecahedra cages are protruding they show less relative distortion ($\frac{D-D^{bulk}}{D^{bulk}}$) compared to the buried dodecahedra cages. The relative values of the D index (with respect to the bulk) for the surface models considered for BaAuGe(110) and for the $F^{Ba}_{(100)surface}$ model of BaAuGe(100) are plotted in Fig. 4.14.

4.4.4 Simulated STM images

Simulated STM images (3×6 unit cell) for the considered models are shown in Fig 4.15. These images are plotted at a constant current for isodensity values in the range 3×10^{-4} - 1.6×10^{-5} e/Å^3. All surface models present non-negligible corrugations, the calculated contrast is therefore attributed to both positional and electronic effects. The latter mostly originate from surface Ge $4p$ states in the vicinity of the Fermi level in the DOS. The simulated STM images show a strong bias dependency for all models, except for C^{Ba}. Indeed, in the latter case, the surface electronic structure is calculated to be symmetric around the Fermi level (see section 4.4.8). The Ba atoms of the P model are imaged dark, whatever is the bias voltage, because these atoms are located below the topmost atoms (2.16 Å). For

the F, P^{Ba}_{Au} and p models, there is an interesting bias dependence of the contribution from Ba atoms, which appears rather dark for filled states (negative bias) and brighter for empty states (positive bias). Similar but less obvious bias dependence of protruding Ba atoms can be seen for P^{Ba} and P^{Ba}_{noAu}, where discrete bright points in a row (occupied states imaging) transform to continuous bright lines (unoccupied states imaging). This is consistent with an electron transfer from the Ba adatom to the surface, as demonstrated by the Bader charge analysis (see section 4.4.7).

The typical features that can be extracted from these simulated STM images are bright zig-zag rows with discrete dots for positive bias and bright wavy lines for the negative bias. In both cases, bright rows are followed by dark rows. The flat (F) model shows bright zig-zag motifs but is not followed by dark lines for positive bias. While for negative bias it exhibits departure from the common feature and also no dark rows are present. The positional effects are absent for the F termination due to its flatness. The other bulk truncated p model show no dark rows for negative bias due to electronic effect of Ba atoms which are above Ge atoms. Despite the fact that P (cage preserving) model has the same surface composition as p, they reveal motifs very different from each other. This is explained by the opposite position of Ba and Au atoms in the two models, they are below Ge atoms in the P model. The C- and P-type models mainly show zig-zag pattern with different spacing in between the bright rows. Thus, a close inspection of simulated images belonging to each model brings into picture peculiarities of the surface pertaining to the local electronic environment.
In the next sub-section, we take it further with a direct comparison between the experimental and simulated STM images for P^{Ba}, P^{Ba}_{Au}, C^{Ba} and P models. We also compare the experimental and theoretical results by taking into account the combined inference of simulated STM and surface energy calculations.

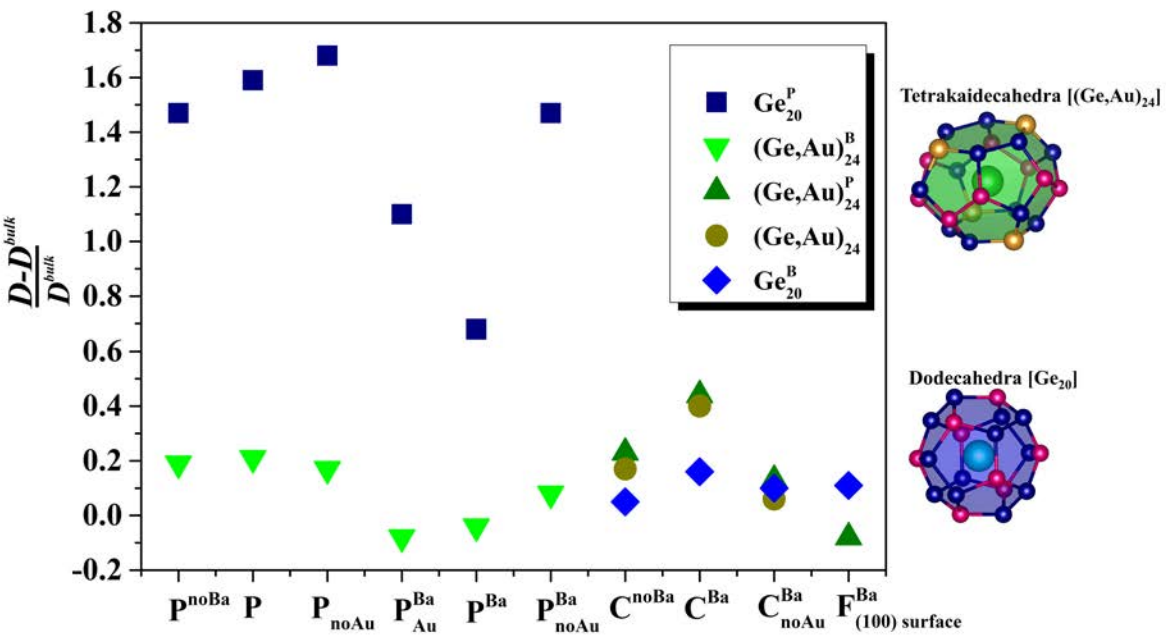

FIGURE 4.14: Distorsion index calculated for the two types of cages [Ge_{20} and $(Ge,Au)_{24}$] of the considered surface models. The ^{P} and ^{B} superscripts stand for Protruding and Buried, respectively.

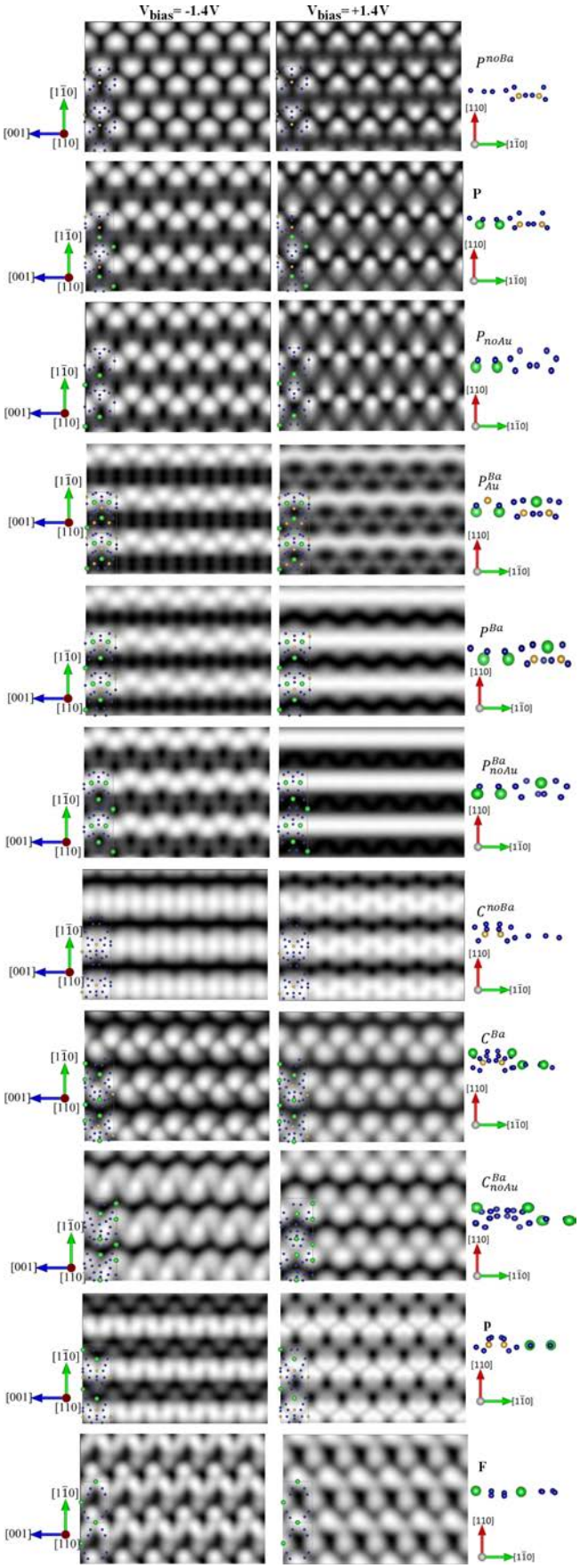

FIGURE 4.15: Simulated STM images of a 3×6 unit cell for the considered models.

4.4.5 Comparison of experimental and stimulated STM images

On comparing the experimental with simulated STM images, interesting arguments emerge supporting few models depending on the bias voltage (V_{bias}) shown in Fig. 4.16. The simulated images in Fig.4.16 are plotted using the constant current mode and then are rotated according to the experimental images to have an easy comparison between the two. The complexity of the experimental STM images, their bias voltage dependence and the presence of defects, make the analysis difficult. Also, the "non-periodic" pattern seen experimentally can be due to structural disorder. However, the simulation of STM images based on the eleven considered models helps to determine the atomic structures of the observed features. Among the three stable models appearing in the surface phase diagram (Figs. 4.12, 4.13), P^{Ba}_{noAu} shows disagreement with experimental STM images. The comparison of the simulated images calculated for the C^{Ba} and P models shows similarities with the experimental images, for positive-bias and negative bias, respectively. However, these models were not identified as stable ones according to surface energy calculations.
The STM images of the two stable models (P^{Ba} and P^{Ba}_{Au}) reflect the experimentally observed electronic features. Although, the best agreement between experimental and theoretical STM images is found for the P^{Ba} model. Indeed, it is the only model that presents wavy bright lines for positive bias and an arrangement of dotted lines for negative bias (Fig. 4.16).
Hence, the combination of surface energy calculations and STM image simulations leads to the conclusion that the $Ba_8Au_{5.25}Ge_{40.75}$(110) surface is well described by the P^{Ba} model.

Further, we examine the electronic structure of the considered models using electron localization function calculations, Bader charge analysis and DOS calculations.

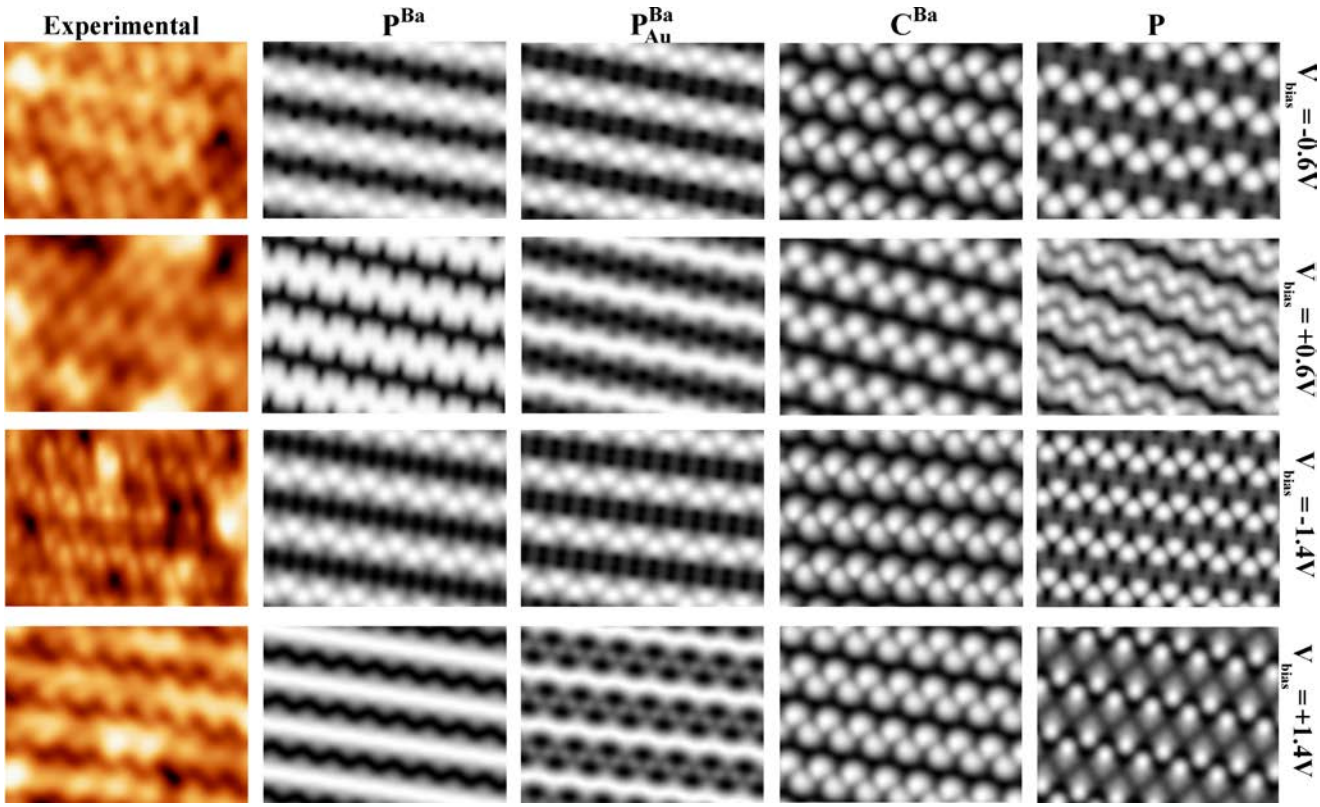

FIGURE 4.16: (Top) 9.9×4.8 nm^2 STM images obtained at $V_{bias} = \pm 0.6$ V (Top) and $V_{bias} = \pm 1.4$ V (bottom) using P^{Ba}, P^{Ba}_{Au}, C^{Ba} and P models. Experimental STM images (identical bias and image size) are also presented for a comparison with the surface models.

4.4.6 Electron localization function

Our ELF calculations highlight the electron pair probability density at the BaAuGe(110) surface. Its graphical representation can add to the understanding of electron localization, here mostly related to the low coordination of the surface Ge atoms. These calculations identified dangling bonds for all surface models considered in the study. They are found to be located at the sp^2 Ge atoms in all the models. The higher values of ELF ($\sim$ 0.8) are also situated at the Ba sites, this is because of the presence of large number of inner bands. Electronegative Au atoms are expected to gain charges from electropositive Ba atoms to complete their $6s$ outer shell. Since s electrons are highly delocalized, the ELF value around Au atoms is $\sim$ 0.5. ELF values of 0.5 are characteristic of a free electron gas, so the ELF images indicate there is negligible charge localization near the gold atoms in the structure. Interestingly, around the Au atoms there is a formation of trigonal shape with an elongation towards Ba2 atoms (see Fig. 4.17). This indicates a covalent character of the bonds between the two. This feature is also observed by Ref. [18] in bulk BaAuGe by ELI-D calculations. The ELF maxima value equal to 0.9 provides us with the number of dangling bonds for the considered surface models. The ELF images for P-type models (Fig. 4.17), C-type models and bulk truncated (F;p) models (Fig. 4.18) have been plotted for ELF value in the range 0-0.9, where color white/pink colors represent regions of either non-bonding lone pairs or covalent bonds.
The saturation of dangling bonds observed on sp^2 Ge atoms depends on the charge transfer at the surface (see section 4.4.7). The combination of the Bader charge and ELF analysis gives insight into the mechanism at the origin of the surface stability. In P^{noBa}, P and P_{noAu} models, six, four and two dangling bonds per unit cell, respectively are highlighted. They are not saturated, since the Ge atoms lose charges and the dangling bonds are oriented away from Ba atoms (if present). Similarly in the case of C^{noBa} and p models, four dangling bonds per unit cell are determined to be unsaturated. Hence, we can conclude that in the models presenting no or insufficient protruding Ba atoms, the non-saturated dangling bonds lead to higher surface energy values. The remaining models have all dangling bonds saturated due to sufficient charge transfer from surface Ba atoms. Their enumeration is provided in Tab. 4.4.

Surface relaxations inducing the changes in electronic structure or vice-versa through charge transfer are further investigated using Bader charge analysis in the following section.

Model	Surface composition			After surface relaxations	
	Ba	Au	Ge	No. of surface sp^2 Ge atoms	No. of DBs at ELF=0.9
P^{noBa}	0	2	16	10	6
P	2	2	16	10	6
P_{noAu}	2	0	16	16	12
P^{Ba}_{Au}	4	4	16	6	6
P^{Ba}	4	2	16	10	10
P^{Ba}_{noAu}	4	0	16	16	10
C^{noBa}	0	2	20	12	4
C^{Ba}	4	2	20	12	6
C^{Ba}_{noAu}	4	0	20	16	8
F	2	0	8	8	6
p	2	2	16	16	6

TABLE 4.4: Chemical surface composition and number of dangling bonds observed at ELF value equal to 0.9 for all models considered in the study.

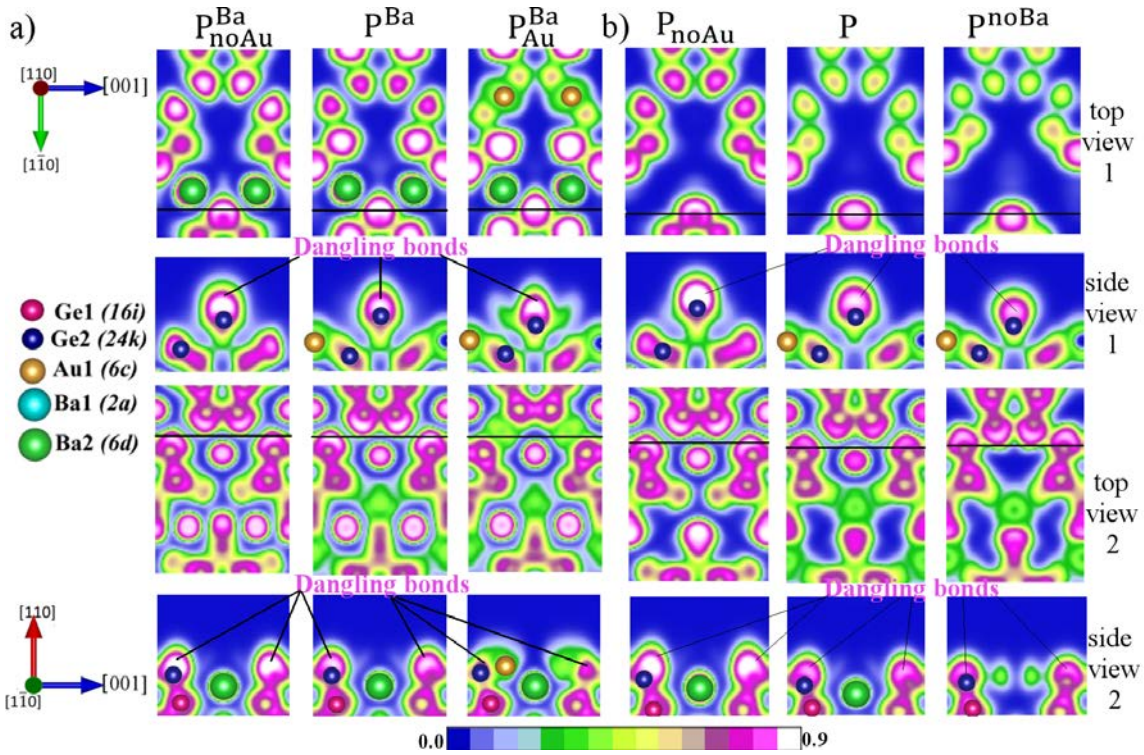

FIGURE 4.17: Electron localization function for P-type models is shown, (a) wih 4 surface Ba atoms and (b) with 2 surface Ba atoms. The regions of high charge localization are highlighted in white color. Top view 1 (x=0.61) shows ELF at extreme periphery of the surface while top view 2 (x=0.57) projects ELF at mean height of puckered surface plane. The black lines show the trace of the plane chosen for the side views (along the [1$\bar{1}$0] direction).

4.4.7 Bader charge analysis

The Bader charge analysis delineates the role of surface Ba atoms in inducing charge balance at the surface. Fig. 4.19 reveals the average charge gain at each Wyckoff site for bulk and surface models. The bulk values provided in Ref. [17] are also added as data set of literature. From this graph, it is evident for the X^{noBa} (X=P,C) series of models that charge gain at the Au and Ge sites are not comparable to bulk values. Also, our bulk calculations are in complete coherence with literature except for Au site but the difference is too small. However, from this representation it is not easy to extract something particular about other surface models. It can be seen for all the other models that there is a charge transfer from Ba to host (Au,Ge) atoms, but quantitatively the surface scenario is much more complex.

Before looking into the charge transfer of the considered surface models in details, it is important to bring into picture their surface planar symmetry. The unrelaxed modeled BaAuGe(110) surface present $p2mg$ symmetry (Fig. 4.20, explains the labels of Tabs. 4.5 & 4.6). Charge transfers are calculated with $\Delta Q_X = Q_X^{ref} - Q_X^{slab}$ where Q_X^{ref} is the number of valence electrons for element X and Q_X^{slab} is the number of valence electrons for X in the slab. Values for the Bader charges are roughly the same when calculated within the PBE or DFT-D3 schemes (Tabs. 4.5 and 4.6). The few minor differences are represented in bold text in Tab. 4.6.

We discuss here the values calculated within the PBE approach. They are consistent with the electronegativities of the elements, according to the Pauling scale (2.54 for Au, 2.01 for Ge and 1.81 for Ba) [167]. As highlighted by surface energy calculations, the topmost surface Ba atoms play a non negligible role in the surface stabilization. Indeed, for the stable models P^{Ba}_{Au}, P^{Ba} and P^{Ba}_{noAu}, they induce a charge transfer ($\Delta Q_{Ba} \in [1.31, 1.41]$ e) to surface Au and Ge atoms ($\Delta Q_{Au1} \in [-0.79, -0.81]$

e and $\Delta Q_{\mathrm{Ge}} \simeq -0.20$ e), so that surface atoms recover a charge similar to the one in the bulk ($\Delta Q_{\mathrm{Ba2}} = 1.37$ e, $\Delta Q_{\mathrm{Au}} = -0.84$ e, $\Delta Q_{\mathrm{Ge1}} = -0.17$ e, $\Delta Q_{\mathrm{Ge2}} = -0.12$ e).
A few exceptions are noticeable, $\Delta Q_{\mathrm{Ge5}} = -0.02$ e for the $\mathrm{P}^{\mathrm{Ba}}_{\mathrm{Au}}$ model for example, where Ge5 is the surface Ge atom located close to the Au1′ adatom. In that case, there is a non negligible charge transfer from Ge5 to Au1′ ($\Delta Q_{\mathrm{Au'}} = -0.56$ e) and it is the origin of the low value found for Ge5. Another exception is the one of the Ge3 surface atom ($\Delta Q_{\mathrm{Ge3}} = -0.40$ e) in P-type models with protruding Ba atoms. As the Ge3 surface atoms are close to Ba2 (3.42 Å) and quite far from Au1 (4.53 Å), they have an exceptional charge gain. The Ge4 atoms, which are at the same distance from Ba2′(3.41 Å) but close to Au1 (2.53 Å), gain approximately half of ΔQ_{Ge3}. This becomes obvious in the case of $\mathrm{P}^{\mathrm{Ba}}_{\mathrm{Au}}$, where the charge gained by both Ge3 and Ge4 atoms is equal.
Finally, the formation of surface Au vacancies leads to a general increase of the charge carried by surface Ge atoms, since the charge on surface Ba atoms remains roughly the same. On the contrary, the absence of protruding surface Ba atoms in the case of the $\mathrm{P}^{\mathrm{noBa}}$ and $\mathrm{C}^{\mathrm{noBa}}$ models leads to several surface Ge with a positive charge leaving unsaturated dangling bonds. This explains the corresponding rather large surface energy calculated for these models. The total net charge in P-type models can be calculated as:

$$\Sigma^{\mathrm{Surface}}_{\mathrm{P-type}} = 4 * [\frac{1}{2}(\Delta Q_{Ba2'} + \Delta Q_{Ba2} + \Delta Q_{Au1} + \Delta Q_{Ge3} + \Delta Q_{Ge4}) + \Delta Q_{Ge1} + \Delta Q_{Ge2} + \Delta Q_{Ge5}] \tag{4.2}$$

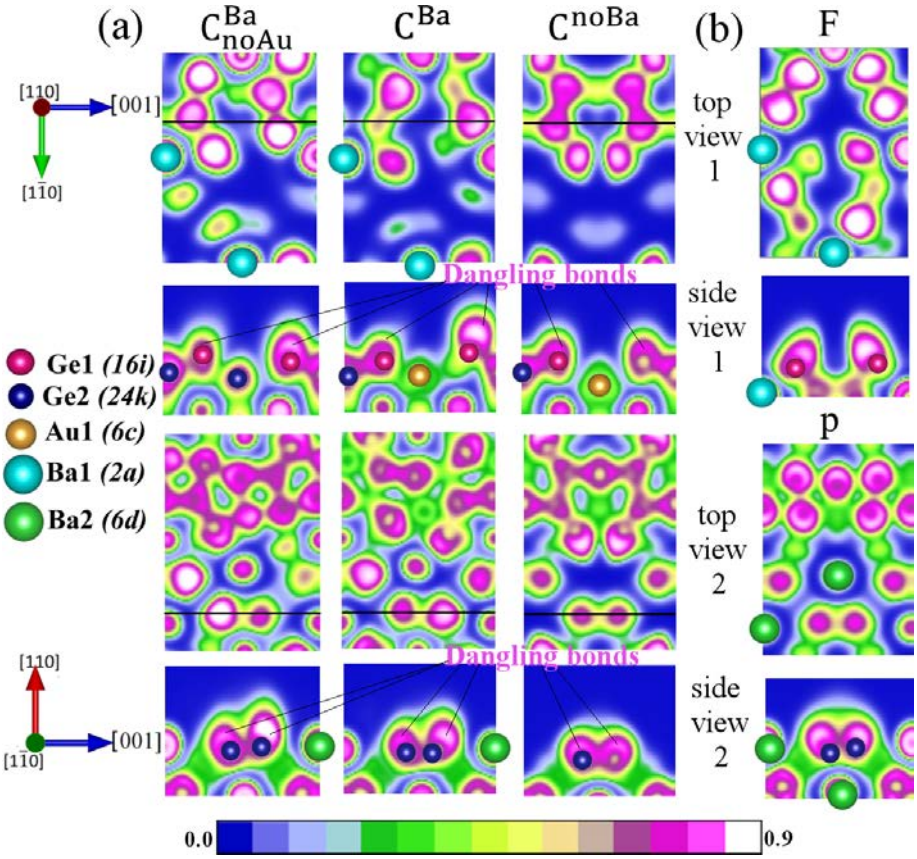

FIGURE 4.18: Representation of the Electron localization function using (a) C-type models and (b) non-cage preserving models. Top view 1 (x=0.61) shows ELF at extreme periphery of surface while top view 2 (x=0.57) projects ELF at mean height of puckered surface plane. The black lines show the trace of the plane chosen for the side views (along [1$\bar{1}$0] direction).

While for the C-type models, the total net charge can be calculated by the equation below

$$\Sigma^{\text{Surface}}_{\text{C-type}} = 4 * [\frac{1}{2}(\Delta Q_{Ba1} + \Delta Q_{Ba2} + \Delta Q_{Au1} + \Delta Q_{Ge3+Ge4}) + \Delta Q_{Ge1} + \Delta Q_{Ge2} + \Delta Q_{Ge5} + \Delta Q_{Ge6}] \quad (4.3)$$

The bulk shows perfect charge balance as the total net charge is equal to zero. It is determined by the equation below:

$$\Sigma^{\text{Bulk}} = 2 * \Delta Q_{Ba1(2a)} + 6 * \Delta Q_{Ba2(6d)} + 6 * \Delta Q_{Au1(6c)} + 16 * \Delta Q_{Ge1(16i)} + 24 * \Delta Q_{Ge4(24k)} \quad (4.4)$$

As discussed above, the presence of surface Ba atoms leads to a charge balance at the surface (like in the bulk) with a complete saturation of the dangling bonds. Only in the case of P^{Ba} and P^{Ba}_{Au}, the total net charge (using Equation 4.2) is the same as the bulk (Equation 4.4). While, the effective charge gain is more than in the bulk for the surface models with Au vacancies (P^{Ba}_{noAu} and C^{Ba}_{noAu}). All above previous observations can be synthesized in the following way. In the Au-rich limit, stable models are those which minimize the ratio $\frac{N_{Ge-sp^2}}{N_{Ba}}$, where N_{Ge-sp^2} and N_{Ba} are the number of surface sp^2 Ge and Ba atoms. This ensures a favorable saturation of the surface dangling bonds (Tab. 4.4).

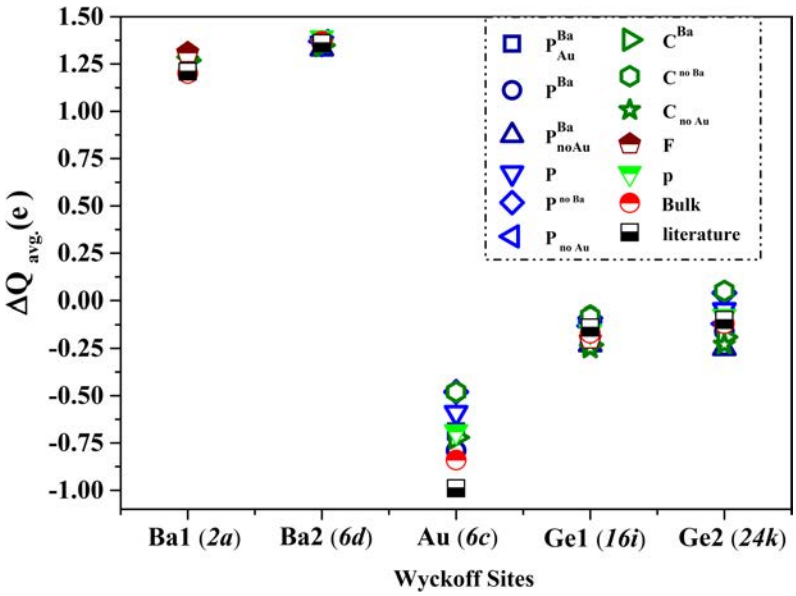

FIGURE 4.19: Average charge gain at each (bulk) Wyckoff site for the considered surface models using Bader charge analysis. The values calculated for the bulk and the one in the Ref. [17] are included.

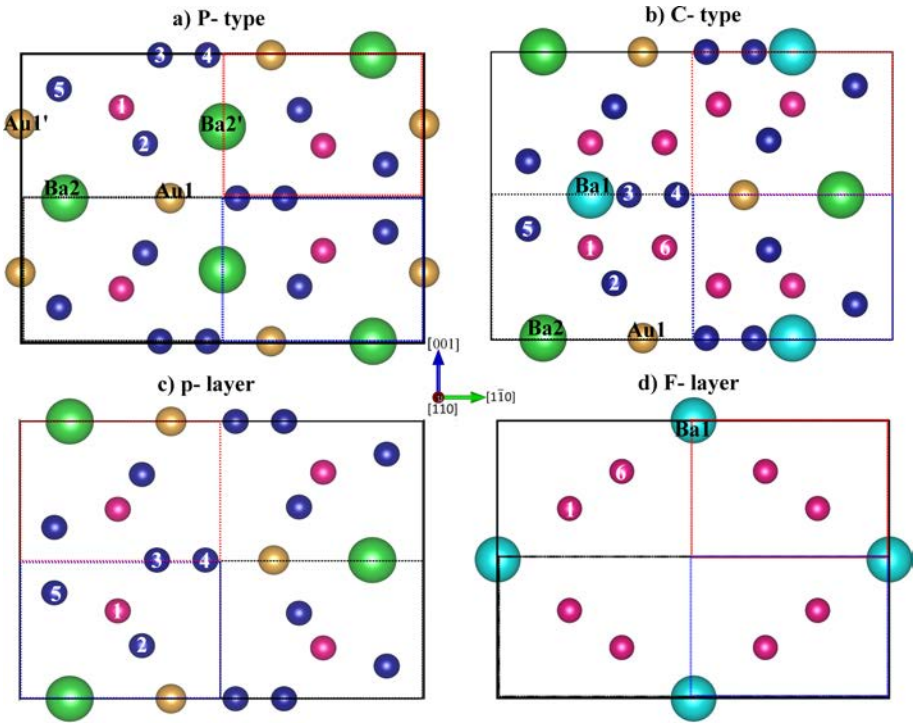

FIGURE 4.20: Top view of surface unit cell of ideal (a) P-type, (b) C-type, (c) p and (d) F models showing the label of surface sites according to the bulk Wyckoff positions as mentioned in Tabs. 4.5 and 4.6.

site		Bulk	P^{noBa}	P	P_{noAu}	P^{Ba}_{Au}	P^{Ba}	P^{Ba}_{noAu}	C^{noBa}	C^{Ba}	C^{Ba}_{noAu}	p	F
Ba1	$2a$	+1.20	-	-	-	-	-	-	-	+1.28	+1.27	-	+1.31
Ba2	$6d$	+1.37	-	+1.36	+1.37	+1.41	+1.37	+1.35	-	+1.35	+1.36	+1.39	-
Ba2′	$6d$	-	-	-	-	+1.34	+1.34	+1.31	-	-	-	-	-
Au1	$6c$	-0.84	-0.48	-0.59	-	-0.81	-0.79	-	-0.48	-0.72	-	-0.69	-
Au1′	$6c$	-	-	-	-	-0.57	-	-	-	-	-	-	-
Ge1	$16i$	-0.17	-0.09	-0.14	-0.13	-0.21	-0.22	-0.23	-0.08	-0.30	-0.29	-0.16	-0.16
Ge2	$24k$	-0.12	+0.01	-0.12	-0.27	-0.16	-0.20	-0.37	+0.21	-0.16	-0.24	-0.00	-
Ge3	$24k$	-	+0.07	+0.05	+0.04	-0.44	-0.40	-0.42	-0.01	-0.14	-0.33	-0.23	-
Ge4	$24k$	-	+0.00	+0.05	-0.02	-0.21	-0.24	-0.43	-0.07	-0.16	-0.13	-0.11	-
Ge5	$24k$	-	+0.08	-0.19	-0.24	-0.02	-0.21	-0.20	+0.08	-0.30	-0.23	-0.17	-
Ge6	$16i$	-	-	-	-	-	-	-	-0.07	-0.15	-0.22	-	-0.23

TABLE 4.5: Bader charge analysis for surface atoms of the models considered in the study. Atoms are labeled according to Fig. 4.20. The calculations are performed within PBE scheme.

site		Bulk	P^{noBa}	P	P_{noAu}	P^{Ba}_{Au}	P^{Ba}	P^{Ba}_{noAu}	C^{noBa}	C^{Ba}	C^{Ba}_{noAu}	p	F
Ba1	$2a$	+1.20	-	-	-	-	-	-	-	**+1.27**	+1.27	-	**+1.30**
Ba2	$6d$	**+1.36**	-	+1.36	+1.37	**+1.40**	+1.37	+1.35	-	+1.35	+1.36	**+1.40**	-
Ba2′	$6d$	-	-	-	-	+1.34	+1.34	+1.31	-	-	-	-	-
Au1	$6c$	-0.84	**-0.47**	**-0.55**	-	-0.81	**-0.78**	-	**-0.70**	-0.72	-	**-0.70**	-
Au1′	$6c$	-	-	-	-	-0.57	-	-	-	-	-	-	-
Ge1	$16i$	-0.17	**-0.08**	**-0.12**	-0.13	-0.21	**-0.21**	-0.23	**-0.09**	**-0.29**	-0.29	**-0.17**	**-0.17**
Ge2	$24k$	-0.12	+0.01	-0.12	-0.27	**-0.18**	**-0.19**	**-0.35**	**+0.22**	-0.16	-0.24	-0.00	-
Ge3	$24k$	-	**-0.01**	**+0.04**	+0.04	**-0.45**	-0.40	**-0.43**	**-0.02**	-0.14	-0.33	**-0.22**	-
Ge4	$24k$	-	**-0.01**	**+0.04**	-0.02	**-0.22**	**-0.26**	-0.43	**-0.04**	**-0.15**	**-0.12**	-0.11	-
Ge5	$24k$	-	**+0.07**	-0.19	-0.24	-0.02	-0.21	-0.20	+0.08	-0.30	**-0.30**	**-0.16**	-
Ge6	$16i$	-	-	-	-	-	-	-	**-0.08**	-0.15	-0.22	-	**-0.24**

TABLE 4.6: Bader charge analysis for surface atoms of the models (see Fig. 4.20) considered in the study. The calculations are performed using DFT-D3 VDW scheme.

4.4.8 Density of States

The characteristics of the electronic structure of the BaAuGe(110) surface are investigated using all surface models. In order to compare the surface electronic structure of BaAuGe(110) with the bulk one, we recall its electronic bulk properties. The Ba- sd states (small intensity) contribute mainly in the energy range [-7.5 : 0.15 eV] and overlap with Au-sd states in this region except in range [-6.3 : -4.4 eV]. There is also overlapping between Ba-s (respectively Ba-d) states and Ge-sp states in the valence (respectively in the conduction) region of DOS. It is in complete accordance with a charge transfer from Ba atoms. The number of states at Fermi energy [n(Ef)] is [n(E_f)] is 13.46 states/(eV-cell) and the reported value is around 10 states/(eV-cell) (Ref. [18]). This difference can be attributed to a different calculation method (LDA with TB-LMTO-ASA code).

Surface electronic structure is crucial when considering possible applications based on the Ba-Au-Ge surface. The surface electronic structures for the three stable models are represented in Fig. 4.21. They present several similarities with the bulk one. For example, the gap (above E_f) occurring at 0.15 eV above the Fermi energy in the bulk, is still present at the surface. Its width is reduced compared to the one in the bulk (270 meV), by 90 meV for the P^{Ba}_{Au} (180 meV) and 190 meV P^{Ba} (80 meV). Also, the main contribution of Ba-states is present above this gap in both bulk and surface. The gap is shifted towards lower energies (160 meV) in the series $P^{Ba} \xrightarrow{+2Au} P^{Ba}_{Au}$, while the d-states (180 meV) are shifted towards higher energies. Interestingly, a thin (7 meV) gap appears at the Fermi level for P^{Ba}_{noAu}. These calculations highlight that it is possible to tune the electronic properties of this surface by controlling the amount of Au surface atoms, i.e. by controlling the chemical potential of Au.
The DOS calculations of the remaining models have been summarized in Tab. 4.7. It is also worth noticing that above above E_f Ba-d states contribution is comparable to Ge-sp contribution (like in the bulk) only in case of the three stable models. It is indicative of the charge balance in these models. While for the other models the conspicuous presence of Ge-p states above E_f indicates unsaturated dangling bonds (see Figs. 4.22, 4.23 and 4.24).

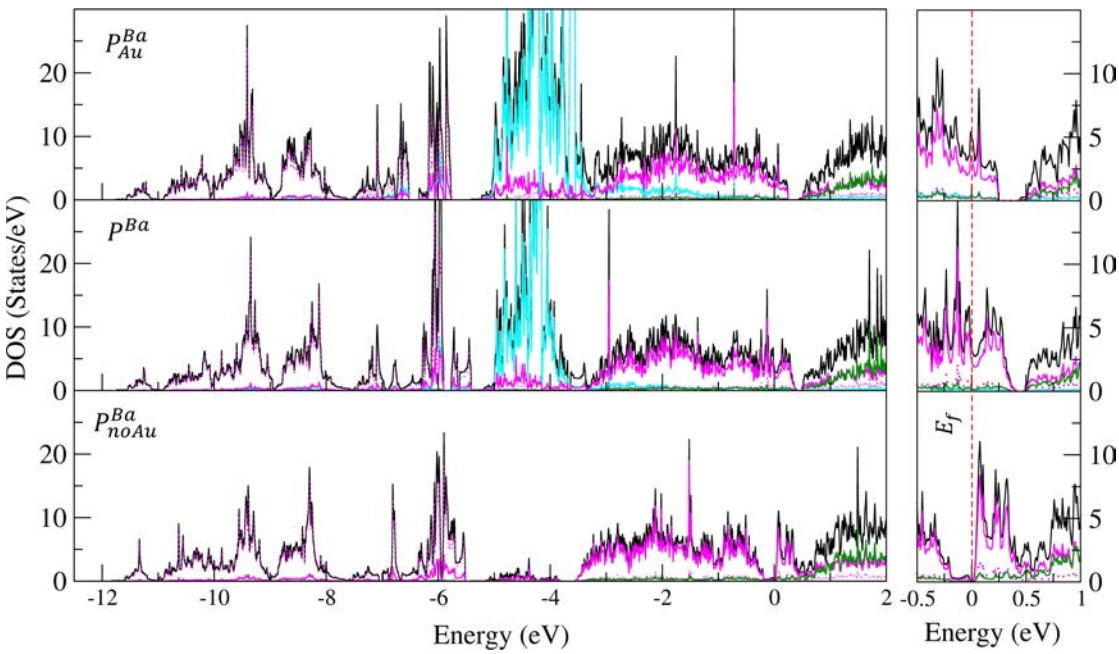

FIGURE 4.21: The projected density of states (PDOS) of series of P^{Ba} models (with a variation in the Au content) showing the surface layer contribution. The Au $5d$, Ba $5d$, Ge $4p$ and Ge $4s$ states depicted cyan, green, magenta and magenta (dotted lines), respectively.

	$n(E_f)$	Δd-band	Gap location	Width of the gap
	States/eV	eV	eV	meV
Bulk	13.46	0	0.15	270
P^{Ba}_{Au}	5.11	0.64	0.25	180
P^{Ba}	3.03	0.46	0.41	80
P^{Ba}_{noAu}	0	-	E_f	7
P	3.14	0.55	0.11	surface states
P^{noBa}	4.20	0.78	-	-
P_{noAu}	4.08	-	0.30	110
C^{Ba}	3.78	0.15	-	-
C^{noBa}	3.65	0.29	-	-
C^{Ba}_{noAu}	2.38	-	-	-
p	4.36	0.31	0.40	60
F	1.55	-	-	-
$F^{Ba}_{(100)surface}$	4.59	0.48	0.33	120

TABLE 4.7: The features of DOS are summarized for the considered models in the study. The values related to bulk and the most stable model of $Ba_8Au_6Ge_{40}$(100) surface are provided. The d-band center shift (Δd-band) is calculated w.r.t. bulk.

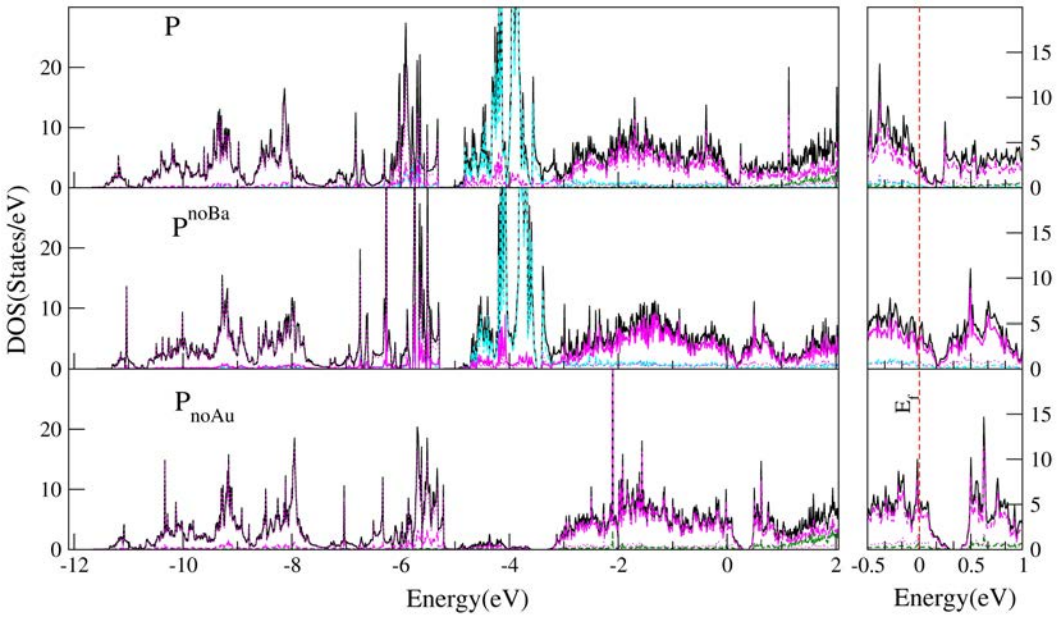

FIGURE 4.22: The projected density of states (PDOS) of P-type models (with 2 surface Ba atoms) showing the surface layer contribution. The Au $5d$, Ba $5d$, Ge $4p$ and Ge $4s$ states depicted cyan, green, magenta and magenta (dotted lines), respectively.

4.4.9 Work function

The work function values calculated for all considered surface models agree with the Bader charge analysis performed on these models (see Tab. 4.8).

The nature of the charge transfers generally affects the work function of the surface [168]. The latter are calculated to be rather low, i.e. 3.75 eV (3.83 eV), 3.55 eV (3.58 eV) and 3.18 eV (3.75 eV) within PBE

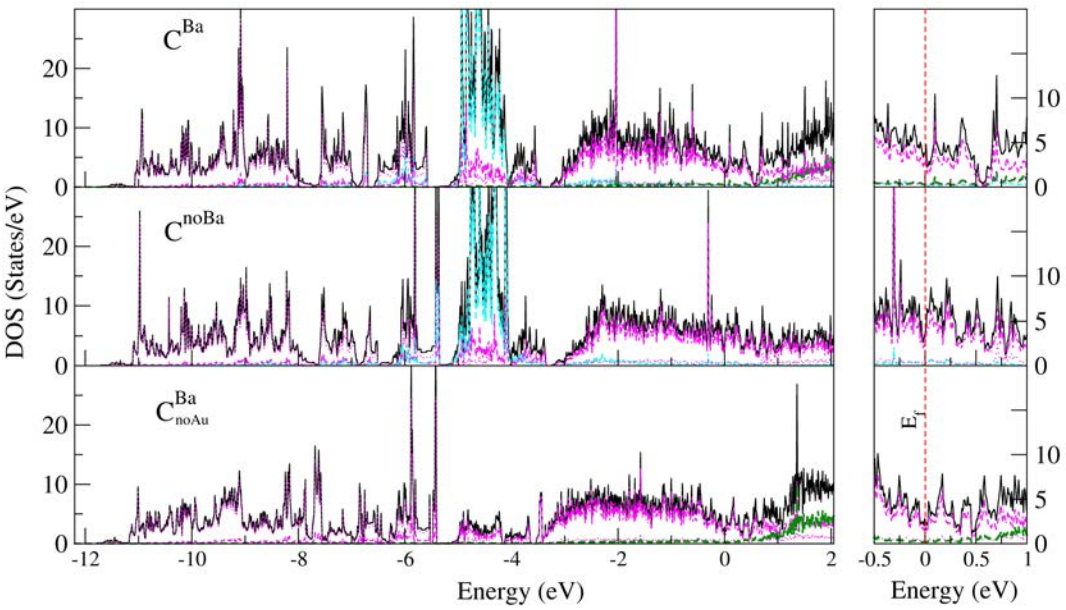

FIGURE 4.23: Surface contribution of DOS for the C-type models. The Au $5d$, Ba $5d$, Ge $4p$ and Ge $4s$ states depicted cyan, green, magenta and magenta (dotted lines), respectively.

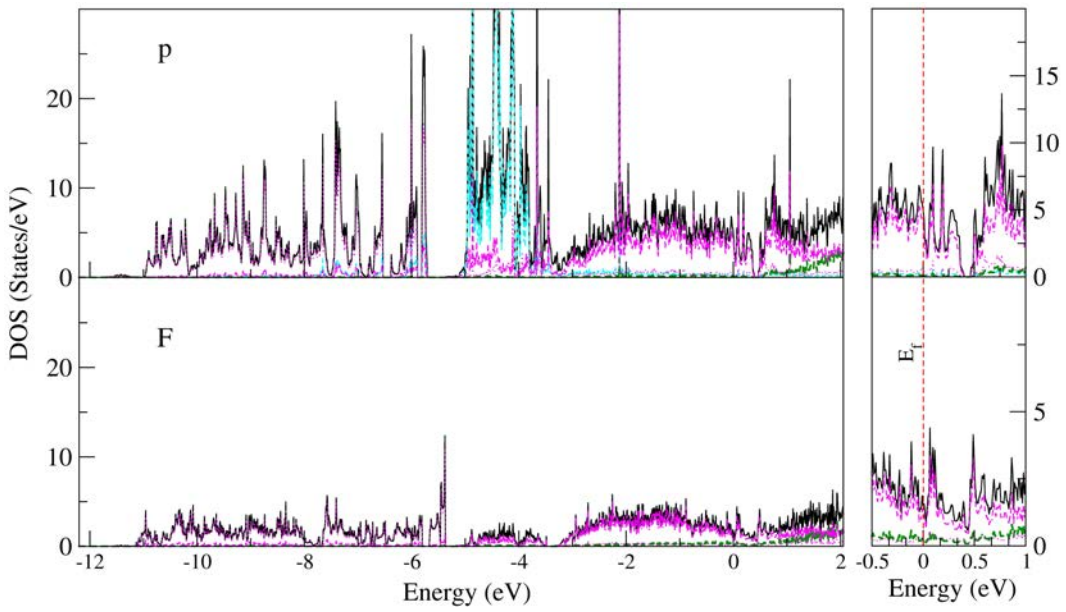

FIGURE 4.24: Density of states (PDOS) of non-cage preserving models (a) p and (b) F showing the surface contribution. The Au $5d$, Ba $5d$, Ge $4p$ are plotted in cyan, green and magenta, respectively.

(and DFT-D3) approaches for the P^{Ba}_{Au}, P^{Ba} and P^{Ba}_{noAu}, respectively. Such low values are induced by the presence of surface Ba atoms, as highlighted by Tab. 4.9. This is in agreement with the electropositive character of the Ba atoms. The variation of the work function is much smaller when Ba atoms are not the topmost atoms, in agreement with the smaller value for the surface dipole. A positive variation of the work function is calculated with Au adatoms, in agreement with their electronegative character. Again, the value is influenced by the z-position of the Au atoms, the variation of the work function almost vanishing when the Au atoms are the ones of the rigid Ba-Au-Ge network. The value for the model observed experimentally (P^{Ba}) is lower than Ge(100)-(2x1) (4.67 eV) [169] which can be advantageous in molecular electronic applications.

Model	PBE	DFT-D3	Model	PBE	DFT-D3
P^{noBa}	4.51	4.60	C^{noBa}	4.42	4.47
P	4.21	4.29	C^{Ba}	3.13	3.14
P_{noAu}	4.27	4.29	C^{Ba}_{noAu}	2.81	2.81
P^{Ba}_{Au}	3.75	3.83	p	3.84	3.88
P^{Ba}	3.55	3.58	F	3.61	3.68
P^{Ba}_{noAu}	3.18	3.16	$F^{Ba}_{(100)surface}$	3.32	-

TABLE 4.8: Work function of surface models considered in the study.

		$\Delta\Phi$ (eV)	
		PBE	DFT-D3
Ba	$C^{noBa} \xrightarrow{+4\,Ba} C^{Ba}$	-1.29	-1.33
	$P^{noBa} \xrightarrow{+2\,Ba} P$	-0.31	-0.30
	$P \xrightarrow{+2\,Ba} P^{Ba}$	-0.66	-0.71
	$P^{noBa} \xrightarrow{+4\,Ba} P^{Ba}$	-0.96	-1.02
	$P_{noAu} \xrightarrow{+2\,Ba} P^{Ba}_{noAu}$	-1.09	-1.13
	$F^{noBa}_{(100)surface} \xrightarrow{+3\,Ba} F^{Ba}_{(100)surface}$	-1.24	-
Au	$C^{Ba}_{noAu} \xrightarrow{+2\,Au} C^{Ba}$	+0.32	+0.33
	$P^{Ba}_{noAu} \xrightarrow{+2\,Au} P^{Ba}_{Au}$	+0.57	+0.67
	$P^{Ba}_{noAu} \xrightarrow{+2\,Au} P^{Ba}$	+0.37	+0.42
	$P_{noAu} \xrightarrow{+2\,Au} P$	-0.06	0

TABLE 4.9: Change of the work function induced by the presence of adatoms

4.5 Comparison between the BaAuGe(110) and BaAuGe(100) surfaces

For the BaAuGe(110) model, the combination of the thermodynamic approach and the simulated STM calculations identify the P^{Ba} model as the one in better agreement with the experimental data. For BaAuGe(100), the same approach leads to the F^{Ba} model. The comparison will be done on several items.

To start with the energetics, the F^{Ba} is more stable in the Au-rich limit while P^{Ba} model is more stable in the region characterized by $\Delta\mu_{Au}$ in [-0.5 : -0.95 eV] (Tab. 4.1). The surface relaxations of BaAuGe(100) and BaAuGe(110) are different, as well as the type of protruding cages leading to contrasted surface corrugations (the (110) surface is highly corrugated while the (100) surface is rather flat (Tab. 4.3). When looking at STM image simulations, a bias dependence is observed for both surface orientations. In the case of BaAuGe(110), for negative bias, the pattern obtained is more discrete (like arrangement of bright dots) while for positive bias it is made of a continuous bright wavy motif.

For BaAuGe(100), the pattern for negative bias is oblong-shaped lobes forming a square while for positive bias, it corresponds to bright spots forming square lattice.

A combination of ELF and Bader analysis for the two surfaces highlights the role of surface Ba atoms in maintaining the charge balance. The net charge for the (110) surface modeled by P^{Ba} is similar to the bulk, while for the (100) surface the charge gain is more than the bulk (by 0.6 e). The work function value of the (110) surface is 3.55 eV while for the (100) surface, it is slightly lower (3.32 eV). Generally for elemental metals, the surface energy increases and the work function decreases as the surface becomes more open [170], trend also followed for the Ba-Au-Ge clathrate surfaces. Here, the BaAuGe(100) surface is more open (surface corrugation, Δ_x^r = 0.03 Å) compared to the BaAuGe(110) surface (Δ_x^r = 2.58 Å). While the two low index surfaces present different protruding nano-cage structures at the surface, their surface electronic properties are similar. Indeed, both of them are metallic and present rather low work functions.

4.6 Conclusion

The (110) surface structure of the $Ba_8Au_{5.25}Ge_{40.75}$ compound was investigated by a combination of experimental and theoretical approaches. Theoretical surface energy calculations selected three possible surface models, depending on the Au chemical potential. The comparison of the experimental and simulated STM images points towards the P^{Ba} model, obtained by cleaving the ideal $Ba_8Au_6Ge_{40}$ crystal at $x = 0.25^-$, thus preserving the cluster substructure at the surface. First principles calculations show that such surface model is stabilized by electron charge transfers from protruding Ba to surface Ge and Au atoms, saturating the Ge dangling bonds. The cages protruding at the (110) surface are the dodecahedra cages, inducing a surface nanostructuration different from the one obtained at the (100) surface, built with topmost tetrakaidecahedra cages. The surface electronic structure indicates a surface with a metallic character and a low work function for the experimentally observed surface model, which can be interesting as electron emitters for vacuum electronic devices. Further control of the surface electronic properties may be achieved by tuning the Au chemical potential.

Chapter 5

Wetting properties: from simple metals to Al-based complex intermetallic surfaces

5.1 Introduction

Interfaces of materials play a vital role in technological applications. As a result, many studies on metal-metal interfaces, as well as for metal-ceramic, and other metal-nonmetal systems have been performed. While these studies have addressed many issues, such as interfacial structure, chemical bonding, and interfacial reactions, there has been a limited number of studies devoted to the intrinsic wetting properties.

Also applications of the fundamental knowledge acquired from these studies are scarcely translated to the complex surfaces. This constitutes the primary motivation of our study using both experimental and DFT approaches. We have attempted to perform in situ wetting experiments on CMA surfaces using a simple metal as a probe. Furthermore, we have tested various models using DFT to calculate interfacial energies. The understanding of the influence of the surface structure on the wetting properties of simple metals to CMAs is developed using theoretical calculations.

In this chapter first we report the wetting experiments performed under UHV. This is followed by the theoretical approach using the DFT calculations. Then, the implementation of this approach on Pb/Al(111) is presented. Section 5.3.5 shows the results obtained for the Pb/$Al_{13}Co_4$(100) interface. A comparison of Pb/Al(111) and Pb/$Al_{13}Co_4$(100) is done to understand the role of the surface complexity on the wetting behavior. At the end, a discussion combining the experimental and theoretical studies is carried out.

5.2 Contact angle measurements under UHV

5.2.1 Why Pb is used as a metal probe?

Primarily, Pb is one of the few metals which possesses a relatively low vapor pressure at the melting point (T_m). Since the experimental process used here needs melting the metal under UHV, this property of Pb is important as it leads to the minimization of material loss by vaporization. Secondly, Pb is chemically non-reactive which minimizes the risk of surface contamination for other experiments. Pb has a *fcc* structure along with the experimental advantages which makes it interesting for the modeling of the interface in some systems [171]. Pb and Al are also immiscible which limits the surface alloy formation with Al-rich or pure surfaces.

5.2.2 Sample preparation

The sample surface was cleaned by a few cycles of Ar-ion sputtering and annealing at a temperature dependent on the compound surface. The clean and flat surfaces were used for Pb deposition. Then, Pb was dosed for a few minutes to form a thick uniform layer on the substrate surface. The parameters of Pb dosing are provided in section 2.1.6.1. Upon ramping the temperature up till T_m of Pb, this led to the fragmentation of Pb film to form spherical droplets of various sizes. The temperature was then decreased gradually below the melting point of Pb. In the case of dewetting of Pb on the 5-fold i-Al-Pd-Mn substrate, a different recipe was used. The process could be summarized using the illustration in Fig. 5.1

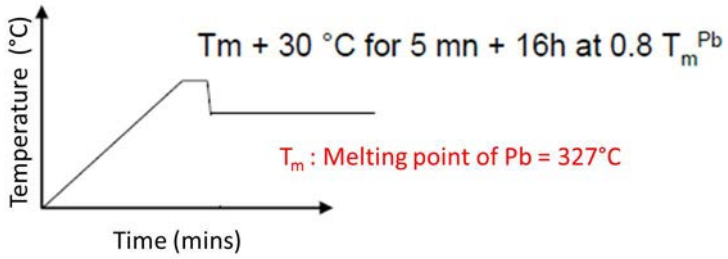

FIGURE 5.1: Dewetting scheme used for the quasicrystalline surface.

5.2.3 Measurements of contact angle

After successful dewetting, the obtained Pb droplets have been investigated using the SEM technique at room temperature. *In situ* SEM imaging system was used to obtain high resolution micrographs for contact angle measurements.

In general, the equilibrium shape of a droplet is determined by a balance of the surface tension and the gravity forces. However, the average size of the droplets in the present experiment is of the order of 3 µm. Hence, the gravity effects at this size are negligible in comparison with surface tension forces. The shape of Pb droplets at room temperature has been observed to be typically spherical, with small flat facets in certain regions.

The presence of faceted regions is due to the small anisotropy of the Pb surface energy. For contact angle measurements involving curve fitting, care is taken to avoid points very close to any crystal facet, otherwise significant errors may result.

5.2.4 Determination of contact angles

For contact angle determination, SEM micrographs were taken with samples tilted by 60° to 70°. Since a sphere projects as a circle, the radius of curvature, r, of the spherical portion of the surface can be obtained at any tilt angle.

Images were analyzed by means of standard ImageJ software, so as to obtain the outline of a frozen droplet, and the contact area diameter. The circular-curve fitting was performed to obtain the value of the contact angle through simple geometry using the droplet radius and the contact diameter.

Here, the images used were those where the presence of facets along the drop boundaries, and in particular near the contact line of the droplet on the surface, was avoided. Contact angle hysteresis is prevented by preparing flat surfaces under UHV.

Our approach to measure contact angles
In the vicinity of the triple line, the distance between interfaces becomes very small and the line tension affects the wetting angle measurements for micro- or nanometer sized droplets. It is also reported in Ref. [33] that the interactions across the triple (or contact) line may cause local distortions of the liquid surface.

In order to avoid any errors due to local distortions or errors subjective to points chosen for curve fitting, we took the average contact angle (θ_{avg}). This ensures the homogenization of our measurement approach. Here, the wetting angle values are defined as the average of the apparent angle values (from simple angle tool) and the fitted angle values (from curve-fitting). The pictorial illustration of the three angles measured using our practical approach is shown in Fig. 5.2.

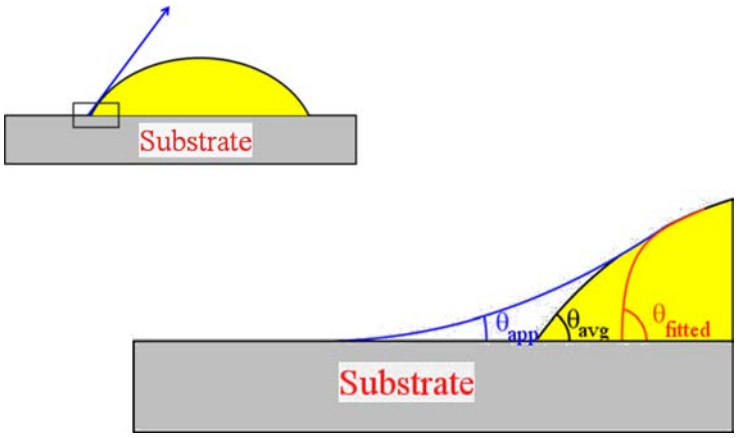

FIGURE 5.2: Schematic for contact angle measurements [33].

5.2.4.1 Influence of the droplet size

The Pb droplets formed on the single crystalline substrates after dewetting are typically of size 1-3 μm. It would be interesting to investigate if there is an influence of droplet sizes on the contact/wetting angles. In order to so, we performed a systematic analysis on two surfaces: $Al_{13}Co_4$(010) and Al_5Co_2(001) where micro Pb droplets have been formed. In Fig. 5.3 multiple "frozen-in" droplets of Pb metal on two Al-based CMAs are shown. The two SEM graphs shown in Fig. 5.3 were obtained for the sample stage tilted by 70°. For initial wetting analysis, we have taken 5 to 8 representative droplets on each surface with varying droplet sizes. The chosen droplets for measurements are shown with numbering in red color. The above mentioned simple/circular fittings have been used to obtain the apparent and fitted angles. The values are reported in Tabs. 5.1 and 5.2.

The comparison of simple angle tool measurements with circular fitting values gives a variation range of 5-15° for the two surfaces. We believe that the observed angle is the average value obtained from the two modes of measurement. The resulting average values present a standard deviation of 3-4° depending on the surface. The graph illustrated in Fig. 5.4 summarizes the contact angle versus the droplet size for the two surfaces under consideration.

The average contact angle values as a function of the droplet size display no or little noticeable dependence. It can be confirmed as any variation falls within the standard deviation of the measurement for both surfaces. The final contact angle value of Pb/$Al_{13}Co_4$(010) droplets is found to be less than Pb/Al_5Co_2(001). The difference can come from distinct surface structures and orientation as well. In the present scenario, it is possible to calculate the interfacial energy (γ_{int}) as well as the interfacial

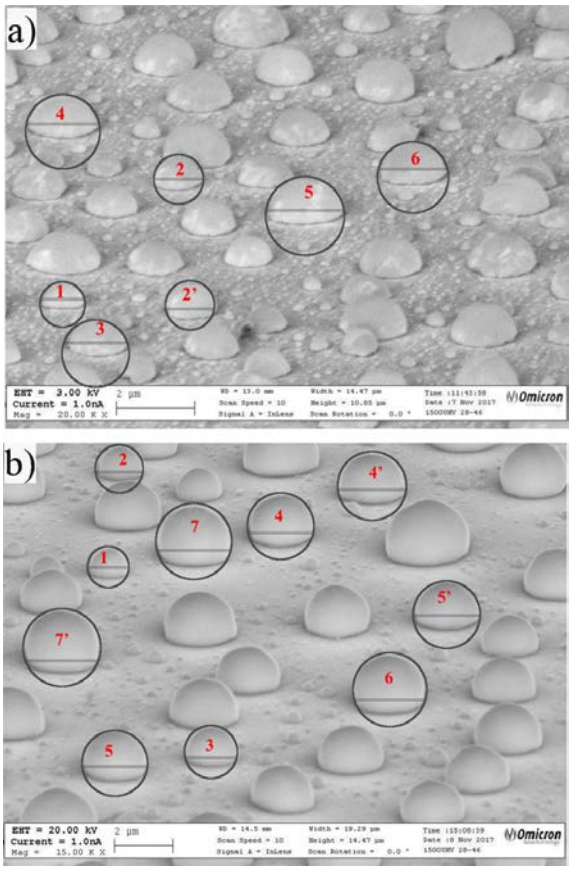

FIGURE 5.3: SEM micrographs showing Pb droplets on (a) $Al_{13}Co_4(010)$ and (b) $Al_5Co_2(001)$. Some droplets are curve-fitted (black circles) for contact angle measurements. The red labels correspond to the droplet sizes in the respective tables 5.1 and 5.2.

	Droplet size μm	Contact angle, θ degrees		
		θ_{fitted}	θ_{app}	θ_{avg}
1	1.06	78.8	71.7	75.25
2	1.32	77.5	72.5	75.02
3	1.44	77.6	72.2	74.9
4	1.88	85.6	76.6	81.1
5	1.94	86.7	75.4	81.05
6	2	86.5	77.8	82.15
		Avg $\pm$ SD		78.24 $\pm$ 3.52

TABLE 5.1: Contact angle measurement for interface of Pb/$Al_{13}Co_4(010)$ for a tilt value equal to 70°.

work of adhesion (W_{ad}) if the surface energy of the substrates (γ_{surf}) is known. The surface energy determines the equilibrium shape and plays an important role in wetting. The experimental evaluation of the surface energy is difficult.

In Ref. [84] the theoretical surface energy value for the $Al_5Co_2(001)$ surface was reported. It was also shown that the structure of $Al_5Co_2(001)$ surface is influenced by the annealing temperature and the chemical potential. Here, the surface was prepared at an annealing temperature value of 978 K before

	Droplet size μm	Contact angle, θ degrees		
		θ_{fitted}	θ_{app}	θ_{avg}
1	1.36	98.6	85.4	92
2	1.62	101.3	86.3	93.8
3	1.78	101.8	85.9	93.85
4	2.04	102.8	86.7	94.75
5	2.29	103.3	88.5	95.56
6	2.38	108.9	89.8	99.35
7	2.41	109.1	89.6	99.5
		Avg ± SD		95.54 ± 2.86

TABLE 5.2: Contact angle measurement for the interface of Pb/Al_5Co_2(001) for a tilt value equal to 70°.

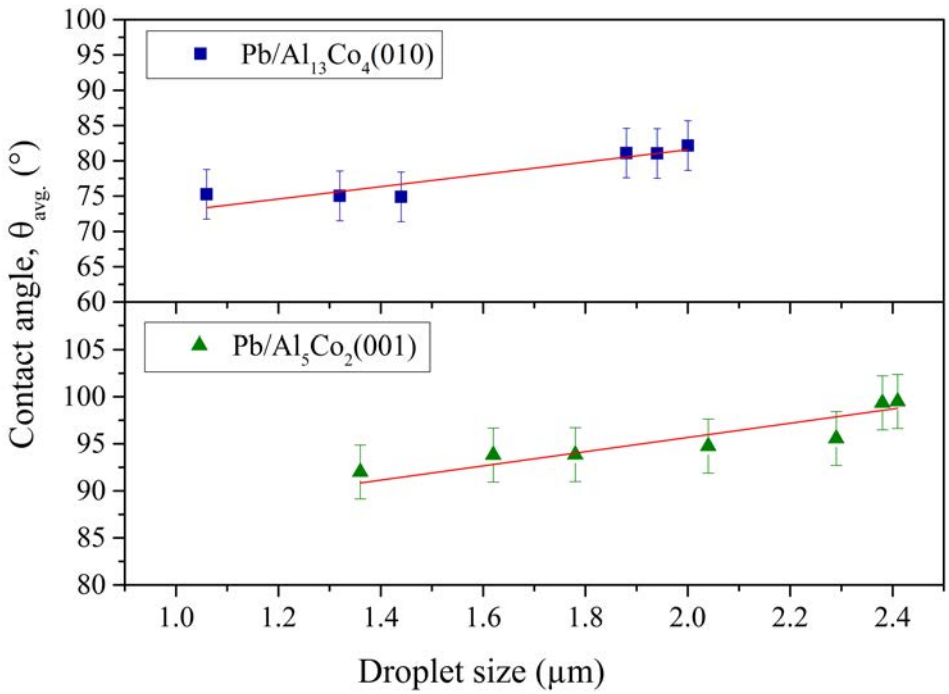

FIGURE 5.4: Contact angle, θ_{avg}, of Pb droplets on single crystals: $Al_{13}Co_4$(010) and Al_5Co_2(001) as a function of their droplet size. The red line is a linear fit to the curve.

dosing. According to Ref. [84], and if $\mu_{Al} = \mu_{Al}^{bulk}$ then the value of $\gamma_{Al_5Co_2(001)}$ is equal to 1.3 J/m^2. In the following we use the latter value to evaluate the interfacial energy and the work of adhesion of the Al_5Co_2(001) surface.

For metal-on-metal systems, W_{ad} value has been used as a measure of interfacial strength. W_{ad} is firmly linked to the wetting behavior and is defined as:

$$W_{ad} = \gamma_m + \gamma_{surf} - \gamma_{int} \tag{5.1}$$

where γ_m is the surface energy of "frozen-in" metal droplets. Equation 5.1 is the Young-Dupré equation and can be rewritten as

$$W_{ad} = (1 + cos\theta)\gamma_m \tag{5.2}$$

The above modification is obtained using Young's equation and in the present case can be expressed as:

$$cos\theta = \frac{\gamma_{surf} - \gamma_{int}}{\gamma_m} \tag{5.3}$$

We obtain γ_{int} equal to 1.36 J/m^2 (or 0.08487 eV/Å^2) for the Pb/Al_5Co_2(001) interface using the values of γ_{Pb} (0.6 J/m^2 [172]) and γ_{surf} (1.3 J/m^2) in the Equation 5.3 along with the experimentally obtained contact angle (θ = 95.54°). Also, its W_{ad} value is deduced to be equal to 0.54 J/m^2 (or 0.0338 eV/Å^2) using Equation 5.1.

The surface energy value of $Al_{13}Co_4$(010) is still unknown experimentally as well as theoretically. Although, the W_{ad} value for Pb/$Al_{13}Co_4$(010) is calculated to be 0.72 J/m^2 (or 0.0451 eV/Å^2) using Equation 5.2 with γ_{Pb} = 0.6 J/m^2 [172] and θ = 78.24° values.

5.2.4.2 Influence of tilt

We also performed contact angle measurements on the same surface region of the two samples under consideration with the sample stage at 60°. The simple and circular fitting values for these measurements are provided in Appendix C (see Tabs. C.1 and C.2). In Fig. 5.5, the contact angle values (θ_{avg}) as a function of the droplet size are shown simultaneously for both 70° and 60° tilt for the interfaces: Pb/$Al_{13}Co_4$(010) and Pb/Al_5Co_2(001), respectively. Insignificant changes in θ_{avg} values are observed for droplets with similar sizes for different tilt values. Even with the variation of the droplet size, the measured values vary within the standard deviation limits represented by error bars.

5.2.4.3 Summary of contact angle measurements

Following the approach explained above, we have carried out the wetting analysis on other substrates. Fig. 5.6 shows the variation of θ_{avg} with respect to the size of Pb nano-droplets on the quasicrystalline surface (i-Al-Pd-Mn). The size of the Pb droplets on this surface is quite small compared to the one of the Al-based CMAs reported above. However, the measured contact angle value is similar to the one obtained for the $Al_{13}Co_4$(010) surface.

For other samples we just report their final contact angle values measured on Pb droplets in Tab. 5.3. The values of bulk-DOS at the Fermi level for the considered substrates are also tabulated. SEM micrographs of the substrates considered in the present study are shown in Fig 5.7. Those presented in Fig 5.7 (top panel) are obtained *in situ* while the other values (bottom panel) are obtained *ex situ*.

The correlation between the wetting angles of Pb droplets on different substrates and the intrinsic bulk property (such as the DOS at E_f) of the substrates is shown in Fig. 5.8. From this graph, we are not able to capture a conclusive trend of the wetting behavior depending on the bulk-DOS of the substrate. Although, higher contact angles and lower values of DOS at E_f are observed for complex

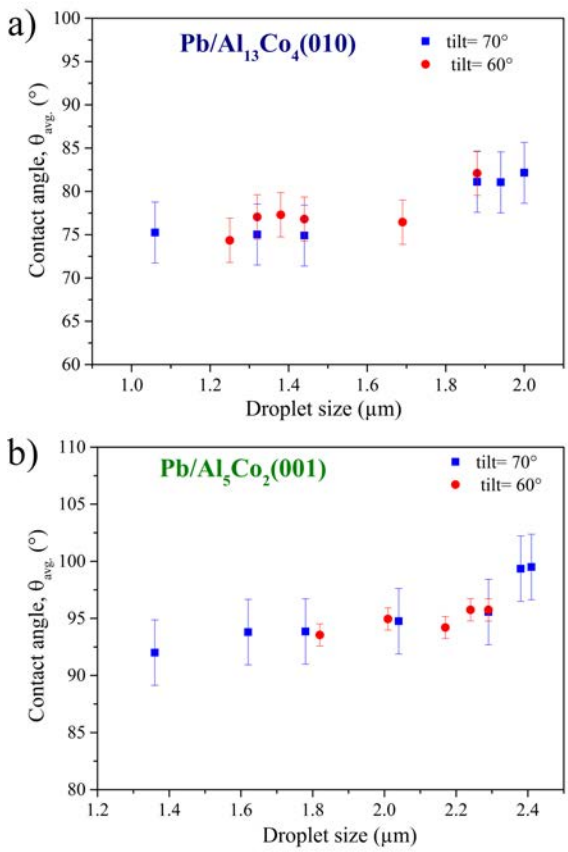

FIGURE 5.5: Contact angle, θ_{avg}, of Pb droplets on single crystal of (a) $Al_{13}Co_4(010)$ and (b) $Al_5Co_2(001)$, respectively, for different tilt values. The error bars represent the standard deviation in plotted data.

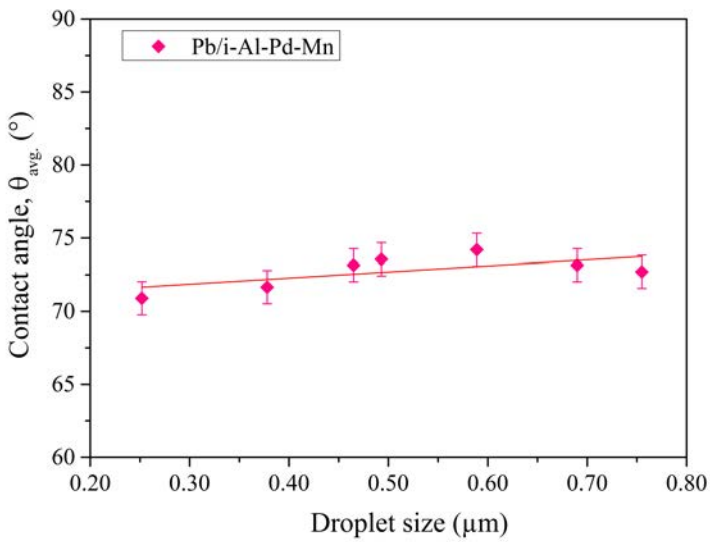

FIGURE 5.6: Contact angle, θ_{avg}, of Pb droplets on i-Al-Pd-Mn as a function of their droplet size. The red line is a linear fit to the curve.

metallic phases (including QCs) in comparison to simple metals. Also, linking the wetting angles with other physical properties may provide a correlation. One such attempt found in literature in the same direction is shown in chapter 1 (Fig. 1.5).

Label		θ degrees	$\rho^{\text{Bulk}}_{substrate}(E_f)$ states/(eV-atom)	Melting point (T_m) °C
S1	Pb/ $Al_{13}Co_4$(010)	78.24 ± 3.52	0.22	1093 [173]
S2	Pb/Al_5Co_2(001)	95.54 ± 2.86	0.12 [84]	1181 [173]
S3	Pb/i-Al-Pd-Mn (QC)	72.76 ± 1.13	0.17 [174]	870 [173]
S4	Pb/d-Al-Ni-Co (QC)	67.59 ± 0.10	0.13 [175]	1150[173]
S5	Pb/Al(111)	27.93	0.43	660
R1	Pb/Cu(111)	48 ± 1.80 [176]	1.25 [177]	1080
R2	Pb/Ni(111)	54 ± 1.00 [178]	0.95 [177]	1456
R3	Pb/Fe(111)	59 [42]	12.25 [177]	1538
R4	Pb/Co (polycrystalline film)	50 ± 6 [179]	70 [177]	1495
R5	Pb/AlCo (polycrystalline film)	42 ± 5 [179]	0.33 [180]	1671 [173]

TABLE 5.3: Contact angle values of Pb droplets on different substrates.

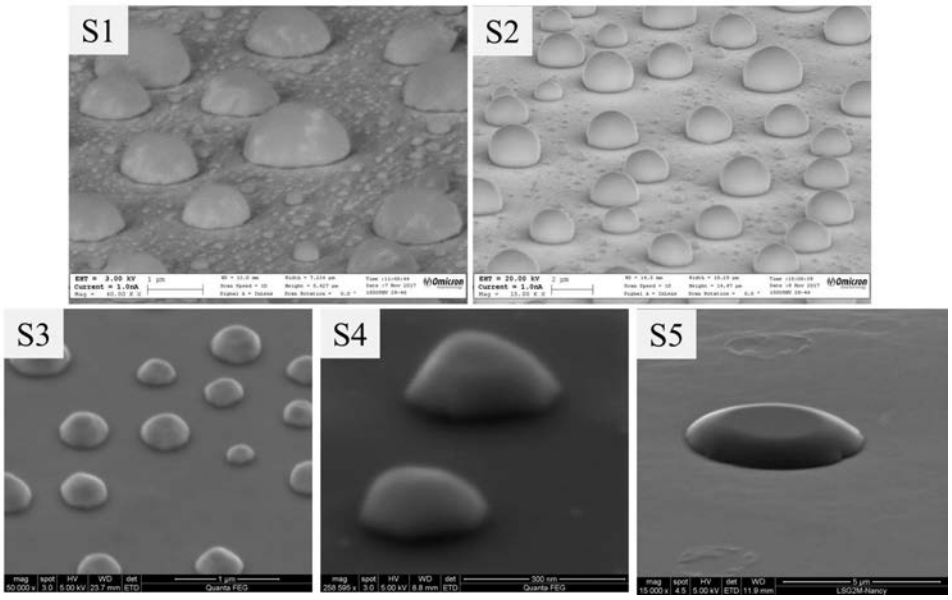

FIGURE 5.7: SEM micrographs for different interfaces with Pb as a metal probe. The labels S1,S2 and so on correspond to the distinct interfaces studied in this work and are mentioned in Tab 5.3.

In Fig. 5.9, the wetting angle of Pb droplets as a function of the melting point (T_m) value of the substrates is depicted. Some data points are obtained from the in-house experiments and others are gathered from the literature. Wetting angles between Pb droplets and single crystal of pure metals seem to follow a linear trend w.r.t. the melting point of the latter. A red dotted line is used to highlight this linear behavior (see Fig. 5.9). The wetting angle values for CMA surfaces are rather higher and appear assembled above this line. For the polycrystalline substrates, we can observe a random behavior for both simple metal (Co) and CMA (AlCo). We obtain similar values for Pb/Al(111) compared to the one plotted in Fig. 1.5 (Ref. [42]) within the error bars.

5.2.5 AES on Pb/CMAs

The surface chemistry of the Al-based CMAs between the droplets was examined by AES. No adsorbed carbon was detected but traces of oxygen and lead are present at these CMA surfaces. In

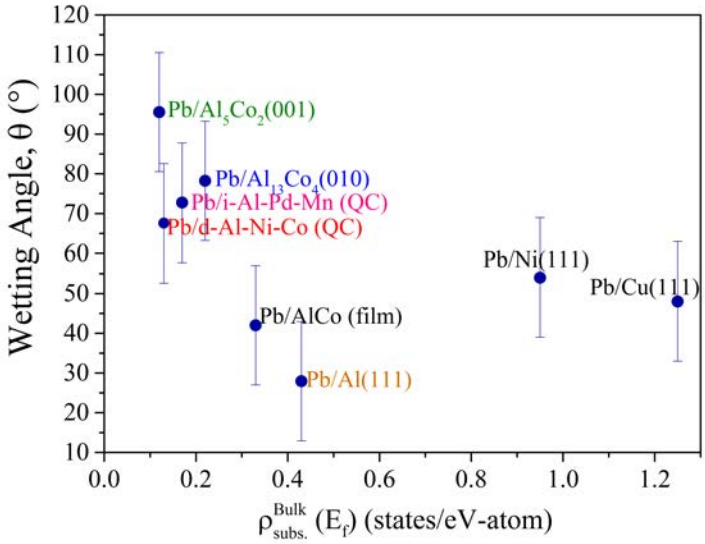

FIGURE 5.8: Contact angle, θ as a function of the bulk density of states at the Fermi level for the considered substrate.

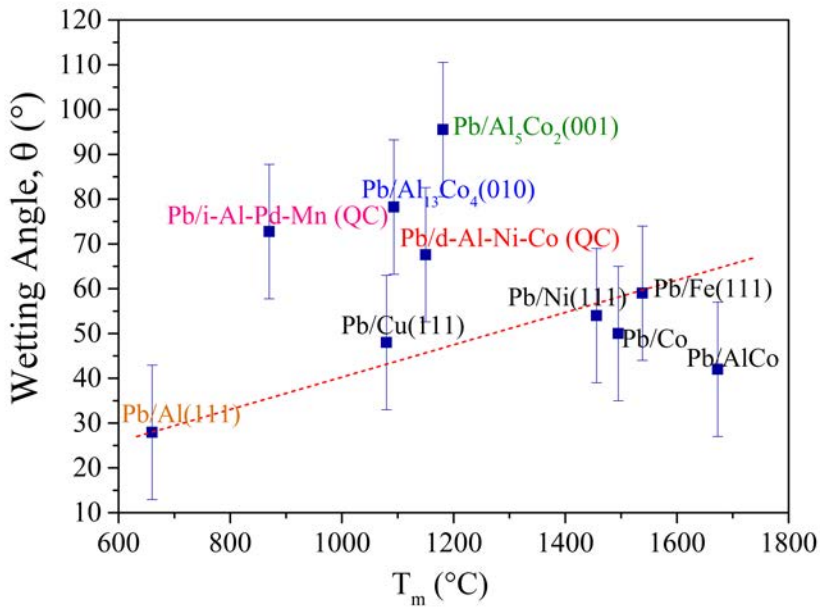

FIGURE 5.9: Contact angle, θ as a function of melting point (°C) of the considered substrate. The red dotted-line highlights the linear trend for Pb/simple metals. All in-house measurements are shown in the colored labels. The labels in black correspond to the references mentioned in Tab 5.3.

Fig. 5.10, the Auger spectra in the derivative mode taken on different regions of $Al_{13}Co_4$(010) and Al_5Co_2(001) are shown. It can be further confirmed from Auger line scans that Pb droplets have no oxygen content. Even from raster survey scan at the surface only small peaks of oxygen were detected. The Pb droplets were formed and scanned *in situ* for wetting measurements. Also, the presence of Pb monolayer in between the droplets is expected. No exposure to air in between the experiments maximizes the probability of intrinsic wetting studies.

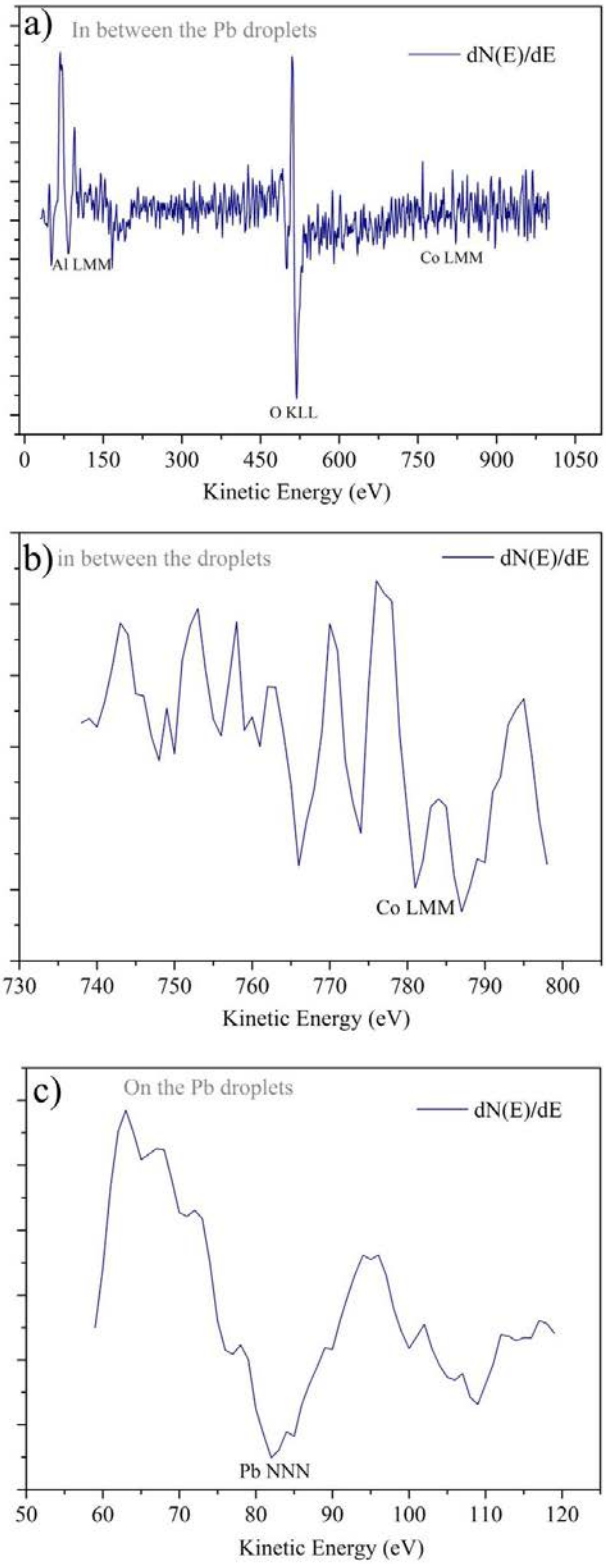

FIGURE 5.10: (a) Auger spectra in the derivative mode of the surface $Al_{13}Co_4(010)$ in between the Pb droplets obtained after dewetting. (b) The Auger peak of CoLMM on the surface of $Al_5Co_2(001)$ in between the droplets. (c) Auger line scan on the Pb droplet present on the $Al_5Co_2(001)$ surface.

5.3 Theoretical Methods

A theoretical approach was used to determine the contact angles. Two interfaces are considered: Pb/Al(111) and Pb/$Al_{13}Co_4$(100). The electronic structures of the two compounds are quite different, Al is a simple *sp* metal while the density of states of $Al_{13}Co_4$ contains a *d*-band and presents a pseudo-gap close to the Fermi energy.

In the following, the objectives are (i) to improve the theoretical determination of the Pb/Al(111) interfacial energy [181], using a structural model based on the experimental observations at the atomic scale [182] and (ii) to validate the theoretical approach used to determine the contact angle, in the two considered cases where the adsorbate-substrate interactions are expected to be rather different.

5.3.1 Interfacial energy calculations

The DFT calculations are performed using the PBE-GGA scheme as implemented in the VASP [66–69]. The electron-ion interaction is described by the PAW scheme [87, 88]. The kinetic cut-off energy of 450 eV is used for plane wave functions. The surface is modeled by periodically repeated asymmetric slabs, with a void thickness equal to 15 Å.

The role of the surface complexity on the surface wetting properties is investigated using two different systems: Pb/Al(111) and Pb/$Al_{13}Co_4$(100). For Pb/Al(111), we used an Al(111) substrate built with 9 Al bulk layers. The considered Pb adlayers are 1-layer to 4-layer thick. Two surface cells are considered: an experimentally observed moiré ($(\sqrt{31} \times \sqrt{31})\ R8.95°$) and a simple (1x1) unit cell. For the Pb/$Al_{13}Co_4$(100) system, 7-layer thick slabs are built for the substrate, while the density of the Pb adlayer varies from 0.05 at./Å^2 to 0.10 at./Å^2.

The atomic structures are relaxed using the conjugate gradient method until the forces are lower than 0.020 eV/Å . The Brillouin zone integration is performed using a 5×5×1 Monkhorst–Pack mesh [91] for Pb/Al(111) while 1×7×7 for Pb/$Al_{13}Co_4$(100).

5.3.2 Interfacial energy and contact angle

The method used to evaluate the interfacial energy and the contact angle is discussed below:

Theoretical approach:

In this approach the total energy of a slab containing an adlayer is expressed as a sum of the cohesive energies of the constituent metals and the surface and interfacial energies. The interfacial energy (γ_{int}) is given by:

$$\gamma_{int} = \frac{E^{total}_{Pb+subs} - \gamma_{Pb} \cdot A_{surf} - n_{Pb} \cdot E^{coh}_{Pb} - n_{subs} \cdot E^{coh}_{subs} - \gamma^{NR}_{subs} \cdot A_{surf}}{A_{surf}} \tag{5.4}$$

where the surface and interfacial energy labels are illustrated in Fig. 5.11(a).

Here, $E^{total}_{Pb+subs}$ is the total energy of the slab with a Pb adlayer, while E^{coh}_{Pb} and E^{coh}_{subs} are the cohesive energies (eV/at.) of Pb and the substrate, respectively. The surface energy terms are γ^{NR}_{subs} and γ_{Pb}, i.e. the non relaxed surface energy at the bottom of the slab and the Pb surface energy, respectively. Other terms such as A_{surf}, n_{Pb}, and n_{subs} denote the area of the slab, the number of Pb atoms and the number of substrate atoms in the slab.

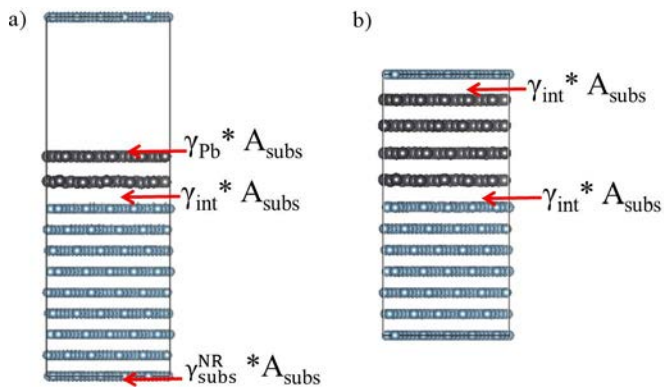

FIGURE 5.11: Various interfacial energy contributions present in a slab with vacuum (left) and without vacuum (right).

Adhesion energy and modification of surface energy due to adsorption of a single monolayer of Pb

This part consists of deriving the adhesion energy and calculating the variation of surface energy caused by Pb adsorption, making the assumption that the Pb chemical potential is the same as in bulk Pb. The adsorption of the Pb adlayers are evaluated using two perspectives:
(a) using free standing Pb layers (from 1 ML to 4 MLs) i.e.

$$E_{adhesion} = E^{total}_{Pb+subs} - E^{total}_{subs} - E^{free-standing}_{Pb} \tag{5.5}$$

(b) considering atom-wise adsorption i.e.

$$E_{ads} = E^{total}_{Pb+subs} - E^{total}_{subs} - n_{Pb} \cdot E^{coh}_{Pb} \tag{5.6}$$

In the previous equations, $E^{total}_{Pb+subs}$, $E^{free-standing}_{Pb}$ and E^{total}_{subs} are, respectively, the energies of the total system, an N-layer free standing Pb layer (N varies from 1 to 4) and the substrate surface. Exothermic processes are indicated by negative values.

Modeling lead

The theoretical approach requires the calculation of the cohesive and surface energies for lead. Different functionals and corrections have been tested (Tab.5.4), using bulk lead, a Pb(111) slab and a Pb bilayer adsorbed on Al(111).

The cohesive energy and surface energy [(111) surface] for Pb calculated within the GGA-PBE scheme (E^{coh}_{Pb} = -2.94 eV/at. & $\gamma^{calc.}_{Pb}$ = 0.0178 eV/Å^2) is in good agreement with a previous theoretical work (E^{coh}_{Pb} = -2.99 eV/at. & $\gamma^{calc.}_{Pb}$ = 0.0172 eV/Å^2) [183] and in reasonable agreement with the experimental values (E^{coh}_{Pb} = -2.03 eV/at. & $\gamma^{exp.}_{Pb}$=0.0275 eV/Å^2 [184]). No improvement is obtained using the DFT-D3 functional (E^{coh}_{Pb} = -3.67 eV/at.). The consideration of non-linear spin-orbit coupling (NL-SOC) leads to a value for the cohesive energy in better agreement with the experimental value (E^{coh}_{Pb} = -1.98 eV/at.), as already mentioned in Ref. [185]. However, no improvement is found for the surface energy ($\gamma^{calc.}_{Pb}$ = 0.0153 eV/Å^2), using the same approach.

Calculation of the contact angle

Methods	E_{ads} (eV)	$\gamma_{Pb}^{calc.}$ (eV/Å^2)	$E_{Pb}^{coh.}$ (eV)	$E_{adhesion}$
PBE-GGA	-2.22	0.0178	-2.94	-8.56
NL-SOC	-2.79	0.01535	-1.98	-8.53
DFT-D3	-3.26	0.05783	-3.17	-14.64
IDIPOL	-2.20	0.03723	-2.94	-8.54

TABLE 5.4: Impact of different functionals and dipole correction on the surface energy of Pb and the adsorption energy calculated for Pb/Al(111) system (moiré slab).

Finally, we can also derive the modification of surface energy of top of the substrate due to the presence of wetting layer of Pb in between the droplets, by defining modified surface energy as expressed below:

$$\gamma_{surf}^{mod} = \gamma_{subs} + \frac{E_{ads}}{A_{surf}} \tag{5.7}$$

This imply that the contact angle of Pb droplets on the top of the surface can be deduced from the Young's equation (YE) as:

$$cos\theta = \frac{\gamma_{surf}^{mod} - \gamma_{int}}{\gamma_m} \tag{5.8}$$

where γ_{surf}^{mod}, γ_{int} and γ_m are the modified surface energies of the substrate, the interfacial energy and the Pb surface energy, respectively.

Results obtained for the Pb/Al(111) system are gathered in Tab. 5.5. The calculated value of γ_{Pb} (our work, γ_{Pb}= 0.0178 eV/Å^2) has been considered in equation 5.4: to calculate the interfacial energies. The corresponding contact angle values calculated for varying Pb ad-layer (2 to 4 layers) thickness are also reported.

In the next section, we apply the discussed approach for the determination of the contact angle of Pb/Al(111). All calculations are done within the GGA-PBE scheme.

5.3.3 Pb/Al(111) interface

5.3.3.1 Structure of the interface

The Pb and Al crystals present a fcc structure but the lattice mismatch is rather large (22 %). Several studies were already undertaken on the Pb/Al interface. The equilibrium shapes of small solid Pb inclusions embedded in an Al matrix are size dependent. For small inclusions of a few nanometers in size, equilibrium shapes with smooth {111} facets are observed experimentally [186]. Further investigation of the Pb/Al interface based on Monte Carlo simulations using empirical potentials [181] theoretically determined the free energy ratios for the Pb/Al(100) and Pb/Al(111) interfaces. The formation of a moiré superstructure was mentioned due to the lattice mismatch. Afterwards, an experimental study of Pb/Al(111) interface for the contact angle measurements under UHV was reported [187].
In 2009, the interfacial structure of Pb/Al(111) was revisited (Ref. [182]) and a moiré pattern with rotation of 8.95° with respect to the Al lattice was predicted. This higher-order commensurate structure (HOC) was explained to be the result from the different lattice parameters of the Pb layer and

the Al(111) surface [(a_{Pb}=3.5 Å /a_{Al}=2.86 Å)=1.22]. The appearance of such superstructures is also attributed to larger lateral interaction within the Pb adlayer compared to substrate-adlayer lateral interaction. The proposed HOC structure (unit cell parameter of 15.9 Å) is shown in Fig. 5.12.

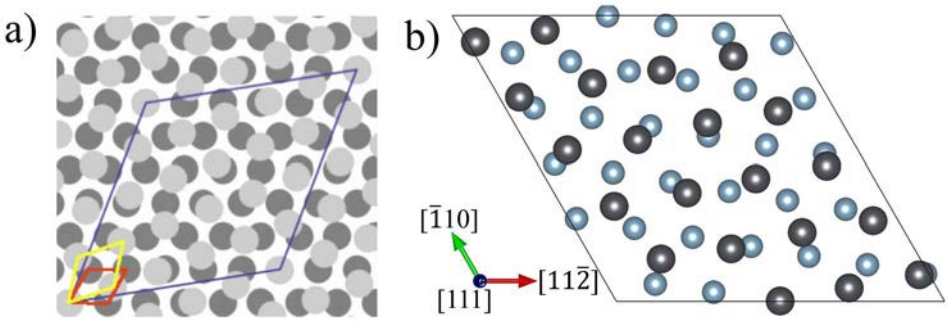

FIGURE 5.12: (a) Schematic diagram of the $\sqrt{31} \times \sqrt{31}\ R8.95°$ higher-order commensurate structure (HOC) with dark circles representing the locations of Al atoms and light circles representing the locations of Pb atoms. The Al substrate, the Pb-layer and the HOC unit cell are shown by the red (2.86 Å), yellow (3.5 Å) and blue rhombi (15.9 Å), respectively [182]. The angle between the Al and Pb primitive unit cells is 19.84°. (b) Top view of theoretical model with 1 ML of Pb built following the experimental model in (a). The shown unit cell has lattice parameter of 15.9 Å. The blue spheres represent Al atoms while gray spheres denote Pb atoms.

In the following, the Pb/Al(111) interfacial energy is determined using the theoretical approach described previously. It is also followed by the determination of contact angle using YE equation 5.8, taking into account the variation in surface energy due to Pb adsorption. Previous works based on a cube-on-cube adlayer structure for Pb/Al(111), leads to a higher interfacial energy than the experimental one (0.01356 eV/Å^2)[181, 187]. The variation in interfacial energies (from 0.028963 eV/Å^2 to 0.03763 eV/Å^2) depending on the surface orientation was also calculated in this work [181]. One first objective here is to improve the theoretical determination of the Pb/Al(111) interfacial energy, using a more realistic structural model, based on experimental observations. More generally, this model system is also used to develop an approach to determine the interfacial energy and wetting properties, utilizing Pb as a probe.

5.3.4 Interfacial energy

The Pb/Al(111) interfacial structure is described by the moiré pattern shown in Fig. 5.12. Several thickness were considered for the Pb adsorbates (one to four layers).

Theoretical approach

In Ref. [187] the γ_{int} value for Pb crystallites on the Al(111) single crystal was reported to be 217 $\pm$ 30 mJ/m^2 (0.01356 eV/Å^2). To avoid the influence of γ_{Pb} on the determination of the interfacial energy, we built a model system without any void (see Fig. 5.11(b)). The γ_{int} value, calculated using Equation 5.9:

$$\gamma_{int}^{novoid} = \frac{E_{Pb+subs}^{total} - n_{Pb} \cdot E_{Pb}^{coh} - n_{subs} \cdot E_{subs}^{coh}}{2 \cdot A_{surf}} \tag{5.9}$$

The interfacial energy is calculated to be 0.0185 eV/Å^2 which is close to the one reported in Ref. [187].

γ_{Pb} (eV/Å^2)	MODEL	No. of Pb atoms	γ_{int} (eV/Å^2)	cosθ	θ (degree)
	1 layer Pb	21	**0.01971**		
0.0178	2 layer Pb	42	**0.02206**	0.87	29
	3 layer Pb	63	**0.02343**	0.71	37
	4 layer Pb	84	**0.02295**	0.72	34
	4 layer w/O void	84	**0.01852**		
$\gamma_{surf}^{mod.}$ = 0.03763 eV/Å^2					
w/O: without					

TABLE 5.5: Interfacial energies of Pb/Al(111) (a structural model based on the moiré pattern).

Consistent results for the interfacial energy are obtained with the theoretical approach based on the calculated γ_{Pb} surface energy. Here, values for the interfacial energy are calculated to be of the order of 0.023 eV/Å^2. The experimental contact angle of Pb/Al(111) in Ref. [187] was reported to be 27.3°± 0.8°. Contact angles in reasonable agreement with the experimental value are further obtained using the γ_{Pb}^{calc} (solid phase) surface energy in the YE equation (∼ 34°).

γ_{Pb} (eV/Å^2)	MODEL	No. of Pb atoms	γ_{int} (eV/Å^2)	cosθ	θ (degree)
	1 layer Pb	1	0.19321	-	-
0.0178	2 layer Pb	2	0.37865	1.1	ND
	3 layer Pb	3	0.56422	-9.3	ND
	4 layer Pb	4	0.75304	-19.9	ND
$\gamma_{surf}^{mod.}$ = 0.39774 eV/Å^2					
ND: Not defined					

TABLE 5.6: Interfacial energies of simple (cube-on-cube) Pb/Al(111) interface.

Compared to Tab. 5.5, Tab. 5.6 takes into account a non-reconstructed cube-on-cube structure for Pb/Al(111) interface. The calculated interfacial energy values are at least one order of magnitude larger than the values reported in Tab. 5.5, which leads to out of range values of cos θ. This is due to the assumptions of a simple cube-on-cube approach.

Adhesion energy and adsorption energy calculations

Tab. 5.7 summarizes the adhesion energies and adsorption energies calculations for moiré slab using (i) the free standing Pb slab and (ii) the cohesive energy of Pb. In these calculations, up to four layers of Pb were considered. The adhesion energy values indicate the energy cost of separating the Pb film from the substrate while adsorption energies give the variation of surface energy caused by the Pb adsorption.

In comparison to Tab. 5.7, Tab. 5.8 takes into account a simple cube-on-cube structure for Pb/Al(111) interface. The calculated adsorption energies for (1x1) surface cell of Pb/Al(111) are positive indicating the enormous strain in the system on adsorption. Also, corresponding to these values we observe

Adhesion energy calculated using free standing Pb adlayers		
MODEL	$E_{adhesion}$ (eV)	
1 layer Pb	-14.39	
2 layer Pb	-8.56	
3 layer Pb	-11.15	
4 layer Pb	-9.02	
Adsorption energy using cohesive energy of Pb		
MODEL	E_{ads} (eV)	γ_{surf}^{mod} (eV/Å^2)
1 layer Pb	-2.73	0.03763
2 layer Pb	-2.22	0.03998
3 layer Pb	-1.92	0.04135
4 layer Pb	-2.02	0.04087

TABLE 5.7: Adhesion energy and adsorption energy measurements for the Pb/Al(111) (moiré slab).

high alteration of surface energy due to Pb adsorption. These values remind us the fact that simple cube on cube model (lattice mismatch = 22 %) misrepresent Pb/Al(111) interface.

Adsorption energy using cohesive energy of Pb		
MODEL	E_{ads} (eV)	γ_{surf}^{mod} (eV/Å^2)
1 layer Pb	1.146	0.21230
2 layer Pb	2.457	0.39774
3 layer Pb	3.768	0.58331
4 layer Pb	5.103	0.77213

TABLE 5.8: Adsorption energies for non-reconstructed Pb/Al(111)interface.

5.3.4.1 Electronic structure of the Pb/Al(111) moiré

STM

Fig. 5.13 illustrates the moiré patterns when considering single and bilayer of Pb in the simulated STM images. In Fig. 5.13 the green hexagon corresponds to the moiré unit cell observed in the two simulated STM images as well as in the experimental image. The simulated STM images are in agreement with experimental STM images.

Density of states

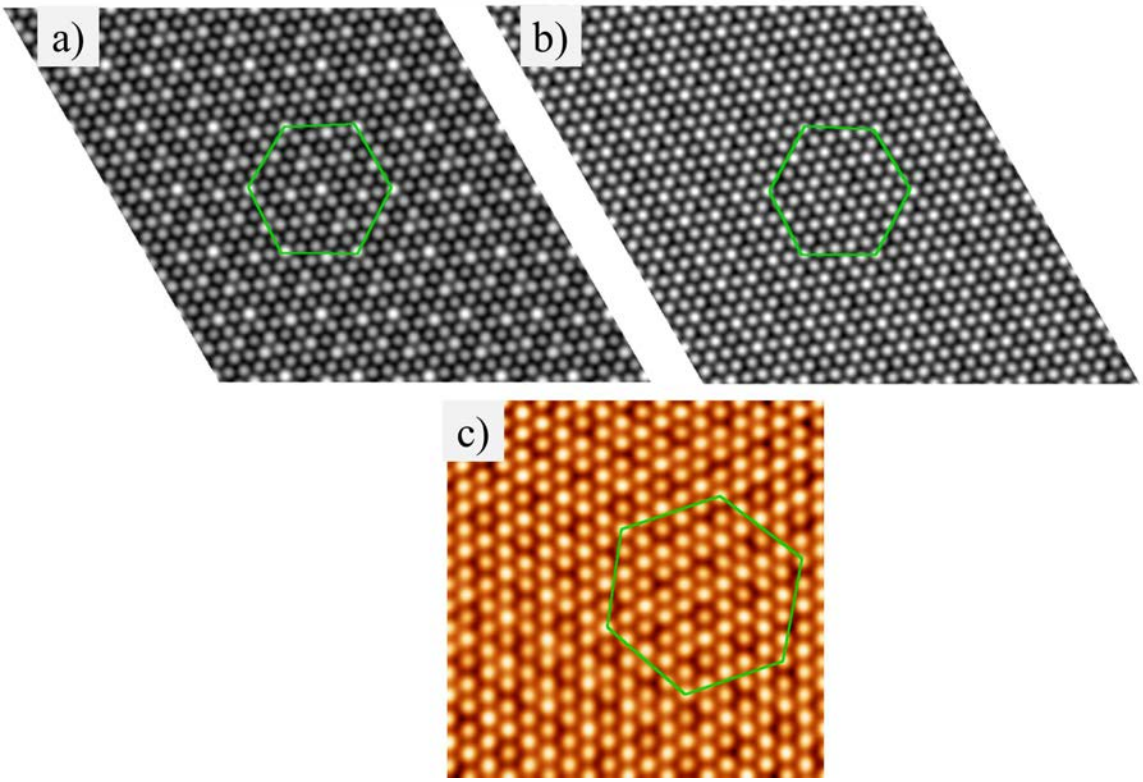

FIGURE 5.13: (a),(b) Simulated STM images of 6×6 unit cell for bias value of -0.5 V. (c) Fourier filtered STM image obtained at bias voltage of -0.5 V. The size of the STM image is 6×6 nm^2.The green hexagon corresponds to the moiré unit cell in these STM images.

Figure 5.14 presents the bulk Pb density of states (DOS). It is in good agreement with the one calculated by Krajci *et al*. [188], even if the different cell parameters used in both cases lead to small shifts in the band energies. The s and p bands are separated: the s and p bands extends from -11.5 eV to -6.7 eV and from -4.0 eV to 6.6 eV, respectively. A gap is then formed, of width 2.7 eV. This gap is not induced by the structure, since it is found even in the electronic DOS of liquid Pb [189].

The DOS of the free-standing Pb layer presents a s band characterized by a smaller width, compared to the bulk one. The value of the gap is also different.

The DOS contribution of two Pb adlayers on the Al(111) is shown in Fig. 5.15. A few states are visible in the gap, due to the interaction with Al, but the intensity is weak. However, the interaction of the Pb adlayer with the Al substrate is rather small, since the DOS of the topmost Al and adsorbate Pb layers being almost not modified compared to the elemental ones.

Bader charge analysis of the Pb/A(111) moiré

Tab. 5.9 gathers the Bader atomic charges averaged over atoms in Pb (21 at./layer) or Al (31 at./layer) layers in the Pb/Al(111) moiré system. In the Al substrate, the center layer atoms bear a charge of 3.00 e. This value corresponds to the number of valence electrons included in the Al pseudopotential. In the considered system (from 1 Pb MLs to 4 Pb MLs), the charges on Al atoms are almost not modified. The same is observed for Pb layers (the valence charge on Pb atoms is 4.00 e).

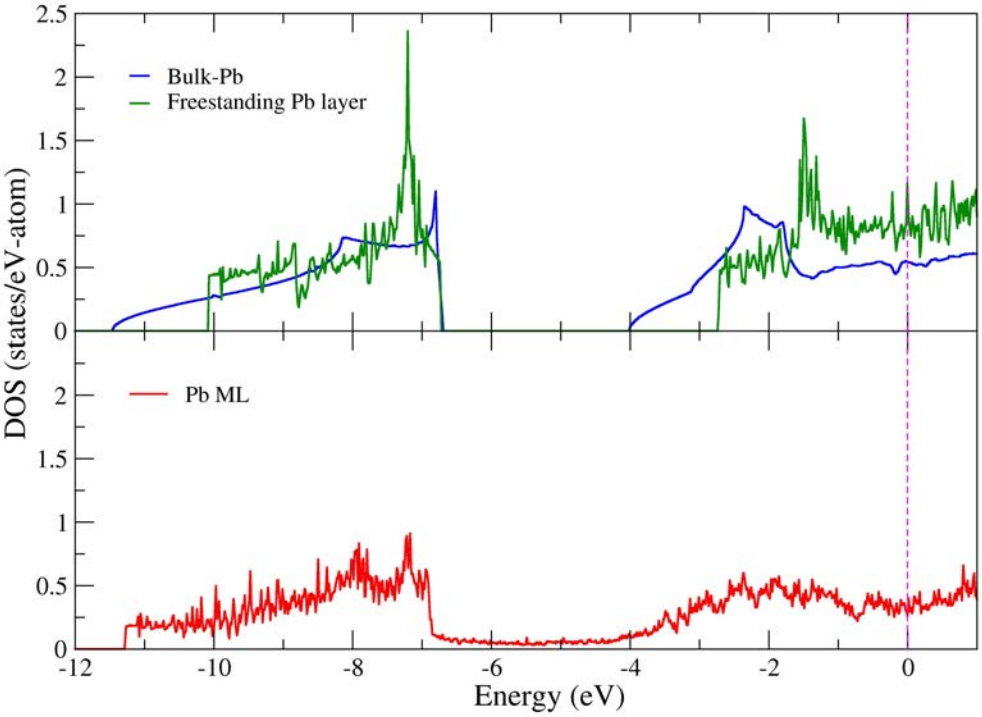

FIGURE 5.14: DOS of the bulk (blue) and free standing of Pb (green). The calculation for bulk Pb was performed using ISMEAR = -5 and 45×45×45 k-point grid while for freestanding Pb layer, the latter value is 15×15×1. The lower panel shows DOS of Pb ML adsorbed on the Al(111) surface (using ISMEAR = -5 and 15×15×1 k-point grid).

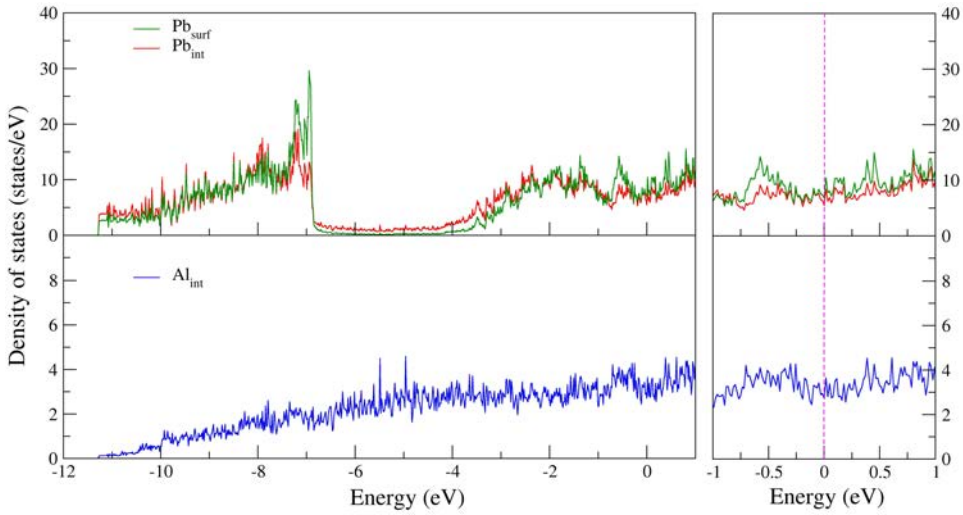

FIGURE 5.15: (Left) DOS at the interface of Pb/Al(111) (moiré slab) with two Pb adlayers. The DOS contribution of Pb atoms at the interface layer is plotted in red and for Al atoms in blue. The DOS contribution from second layer of Pb (*i.e.* Pb_{int+1}) is shown in green. (Right) Zoom of DOS around Fermi level for Pb/Al(111). The calculation was performed using ISMEAR= -5 and 15×15×1 k-point grid.

	1 ML	2 ML	3ML	4ML
Pb_{surf}	-	-	-	3.994±0.004
Pb_{int+2}	-	-	3.994±0.003	4.005±0.003
Pb_{int+1}	-	3.985±0.008	3.994±0.005	3.984±0.006
Pb_{int}	4.043±0.019	4.035±0.008	4.039±0.014	4.049±0.012
Al_{int}	2.978±0.023	2.979±0.011	2.984±0.012	2.974±0.010
Al_{int-1}	2.980±0.024	3.000±0.010	2.987±0.012	2.994±0.012
Al_{int-2}	3.005±0.012	3.004±0.008	3.004±0.006	3.008±0.007
Al_{center}	3.004±0.005	3.000±0.005	3.003±0.005	3.001±0.006

TABLE 5.9: Average Bader atomic charges computed on layers in the Pb/Al(111) moiré system with 1 ML to 4 MLs of Pb.

5.3.5 The Pb/$Al_{13}Co_4$(100) interface

Two different models for the substrate are considered (S1 and S2). They are illustrated in Fig. 5.17, supporting a Pb adlayer (Pb coverage of 0.084 at./Å^2). The two interfaces shown here are obtained after atomic relaxations and differ mainly in the substrate surface layer. The S1 model considers a dense Al-rich termination (22 Al and 2 Co atoms per surface cell), while the S2 surface (22 Al atoms) is obtained by removing all surface Co atoms. Also a recent Surface-XRD analysis suggested an occupancy equal to 0.6 for the 2 surface Co atoms lying below the mean position of plane for the $Al_{13}Co_4$(100) surface [190].

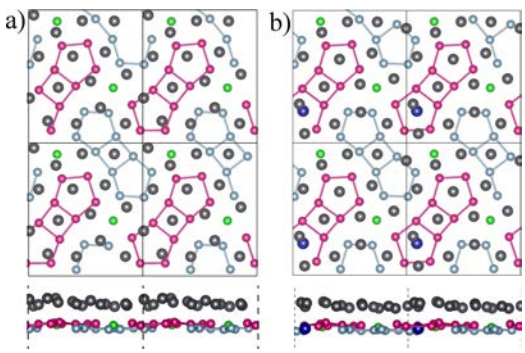

FIGURE 5.16: Pb/$Al_{13}Co_4$(100) interface for the coverage of 0.084 at./Å^2. (a) The substrate surface is a puckered plane with 22 Al atoms (S2 model). (b) The substrate surface is represented by a puckered plane with 22 Al atoms and 2 Co atoms (S1 model). The protruding bipentagonal pattern of the topmost substrate layer is shown in pink (black) while the one slightly below the mean position of the topmost substrate layer is shown in grey (blue). The Co atoms are spheres in blue and Pb atoms are represented by large dark-grey spheres. The top view presents a 2×2 surface unit cell while the side view shows a 2×1 surface unit cell in both (a) and (b).

Mostly the interfacial energy calculations have been performed using the S2 model.The comparison with calculations done using the S1 model allows to highlight the effect of surface Co atoms. Additionally, we have performed energy calculations for another configuration of S2 model denoted by "S2 model (15+1)". Here, a single monolayer containing 15 Pb atoms is adsorbed on the $Al_{13}Co_4$(100) surface, while the 16th atom has been placed on top of the first Pb monolayer. It has been followed

by testing many adsorption sites on top of the first overlayer of Pb atoms on the $Al_{13}Co_4(100)$ surface.

In the following, we present the interfacial energy calculations performed on the models discussed in this section.

5.3.5.1 Interfacial energy calculations

Following the theoretical approach explained in section 5.3.2, we have summarized the modified surface energy calculations in Fig 5.17. It illustrates the variation in surface energy of $Al_{13}Co_4(100)$ as a function of the Pb coverage.

The Pb adlayer has been built by filling all favorable adsorption sites, up to a coverage of 0.084 at./layer, which correspond to 15 atoms in the surface unit cell. When increasing the coverage, the question raises about the structure of the Pb adlayer. A first possible structure is the one with 16 atoms directly adsorbed on $Al_{13}Co_4(100)$. Another possibility is to adsorb 15 atoms directly on $Al_{13}Co_4(100)$, while the additional atom is positioned on the adsorbate layer.

The modified surface energies calculated with our approach range from 0.032 to 0.061 eV/Å^2. The variation is calculated to be rather constant for coverages in the range [0.05 - 0.084] at./Å^2 (from 0.032 to 0.041 eV/Å^2). A discontinuity is observed for a coverage equal to 0.089 at./Å^2. Indeed, the value obtained for the structural model consisting in 15 Pb atoms directly adsorbed on $Al_{13}Co_4(100)$ and one additional atom positioned on the Pb adsorbate layer is lower than the one calculated using a model with 16 Pb atoms directly adsorbed on $Al_{13}Co_4(100)$. This means that it is more favorable to start growing the second Pb adlayer after building the first Pb adlayer with 15 Pb atoms per surface unit cell. Therefore, we consider this coverage value to be the threshold value of Pb ML on $Al_{13}Co_4(100)$. This coverage value corresponds to the experimentally deduced value for Pb ML [191]. For coverages in the range [0.089 - 0.10] at./Å^2, a rather constant and higher value is obtained for the modification in surface energy due to Pb adsorption. In the latter case, the relaxation leads to a bilayer of lead on $Al_{13}Co_4(100)$ (see Tab. 5.10).

Pb coverage (at./Å^2)	N_{Pb} (layer 1)	N_{Pb} (layer 2)
0.056	10	0
0.062	11	0
0.067	12	0
0.073	13	0
0.078	14	0
0.084	15	0
0.090	12	4
0.095	13	4
0.101	11	7

TABLE 5.10: Formation of bi-layer of Pb on the $Al_{13}Co_4(100)$ surface after relaxation for certain value of Pb coverage.

At least, no significant differences are calculated when comparing the modified surface energies evaluated using the structural models S1 or S2 for the $Al_{13}Co_4(100)$ substrate.

5.3.5.2 Electronic structure of Pb/$Al_{13}Co_4(100)$ (coverage = 0.084 at./Å^2)

STM

The experimental analysis performed previously in Ref. [191] demonstrates that the growth of Pb ML

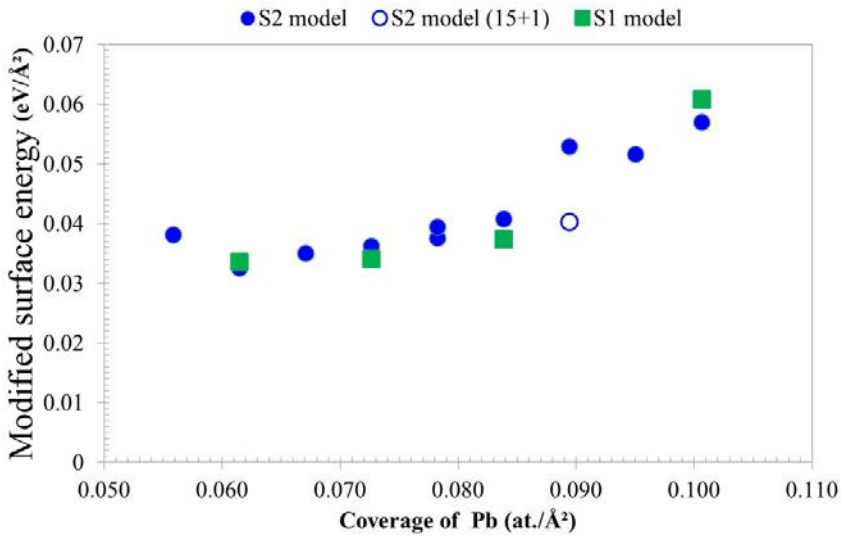

FIGURE 5.17: Modified surface energy of Pb/$Al_{13}Co_4$(100) system.

on the $Al_{13}Co_4$(100) substrate is pseudomorphic from 300 K to 573 K. The corresponding atomically resolved STM image is shown in Fig. 5.18 (Figure taken from [191]). It shows that the surface plane mainly consisted of pentagonal atomic patterns distributed on a periodic substrate. The inhomogeneous contrast can be seen among the motifs (oriented up or down) in this experimental STM image. In Ref. [191], it has been explained as a consequence of the presence of protruding adatoms. A small buckling of the ML has also been mentioned, to partly relieve the build up strain in the adsorbed layer. The density of 1 ML of Pb on $Al_{13}Co_4$(100) has been reported to be approximately equal to 0.09 at./Å^2.

The simulated STM images for similar Pb coverages are shown in Fig. 5.18. The constant current STM image of Pb on the S2 model (Fig. 5.18b)) corresponds to the isodensity value of 9×10^{-5} e/Å^3 while that of Pb on the S1 model (Fig. 5.18d) is equal to 1×10^{-3} e/Å^3. The simulated STM images at constant height of 3 Å above the Pb ML have been plotted for the substrate models and are shown in Figs. 5.18c) and e). There is not a good agreement between the simulated and the experimental STM images, showing that the structure of the Pb adlayer taken for the simulations does not correspond to the atomic arrangement experimentally observed. However, a few simulated STM images exhibit faint pentagonal arrangement of bright spots.

DOS

The electronic structures of the considered Pb/$Al_{13}Co_4$(100) (S1 and S2 models for the substrate, Pb coverage equal to 0.084 at./Å^2) are presented in Fig. 5.19. The interactions of the Pb layer with the substrate is clearly highlighted, especially in the range [-4 : 0] eV. The filling of s-p gap present in fcc Pb (range [-7 : -4] eV) is due to the hybridization of Pb orbitals with the substrate states. No pseudogap is visible on the DOS contributions from the substrate.

Fig. 5.20 shows the DOS of fcc Pb (blue) and of the freestanding Pb layer (green). The bottom panel of this graph presents the DOS contributions from Pb ML (in states/eV-atom) adsorbed on S2 (black) and S1 (red) surfaces, respectively. The s-p gap present in the DOS of the freestanding Pb layer is broader (3.84 eV) and shifted with respect to the bulk one.

Bader charge analysis

Tab. 5.11 summarizes the results obtained for the Bader charge analysis performed for the two models (S1 and S2). The Bader charge and the net charge acquired (ΔQ_X) are tabulated for the X atoms

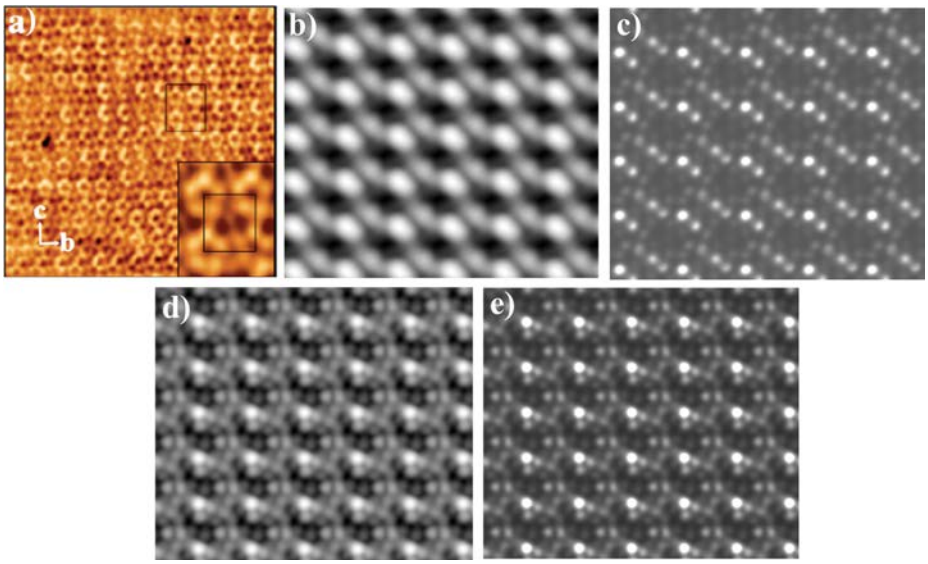

FIGURE 5.18: (a) A 18×18 nm^2 STM image showing 1 ML of Pb deposited on $Al_{13}Co_4$(100) at 573 K [191]. Simulated STM images of the Pb/$Al_{13}Co_4$(100) for a coverage of 0.084 at./Å. (b) A constant current and (c) a constant height simulated STM images of Pb on the S2 surface model for V_{bias} = -0.5 V. Similarly (d),(e) are corresponding to constant current and constant height, respectively of a Pb ML on the S1 surface model for the same bias. The size of the simulated STM images is 7.4 ×8.7 nm^2.

at the interface (int) as well as at "int+1" and "int+2" layers. We see that the average net charge gained by Pb atoms is nearly independent of the presence or absence of surface Co atoms. However, the standard deviation of the charge transfer depends on the substrate type (S1 or S2). The charge carried by interfacial Al atoms is rather small (+0.4 and +0.6 for the S2 and S1 models, respectively), compared to their charge in bulk $Al_{13}Co_4$ (+1.1). Similarly, the charge carried by interfacial Co atoms is rather small (-3.4 for the S1 model), compared to their charge in bulk $Al_{13}Co_4$ (-4.0).

	S2 model		S1 model	
	Q_X^{ref} (e)	ΔQ_X (e)	Q_X^{ref} (e)	ΔQ_X (e)
Pb_{int}	4.065	-0.065±0.050	4.064	-0.064±0.102
Al_{int}	2.637	0.363±0.134	2.432	0.568±0.205
Co_{int}	-	-	12.504	-3.441±0.088
Al_{int+1}	2.057	0.943±0.241	1.866	1.134±0.233
Co_{int+1}	12.425	-3.425±0.467	12.469	-3.469±0.389
Al_{int+2}	1.897	1.103±0.107	1.817	1.183±0.418
Co_{int+2}	13.000	-4.000±0.243	12.872	-3.872±0.117

TABLE 5.11: Average Bader atomic charges evaluated on layers in the Pb/$Al_{13}Co_4$(100) system for a coverage of 0.084 at./Å. The charge transfer values $\Delta Q_X = Q_X^{ref} - Q_X^{slab}$ are provided where Q_X^{ref} and Q_X^{slab} are the number of electrons of isolated X atoms and of X atoms in the slab, respectively ($X = Pb, Al, Co$). The subscript $_{int}$ denotes the atoms present at the interface layer and on moving away from the interface, the atoms in subsequent layers are denoted by subscripts $_{int+1}$ and $_{int+1}$, respectively.

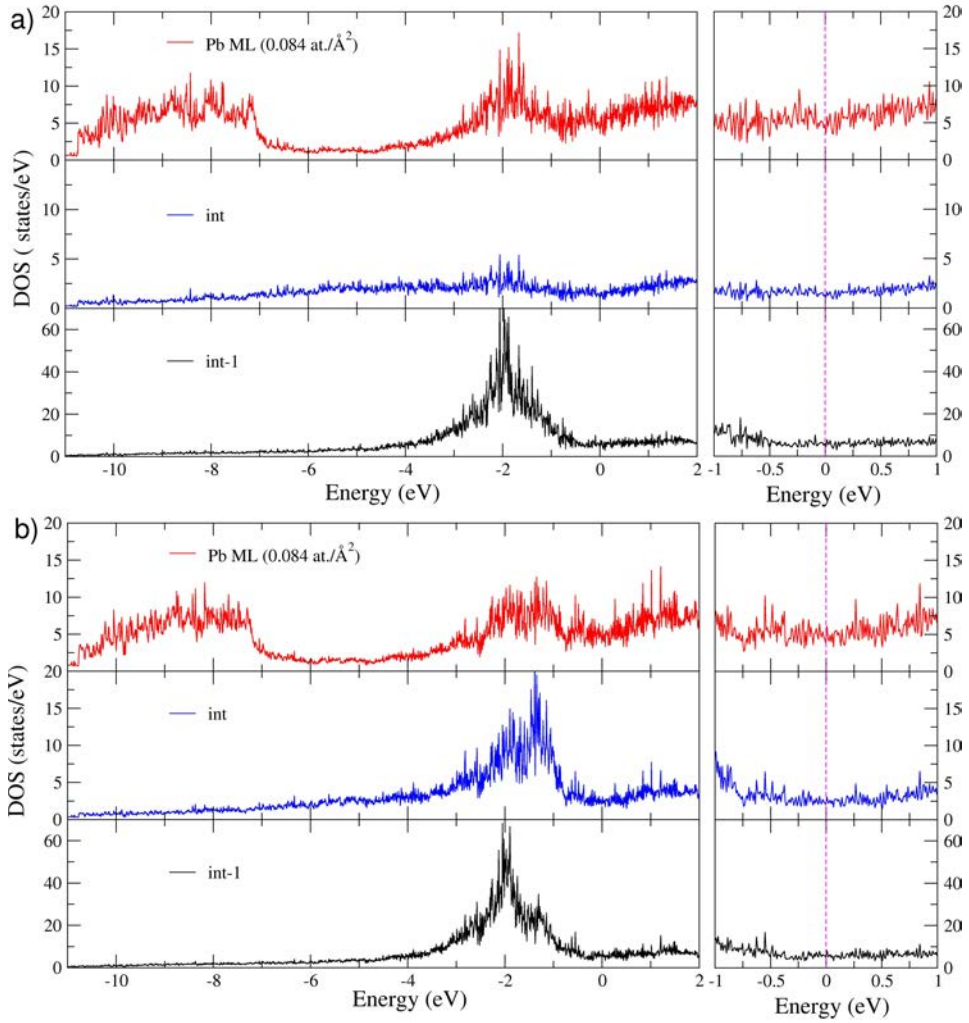

FIGURE 5.19: DOS at the interface of Pb/$Al_{13}Co_4$(100). Contributions of the interface (blue) and sub-interface (black) planes (*int* and *int-1*, respectively) to the density of states for the (a) S2 model and (b) S1 models representing the substrate. The red line is the total DOS of the adsorbed Pb ML (0.084 at./Å^2. The calculations was performed using ISMEAR =-5 and 1×11×11 k-point grid.

5.4 Conclusion

The intrinsic wetting properties of Al-based complex intermetallic compounds have been studied through a combination of theoretical and experimental approaches. Lead was chosen as the metal probe.

In situ wetting experiments were performed on pure Al and several Al-based CMA surfaces. The contact angles of the Pb droplets were determined using the SEM technique. The effect of several parameters on the wetting analysis, such as the size of the droplets and the geometry of the experiment, were studied. The work of adhesion values calculated (using θ_{exp}) for Al_5Co_2(001) and $Al_{13}Co_4$(010) are reported. We determined a correlation between the measured wetting angles and the melting point of the substrates.

Theoretically, two different types of interfaces have been investigated: Pb/Al(111) and Pb/$Al_{13}Co_4$(100). While the surface structure of both substrates are made of Al atoms, their wetting properties towards Pb are quite different.

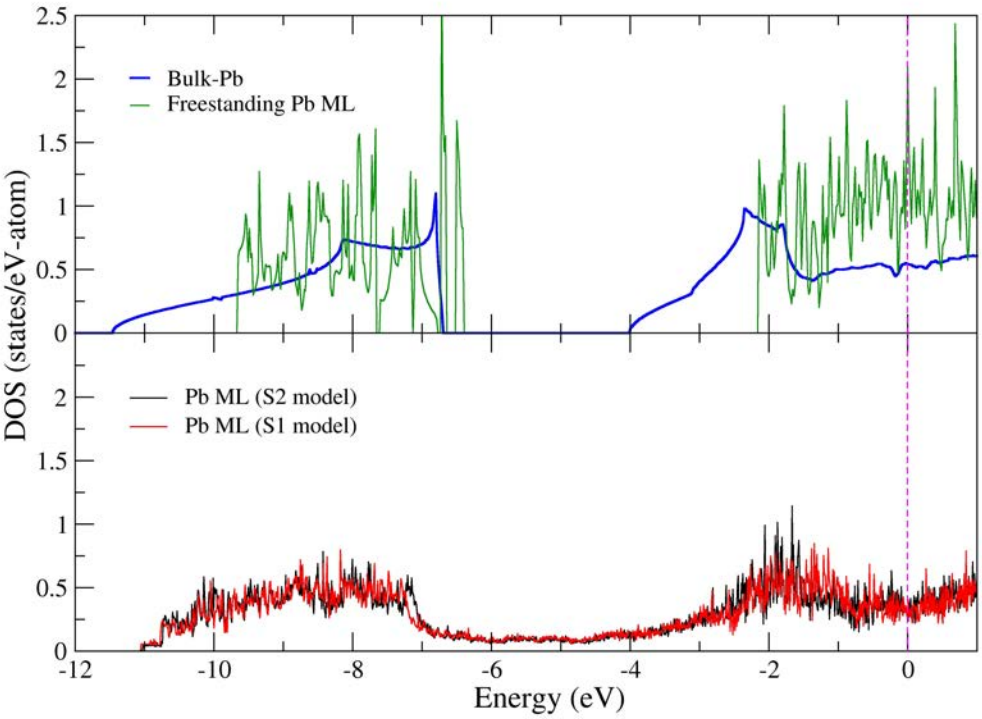

FIGURE 5.20: (Top panel) DOS of fcc crystalline Pb (blue) and freestanding layer of Pb (green) for a surface density equal to 0.084 at./Å^2. (Bottom panel) The DOS contribution of the Pb ML supported by S2 (black) and S1 (red) surfaces, respectively.

The interaction between Pb and the elemental Al substrate appears to be rather weak. No significant charge transfer occurs at the interface. The electronic structures of the Pb and Al layers in contact are almost not modified compared to the ones of the elemental metals. Our theoretically approach gives results consistent with the experimental observations (θ_{calc} =34° & θ_{exp} = 27.3°).

The interaction between Pb and the $Al_{13}Co_4$(100) substrate appears to be stronger than in the previous case. The Pb density of states are modified by the presence of the substrate. Rather significant charge transfer also occurs at the interface. For Pb/$Al_{13}Co_4$(100) interface, only the surface energy of the substrate covered with a Pb monolayer has been computed, so we have no information on the interfacial energy. However, the comparison with Al shows that there is a stronger interaction between a Pb monolayer on $Al_{13}Co_4$(100) than on Al(111). So we expect that the deformation of Pb induces a larger interfacial energy, thus leading to an increase of the contact angle. Experimentally, for a Pb/$Al_{13}Co_4$(100) polycrystalline film [41] higher contact angle value (θ_{exp} = 49.0°) is reported.

Our theoretical approach is maybe the most classical approach to calculate interfacial energies. However, the knowledge of the surface structure seems to be a key parameter in this case. Indeed, the model fails to provide reasonable values for the surface energies when using a cube on cube structure for the Pb/Al(111) structure, or when using a Pb adlayer for Pb/$Al_{13}Co_4$(100) leading to non consistent simulated and experimental STM.

Experimentally, it is possible to grow a rather thick Pb film on Al(111) [191], while a single layer only can be deposited on $Al_{13}Co_4$(100) within the experimental dosing conditions [182]. From our calculations, the interfacial energy Pb/Al(111) is quite constant as a function of the Pb film thickness

(one to four layer thick Pb layers were considered), meaning that the additional layers of Pb deposited on Al(111) do not change the interfacial energy. While the surface energy of $Al_{13}Co_4(100)$ due to Pb adsorption increases significantly when going from a single layer deposition to a bilayer. It means that the wetting properties of $Pb/Al_{13}Co_4(100)$ are strongly modified by the thickness of the Pb film. Experimentally, the consequence of the modification of the surface energy due to adsorption should affect the wetting properties, leading to the impossibility of growing thick Pb films on $Al_{13}Co_4(100)$ under controlled flux [182].

Chapter 6

Conclusions and future outlook

In this thesis, the surface structure and the properties of selected complex intermetallic compounds have been investigated at the nanoscale. Our approach combines theoretical calculations based on the Density Functional Theory with experimental observations at the atomic scale.

The design of surfaces with specific properties is a challenge in nanoscience. Several strategies can be used to achieve this goal, such as surface modifications based on atomic or molecular adsorption. Complex intermetallics can also be considered to reach this aim. They indeed present a large variety of atomic and electronic structures [42], the appropriate compound may be chosen for its intrinsic properties.

In the first part of the thesis, we focus on the determination of the low-index surface structures of the Ba-Au-Ge clathrate. Bulk Ba-Au-Ge is a cage compound that has an atomic structure is built with two types of cages (dodecahedra and tetrakaidecahedra cages), and its electronic structure can be controlled by tuning its chemical composition [18, 135].

In a second part, our work is oriented towards the surface properties of complex intermetallics. Here we focus on the intrinsic wetting properties of several Al-based complex intermetallic compounds, in comparison to elemental metals. The objective here is to discuss the role of the surface complexity on the wetting properties.

In the following, we present a summary of our work, along with a few perspectives.

6.1 Conclusions

6.1.1 Low index surfaces of the intermetallic clathrate Ba-Au-Ge

The bulk properties of this compound were widely studied for the thermoelectric applications. But their surfaces remain scarcely explored, although the covalently-bonded nano-cages present in the bulk structure could potentially induce interesting nanostructurations at the surface.

The experimental study is based on a single crystal grown by the Bridgman method. It is provided by our collaborators: C. Allio; C. Krellner from Physikalisches Institut, Goethe-Universität, Frankfurt, Frankfurt am Main, Germany and H. D. Nguyen, M. Baitinger, Yu. Grin from Max-Plank Institut für ChemischePhysik fester Stoffe, Dresden, Germany. This single crystal presents the composition $Ba_8Au_{5.25}Ge_{40.75}$ and is of metallic character. The experimental investigation of the $Ba_8Au_xGe_{46-x}$(100) and $Ba_8Au_xGe_{46-x}$(110) surfaces shows that no significant surface segregation occurs at the surface (XPS) and no surface reconstruction (LEED) could be observed. The surface cell parameters determined by LEED and STM are in good agreement with the bulk ones. The STM images show surfaces with a step-terrace morphology with a unique step height, equal to half the crystal parameter in the direction perpendicular to the surface. This highlights the selection of a bulk-truncated plane at the surface.

Our determination of the precise surface structure is based mainly on surface energy calculations, as well as on the comparison of experimental and theoretical STM images. Several surface models were built, for both surface orientations, and the corresponding surface energies were calculated as a function of the Au and Ge chemical potentials. Two types of terminations were considered. In the first group, the bulk cages are intact at the surface, while in the second group, the corrugation of the termination plane is minimized, which requires to break the nanocages at the surface. For both orientations, we found that the most stable models are the ones preserving intact cages at the surface. The latter cages are not so strongly distorted. The type of cages protruding depends on the surface orientation: tetrakaidecahedra and dodecahedra for the (100) and the (110) surfaces, respectively.

Cages are mostly made of germanium atoms, which are in the sp^2 configuration at the surface. It implies the presence of surface dandling bonds, which have a destabilizing character. The surface structure also contains protruding surface Ba atoms. Bader charge calculations highlight a charge transfer from surface Ba atoms to surface Ge atoms, saturating the dandling bonds, thus contributing to the surface stabilization. The presence of surface Ba atoms also contributes to the rather low work function for these surfaces (3.32 eV and 3.55 eV for the (100) and (110) surfaces, respectively). Corresponding electronic structure calculations show that these surfaces are metallic.

6.1.2 Wetting properties of Al-based complex intermetallic surfaces

The intrinsic wetting properties of Al-based complex intermetallic compounds have been studied through a combination of theoretical and experimental approaches. Lead was chosen as the metal probe.

In situ wetting experiments were realized on pure Al and several Al-based intermetallic substrates (CMAs and quasicrystals). The contact angles of the Pb nano-droplets were determined by SEM. The influence of several parameters on the measurements, such as the size of the droplets and the geometry of the experiment, were carefully investigated. We found a correlation between the measured wetting angles and the melting point of the substrates.

Our theoretical approach focused on two different interfaces: Pb/Al(111) and Pb/$Al_{13}Co_4$(100). The considered thermodynamic model is discussed. This model highlights the influence of the adlayer structures or the adlayer-substrate interactions on the theoretical determination of the contact angle.

The lattice parameters of Pb and Al are quite different (lattice mismatch of 22 %). To minimize it, the Pb/Al(111) system adopts a moiré structure. Interfacial energies have been determined from this model. The calculated values are in good agreement with the experimental data, leading to values for the contact angle (deduced from the Young's equation) also in good agreement with the experimental ones (θ_{calc} =34° and θ_{exp} = 27.3°). For thin films (one to four adlayers), the thickness of the film is not found to have a strong influence on the interfacial energy. Here, electronic structure calculations show a weak interaction between the Pb film and the substrate, which is consistent with the metallic character of the two elements at the interface.

For Pb/$Al_{13}Co_4$(100), a first step was to develop a structural model for the interface. The lattice parameters of $Al_{13}Co_4$(100) and of a Pb(111) supercell are similar (lattice mismatch less than 3 %). We thus adopt a (1x1) surface cell for the adsorbate, in agreement with the experimental observations. To further develop the model, we have determined the variation in surface energies as a function of the atomic density of the Pb film. It is calculated to be almost constant until a Pb density equal to 0.84 at./Å^2. For higher atomic densities, it increases substantially. This change is accompanied by a change in the interfacial structure: up to a density of 0.84 at./Å^2, the Pb atoms are arranged in a single plane (almost no corrugation). A bilayer appears for higher coverages. Electronic structure calculations show a significant interaction between the Pb adlayer and the substrate. This is also supported by the Bader charge analysis. The corresponding wetting angle is expected to be higher than

that of Pb/Al(111) interface, due to the stronger interaction between Pb adlayer and the substrate ($Al_{13}Co_4$(100)).

Experimentally, a layer-by-layer growth of Pb on Al(111) is observed [191], while only a single layer could be deposited on the complex $Al_{13}Co_4$(100) surface within the experimental dosing conditions [182]. Our calculations support these observations, when considering the influence of the Pb adlayer thickness on the interfacial energy and modified surface energy. This behavior is found to be induced by the specific Pb adlayer-substrate interaction.

6.2 Future outlook

All our results and conclusions have opened several perspectives to further investigate these systems.

The nanostructured $Ba_8Au_{5.25}Ge_{40.75}$(100) and $Ba_8Au_{5.25}Ge_{40.75}$(110) surfaces are potentially interesting as templates for pattern formations / novel nano-structures. Our work on the low index surfaces of $Ba_8Au_{5.25}Ge_{40.75}$ is a first step towards the study of molecular adsorption on these surfaces. The latter exhibit different types of nano-cages depending on the orientation. It is foreseen that novel molecular 2D architecture could be grown on these templates. A particular attention should be put on the molecule choice with respect to the surface unit cell. For instance, it has been shown that C_{60} molecules order in a quasiperiodic manner on quasicrystalline substrate due to the adsorption site inter-distance consistent with the C_{60} diameter [192]. Preferential adsorption sites and atomically resolved structure of the film adsorbed could be predicted using the DFT calculations.

More generally, several molecular self-assembly phenomena have been observed on semiconducting Ge surfaces. Similar or contrasting results may be obtained from the Ge-based clathrate surfaces. In this work, we found that the BaAuGe(100) and BaAuGe(110) surfaces are intrinsically passivated by surface Ba atoms. The control of the dangling bonds at the surface may be possible through the control of the surface atomic density of protruding Ba atoms. This may help to tune the molecule/surface interactions.

Electronic structure calculations have been performed. These could be completed by band structure calculations, as well as angle-resolved photoelectron spectroscopy (ARPES). The low index surfaces of the investigated crystal have been found to present a metallic character. However, this character was found to depend on the surface Au concentration at the surface. Such conclusion may be tested experimentally.

In the second part of the manuscript, we focused on the wetting properties of Al-based complex intermetallic compounds. A few important and open-ended questions have been raised from our study. One first point would be to increase consequently the number of Al-based surfaces tested experimentally, for example, using Al_9Co_2(100) and $Al_{13}Fe_4$(100). This would also help to determine the influence of the surface orientation on the wetting properties for a given system.

Ab initio molecular dynamic (AIMD) calculations could be another approach to study the Pb/Al(111) and Pb/$Al_{13}Co_4$(100) interfaces. It is maybe a more realistic approach as it takes into account the temperature factor. Also, the combination of AIMD followed by static DFT calculations can be used to test additional structural models for the interface. Such approach has been recently applied to model oxide layers on metal surfaces [193].

At last, our study is limited to the intrinsic wetting properties of Al-based complex intermetallic compounds. However, when used for applications, these surfaces are oxidized. The corresponding wetting properties may be affected by this surface modification. The investigation of the wetting

properties of such surfaces in operando conditions may help to optimize such surfaces for applications as coatings for example.

Chapter 7

Résumé en français

7.1 Introduction

7.1.1 Les phases intermétalliques complexes et leurs surfaces

Les intermétalliques complexes sont des composés définis, formés à partir de plusieurs éléments métalliques, dont la structure est décrite par une maille géante contenant de quelques dizaines à plusieurs milliers d'atomes, généralement regroupés en agrégats de symétrie élevée. Les quasicristaux représentent le cas limite, avec la perte de la périodicité de translation et l'apparition de symétries de rotation "interdites" (le plus souvent d'ordre 5 ou 10). Cette perte progressive du caractère périodique lorsque le nombre d'atomes dans la maille augmente est accompagnée par l'émergence de propriétés physiques qui diffèrent de celles des métaux et alliages simples [1, 3, 194].

Les arrangements quasipériodiques ont été découverts dans un grand nombre de composés intermétalliques (> 100) [195, 196] ainsi que dans des systèmes du domaine de la matière molle [197, 198]. Des oxydes bidimensionnels présentant un arrangement quasipériodique ont également été observés. [199]. Aucun de ces systèmes n'est mono-élément. Une approche théorique a montré que les arrangements quasicristallins peuvent émerger de simulations de dynamique moléculaire à partir d'un système de particules à un composant, interagissant via un potentiel de paire isotrope [200]. Une exploration de l'espace des paramètres a permis d'identifier des composés voisins des phases quasicristallines, comme les clathrates et d'autres phases complexes dont la structure est également décrite par un empilement d'agrégats atomiques de haute symmétrie.

Les propriétés de surface de ces phases complexes sont particulièrement intéressantes. Plusieurs phases quasicristallines ou approximantes présentent des surfaces caractérisées par une grande dureté et un coefficient de frottement faible [5, 7, 201]. La résistance à l'oxydation de ces matériaux est également citée [1, 4, 40, 42]. Plus récemment, plusieurs phases complexes ont montré de bonnes performances en catalyse, qu'elles soient utilisées comme telles ou traitées par une attaque chimique [202–206].

7.1.2 Objectifs de la thèse

Le design de surfaces présentant des propriétés spécifiques est un objectif général en nanosciences. Plusieurs stratégies peuvent être utilisées pour atteindre ce but, comme par exemple des modifications de la surface via la formation de films atomiques ou moléculaires. Une autre approche pourrait reposer sur la grande variété de structures atomiques et électroniques des intermétalliques complexes. C'est ce qui a motivé la première partie de cette thèse, c'est-à-dire l'étude des surfaces de bas indice du clathrate Ba-Au-Ge. La structure atomique de ce composé est formée de cages, sa structure électronique peut être contrôlée par sa composition. Dans une première partie, notre objectif est la

détermination précise de la structure des surfaces de bas indice de ce composé cage, en utilisant une combinaison de méthodes théoriques et expérimentales.

Dans une seconde partie, notre travail s'est orienté vers les propriétés de surface des intermétalliques complexes, en particulier les propriétés de mouillage intrinsèque. Nous nous sommes intéressés à plusieurs intermétalliques à base d'aluminium, un des objectifs étant de discuter le rôle de la complexité de la surface sur les propriétés de mouillage.

7.2 Surfaces de bas indice du composé cage Ba-Au-Ge

Le clathtrate Ba-Au-Ge est un matériau présentant des propriétés thermoélectriques intéressantes. La possibilité de contrôler sa structure électronique en jouant sur sa composition chimique exacte est également séduisante du point de vue de ses propriétés de surfaces, que l'on peut espérer contrôler via ce levier. Dans la suite, nous nous sommes intéressés aux surfaces de bas indice (100) et (110).

7.2.1 Le clathrate Ba-Au-Ge

La structure de ce cristal est illustrée sur la figure 7.1 (groupe d'espace $Pm\bar{3}n$, maille cubique contenant 54 atomes, paramètre de maille égal à 10.7987 Å [18]). Elle peut être décrite par un empilement de deux types de cages: des tetrakaidécaèdres [(Ge,Au)$_{24}$]) et des dodécaèdres [Ge$_{20}$], ces derniers étant organisés selon un arrangement cubique centré. Ces cages contiennent chacune un atome de Barium au centre.

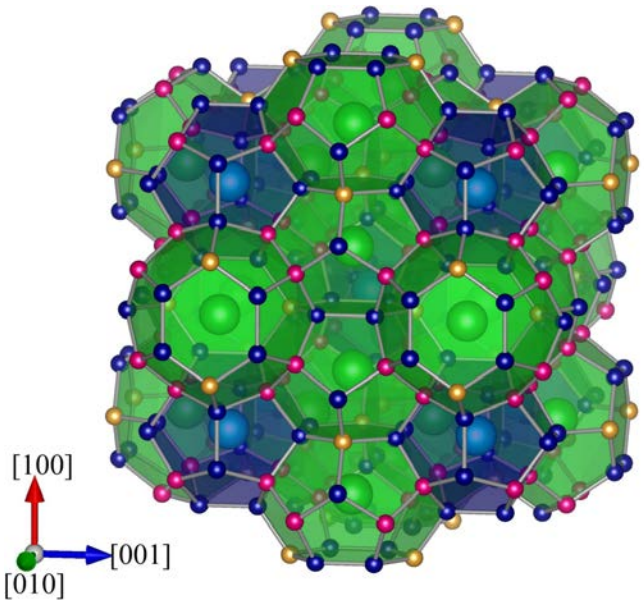

FIGURE 7.1: Structure du massif du composé clathrate $Ba_8Au_{5.25}Ge_{40.75}$.

L'analyse de la liaison chimique dans le composé Ba$_8$Au$_x$Ge$_{46-x}$ avec $x = 5.33$ a mis en évidence le caractère covalent des liaisons Ge-Ge et Ge-Au. Une liaison à caractère covalent a également été identifiée entre l'atome de Ba au centre des cages et l'atome Au des cages [(Ge,Au)$_{24}$]. [18].

Le monocristal que nous avons utilisé a pour composition Ba$_8$Au$_{5.25}$Ge$_{40.75}$ (croissance réalisée par nos collaborateurs allemands à Dresde et à Francfort sur le Main). Cela lui confère un caractère métallique (Fig. 7.1). La démarche adoptée pour l'étude des surfaces de bas indice de Ba$_8$Au$_x$Ge$_{46-x}$ repose sur une combinaison de méthodes expérimentales et théoriques.

7.2.2 Résultats expérimentaux

Expérimentalement, aucune reconstruction n'est observée par diffraction d'électrons lents (LEED Low Energy Electron Diffraction). Les paramètres des mailles de surface sont 10.80 Å ± 0.40 Å pour $Ba_8Au_xGe_{46-x}$(100) et $b' = 15.58 \pm 0.2$ Å et $c = 10.45 \pm 0.4$ Å pour $Ba_8Au_xGe_{46-x}$(110). Dans les deux cas, ces mesures sont cohérentes avec le paramètre de maille du crystal. La surface est formée de larges terrasses séparées par des marches d'une hauteur spécifique à chaque orientation: 5.0 ± 0.2 Å pour $Ba_8Au_xGe_{46-x}$(100) et 7.60 ± 0.15 Å pour $Ba_8Au_xGe_{46-x}$(110). Dans les deux cas, cette distance correspond à la moitié du paramètre de maille dans la direction perpendiculaire à la surface ($\frac{a}{2} = 5.40$ Å et $\frac{a\sqrt{2}}{2} = 7.64$ Å, respectivement), mettant en évidence une sélection de terminaison à la surface.

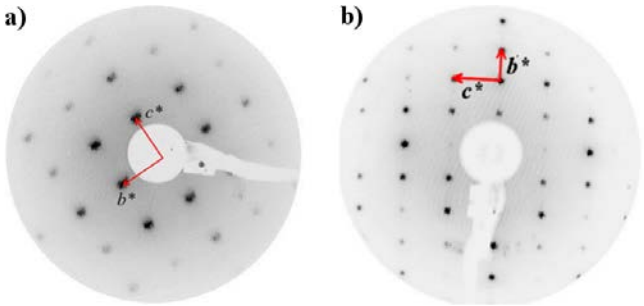

FIGURE 7.2: Cliché de diffraction lents des surfaces $Ba_8Au_{5.25}Ge_{40.75}$(100) et the $Ba_8Au_{5.25}Ge_{40.75}$(110).

7.2.3 Calcul des énergies de surface et simulation d'images STM

La détermination des énergies de surface a été réalisée grâce à une approche théorique basée sur la théorie de la fonctionnelle de la densité. L'approche décrite dans la Ref. [103] a été adoptée. Pour chaque orientation, plusieurs modèles de surface ont été élaborés, leur énergie de surface déterminée en fonction du potentiel chimique de deux élements (ici, Au et Ba). Les modèles sont construits de telle sorte à minimiser la corrugation de surface (ce qui requiert généralement de "briser" les cages à la surface), ou bien en préservant l'un ou l'autre type de cages à la surface.

Notre étude montre que ces cages sont préservées aux surfaces $Ba_8Au_xGe_{46-x}$(100) et $Ba_8Au_xGe_{46-x}$(110). Le type de cage qui protrude dépend de l'orientation de la surface: dodécaèdres ou tétrakaidécaèdres pour les orientations (110) et (100), respectivement.

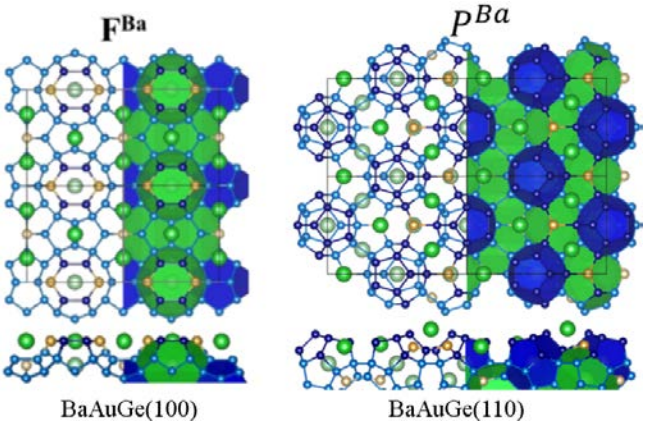

FIGURE 7.3: Modèles de surface stable observée expérimentalent pour les surfaces (gauche) $Ba_8Au_{5.25}Ge_{40.75}$(100) et (droite) $Ba_8Au_{5.25}Ge_{40.75}$(110)

Les images de microscopie à effet tunnel (STM pour Scanning Tuneling Microscopy) simulées à partir des modèles précédents sont en bon accord avec les images expérimentales (Fig. 7.4), ce qui étaye les conclusions des calculs d'énergie de surface.

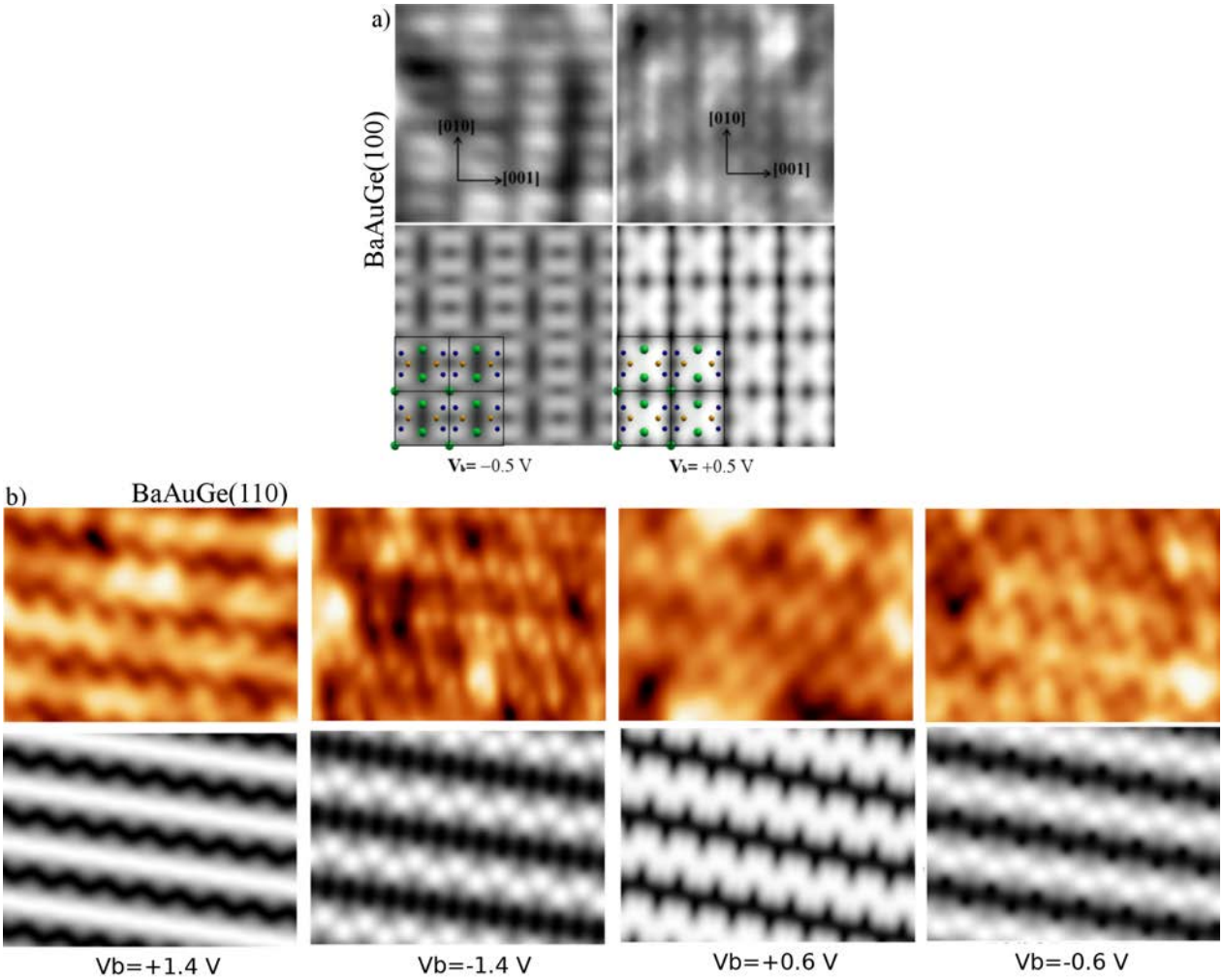

FIGURE 7.4: Images STM expérimentales et simulées des surfaces (100) et (110) du composé clathrate de type-I $Ba_8Au_{5.25}Ge_{40.75}$.

7.2.4 Facteurs à l'origine du modèle de surface observé

Les modèles des surfaces $Ba_8Au_xGe_{46-x}$(100) et $Ba_8Au_xGe_{46-x}$(110) impliquent la présence de liaisons pendantes, liées aux atomes de germanium sp^2 à la surface. Les liaisons pendantes ont un caractère déstabilisant, et sont à l'origine de reconstructions de surface de nombreux semi-conducteurs. Ici, aucune reconstruction n'est observée, puisque les atomes de barium, qui protrudent à la surface, assurent un transfert de charge de telle sorte à passiver la surface. Cela a pu être mis en évidence par notre approache théorique.

7.3 Propriétés de mouillage d'intermétalliques complexes à base d'aluminium

Les propriétés de mouillage intrinsèques d'intermétalliques complexes à base d'aluminium ont été étudiées grâce à une combinaison d'approches expérimentale et théorique. Le plomb a été choisi comme métal sonde.

7.3.1 Approche expérimentale

Nous avons effectué des expériences de mouillage in situ sur plusieurs substrats à base d'aluminium: cristal d'aluminium, alliages simples et complexes, quasicristaux. Les angles de contact des nano gouttelettes de Pb sont déterminés par la Microscopie Electronique à Balayage (MEB). L'influence de plusieurs paramètres sur les mesures, comme la taille des gouttelettes et la géométrie de l'expérience a pu être étudiée. Les mesures ont permis d'établir une corrélation entre les angles de mouillage mesurés et le point de fusion des substrats.

7.3.2 Approche théorique

Deux types d'interfaces ont été considérées: Pb/Al (111) et Pb/$Al_{13}Co_4$(100). Deux types de modèles thermodynamiques ont été considérés et discutés.

7.3.2.1 Pb/Al(111)

: Les paramètres de maille du plomb et de l'aluminium sont assez différents ("désaccord de maille" de l'ordre de 20%). Pour minimiser les contraintes à la surface, ce système adapte une structure en moiré. L'énergie d'interface a été déterminée à partir de ce modèle, ce qui permet d'obtenir des valeurs en bon accord avec les données expérimentales, puis d'en déduire l'angle de mouillage grâce à l'équation de Young (θ_{calc} = 34°, θ_{exp} = 27,3°). Les calculs de l'énergie d'interface en fonction de l'épaisseur de la couche de plomb montrent que cette dernière ne dépend pas de l'épaisseur du film.

Les calculs de structure électronique mettent en évidence une faible interaction entre le film de plomb et le substrat, ce qui est cohérent avec le caractère métallique des deux éléments à l'interface.

7.3.2.2 Pb/$Al_{13}Co_4$(100)

Une première étape a consisté à élaborer un modèle d'interface dans ce cas. Lorsqu'on compare les différences de paramètres de maille de $Al_{13}Co_4$(100) et d'une supermaille de Pb(111), on s'aperçoit que ces différences sont petites ("lattice mismatch" inférieur à 3%). Cela permet de faire l'hypothèse d'une maille (1x1) pour l'adsorbat, en accord avec les observations expérimentales. Nous avons pour cela déterminé les énergies d'interface en fonction de la densité du film de plomb. Cette dernière est constante jusqu'à une densité de plomb de 0.84 at./$Å^2$. Elle augmente sensiblement ensuite. Cette modification s'accompagne d'un changement de structure: jusqu'à une densité de 0.84 at./$Å^2$, les atomes de plomb sont organisés sur un seul plan. Une bicouche apparaît pour des taux de recouvrement plus importants.

Les calculs de structure électronique montrent une interaction non négligeable entre la couche de plomb et le substrat. Cela se traduit également par un transfert de charge identifié par un calcul des charges de Bader.

Appendix A

Additional information on BaAuGe(100)

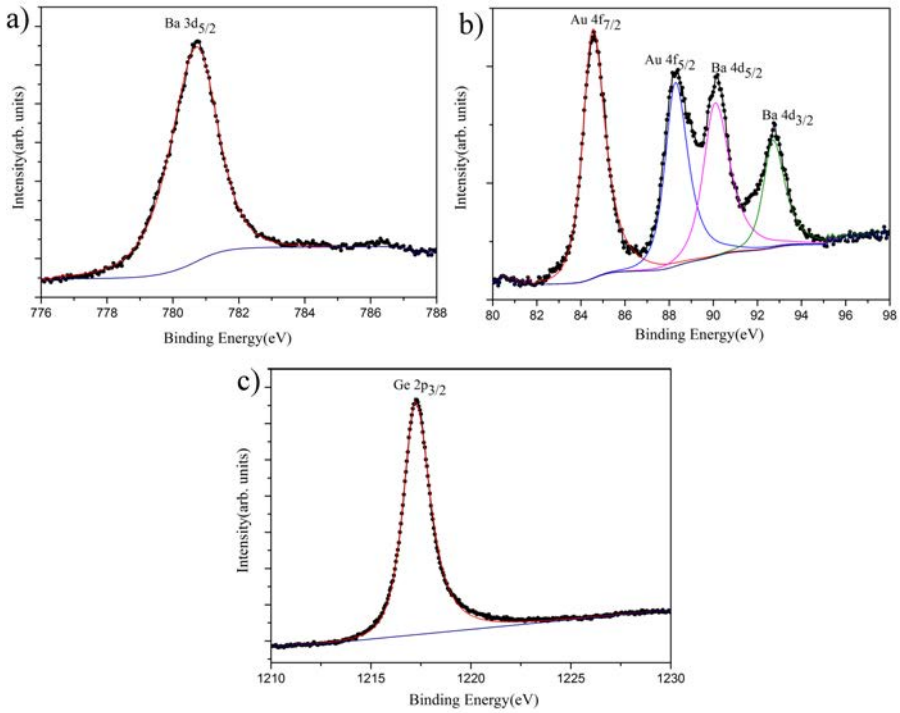

FIGURE A.1: (a),(b),(c) Angle-resolved XPS Ba $3d_{5/2}$, Au $4f_{7/2}$ and Ge $2p_{3/2}$ core-level lines (shown by dotted black line), respectively, measured at 45° take-off angle. The red thin lines are XPS fitting curves (deconvoluted spectra) associated to the experimental spectra. The blue thin lines represent the background-type used in XPS fitting. (b) The remaining colored lines are the fit to the peaks appearing with the main Au $4f_{7/2}$ peak.

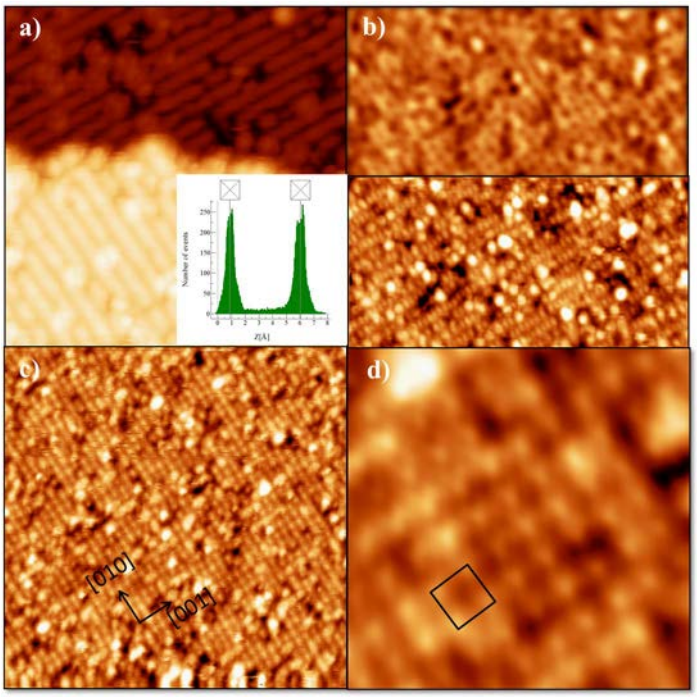

FIGURE A.2: (a) A 20×20 nm^2 STM image of the $Ba_8Au_{5.25}Ge_{40.3}\square_{0.45}$(100) surface with rotated motifs between adjacent terraces, prepared at 933 K (V_b=-1.4 V ; I_t= 0.08 nA). An inset histogram showing the unique step height of this clathrate compound equal to 5.0±0.2 Å (b) 30×30 nm^2 STM images of the (100) surface plane obtained at 933 K for V_b=+ 0.7 V and V_b= −0.7 V, respectively. (c) 41×41 nm^2 STM image at 933 K for V_b=−1.1 V. (d) A 10×10 nm^2 Fourier filtered image corresponding to Fig. A.2 (c) showing the unit cell of the surface.

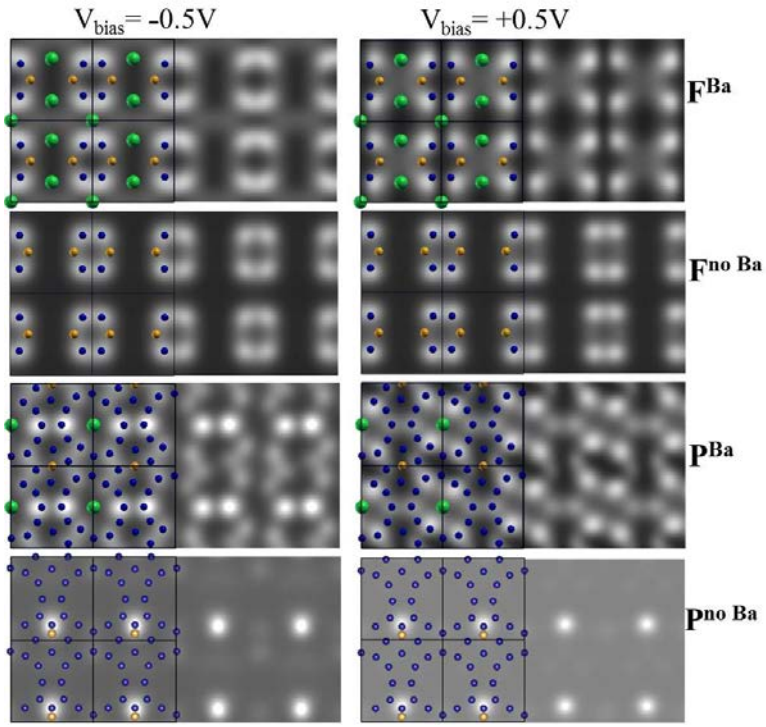

FIGURE A.3: Simulated STM images at constant height (2.16 × 2.16 nm^2) obtained at V_b = ± 0.5 V for different models considered.

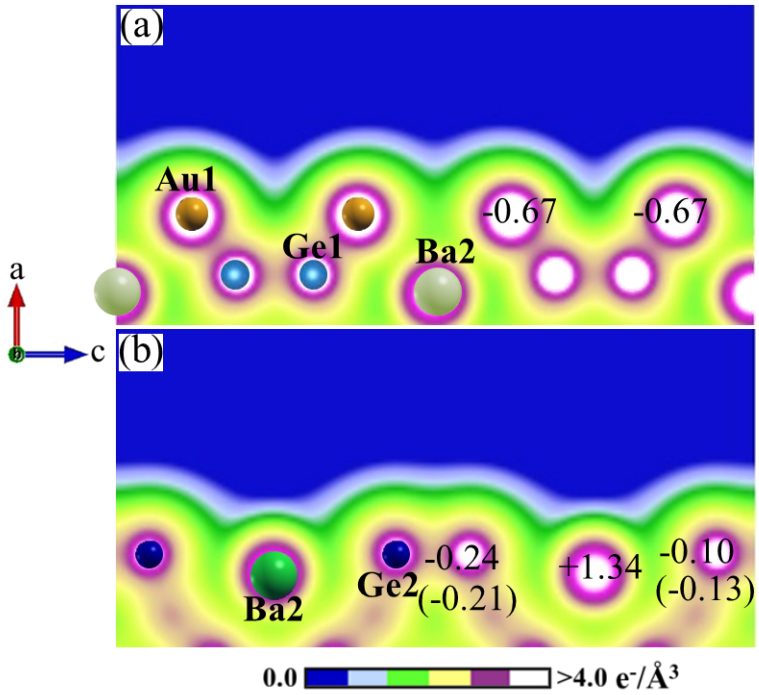

FIGURE A.4: Electron density (log scale) using the F^{Ba} model. Side views plotted along the [010] direction ($\vec{b}$) at $y = 0$ (a) and $y = 0.25$ (b). The numbers correspond to the charge transfer $\Delta Q_X = Q_X^{iso} - Q_X^{slab}$ where Q_X^{iso} and Q_X^{slab} are the number of electrons of isolated X atoms and of X atoms in the slab, respectively ($X = Ba, Au, Ge$). The number in parenthesis corresponds to Q_{Ge} for surface Ge atoms at $y = 0.75$. The value Q_{Ba1} related to surface Ba1 atoms, located at fractional coordinate, $y = 0$, is $+1.30$ (not shown).

Appendix B

Some additional test calculations using DFT

B.1 Cut-off energy and k-point grid

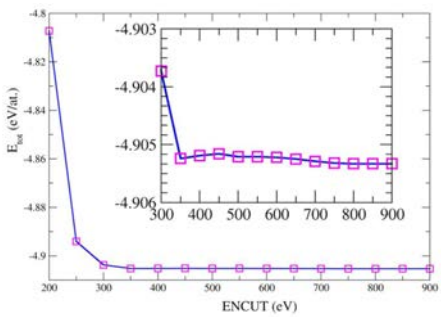

FIGURE B.1: Total energy of bulk o-$Al_{13}Co_4$ as a function of cut-off energy (ENCUT) for a k-point mesh: $11 \times 7 \times 7$.

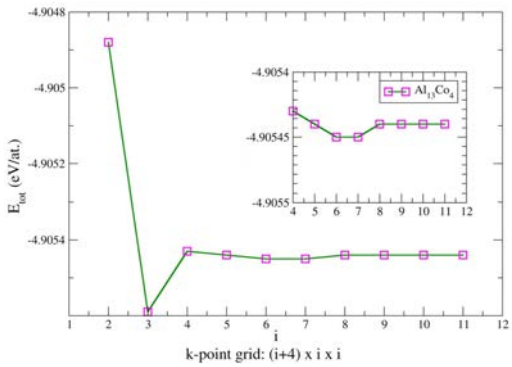

FIGURE B.2: Total energy of bulk o-$Al_{13}Co_4$ as a function of a k-point mesh: $(i+4) \times i \times i$ using ENCUT value of 450 eV.

Total-energy calculations on the bulk model of o-$Al_{13}Co_4$ were realized using a cutoff energy of 450 eV and within the Brillouin zone spanned by k-mesh: $11 \times 7 \times 7$, led to an energy precision 0.06 meV/atom.

B.2 Smearing methods

In reciprocal (k-) space, the integration of the probability density function performed over Brillouin zone (see Equation 2.49) is discontinuous at the Fermi level and in practice, the step function is

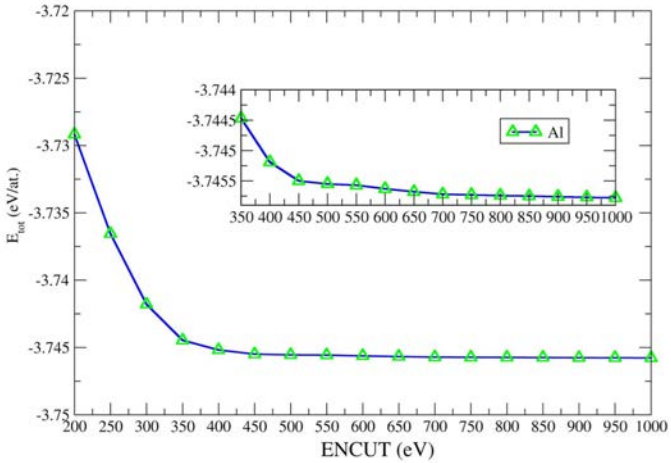

FIGURE B.3: Total energy of fcc Al as a function of cut-off energy (ENCUT) for a k-point mesh: $21 \times 21 \times 21$.

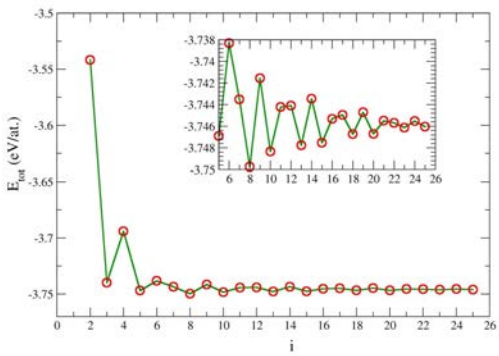

FIGURE B.4: Total energy of bulk Al as a function of a k-point mesh: $i \times i \times i$ using ENCUT value of 300 eV.

replaced by the smoother function as shown in equation below:

$$\sum_{nk} \omega_{nk} \epsilon_{nk} \Theta(\epsilon_{nk} - \mu) \rightarrow \sum_{nk} \omega_{nk} \epsilon_{nk} f(\frac{\epsilon_{nk} - \mu}{\sigma}) \tag{B.1}$$

where f_{nk} are the partial occupancies corresponding to the nk state, σ is the smearing parameter and can be interpreted as finite temperature [207].

This function f can be interpreted by applying different methods such as Gaussian smearing, Fermi-Dirac smearing, Methfessel-Paxton method and the tetrahedron method with Blöchl corrections. In this thesis, we used Methfessel-Paxton method of order 1 [208] for structure optimization and the tetrahedron method for electronic structure calculations. The value of sigma= 0.02 was chosen (almost tending to zero) to find the ground state energy of $Ba_8Au_6Ge_{40}$ system and a calculation of total energy as a function of SIGMA parameter in VASP was performed (see Fig. B.5). While based on previous works [180, 209] sigma =0.2 was used for $Al_{13}Co_4$ system.

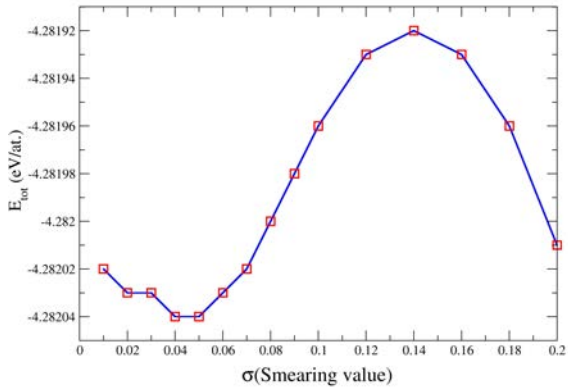

FIGURE B.5: Total energy of bulk $Ba_8Au_6Ge_{40}$ as a function of a smearing parameter (σ) in the range [0.01 - 0.2].

B.3 DOS of bulk o-$Al_{13}Co_4$

The electronic structure of the o-$Al_{13}Co_4$ determined by the DOS calculations consists of a Co d band superimposed on a comparatively broad Al sp band. Its complex bulk structure is depicted by the "spiky" DOS [210] and the presence of a shallow pseudogap (at 0.38 eV below E_F) with minimal DOS of $n(E) = 0.22$ states/(eV atom). The location and the value of $n(E)$ mentioned here for the pseudogap are in complete agreement with Ref. [140]. The presence of such a pseudogap near E_F is a key feature in bulk CMAs and often considered to be linked with the stabilization mechanism in Hume-Rothery alloys [1].
The DOS calculation for bulk shown in Fig. B.6 was performed with parameters ENCUT = 450 eV and k-point grid: $15 \times 7 \times 7$ using the tetrahedron method in VASP.

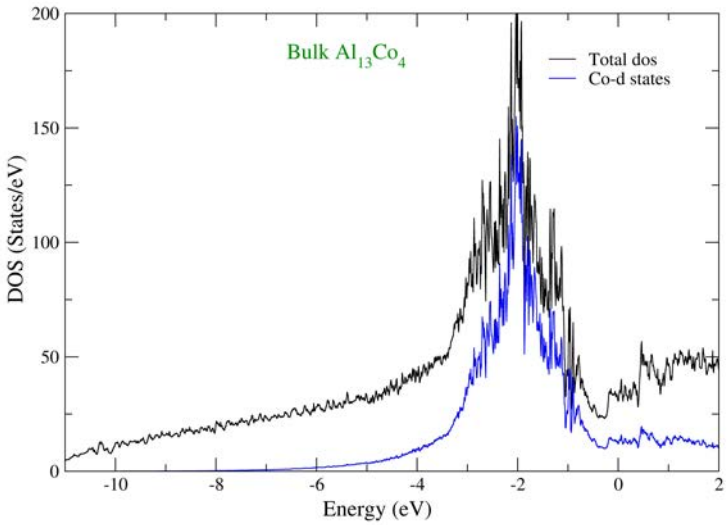

FIGURE B.6: Density of states of bulk o-$Al_{13}Co_4$.

Appendix C

Supplementary material on wetting properties of metallic surfaces

C.1 Wetting experiments

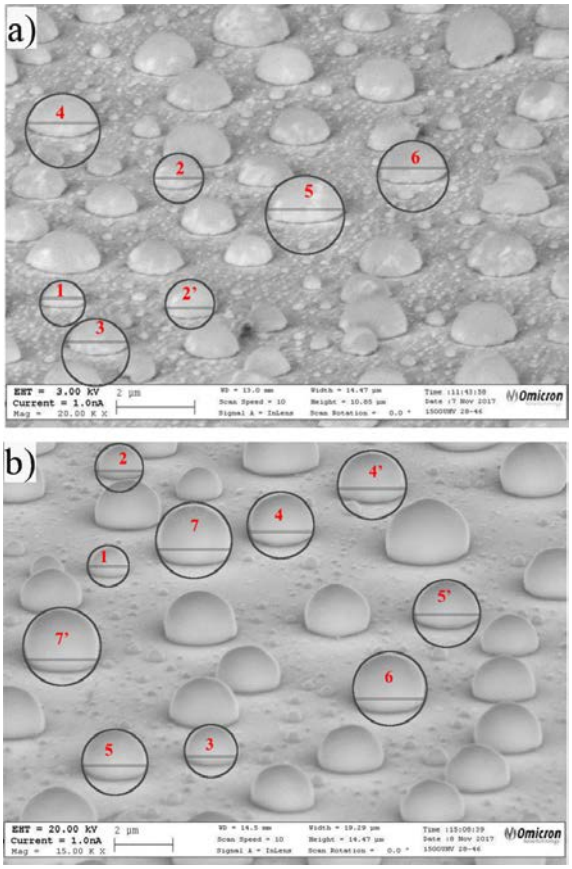

FIGURE C.1: SEM micrographs showing Pb droplets on (a) $Al_{13}Co_4(010)$ and (b) $Al_5Co_2(001)$ for a tilt value equal to 60°. Some droplets are curve-fitted (black circles) for contact angle measurements. The red labels correspond to the droplet sizes in the respective tables C.1 and C.2.

	Droplet size μm	Contact angle, θ degrees		
		θ_{fitted}	θ_{app}	θ_{avg}
1	1.25	76.9	71.8	74.35
2	1.32	80.5	73.6	77.05
3	1.38	81.2	73.4	77.3
4	1.44	79.5	74.1	76.8
5	1.69	78.6	74.3	76.45
6	1.88	87.3	76.9	82.1
		Avg $\pm$ SD		77.34 $\pm$ 2.559

TABLE C.1: Contact angle measurement for interface of Pb/$Al_{13}Co_4$(010) for a tilt value equal to 60°.

	Droplet size μm	Contact angle, θ degrees		
		θ_{fitted}	θ_{app}	θ_{avg}
1	1.82	100.9	86.2	93.55
2	2.01	102.6	87.3	94.95
3	2.17	101.9	86.5	94.2
4	2.24	103.1	88.4	95.75
5	2.29	102.8	88.7	95.75
		Avg $\pm$ SD		94.84 $\pm$ 0.967

TABLE C.2: Contact angle measurement for interface of Pb/Al_5Co_2(001) for a tilt value equal to 60°.

	Droplet size μm	Contact angle, θ degrees		
		θ_{fitted}	θ_{app}	θ_{avg}
1	0.252	77.6	64.2	70.9
2	0.378	79.5	63.8	71.65
3	0.465	80.15	66.15	73.15
4	0.493	80.6	66.5	73.55
5	0.589	80.8	67.6	74.2
6	0.69	78.6	67.7	73.15
7	0.755	79.5	65.9	72.7
		Avg $\pm$ SD		72.76 $\pm$ 1.132

TABLE C.3: Contact angle measurement for interface of Pb/i-Al-Pd-Mn.

C.2 DFT calculations: electronic structure of Pb/Al(111) moiré

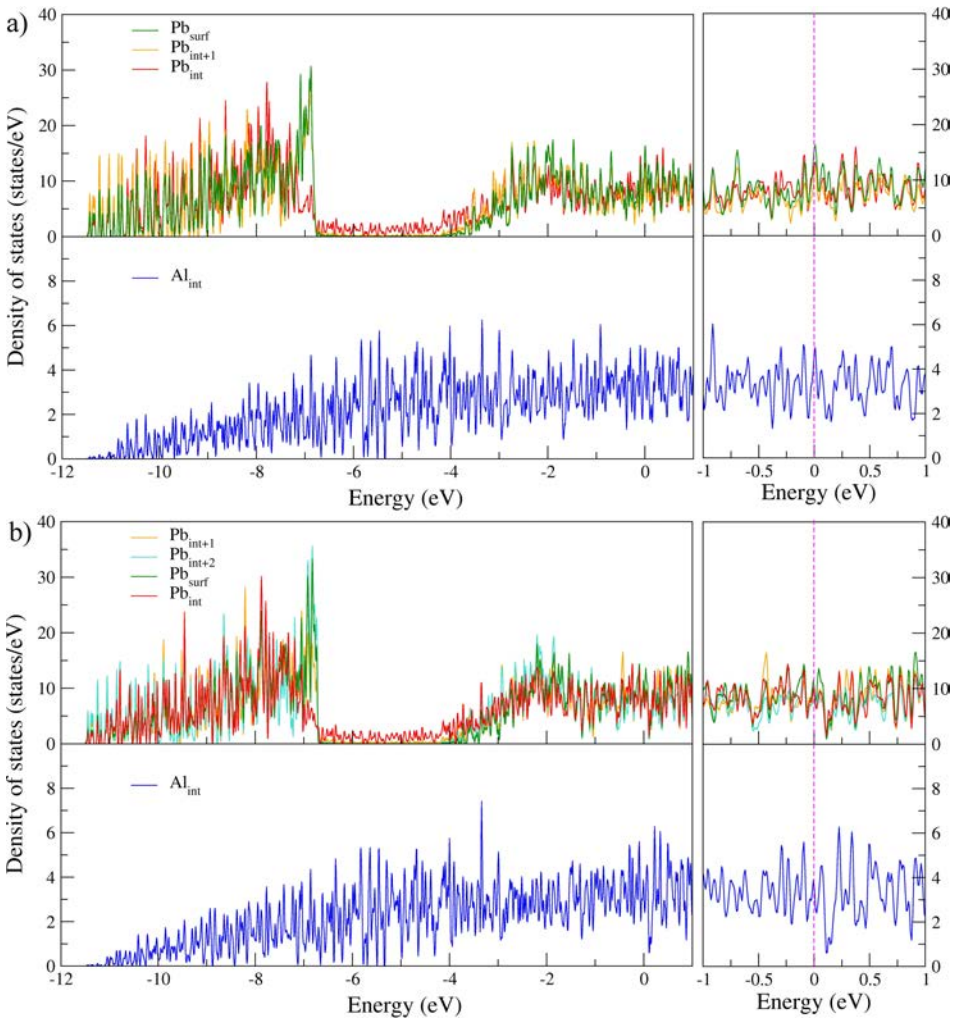

FIGURE C.2: DOS at the interface of Pb/Al(111) for 3 ML and 4 ML thickness of Pb, respectively. The calculation was performed using ISMEAR= -5 and 5×5×1 k-point grid.

Bibliography

1. Urban, K., Dubois, J.-M. & Belin-Ferré, E. *Complex metallic alloys: fundamentals and applications* (John Wiley&Sons, 2010).
2. Shechtman, D., Blech, I., Gratias, D. & Cahn, J. W. Metallic Phase with Long-Range Orientational Order and No Translational Symmetry. *Phys. Rev. Lett.* **53,** 1951–1953 (1984).
3. *Properties and applications of complex intermetallics* (ed Belin-Ferré, E.) (2008).
4. Dubois, J.-M. Properties-and applications of quasicrystals and complex metallic alloys. *Chemical Society Reviews* **41,** 6760–6777 (2012).
5. Dubois, J.-M. The applied physics of quasicrystals. *Physica Scripta* **1993,** 17 (1993).
6. Chan, K. S., Miller, M. A. & Peng, X. First-principles computational study of hydrogen storage in silicon clathrates. *Materials Research Letters* **6,** 72–78 (2018).
7. Dubois, J.-M. & Belin-Ferré, E. Wetting and adhesion properties of quasicrystals and complex metallic alloys. *Applied Adhesion Science* **3,** 28. ISSN: 2196-4351 (2015).
8. Park, J. Y., Ogletree, D. F., Salmeron, M., Ribeiro, R. A., Canfield, P. C., Jenks, C. J. & Thiel, P. A. Elastic and inelastic deformations of ethylene-passivated tenfold decagonal $\mathrm{Al-Ni-Co}$ quasicrystal surfaces. *Phys. Rev. B* **71,** 144203 (2005).
9. Gratias, D. *Quasicrystals: Current Topics, edited by E. Belin-Ferre, C. Berger, M. Quiquandon & A. Sadoc* (World Scientific Publishing, 2000).
10. Kovnir, K., Armbrüster, M., Teschner, D., Venkov, T., Jentoft, F. C., Knop-Gericke, A., Grin, Y. & Schlögl, R. A new approach to well-defined, stable and site-isolated catalysts. *Science and Technology of Advanced Materials* **8,** 420 (2007).
11. Slack, G. in *CRC Handbook of Thermoelectrics* (ed Rowe, D.) (CRC Press, Boca Raton, 1995).
12. Nolas, G., Cohn, J., Slack, G. & Schujman, S. Semiconducting Ge clathrates: Promising candidates for thermoelectric applications. *Applied Physics Letters* **73,** 178–180 (1998).
13. Toberer, E. S., Christensen, M., Iversen, B. B. & Snyder, G. J. High temperature thermoelectric efficiency in $Ba_8Ga_{16}Ge_{30}$. *Phys. Rev. B* **77,** 075203 (2008).
14. Takabatake, T., Suekuni, K., Nakayama, T. & Kaneshita, E. Phonon-glass electron-crystal thermoelectric clathrates: Experiments and theory. *Rev. Mod. Phys.* **86,** 669–716 (2014).
15. Zintl, E & Brauer, G. Metals and Alloys. X. Valence Electron Rule and the Atomic Radius of Non-noble Metals in Alloys. *Z. Phys. Chem. B* **20,** 245–271 (1933).
16. Schäfer, H. On the problem of polar intermetallic compounds: the stimulation of E. Zintl's work for the modern chemistry of intermetallics. *Annual Review of Materials Science* **15,** 1–42 (1985).
17. Baitinger, M., Böhme, B., Ormeci, A. & Grin, Y. in *The Physics and Chemistry of Inorganic Clathrates* 35–64 (Springer, 2014).
18. Zhang, H., Borrmann, H., Oeschler, N., Candolfi, C., Schnelle, W., Schmidt, M., Burkhardt, U., Baitinger, M., Zhao, J.-T. & Grin, Y. Atomic interactions in the p-type clathrate I $Ba_8Au_{5.3}Ge_{40.7}$. *Inorganic Chemistry* **50,** 1250–1257 (2011).
19. Zeiringer, I, Melnychenko-Koblyuk, N, Grytsiv, A, Bauer, E, Giester, G & Rogl, P. Phase Equilibria, Crystal Chemistry and Physical Properties of Au-Ba-Ge Clathrates. *Journal of Phase Equilibria and Diffusion* **32,** 115–127 (2011).
20. Nolas, G. S. *The physics and chemistry of inorganic clathrates* (Springer, 2014).
21. Cordier, G. & Woll, P. Neue ternäre intermetallische Verbindungen mit Clathratstruktur: Ba_8 (T, Si)$_6Si_{40}$ und Ba_6(T, Ge)$_6Ge_{40}$ mit T $\sim$ Ni, Pd, Pt, Cu, Ag, Au. *Journal of the Less Common Metals* **169,** 291–302 (1991).

22. Candolfi, C., Ormeci, A., Aydemir, U., Baitinger, M., Oeschler, N., Grin, Y. & Steglich, F. Multiband conduction in the type-I clathrate $Ba_8Ge_{43}\square_3$. *Phys. Rev. B* **84,** 205118 (2011).
23. Candolfi, C, Aydemir, U, Baitinger, M, Oeschler, N, Steglich, F & Grin, Y. High temperature thermoelectric properties of the type-I clathrate $Ba_8Au_xSi_{46-x}$. *Journal of Applied Physics* **111,** 043706 (2012).
24. Carrillo-Cabrera, W., Budnyk, S., Prots, Y. & Grin, Y. Ba_8Ge_{43} revisited: a 2a'× 2a'× 2a' Superstructure of the Clathrate-I Type with Full Vacancy Ordering. *Zeitschrift für anorganische und allgemeine Chemie* **630,** 2267–2276 (2004).
25. Ormeci, A. & Grin, Y. Coexistence of ionic and covalent atomic interactions (bonding inhomogeneity) and thermoelectric properties of intermetallic clathrates. *Journal of Thermoelectricity,* 16–32 (2015).
26. Aydemir, U, Candolfi, C, Borrmann, H, Baitinger, M, Ormeci, A, Carrillo-Cabrera, W, Chubilleau, C, Lenoir, B, Dauscher, A & Oeschler, N. Crystal structure and transport properties of $Ba_8Ge_{43}\square_3$. *Dalton Transactions* **39,** 1078–1088 (2010).
27. Euchner, H., Pailhès, S., Giordano, V. M. & de Boissieu, M. Understanding lattice thermal conductivity in thermoelectric clathrates: A density functional theory study on binary Si-based type-I clathrates. *Phys. Rev. B* **97,** 014304 (2018).
28. Herrmann, R. F. W., Tanigaki, K., Kawaguchi, T., Kuroshima, S. & Zhou, O. Electronic structure of Si and Ge gold-doped clathrates. *Phys. Rev. B* **60,** 13245–13248 (1999).
29. Zhao, J., Buldum, A., Ping Lu, J. & Fong, C. Y. Structural and electronic properties of germanium clathrates Ge_{46} and K_8Ge_{46}. *Phys. Rev. B* **60,** 14177–14181 (1999).
30. Saito, S. & Oshiyama, A. Electronic structure of Si_{46} and $Na_2Ba_6Si_{46}$. *Phys. Rev. B* **51,** 2628–2631 (1995).
31. Kawaji, H., Horie, H.-o., Yamanaka, S. & Ishikawa, M. Superconductivity in the Silicon Clathrate Compound (Na,Ba) $_xSi_{46}$. *Phys. Rev. Lett.* **74,** 1427–1429 (1995).
32. Fournée, V., Ledieu, J. & Park, J. Y. Surface Science of Complex Metallic Alloys. *Complex Metallic Alloys: Fundamentals and Applications,* 155–206 (2010).
33. Kaplan, W. D., Chatain, D., Wynblatt, P. & Carter, W. C. A review of wetting versus adsorption, complexions, and related phenomena: the rosetta stone of wetting. *Journal of Materials Science* **48,** 5681–5717 (2013).
34. Snoeijer, J. H. & Andreotti, B. A microscopic view on contact angle selection. *Physics of Fluids* **20,** 057101 (2008).
35. Young, T. III. An essay on the cohesion of fluids. *Philosophical transactions of the royal society of London* **95,** 65–87 (1805).
36. Yuan, Y. & Lee, T. R. in *Surface science techniques* 3–34 (Springer, 2013).
37. Rao, G, Zhang, D. & Wynblatt, P. A determination of interfacial energy and interfacial composition in Cu-Pb and Cu-Pb-X alloys by solid state wetting measurements. *Acta metallurgica et materialia* **41,** 3331–3340 (1993).
38. Léopoldès, J. & Damman, P. From a two-dimensional chemical pattern to a three-dimensional topology through selective inversion of a liquid–liquid bilayer. *Nature materials* **5,** 957 (2006).
39. Aronov, D., Molotskii, M. & Rosenman, G. Electron-induced wettability modification. *Phys. Rev. B* **76,** 035437 (2007).
40. Dubois, J., Fournée, V, Thiel, P. & Belin-Ferré, E. Measurements of contact angles of water on Al-based intermetallic surfaces. *Journal of Physics: Condensed Matter* **20,** 314011 (2008).
41. Bergman, C., Girardeaux, C., Perrin-Pellegrino, C., Gas, P., Dubois, J.-M. & Rivier, N. Contact angles of liquid metals on quasicrystals. *Journal of Physics: Condensed Matter* **20,** 314010 (2008).
42. Dubois, J.-M. in *Properties And Applications Of Complex Intermetallics* 1–91 (World Scientific Publishing, 2010).
43. Prutton, M. *Introduction to surface physics* (Clarendon Press, 1994).
44. Hove, M. A., Weinberg, W. H. & Chan, C.-M. *Low-energy electron diffraction: experiment, theory and surface structure determination* (Springer, 1986).

45. Attard, G & Barnes, C. Surfaces, Oxford chemistry primers (1998).
46. Wandelt, K. *Surface and Interface Science: Concepts and Methods* (John Wiley & Sons, 2012).
47. Wagner, C., Riggs, W., Davis, L., Moulder, J. & Muilenberg, G. Handbook of X-ray photoelectron spectroscopy: A reference book of standard spectra for identification and interpretation of XPS data. *Perkin-Elmer Corporation* (1979).
48. Yeh, J. & Lindau, I. Atomic subshell photoionization cross sections and asymmetry parameters: $1 \leqslant Z \leqslant 103$. *Atomic data and nuclear data tables* **32,** 1–155 (1985).
49. Seah, M. P. & Dench, W. A. Quantitative electron spectroscopy of surfaces: A standard data base for electron inelastic mean free paths in solids. *Surface and Interface Analysis* **1,** 2–11. ISSN: 1096-9918 (1979).
50. CasaXPS. Line Shapes. Casa Software Ltd. <http://www.casaxps.com/help_manual/manual_updates/LA_Lineshape.pdf> (2008).
51. CasaXPS: Peak Fitting in XPS. <http://www.casaxps.com/helpmanual/manualupdates/peakfittinginxps.pdf> (2006).
52. Hill, D., Meyer, H. & Weaver, J. Ba oxides: Core level binding energies and defect-related Fermi level pinning. *Surface science* **225,** 63–71 (1990).
53. Seah, M., Smith, G. & Anthony, M. AES: Energy calibration of electron spectrometers. Ian absolute, traceable energy calibration and the provision of atomic reference line energies. *Surface and interface analysis* **15,** 293–308 (1990).
54. Cros, A, Saoudi, R, Hollinger, G, Hewett, C. & Lau, S. An x-ray photoemission spectroscopy investigation of oxides grown on Au x Si1- x layers. *Journal of Applied Physics* **67,** 1826–1830 (1990).
55. McGilp, J. & Weightman, P. The L2, 3M4, 5M4, 5 Auger and photoelectron spectra of germanium. *Journal of Physics C: Solid State Physics* **9,** 3541 (1976).
56. Hofer, W. A., Foster, A. S. & Shluger, A. L. Theories of scanning probe microscopes at the atomic scale. *Rev. Mod. Phys.* **75,** 1287–1331 (2003).
57. Binnig, G. & Rohrer, H. Scanning tunneling microscopy. *Surface science* **126,** 236–244 (1983).
58. Wiesendanger, R. *Scanning probe microscopy and spectroscopy: methods and applications* (Cambridge university press, 1994).
59. Tersoff, J. & Hamann, D. R. Theory and Application for the Scanning Tunneling Microscope. *Phys. Rev. Lett.* **50,** 1998–2001 (1983).
60. Tersoff, J. & Hamann, D. R. Theory of the scanning tunneling microscope. *Phys. Rev. B* **31,** 805–813 (1985).
61. Omicron Nanotechnology GmbH. MATRIX Application Manual, 4.0 ed. (2017).
62. Horcas, I, Fernández, R., Gomez-Rodriguez, J., Colchero, J., Gómez-Herrero, J. & Baro, A. WSXM: a software for scanning probe microscopy and a tool for nanotechnology. *Review of scientific instruments* **78,** 013705 (2007).
63. Narumand, D. & Childs, K. Auger Spectrometers: A Tutorial Review. *Applied Spectroscopy Reviews* **34,** 139–158 (2004).
64. Inkson, B. in *Materials Characterization Using Nondestructive Evaluation (NDE) Methods* 17 –43 (Woodhead Publishing, 2016).
65. Gunawardane, R. P. & Arumainayagam, C. R. in *Handbook of applied solid state spectroscopy* 305–350 (Springer, 2006).
66. Kresse, G. & Hafner, J. *Ab initio* molecular dynamics for liquid metals. *Phys. Rev. B* **47,** 558–561 (1993).
67. Kresse, G. & Hafner, J. Ab initio molecular-dynamics simulation of the liquid-metal–amorphous-semiconductor transition in germanium. *Phys. Rev. B* **49,** 14251 (1994).
68. Kresse, G. & Furthmüller, J. Efficient iterative schemes for ab initio total-energy calculations using a plane-wave basis set. *Physical review B* **54,** 11169 (1996).
69. Kresse, G. & Furthmüller, J. Efficiency of ab-initio total energy calculations for metals and semiconductors using a plane-wave basis set. *Computational Materials Science* **6,** 15–50 (1996).

70. Hohenberg, P. & Kohn, W. Inhomogeneous Electron Gas. *Phys. Rev.* **136,** B864–B871 (1964).
71. Kohn, W. & Sham, L. J. Self-Consistent Equations Including Exchange and Correlation Effects. *Phys. Rev.* **140,** A1133–A1138 (1965).
72. Dirac, P. A. M. Quantum mechanics of many-electron systems. *Proc. R. Soc. Lond. A* **123,** 714–733 (1929).
73. Ceperley, D. M. & Alder, B. J. Ground State of the Electron Gas by a Stochastic Method. *Phys. Rev. Lett.* **45,** 566–569 (1980).
74. Becke, A. D. Density-functional exchange-energy approximation with correct asymptotic behavior. *Phys. Rev. A* **38,** 3098–3100 (1988).
75. Perdew, J. P. & Wang, Y. Pair-distribution function and its coupling-constant average for the spin-polarized electron gas. *Phys. Rev. B* **46,** 12947–12954 (1992).
76. Perdew, J. P., Burke, K. & Ernzerhof, M. Generalized Gradient Approximation Made Simple. *Phys. Rev. Lett.* **77,** 3865–3868 (1996).
77. Hammer, B., Hansen, L. B. & Nørskov, J. K. Improved adsorption energetics within density-functional theory using revised Perdew-Burke-Ernzerhof functionals. *Phys. Rev. B* **59,** 7413–7421 (1999).
78. Perdew, J. P., Ruzsinszky, A., Csonka, G. I., Vydrov, O. A., Scuseria, G. E., Constantin, L. A., Zhou, X. & Burke, K. Restoring the Density-Gradient Expansion for Exchange in Solids and Surfaces. *Phys. Rev. Lett.* **100,** 136406 (2008).
79. Klimeš, J., Bowler, D. R. & Michaelides, A. Chemical accuracy for the van der Waals density functional. *Journal of Physics: Condensed Matter* **22,** 022201 (2009).
80. *DFT-D3 method* <https://cms.mpi.univie.ac.at/vasp/vasp/DFT_D3_method.html>.
81. Grimme, S., Antony, J., Ehrlich, S. & Krieg, H. A consistent and accurate ab initio parametrization of density functional dispersion correction (DFT-D) for the 94 elements H-Pu. *The Journal of chemical physics* **132,** 154104 (2010).
82. Janthon, P., Luo, S., Kozlov, S. M., Vi, F., Limtrakul, J., Truhlar, D. G. & Illas, F. Bulk Properties of Transition Metals: A Challenge for the Design of Universal Density Functionals. *Journal of Chemical Theory and Computation* **10,** 3832–3839 (2014).
83. Gaudry, E., Shukla, A. K., Duguet, T., Ledieu, J., deWeerd, M.-C., Dubois, J.-M. & Fournée, V. Structural investigation of the (110) surface of γ-Al_4Cu_9. *Phys. Rev. B* **82,** 085411 (2010).
84. Meier, M., Ledieu, J., De Weerd, M.-C., Huang, Y.-T., Abreu, G. J. P., Pussi, K., Diehl, R. D., Mazet, T., Fournée, V. & Gaudry, E. Interplay between bulk atomic clusters and surface structure in complex intermetallic compounds: The case study of the $Al_5Co_2(001)$ surface. *Phys. Rev. B* **91,** 085414 (2015).
85. Meier, M., Ledieu, J., De Weerd, M.-C., Fournée, V. & Gaudry, E. Structural investigations of $Al_5Co_2(2\bar{1}0)$ and (100) surfaces: Influence of bonding strength and annealing temperature on surface terminations. *Phys. Rev. B* **93,** 075412 (2016).
86. Vogtenhuber, D. VASP. Basics II: electronic convergence and BZ sampling. <http://www.vasp.at/vasp-workshop/lectures/VASP_lecture_Basics2.pdf> (2016).
87. Blöchl, P. E. Projector augmented-wave method. *Phys. Rev. B* **50,** 17953–17979 (1994).
88. Kresse, G. & Joubert, D. From ultrasoft pseudopotentials to the projector augmented-wave method. *Phys. Rev. B* **59,** 1758 (1999).
89. Marsman, M. *Basics PAW Optimization VASP: Plane waves, the PAW method, and the Selfconsistency cycle* <https://th.fhi-berlin.mpg.de/th/Meetings/DFT-workshop-Berlin2011/presentations/2011-07-14_Marsman_Martijn.pdf>.
90. Vogtenhuber, D. VASP. Basics III: Ionic Relaxation, Stress Cell Shapes, Phonons and Molecular Dynamics. <http://www.vasp.at/vasp-workshop/lectures/VASP_lecture_Basics2.pdf> (2016).
91. Monkhorst, H. J. & Pack, J. D. Special points for Brillouin-zone integrations. *Phys. Rev. B* **13,** 5188–5192 (1976).

92. Lejaeghere, K., Van Speybroeck, V., Van Oost, G. & Cottenier, S. Error Estimates for Solid-State Density-Functional Theory Predictions: An Overview by Means of the Ground-State Elemental Crystals. *Critical Reviews in Solid State and Materials Sciences* **39,** 1–24 (2014).
93. Kittel, C. *Introduction to solid state* (John Wiley & Sons, 1966).
94. Barrett, C. Crystal Structure of Barium and Europium at 293, 78, and 5 K. *The Journal of Chemical Physics* **25,** 1123–1124 (1956).
95. S., C. A. Precise lattice constants of germanium, aluminum, gallium arsenide, uranium, sulphur, quartz and sapphire. *Acta Crystallographica* **15,** 578–582 (1962).
96. Ambrosetti, A. & Silvestrelli, P. L. Cohesive properties of noble metals by van der Waals–corrected density functional theory: Au, Ag, and Cu as case studies. *Phys. Rev. B* **94,** 045124 (2016).
97. Couderc, J., Garigue, G, Lafourcade, L & Nguyen, Q. Standard X-ray diffraction powder patterns. *Zeitschrift für Metallkunde* **50,** 708–716 (1959).
98. Bouad, N., Chapon, L., Marin-Ayral, R.-M., Bouree-Vigneron, F. & Tedenac, J.-C. Neutron powder diffraction study of strain and crystallite size in mechanically alloyed PbTe. *Journal of Solid State Chemistry* **173,** 189–195 (2003).
99. Owen, E. & Jones, D. M. Effect of grain size on the crystal structure of cobalt. *Proceedings of the Physical Society. Section B* **67,** 456 (1954).
100. Müller, S. Bulk and surface ordering phenomena in binary metal alloys. *Journal of Physics: Condensed Matter* **15,** R1429 (2003).
101. Shin, H., Pussi, K., Gaudry, E., Ledieu, J., Fournée, V., Alarcón Villaseca, S., Dubois, J.-M., Grin, Y., Gille, P., Moritz, W. & Diehl, R. D. Structure of the orthorhombic $Al_{13}Co_4$(100) surface using LEED, STM, and ab initio studies. *Phys. Rev. B* **84,** 085411 (2011).
102. Mihalkovi č, M. & Widom, M. First-principles calculations of cohesive energies in the $\mathrm{Al-Co}$ binary alloy system. *Phys. Rev. B* **75,** 014207 (2007).
103. Deringer, V. L. & Dronskowski, R. DFT studies of pristine hexagonal $Ge_1Sb_2Te_4$ (0001), $Ge_2Sb_2Te_5$(0001), and $Ge_1Sb_4Te_7$ (0001) surfaces. *The Journal of Physical Chemistry C* **117,** 15075–15089 (2013).
104. Bechstedt, F. *Principles of surface physics* (Springer Science & Business Media, 2012).
105. Schmidt, W. III-V compound semiconductor (001) surfaces. *Applied Physics A* **75,** 89–99 (2002).
106. Kresse, G, Furthmüller, J & Hafner, J. Ab initio force constant approach to phonon dispersion relations of diamond and graphite. *EPL (Europhysics Letters)* **32,** 729 (1995).
107. Ledieu, J, Gaudry, É, Loli, L. S., Villaseca, S. A., De Weerd, M.-C., Hahne, M., Gille, P., Grin, Y., Dubois, J.-M. & Fournée, V. Structural Investigation of the (010) Surface of the $Al_{13}Fe_4$ Catalyst. *Phys. Rev. Lett.* **110,** 076102 (2013).
108. Ledieu, J., Gaudry, É. & Fournée, V. Surfaces of Al-based complex metallic alloys: atomic structure, thin film growth and reactivity. *Science and technology of advanced materials* **15,** 034802 (2014).
109. *p4vasp* <http://www.p4vasp.at/>.
110. Becke, A. D. & Edgecombe, K. E. A simple measure of electron localization in atomic and molecular systems. *The Journal of Chemical Physics* **92,** 5397–5403 (1990).
111. Silvi, B. & Savin, A. Classification of chemical bonds based on topological analysis of electron localization functions. *Nature* **371,** 683 (1994).
112. Savin, A, Becke, A., Flad, J, Nesper, R, Preuss, H & Von Schnering, H. A new look at electron localization. *Angewandte Chemie International Edition* **30,** 409–412 (1991).
113. Savin, A., Jepsen, O., Flad, J., Andersen, O., Preuss, H. & von Schnering, H. Electron Localization in Solid-State Structures of the Elements: the Diamond Structure. *Angewandte Chemie International Edition in English* (1992).
114. Savin, B A ; Silvi & Colonna, F. Topological analysis of the electron localization function applied to delocalized bonds. *Canadian journal of chemistry* **74,** 1088–1096 (1996).
115. Kohout, M. & Savin, A. Influence of core-valence separation of electron localization function. *Journal of computational chemistry* **18,** 1431–1439 (1997).

116. Popelier, P. An analytical expression for interatomic surfaces in the theory of atoms in molecules. *Theoretica chimica acta* **87,** 465–476 (1994).
117. Popelier, P. A method to integrate an atom in a molecule without explicit representation of the interatomic surface. *Computer physics communications* **108,** 180–190 (1998).
118. Henkelman, G., Arnaldsson, A. & Jónsson, H. A fast and robust algorithm for Bader decomposition of charge density. *Computational Materials Science* **36,** 354–360 (2006).
119. Sanville, E., Kenny, S. D., Smith, R. & Henkelman, G. Improved grid-based algorithm for Bader charge allocation. *Journal of computational chemistry* **28,** 899–908 (2007).
120. Tang, W, Sanville, E & Henkelman, G. A grid-based Bader analysis algorithm without lattice bias. *Journal of Physics: Condensed Matter* **21,** 084204 (2009).
121. Yu, M. & Trinkle, D. R. Accurate and efficient algorithm for Bader charge integration. *The Journal of chemical physics* **134,** 064111 (2011).
122. Group, H. *Code: Bader Charge Analysis* <http://theory.cm.utexas.edu/henkelman/code/bader/>.
123. Anand, K., Allio, C., Krellner, C., Nguyen, H. D., Baitinger, M., Grin, Y., Ledieu, J., Fournée, V. & Gaudry, É. Charge Balance Controls the (100) Surface Structure of the $Ba_8Au_{5.25}Ge_{40.75}$ Clathrate. *The Journal of Physical Chemistry C* (2018).
124. Casalini, S., Bortolotti, C. A., Leonardi, F. & Biscarini, F. Self-assembled monolayers in organic electronics. *Chemical Society Reviews* **46,** 40–71 (2017).
125. Share, K., Westover, A., Li, M. & Pint, C. L. Surface engineering of nanomaterials for improved energy storage–A review. *Chemical Engineering Science* **154,** 3–19 (2016).
126. Nilsson, A., Pettersson, L. G. & Norskov, J. *Chemical bonding at surfaces and interfaces* (Elsevier, 2008).
127. Pitters, J. L., Dogel, I. A. & Wolkow, R. A. Charge control of surface dangling bonds using nanoscale schottky contacts. *ACS nano* **5,** 1984–1989 (2011).
128. Livadaru, L., Xue, P., Shaterzadeh-Yazdi, Z., DiLabio, G. A., Mutus, J., Pitters, J. L., Sanders, B. C. & Wolkow, R. A. Dangling-bond charge qubit on a silicon surface. *New Journal of Physics* **12,** 083018 (2010).
129. Motevalli, B., Taherifar, N., Wu, B., Tang, W. & Liu, J. Z. A density functional theory computational study of adsorption of Di-Meta-Cyano Azobenzene molecules on Si (111) surfaces. *Applied Surface Science* **422,** 557–565 (2017).
130. Yang, S., Prendergast, D. & Neaton, J. B. Tuning semiconductor band edge energies for solar photocatalysis via surface ligand passivation. *Nano letters* **12,** 383–388 (2012).
131. Teplyakov, A. V. & Bent, S. F. Semiconductor surface functionalization for advances in electronics, energy conversion, and dynamic systems. *Journal of Vacuum Science & Technology A: Vacuum, Surfaces, and Films* **31,** 050810 (2013).
132. Vilan, A. & Cahen, D. Chemical modification of semiconductor surfaces for molecular electronics. *Chemical reviews* **117,** 4624–4666 (2017).
133. Ledieu, J, Gaudry, É, Loli, L. S., Villaseca, S. A., De Weerd, M.-C., Hahne, M., Gille, P., Grin, Y., Dubois, J.-M. & Fournée, V. Structural Investigation of the (010) Surface of the $Al_{13}Fe_4$ Catalyst. *Phys. Rev. Lett.* **110,** 076102 (2013).
134. Christensen, M., Johnsen, S. & Iversen, B. B. Thermoelectric clathrates of type I. *Dalton transactions* **39,** 978–992 (2010).
135. Zeiringer, I, Chen, M., Bednar, I, Royanian, E, Bauer, E, Podloucky, R, Grytsiv, A, Rogl, P & Effenberger, H. Phase equilibria, crystal chemistry, electronic structure and physical properties of Ag–Ba–Ge clathrates. *Acta Materialia* **59,** 2368–2384 (2011).
136. Lifshits, V., Saranin, A. & Zotov, A. *Surface Phases on Silicon: Preparation, Structure, and Properties* (John Wiley & Sons, 1995).
137. Srivastava, G. Theory of semiconductor surface reconstruction. *Reports on Progress in Physics* **60,** 561 (1997).

138. Michaelides, A. & Scheffler, M. *An Introduction to the Theory of Crystalline Elemental Solids and their Surfaces* 13–72 (Wiley Online Library, 2013).
139. Lory, P.-F., Pailhès, S., Giordano, V. M., Euchner, H., Nguyen, H. D., Ramlau, R., Borrmann, H., Schmidt, M., Baitinger, M. & Ikeda, M. Direct measurement of individual phonon lifetimes in the clathrate compound $Ba_{7.81}Ge_{40.67}Au_{5.33}$. *Nature communications* **8,** 491 (2017).
140. Kraj čí, M. & Hafner, J. Surface structures of complex intermetallic compounds: An ab initio DFT study for the (100) surface of o-$Al_{13}Co_4$. *Phys. Rev. B* **84,** 115410 (2011).
141. Baur, W. H. & Tillmanns, E. How to avoid unnecessarily low symmetry in crystal structure determinations. *Acta Crystallographica Section B: Structural Science* **42,** 95–111 (1986).
142. Ponson, L., Bonamy, D. & Barbier, L. Cleaved surface of $i-\mathrm{AlPdMn}$ quasicrystals: Influence of the local temperature elevation at the crack tip on the fracture surface roughness. *Phys. Rev. B* **74,** 184205 (2006).
143. Conrad, M., Harbrecht, B., Weber, T., Jung, D. Y. & Steurer, W. Large, larger, largest–a family of cluster-based tantalum copper aluminides with giant unit cells. II. The cluster structure. *Acta Crystallographica Section B: Structural Science* **65,** 318–325 (2009).
144. Steurer, W. Stable clusters in quasicrystals: fact or fiction? *Philosophical magazine* **86,** 1105–1113 (2006).
145. Henley, C., De Boissieu, M & Steurer, W. Discussion on clusters, phasons and quasicrystal stabilisation. *Philosophical magazine* **86,** 1131–1151 (2006).
146. Henley, C. Clusters, phason elasticity and entropic stabilization: a theoretical perspective. *Philosophical Magazine* **86,** 1123–1129 (2006).
147. Rsch, F. & Trebin, H.-R. Comment on ?Cleaved surface of i-AlPdMn quasicrystals: Influence of the local temperature elevation at the crack tip on the fracture surface roughness? *Phys. Rev. B* **78,** 216201 (2008).
148. Zangwill, A. *Physics at surfaces* (Cambridge university press, 1988).
149. Krüger, P. & Pollmann, J. First-principles theory of sulfur adsorption on semi-infinite Ge (001). *Phys. Rev. Lett.* **64,** 1808 (1990).
150. Kirchner, E. & Baerends, E. A theoretical study of oxygen adsorption on Ge (001). *Surface science* **311,** 126–138 (1994).
151. Rohlfing, M., Krüger, P. & Pollmann, J. Quasiparticle band structures of clean, hydrogen-, and sulfur-terminated Ge (001) surfaces. *Phys. Rev. B* **54,** 13759 (1996).
152. Fleischmann, C., Schouteden, K., Merckling, C., Sioncke, S., Meuris, M., Van Haesendonck, C., Temst, K. & Vantomme, A. Adsorption of O2 on Ge (100): Atomic Geometry and Site-Specific Electronic Structure. *The Journal of Physical Chemistry C* **116,** 9925–9929 (2012).
153. Perdew, J. P., Burke, K. & Ernzerhof, M. Emission in symmetric heavy ion reactions at sub-threshold energies. *Phys. Rev. Lett.* **78,** 1396 (1997).
154. Tersoff, J & Hamann, D. Theory and application for the scanning tunneling microscope. *Phys. Rev. Lett.* **50,** 1998 (1983).
155. Kozlowski, D. & Pilmé, J. New insights in quantum chemical topology studies using numerical grid-based analyses. *Journal of computational chemistry* **32,** 3207–3217 (2011).
156. De Santis, L & Resta, R. Surface reconstructions and bonding via the electron localization function: the case of Si (001). *Solid state communications* **111,** 583–588 (1999).
157. Vitos, L., Ruban, A., Skriver, H. L. & Kollar, J. The surface energy of metals. *Surface Science* **411,** 186–202 (1998).
158. Jaccodine, R. Surface energy of germanium and silicon. *Journal of the Electrochemical Society* **110,** 524–527 (1963).
159. Patra, A., Bates, J. E., Sun, J. & Perdew, J. P. Properties of real metallic surfaces: Effects of density functional semilocality and van der Waals nonlocality. *Proceedings of the National Academy of Sciences* **114,** E9188–E9196 (2017).
160. Tran, R., Xu, Z., Radhakrishnan, B., Winston, D., Sun, W., Persson, K. A. & Ong, S. P. Surface energies of elemental crystals. *Scientific data* **3,** 160080 (2016).

161. Singh-Miller, N. E. & Marzari, N. Surface energies, work functions, and surface relaxations of low-index metallic surfaces from first principles. *Phys. Rev. B* **80,** 235407 (2009).
162. Ooi, N., Rairkar, A. & Adams, J. B. Density functional study of graphite bulk and surface properties. *Carbon* **44,** 231–242 (2006).
163. Mathur, A, Sharma, P & Cammarata, R. From our readers: Negative surface energy?clearing up confusion. *Nature Materials* **4,** 186 (2005).
164. Koczorowski, W, Puchalska, A, Grzela, T, Radny, M., Jurczyszyn, L, Schofield, S., Czajka, R & Curson, N. Initial growth of Ba on Ge (001): An STM and DFT study. *Phys. Rev. B* **91,** 235319 (2015).
165. Pieczyrak, B., Trembulowicz, A., Antczak, G. & Jurczyszyn, L. Nature of monovacancies on quasi-hexagonal structure of reconstructed Au (100) surface. *Applied Surface Science* **407,** 345–352 (2017).
166. Bechstedt, F. & Scheffler, M. Alkali adsorption on GaAs (110): atomic structure, electronic states and surface dipoles. *Surface science reports* **18,** 145–198 (1993).
167. Pauling, L. *The Nature of the Chemical Bond and the Structure of Molecules and Crystals: An Introduction to Modern Structural Chemistry* (Cornell university press Ithaca, NY, 1960).
168. Leung, T., Kao, C., Su, W., Feng, Y. & Chan, C. Relationship between surface dipole, work function and charge transfer: Some exceptions to an established rule. *Phys. Rev. B* **68,** 195408 (2003).
169. Walker, M, Tedder, M., Palmer, J., Mudd, J. & McConville, C. Low temperature removal of surface oxides and hydrocarbons from Ge (100) using atomic hydrogen. *Applied Surface Science* **379,** 1–7 (2016).
170. Skriver, H. L. & Rosengaard, N. Surface energy and work function of elemental metals. *Phys. Rev. B* **46,** 7157 (1992).
171. Gangopadhyay, U. & Wynblatt, P. Solid-State wetting of graphite by Pb and Pb-Ni alloys. *Metallurgical and Materials Transactions A* **25,** 607–615 (1994).
172. De Boer, F., Boom, R, Mattens, W., Miedema, A. & Niessen, A. Cohesion in Metals: Transition Metal Alloys. *Elsevier Science Publishers B. V.* **1,** 758 (1988).
173. Stein, F., He, C. & Dupin, N. Melting behaviour and homogeneity range of $B2$ CoAl and updated thermodynamic description of the Al-Co system. *Intermetallics* **39,** 58–68 (2013).
174. Chernikov, M. A., Bernasconi, A., Beeli, C., Schilling, A. & Ott, H. R. Low-temperature magnetism in icosahedral $Al_{70}Mn_9Pd_{21}$. *Phys. Rev. B* **48,** 3058–3065 (1993).
175. Kraj čí, M., Hafner, J. & Mihalkovi č, M. Ab initio study of the surface of a decagonal Al-Co-Ni quasicrystal. *Phys. Rev. B* **73,** 134203 (2006).
176. Wynblatt, P. The effects of interfacial segregation on wetting in solid metal-on-metal and metal-on-ceramic systems. *Acta materialia* **48,** 4439–4447 (2000).
177. Ortiz, C., Eriksson, O. & Klintenberg, M. Data mining and accelerated electronic structure theory as a tool in the search for new functional materials. *Computational Materials Science* **44,** 1042 –1049 (2009).
178. Wang, Z., Wynblatt, P. & Chatain, D. Observation of a sharp transition in contact angle in the wetting of graphite by solid Pb-Ni alloys. *Interface Science* **7,** 173–180 (1999).
179. Bergman, C., Girardeaux, C., Perrin-Pellegrino, C., Gas, P., Chatain, D., Dubois, J.-M. & Rivier, N. Wetting of decagonal $Al_{13}Co_4$ and cubic AlCo thin films by liquid Pb. *Philosophical Magazine* **86,** 849–854 (2006).
180. Villaseca, S. *Ph.D. thesis* 2011.
181. Landa, A, Wynblatt, P, Johnson, E & Dahmen, U. Computer simulation of Pb/Al interfaces. *Acta Materialia* **48,** 2557–2563 (2000).
182. Deniozou, T., Ledieu, J., Fournée, V., Wu, D. M., Lograsso, T. A., Li, H. I. & Diehl, R. D. Aperiodic and modulated Pb thin films on fivefold icosahedral Al-Cu-Fe and Al(111): Tailoring the structure of Pb. *Phys. Rev. B* **79,** 245405 (2009).

183. Yu, D. & Scheffler, M. First-principles study of low-index surfaces of lead. *Phys. Rev. B* **70,** 155417 (2004).
184. Bombis, C., Emundts, A, Nowicki, M & Bonzel, H. Absolute surface free energies of Pb. *Surface science* **511,** 83–96 (2002).
185. Hermann, A., Furthmüller, J., Gäggeler, H. W. & Schwerdtfeger, P. Spin-orbit effects in structural and electronic properties for the solid state of the group-14 elements from carbon to superheavy element 114. *Phys. Rev. B* **82,** 155116 (2010).
186. Dahmen, U., Xiao, S., Paciornik, S., Johnson, E. & Johansen, A. Magic-Size Equilibrium Shapes of Nanoscale Pb Inclusions in Al. *Phys. Rev. Lett.* **78,** 471–474 (1997).
187. Shi, Z., Lowekamp, J. B. & Wynblatt, P. Energy of the Pb {111} ||Al {111} interface. *Metallurgical and Materials Transactions A* **33,** 1003–1007 (2002).
188. Kraj čí, M., Hafner, J., Ledieu, J., Fournée, V. & McGrath, R. Quasiperiodic Pb monolayer on the fivefold i-Al-Pd-Mn surface: Structure and electronic properties. *Phys. Rev. B* **82,** 085417 (2010).
189. Jank, W. & Hafner, J. Structural and electronic properties of the liquid polyvalent elements: The group-IV elements Si, Ge, Sn, and Pb. *Phys. Rev. B* **41,** 1497–1515 (1990).
190. Gaudry, E., Chatelier, C., McGuirk, G. M., Serkovic Loli, L. N., de Weerd, M.-C., Ledieu, J., Fournée, V., Felici, R., Drnec, J., Beutier, G. & de Boissieu, M. Structure of the $Al_{13}Co_4$(100) surface: Combination of surface x-ray diffraction and ab initio calculations. *Phys. Rev. B* **94,** 165406 (2016).
191. Addou, R., Shukla, A., Villaseca, S. A., Gaudry, É., Deniozou, T., Heggen, M., Feuerbacher, M., Widmer, R., Gröning, O., Fournée, V., Dubois, J. & Ledieu, J. Lead adsorption on the $Al_{13}Co_4$(100) surface: heterogeneous nucleation and pseudomorphic growth. *New Journal of Physics* **13,** 103011 (2011).
192. Fournée, V., Gaudry, É, Ledieu, J., De Weerd, M.-C. & Diehl, R. Quasi-ordered C60 molecular films grown on the pseudo-ten-fold (100) surface of the $Al_{13}Co_4$ quasicrystalline approximant. *Journal of Physics: Condensed Matter* **28,** 355001 (2016).
193. Aykol, M. & Persson, K. A. Oxidation Protection with Amorphous Surface Oxides: Thermodynamic Insights from Ab Initio Simulations on Aluminum. *ACS Applied Materials & Interfaces* **10,** 3039–3045 (2018).
194. *Basics of thermodynamics and phase transition in complex intermetallics* (ed Belin-Ferré, E.) (World Scientific Publishing, 2008).
195. Janot, C. *Quasicrystals - A Primer (Monographs on the Physics and Chemistry of Materials)* (Oxford University Press, 1994).
196. Walter, S. & Deloudi, S. *Crystallography of quasicrystals: concepts, methods and structures* (Springer Science & Business Media, 2009).
197. Zeng, X., Ungar, G., Liu, Y., Percec, V., Dulcey, A. E. & Hobbs, J. K. Supramolecular dendritic liquid quasicrystals. *Nature* **428,** 157 (2004).
198. Talapin, D. V., Shevchenko, E. V., Bodnarchuk, M. I., Ye, X., Chen, J. & Murray, C. B. Quasicrystalline order in self-assembled binary nanoparticle superlattices. *Nature* **461,** 964 (2009).
199. Förster, S., Meinel, K., Hammer, R., Trautmann, M. & Widdra, W. Quasicrystalline structure formation in a classical crystalline thin-film system. *Nature* **502,** 215 (2013).
200. Engel, M., Damasceno, P. F., Phillips, C. L. & Glotzer, S. C. Computational self-assembly of a one-component icosahedral quasicrystal. *Nature materials* **14,** 109 (2015).
201. Dubois, J.-M. Quasicrystals. *Journal of Physics: Condensed Matter* **13,** 7753 (2001).
202. Jenks, C. & Thiel, P. A. Comments on quasicrystals and their potential use as catalysts. *Journal of Molecular Catalysis A: Chemical* **131,** 301–306 (1998).
203. Tsai, A. & Yoshimura, M. Highly active quasicristalline Al-Cu-Fe catalyst for steam reforming methanol. *Applied Catalysis* **214,** 237–241 (2001).
204. Yoshimura, M. & Tsai, A. Quasicrystal application on catalyst. *Journal of Alloy and Compounds* **342,** 451–454 (2002).

205. Tanabe, T., Kameoka, S. & Tsai, A. A novel catalyst fabricated from Al-Cu-Fe quasicrystal for steam reforming methanol. *Catalysis Today* **111,** 153–157 (2006).
206. Phung Ngoc, B., Geantet, C., Aouine, M., Bergeret, G., Raffy, S. & Marlin, S. Quasicrystal derived catalyst for steam reforming methanol. *International Journal of hydrogen energy* **33,** 1000–1007 (2008).
207. Eichler, A. VASP. Sampling the Brillouin-zone. <https://www.vasp.at/vasp-workshop/slides/k-points.pdf>.
208. Methfessel, M. & Paxton, A. T. High-precision sampling for Brillouin-zone integration in metals. *Phys. Rev. B* **40,** 3616–3621 (1989).
209. Benali, A. *Ph.D. thesis* 2010.
210. Trambly de Laissardière, G., Julien, J.-P. & Mayou, D. Quantum Transport of Slow Charge Carriers in Quasicrystals and Correlated Systems. *Phys. Rev. Lett.* **97,** 026601 (2006).

Propriétés de surface des intermétalliques complexes à l'échelle du nanomètre: du fondamental aux applications

Les alliages métalliques complexes (CMAs) sont des composés intermétalliques dont la structure cristallographique diffère de celle des alliages conventionnels par le nombre conséquent d'atomes dans la maille (jusqu'à plusieurs milliers d'atomes), généralement arrangés sous forme d'agrégats atomiques de haute symétrie. Ils sont prometteurs pour un certain nombre d'applications technologiques, en particulier les revêtements fonctionnels, en raison de leurs propriétés de surface uniques. Cette thèse a pour objectif, à la fois la détermination de la structure et des propriétés électroniques d'une surface d'un CMA de la famille des clathrates intermétalliques, et des propriétés de mouillage intrinsèques de plusieurs CMAs à base d'aluminium. Dans une première partie, nous nous sommes intéressés aux surfaces de bas indice (100) et (110) du clathrate $Ba_8Au_{5.25}Ge_{40.75}$. Leurs structures atomiques et électroniques ont été déterminées en combinant des expériences de sciences des surfaces et des calculs basés sur la théorie de la fonctionnelle de la densité. La structure tridimensionnelle de $Ba_8Au_{5.25}Ge_{40.75}$, formée d'un réseau de deux types de cages (structure hôte) à base de germanium et d'or, qui emprisonnent les atomes de Ba, induit une nanostructuration de la surface contrôlée par son orientation, puisque le type de cages préservées à la surface diffère pour les surfaces (100) et (110). Dans les deux cas, les atomes de Ba qui protrudent à la surface, ont un rôle primordial pour la stabilité de surface : ils assurent un transfert de charge qui sature les liaisons pendantes des atomes de germanium en surface. Dans une seconde partie, les propriétés intrinsèques de mouillage de plusieurs CMAs à base d'aluminium, ont été déterminées par une approche couplant des mesures de microscopie et des calculs ab initio. Expérimentalement, les angles de contact de gouttes de plomb (métal sonde) sur plusieurs surfaces de CMAs ont été systématiquement mesurés. Les angles précédents étant fonction, entre autres, de l'énergie interfaciale, des calculs d'énergie interfaciale ont été menés, d'une part avec un substrat d'un métal simple, Al(111), et d'autre part sur un substrat de CMA, $Al_{13}Co_4$(100). Les résultats obtenus mettent en évidence une forte influence de la structure de l'interface sur l'énergie interfaciale.

Mots-clés: physique des surfaces, alliages métalliques complexes, mouillage, clathrates, nanoscience, DFT (théorie de la fonctionnelle de la densité)

Surface properties of complex intermetallics at the nanoscale: from fundamentals to applications

Complex metallic alloys (CMAs) are intermetallic compounds possessing a large unit cell containing several tens to hundreds of atoms. Their structure can be described alternatively by the packing of highly symmetric atomic clusters. Clathrate (or cage) compounds are a new class of CMAs having a crystal structure described by a complex arrangement of covalently-bonded cages. The $Ba_8Au_{5.25}Ge_{40.75}$ type-I clathrate is one such cage compound, whose bulk properties have been (and still are) extensively explored for thermoelectric applications. In fact, it is possible to tune the compound electronic structure by a fine control of its bulk composition. Regarding the properties of the $Ba_8Au_{5.25}Ge_{40.75}$ surface, information remains scarce if not inexistent. However, it is known that the surfaces of CMAs often exhibit interesting surface properties. To this end, we have studied two low-index surfaces: BaAuGe(100) and BaAuGe(110) by a combination of experimental (XPS; LEED; STM) and computational (DFT) methods. Experimental results show no evidence for surface segregation and LEED patterns are consistent with (1x1) bulk terminations with no surface reconstruction. The interplay between the 3D nano-caged structure and 2D surfaces is investigated. We demonstrate that the surface structures of the two surfaces considered preserve the bulk structure cages in addition to an ordered arrangement of surface Ba atoms. The two surfaces are formed by a breakage of highly directional covalent bonds present within the framework, hence leading to destabilizing dangling bonds. Ab initio calculations show that the surface structure is stabilized through electron charge transfer from protruding Ba to surface Ge and Au atoms, saturating the dangling bonds. This charge-balance mechanism lifts the possible surface reconstruction envisaged. We reveal how the surface nanostructuration is surface orientation dependent. The results indicate that the surface electronic structure of BaAuGe(110) is impacted by the Au surface concentration. The surface models for BaAuGe(100) and BaAuGe(110) present a metallic character and low work function values, useful for further applications. Such structurally complex surfaces may also be used as templates for novel nanoscale architectures. Further in this work, we also applied the state-of-the-art surface science techniques to investigate the wetting properties of Al-based CMAs. In these experiments, chemically inert Pb element was used as a metal probe. Systematic analysis is done to find the correlation between the wetting properties and the electronic structure properties of these CMAs. Interfacial energy calculations have been performed to model the Pb/CMA interface based on few approaches reported in literature. We have tested these approaches on a moiré patterned Pb(111)/Al(111) interface. This interface is found to be controlled by geometric factors. Hence, an acquired understanding was applied to Pb deposited on $Al_{13}Co_4$(100) (Al-rich side) interface.

Keywords: Surface physics, CMA (Complex Metallic Alloys), wettability, clathrates, nanoscience, DFT (Density Functional Theory)